Corrosion Properties of Nanocrystalline Co and Co-P Alloys

by

Hundal Jung

B.Sc., Hanyang University, Seoul, Korea, 1987

M.Sc. Hanyang University, Seoul, Korea, 1989

THESIS SUBMITTED IN PARTIAL FULFILLMENT OF
THE REQUIREMENTS FOR THE DEGREE OF

DOCTOR OF PHILOSOPHY

in

The Faculty of Graduate Studies

(Materials Engineering)

UNIVERSITY OF BRITISH COLUMBIA

March 2006

ABSTRACT

In this thesis, the corrosion properties of electrodeposited nanocrystalline Co and Co-1.1 and 2.1 wt% P alloys (7 to 20 nm grain size) were investigated in a wide range of solution pH by using polarization and electrochemical impedance spectroscopy techniques along with scanning electron microscopy, energy dispersive X-ray spectroscopy, transmission electron microscopy and X-ray photoelectron spectroscopy analysis. In 0.1 M H_2SO_4 and 0.5 M Na_2SO_4 solutions (pH 1 and 3, rspectively), nanocrystalline Co showed higher anodic and cathodic reaction rates and reduced localized corrosion attack compared to coarse grained Co counterparts. An enhanced electrochemical reaction rate of nanocrystalline Co was correlated to a significant increase in grain boundaries and triple junctions. For pure Co, a catalytic mechanism has been suggested to rationalize a more favorable route for their anodic dissolution reaction. An addition of P leads to a significant increase of corrosion resistance of nanocrystalline Co-P due to the increased elemental P concentration on the corroded surface at E_{oc} following an initial selective dissolution of Co. However, at higher anodic overpotential, the superior corrosion resistance of nanocrystalline Co-P did not last due to the formation of a porous and defective surface film. The excellent corrosion resistance of nanocrystalline Co-P deteriorated from heat treatment at 350 °C and 800 °C due to higher chemical heterogeneity. In a 3.56 % NaCl solution at pH 6.2, nanocrystalline Co-P showed a higher anodic dissolution rate than that of nanocrystalline Co due to a reduced adsorption area of chloride ions. However, the corrosion rate of nanocrystalline Co-P decreased in comparison to nanocrystalline Co due to a much smaller cathodic exchange current density for oxygen reduction on nanocrystalline Co-P. A physical model was elaborated to explain the different response of annealed nanocrystalline Co-P by considering the different adsorption properties of chloride ions. In a 0.1 M NaOH solution at pH 13, all tested Co and Co-P samples exhibited active-passive-transpassive behaviors with the onset of primary and secondary passivations. While anodic polarization curves for poly- and nanocrystalline Co had qualitatively very similar behavior, nanocrystalline Co-P showed higher passivation current densities due to their decreased passive film resistance and reduced film thickness. XPS analysis revealed that the passive film formed in the primary passivation ranges was consisted of mainly $Co(OH)_2$ with a thickness of >10 nm. The passive

film formed during secondary passivation consisted of rather complex compounds such as Co_3O_4, Co_2O_3, $Co(OH)_3$ as well as $Co(OH)_2$ with a thickness of <10 nm. This last finding was common to poly- and nanocrystalline Co and nanocrystalline Co-1.1 wt% P.

Table of Contents

List of Tables

List of Figures

List of Acronyms

AES	Auger Electron Spectroscopy
ASM	The American Society of Metals
ASTM	The American Society for Testing and Materials
CPE	Constant Phase Element
EDX	Energy Dispersive X-ray Spectroscopy
EIS	Electrochemical Impedance Spectroscopy
FCC	Face Centered Cubic
FFT	Fast Fourier Transform
HCP	Hexagonal Close Packed
GPIB	General Purpose Interface Bus Board
PHEDP	Pulsed-High-Energy-Density Plasma
SADP	Selected Area Diffraction Pattern
SCC	Stress Corrosion Cracking
SCE	Saturated Calomel electrode (reference electrode)
SEM	Scanning Electron Microscopy
SHE	Standard Hydrogen Electrode
TAP	Tomography Atom Probe
TEM	Transmission Electron Microscopy
XRD	X-ray Diffraction
XPS	X-ray Photoelectron Spectroscopy
STM	Scanning Tunneling Microscopy

List of Symbols

Δ	Grain boundary thickness (width) (nm)
A_a	Area for anodic site (m^2)
A_c	Area for cathodic site (m^2)
A_{gb}	Total grain boundary area (m^2)
d	Grain size (diameter) (nm)
δ_L	P enriched layer thickness (nm)
ε_o	Permittivity of free space (8.85×10^{-12} F/m)
ε	Permittivity (dielectric constant)
E_{corr}	Corrosion potential (Volt)
E_{crit}	Critical potential (Volt)
$E_{pass(I)}$	Primary passivation potentials (Volt)
$E_{pass(II)}$	Secondary passivation potentials (Volt)
E_{oc}	Open circuit potential (Volt)
E_{rest}	Rest potential (Volt)
E_{trans}	Transpassive potential (Volt)
f	Frequency (Hz)
g	Geometrical factor
γ_{gb}	Specific grain boundary free energy (J/m^2)
$\Delta\vec{G}_{poly}$	Molar activation energy of metal dissolution in polycrystals (J/mol)
$\Delta\vec{G}_{nano}$	Molar activation energy of metal dissolution in nanocrystals (J/mol)
G^{xs}	Excess free energy (J/mol)
H^{xs}	Excess enthalpy (J/mol)
i_a	Anodic current density (A/cm^2)
i_c	Cathodic current density (A/cm^2)
i_{corr}	Corrosion current density (A/cm^2)
i_{crit}	Critical current density (A/cm^2)
$i_{peak(I)}$	Peak anodic current density at the onset of the primary passivation (A/cm^2)
$i_{peak(II)}$	Peak anodic current density at the onset of the secondary passivation (A/cm^2)

i_{pass}	Passivation current density (A/cm^2)
$\vec{k}$	Anodic dissolution rate (mol/m^2s)
$\overleftarrow{k}$	Cathodic reduction rate (mol/m^2s)
μ^o	Standard chemical potential (J/mol)
Q_{dl}	Double layer capacitance (F/cm^2)
Q_e	Equivalent capacitance (F/cm^2)
Q_F	Film capacitance (F/cm^2)
R_i	Interfacial resistance (Ωcm^2)
R_F	Film resistance (Ωcm^2)
σ	Warburg coefficient ($\Omega/s^{1/2}$)
S_{ic}	Surface area fraction of total intercrystalline defects
S_{gb}	Surface area fraction of grain boundaries
S_{tj}	Surface area fraction of triple junctions
S^{xs}	Excess entropy (J/mol•K)
t_F	Passive film thickness (nm)
V_{ic}	Volume fraction of total intercrystalline defects
V_{gb}	Volume fraction of grain boundaries
V_{tj}	Volume fraction of triple junctions
V_m	Molar volume (m^3/mol)
ω	Angular frequency (s^{-1})
Z'	Real part of impedance (Ω)
Z''	Imaginary part of impedance (Ω)
Z_w	Warburg impedance (Ω)

Acknowledgments

I wish to give my sincere thanks to Dr. Akram Alfantazi from the department of Materials Engineering at UBC for his guidance and encouragement through out this research project. I would also like to thank all of my supervisory committee members including Dr. Desmond Tromans, Dr. Rizhi Wang, Dr. Tom Troczynski and Dr. Elod Gyenge as well as my university examiners, Dr. David Wilkinson and Dr. David Dixon for their great help, technical assistance and support.

My thanks are also extended to other faculty and staff members and fellow graduate students for their help, particularly to Edouard Asselin for his help.

Special thanks go to my wife Yoonjung and my daughter Sookyung for their support and understanding during this work.

I would further like to acknowledge the Natural Sciences and Engineering Research Council of Canada, Integran Technologies Inc. and the University of British Columbia for their financial support.

1 Introduction

Since their first introduction in 1981 [Gleiter, H., 1981], the characteristics of nanocrystalline materials (i.e. materials with an average grain size of less than 100 nm) have been the subject of numerous studies. Many reports showed unique and often enhanced mechanical, chemical, and magnetic/electrical properties which arise from their extremely small grain size when compared with their conventional polycrystalline counterparts [Gleiter, H., 1989]. This property can be useful for applications such as corrosion and wear resistant coatings, soft magnetic materials for magnetic recording, and electrocatalysts for hydrogen evolution and oxidation reactions [Erb, U., 2001].

Today, nanocrystalline metals and alloys as well as composites can be produced by gas condensation, spray conversion, ball milling, electrodeposition and other techniques [Hadjipanayis, G. C. and Siegel, R. W., 1993; Michael Nastasi et al, 1991; David L. Bourell 1996]. The electrodeposition method has been identified as an economically viable technique for producing nanocrystalline materials both in bulk form and as coatings on other substrates [Erb, U., 1995]. Direct current and pulsed current plating have been successfully employed in producing pure metals (e.g. Ni, Co), binary alloys (e.g. Ni-P, Ni-Fe, Co-Mo, Co-P, Co-W), ternary alloys (e.g. Ni-Fe-Cr) as well as metal composites (e.g. Ni-SiC). This technique was incorporated in the first large-scale industrial application for structural nanocrystalline materials: the "Electrosleeve^{TM}" technology involves the in-situ electrodeposition of nanocrystalline Ni microalloy sleeves to repair damaged steam generator tubes in nuclear reactors [Palumbo, G., 1997].

Furthermore, nanocrystalline materials in general offer very promising prospects in protective coating applications because of their dramatic improvement in hardness and strength. For example, for electrodeposited nanocrystalline Co at an average grain size of 12 nm, the hardness value was over 525 VHN which was about 2 times higher than that of polycrystalline Co with a 5 μm grain size. The yield and tensile strengths of this nanocrystalline Co also increased about 3 times compared to its polycrystalline Co counterpart as shown in Figure 1-1 [Karimpoor et al., 2002]. In order to approach the higher hardness values of hard chromium coatings, McCrea et al. [McCrea, J., et al. 2001] made an

attempt to increase the hardness of nanocrystalline Co electrodeposits by alloying with P. Also, the annealing of Co-P alloys at elevated temperature lead to a further increase of hardness via a precipitation-hardening mechanism (Figure 1-2).

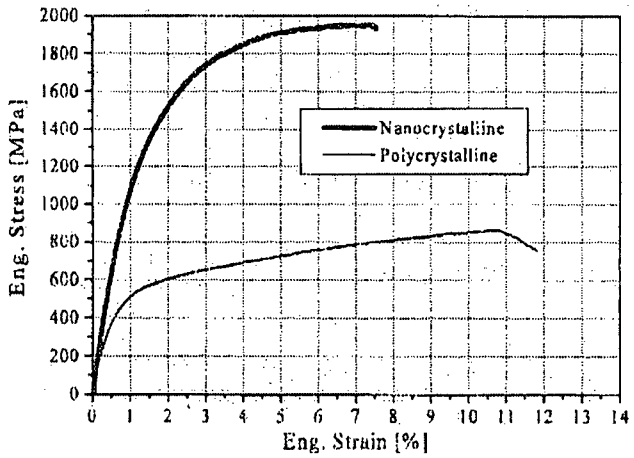

Figure 1-1 Stress-strain curves for nanocrystalline and polycrystalline Co at a strain rate of 5×10^{-4}(1/s) [Karimpoor, A. A. et al. 2002].

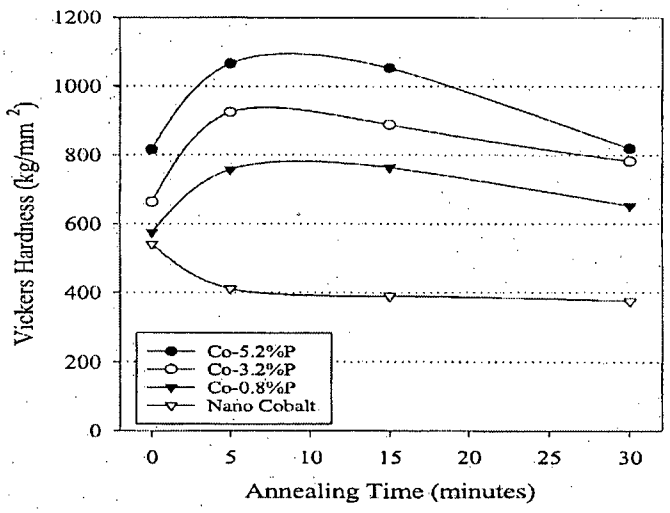

Figure 1-2 Hardness variation with annealing time for various nanocrystalline Co-P deposits. [McCrea, J., et al. 2001].

These nanocrystalline Co and Co alloys have also been shown to possess good magnetic properties, i.e. high saturation magnetization [Aus, M. J. et al, 1998] and good

thermal stability [Hibbard, G. et al, 2001]; coupled with their desirable wear resistance, magnetic recording heads are another possible application for these materials.

Recently, nanocrystalline Co and Co-P alloys have been identified as candidate materials for replacing hexavalent Cr coatings in wear and corrosion resistant coating applications due to their comparable hardness and lower volume wear loss compared to that of hexavalent Cr coatings [Palumbo, G. et al, 2002].

However, corrosion studies on Co in general have been rather limited and to date there has been very little work on the corrosion properties of nanocrystalline Co and Co-P alloys produced by electrodeposition (see section 2.2.3). In order to successfully apply alloy design principles to synthesize better materials than those currently available, an understanding of the corrosion properties of nanocrystalline Co and Co-P alloys is of high importance.

Thus, the main objective of this Ph.D. study is to investigate the corrosion properties of nanocrystalline Co and Co-P alloys prepared by electrodeposition by examining their corrosion behavior in a wide range of solution pH, ranging from 1 to 13, and by comparing this behavior to their coarse grained polycrystalline counterparts. Particular emphasis will be placed on the effects of grain size refinement and P alloying on the electrochemical response of these materials. An attempt will also be made to identify the anodic dissolution mechanism.

Chapter 2 is a literature review that discusses the previous corrosion studies for both conventional polycrystalline Co and Co-P alloys as well as nanocrystalline materials synthesized by several different methods. The unique microstructural characteristics of nanocrystalline materials as presented in the literature will also be addressed in Chapter 2. Research objectives will be presented in Chapter 3. Detailed experimental approach methods and microstructural characterization results are presented in Chapter 4. The main corrosion testing results obtained are addressed in Chapter 5. Finally, overall conclusions and recommendations for future work are presented in Chapters 6 and 7, respectively.

2 Literature Review and Backgrounds

2.1 Conventional Polycrystalline Co and Co-P Alloys

2.1.1 Elemental Co and P

Cobalt (Co) is a member of the iron triad in the eighth group of Mendelef's Table with atomic number 27 and atomic weight 58.94. The electron configurations are $1s^2$ $2s^2$ $2p^6$ $3s^2$ $3p^6$ $3d^7$ $4s^2$ [Jaubert, G. F., 1949]. Cobalt exhibits a valency of 2 or 3, the bivalent state being the stable one for the simple ion when not coordinated to anything but water. The melting point of cobalt is 1493 °C, its boiling point about 3100 °C. Its atomic volume is 6.7 cm^3/g-atom; the effective atomic radius for bivalent cobalt has been reported as 0.72 ~ 0.82 Å and for neutral cobalt atoms, 1.25 ~ 1.39 Å. Cobalt has a density of 8.9 g/ml for most solid forms. Cobalt can exist in two crystalline forms, i.e. hexagonal close-packed (called α-cobalt) and face-centered cubic cobalt (called ε-cobalt). With the use of X-ray analysis, Hull [1919] was the first to detect the transformation near 400 °C from hexagonal cobalt at low temperature to cubic cobalt at high temperature.

Phosphorus (P) is a non-metallic solid with atomic number 15 and atomic weight 30.97. The melting point of phosphorus is 44.3 °C. Its atomic volume is 17 cm^3/g-atom and the atomic radius is 1.23 Å. The density of phosphorus is 1.82 g/ml. Various oxidation states exist. [Pourbaix, M., 1966]

2.1.2 Applications

Early in the 20th century there was an interest in electrodeposited cobalt and cobalt alloy because of their excellent decorative properties and corrosion resistance as well as their ability to be electroformed. Moreover, magnetic properties of Co, Co-Fe, Co-Ni, Co-P and Co-Pt alloys are remarkable in electronic applications, such as recording tapes, memory drums, disks, and cards, particularly in the computer industry [Morral, F. R., 1964; Hibbard, G. et al., 2001]. In addition, the low coefficient of friction and high hardness and wear

resistance of Co-W, Co-P, Co-Mo and Co-Ni alloys are expanding fields for industrial cobalt alloy plating [Safranek, W. H., 1974; Betteridge, W., 1982].

Furthermore, these alloys exhibit low uniform corrosion rates in aggressive chemical environments such as strong acids, oxidized solutions, and alkalides, and also exhibit immunity in some cases to stress corrosion cracking and hydrogen cracking [ASM Handbook, 2003]. These combined advantages make them obvious materials for gas turbines, power generations, oil and gas equipment, chemical processing and steel production. Their resistances to pitting and also crevice corrosion in saline media, along with other favorable properties, suggest their additional use as implants in the human body to strengthen or replace bone structures.

2.1.3 Corrosion Properties of Co and Co-P Alloys

2.1.3.1 Thermodynamic Aspects

The E-pH diagram provides a thermodynamic basis for a better understanding of dissolution and oxide formation phenomena in aqueous solutions at various electrochemical conditions. Regions of stability of solid and soluble species are defined at different activities based on the data of standard free energies.

E-pH diagram for Co-H_2O

Figure 2-1a and b show the E-pH diagrams for conventional Co-H_2O and nanocrystalline Co-H_2O systems, respectively, at 1 atm, 298 K. Thermodynamic data used for constructing this diagram are listed in Table 2-1. With respect to Figure 2-1a and b, the (a) and (b) lines represent the E and pH conditions below which water is reduced to form H_2 and above which it oxidized to form O_2, respectively, as follows.

$$2H^+ + 2e^- = H_2 \qquad (2\text{-}1)$$

$$O_2 + 4H^+ + 4e^- = 2H_2O \qquad (2\text{-}2)$$

The stability of water is determined by two electrochemical reactions, (a) and (b). Standard chemical lines labeled (a) and (b) define the boundaries within which water is thermodynamically stable.

In Figure 2-1a, cobalt becomes unstable and forms cobaltous ions, Co^{2+}, at anodic potential above -0.4549 V_{SHE} in acid and weakly alkaline solutions. In very acid solution, cobaltic ions, Co^{3+}, can be formed at a potential above 1.808 V_{SHE}. With an increase in pH, Co^{2+} reacts with OH^- ions to form cobaltous hydroxide, $Co(OH)_2$, at a low potential. The hydrated oxide, $Co(OH)_2$, is thermodynamically more stable than the anhydrous oxide, CoO, based on the thermodynamic data (see Table 2-1), thus the hydrated form of the oxide is considered. This precipitation begins at pH 9.3 for a 10^{-6} M solution. However the precipitate $Co(OH)_2$ may redissolve as dicobalite ions, $HCoO_2^-$, when the pH is increased to higher than 13.05. Depending on the applied potential, the phases that can be formed during the anodic corrosion of Co are $Co(OH)_2$, Co_3O_4, $Co(OH)_3$, and CoO_2 in weakly alkaline media.

An attempt was made to modify the E-pH diagram for the Co-H_2O system while considering the excess free energy in nanocrystalline Co due to its much higher surface area fraction of intercrystalline defects (i.e., grain boundaries and triple junctions) than conventional Co (see section 2.2.1). The modified E-pH diagram for nanocrystalline Co-H_2O system was constructed by using the standard chemical potential of 1.231 kJ/mol for nanocrystalline Co with a grain size of 20 nm (see Table 2-1). From the calculated E-pH diagram as shown in Figure 2-1b, it was found that the equilibrium lines between nanocrystalline Co and Co^{2+}, $Co(OH)_2$, and $HCoO_2^-$ shifted to more negative potentials in the amount of 6.4 mV as compared to those for the conventional Co-water system. These shifts indicate that nanocrystalline Co has a stronger tendency for active dissolution (acid and strong alakiline solutions) as well as for passivation (weakly alkaline solution) as compared to that of conventional Co.

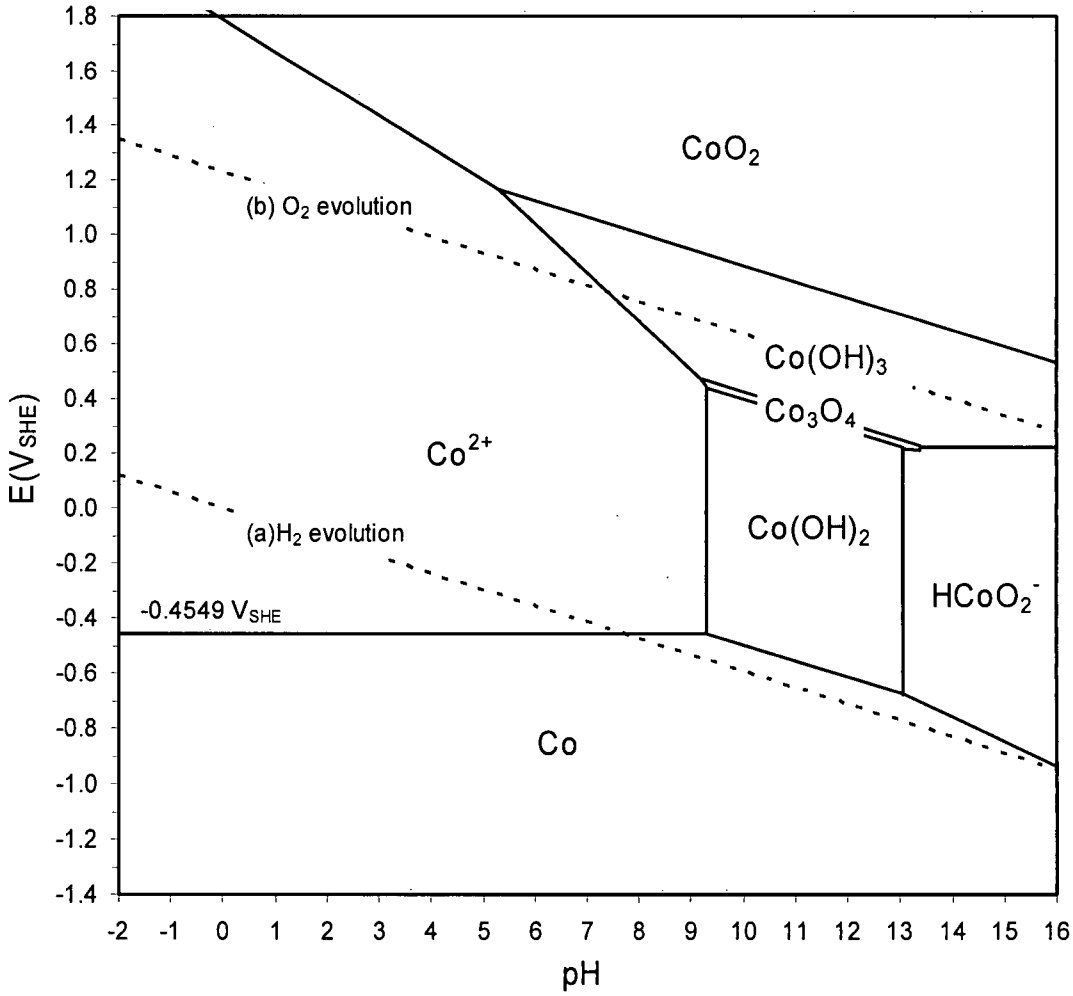

(a)

Figure 2-1 Calculated E-pH diagrams for (a) conventional Co- H_2O and (b) nanocrystalline Co (grain size of 20 nm)- H_2O systems at 298K, 1atm (activity of Co species 10^{-6})

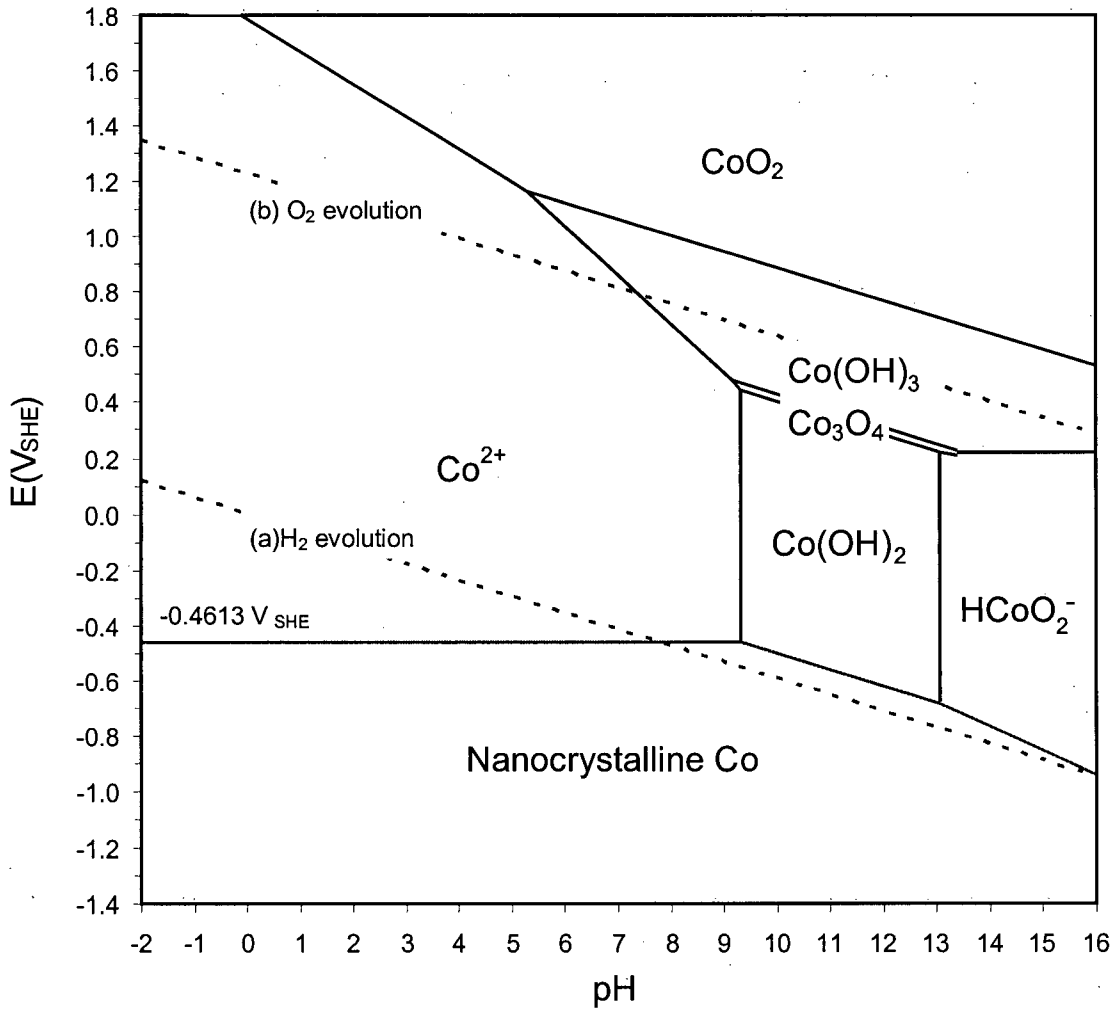

(b)

Figure 2-1 (continued)

Table 2-1 Standard chemical potentials of Co species and water at 298 K

Species	State	μ^o (kJ/mol)
H^+	aqueous	0.00
OH^-	aqueous	-157.30
H_2	gas	0.00
O_2	gas	0.00
H_2O	liquid	-237.18
Co	solid	0.00
Nanocrystalline Co (g.s., 20nm)	solid	1.231*
$Co(OH)_2$	solid	-218.82
CoO	solid	-205.02
Co_3O_4	solid	-702.08
Co_2O_3	solid	-481.58
Co^{2+}	aqueous	-53.56
Co^{3+}	aqueous	120.92
$HCoO_2^-$	aqueous	-347.27
CoO_2	solid	-216.73
$Co(OH)_3$	solid	-596.64

Note: Data from Pourbaix. M., [1966] except the data for nanocrystalline Co.

* The excess free energy for nanocrystalline Co with a grain size of 20 nm was estimated from the equations (5-7) and (5-9) by substitution of the measured excess interfacial enthalpy of its material by Hibbard et al. [2001] (see section 5.1.1.1)

E-pH diagram for P-H_2O

In the case of stability diagrams for P-H_2O system, there are two different diagrams that can exist as shown in Figure 2-2 (not taking into account the hydrides of phosphorous) and Figure 2-3 (considering the hydrides of phosphorous).

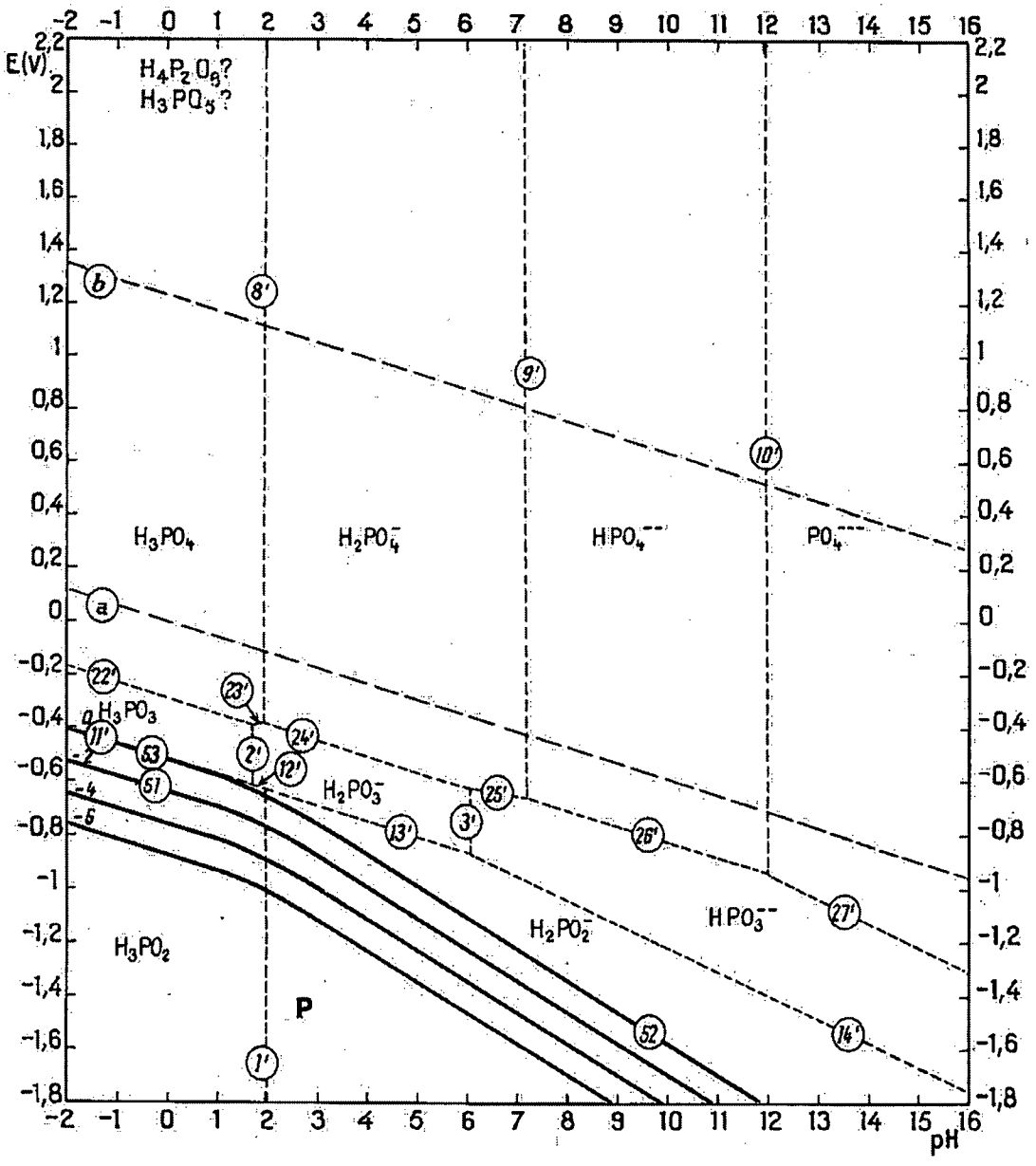

Figure 2-2 E-pH diagram for P-H_2O systems at 298K, 1atm (not taking into account the hydrides of phosphorus: considering white phosphorus) [Pourbaix, M., 1966]

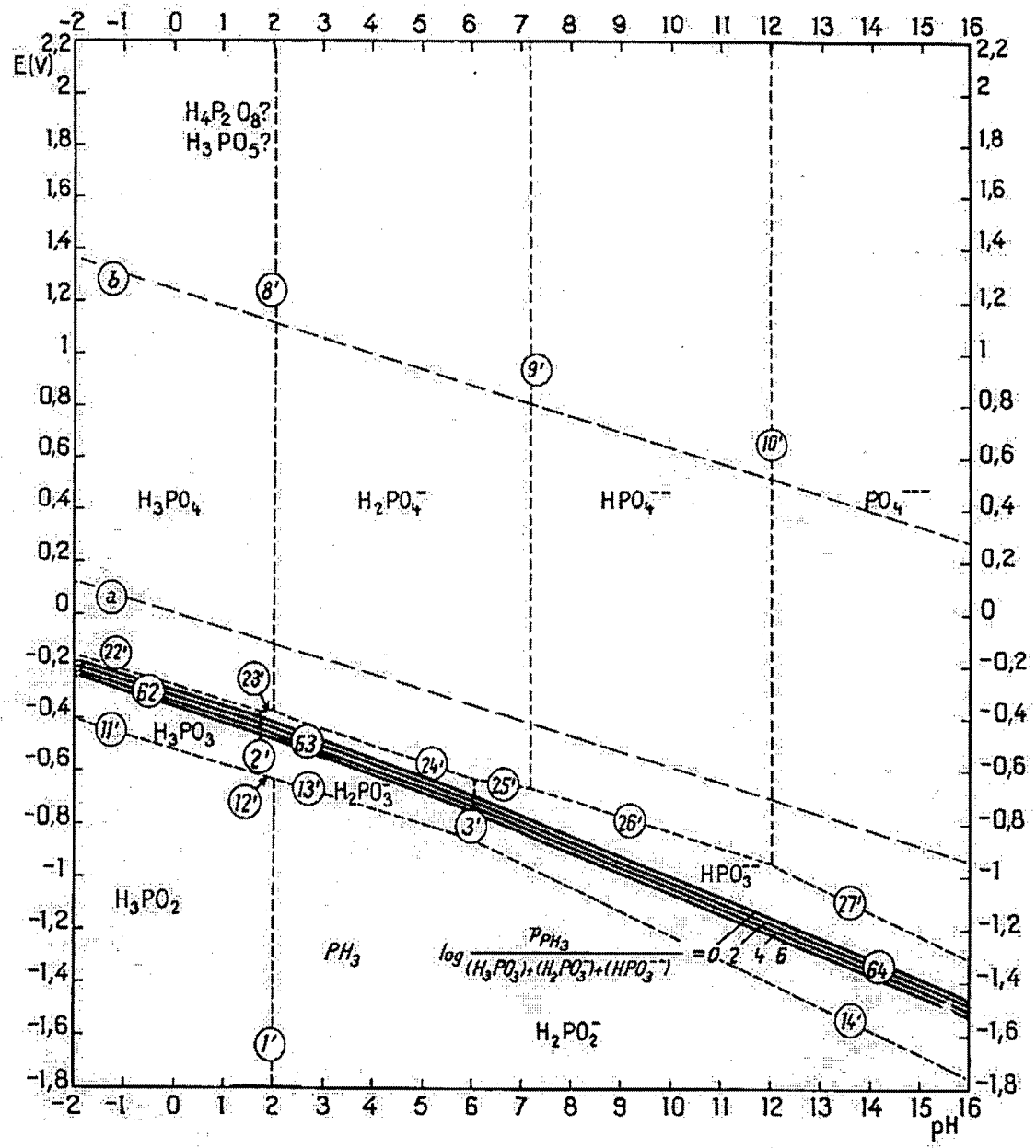

Figure 2-3 E-pH diagram for P-H_2O systems at 298K, 1atm (considering the hydrides of phosphorus) [Pourbaix, M., 1966]

In Figure 2-2, not taking into account the hydrides of phosphorus, since the domain of stability for P lies entirely below the equilibrium potentials to form H_2, P is very unstable thermodynamically in aqueous solutions. Therefore P can be oxidized to hypophophorous acid (H_3PO_2) or hypophosphite ($H_2PO_2^-$), i.e., the monovalent state, and to the trivalent state substance such as phosphorous acid (H_3PO_3) or phosphites ($H_2PO_3^-$, HPO_3^{2-}). Further oxidation can also lead to the formation of phosphoric acid (H_3PO_4) or phosphates ($H_2PO_4^-$, HPO_4^{2-}, PO_4^{3-}), i.e., the pentavalent state as a consequence of increasing oxidizing power (e.g. anodic overpotential).

The gaseous hydride PH_3 can also be formed when the hydrides of phosphorous, i.e., P_4H_2 and P_2H_4 take into account the electrochemical reactions (Figure 2-3). The position of the domain of stability of PH_3 below line (a) characterizes it as a reducing substance, thermodynamically unstable and tending to decompose into phosphorous and hydrogen. The hydride PH_3 can also be oxidized to phosphorous acid (H_3PO_3) or phosphites ($H_2PO_3^-$, HPO_3^{2-}), or to phosphoric acid (H_3PO_4) and phosphates ($H_2PO_4^-$, HPO_4^{2-}, PO_4^{3-}). The liquid hydride P_4H_2 and solid hydride P_2H_4 are thermodynamically unstable with respect to the gaseous hydride PH_3.

It was pointed out by Pourbaix, M., [1966] that hypophosphorous acid (H_3PO_2) and hypophosphites ($H_2PO_2^-$) could be stable in practice due to a very slow reduction process even if these substances are powerful reducing agents, which means thermodynamically unstable in the aqueous solutions of all pH's. E-pH diagrams are only a guide to predict where passivation is likely to occur. Thermodynamic diagrams do not take into account kinetics or possible differences in local solution chemistry at metal surfaces.

2.1.3.2 Anodic Dissolution Mechanism of Fe and Co

Most corrosion processes are of an electrochemical nature. The interpretation of corrosion phenomena is based on the knowledge of the electrochemical kinetics resulting from recent progress in measuring techniques. Although simple systems are fairly well understood at present, not all aspects of the complicated kinetics of transition metal have

been elucidated, especially corroding systems in practical conditions. Even though of little interest for practical corrosion problems, pure metals are extremely basic to any approach of the mechanism of anodic dissolution, which is much simpler than for alloys. The metals belonging to the so-called iron group (e.g. Co and Ni) have been far less extensively investigated than iron itself. Therefore, the previous studies for active dissolution of iron in aqueous solution are also reviewed in this section to gain further understanding of anodic dissolution mechanism.

Iron (Fe)

The active dissolution of iron in acidic solution has been the subject of a very large number of papers over the last 50 years. All reaction mechanisms are based on the generally agreed experimental evidence that the dissolution rate increases with the solution pH at potentials well below the onset of passvation.

The kinetics for iron in acidic solution was studied by Bonhoeffer and Heusler, [1957] starting in the middle of the 1950s. They measured anodic and cathodic polarization curves under both steady state and transient conditions at different pH values and Fe^{2+} concentrations in the bulk solutions. From the anodic Tafel slopes and electrochemical reaction orders, a catalytic charge transfer mechanism involving transfer of Fe(II) in one step was postulated. They found that the anodic Tafel slope was about 30 mV and the reaction order for hydroxyl ion was about two (2) under steady state. According to the catalytic mechanism, charge transfer occurs at kinks. Neglecting pH dependence of the rate, the rate determining step may be written;

$$Fe'Fe_k \Leftrightarrow Fe'_k + Fe^{2+} + 2e^- \qquad (2.3)$$

Fe_k is an atom in a kink which upon dissolving leaves its neighboring atom Fe' in the position of a kink, Fe'_k.

In the beginning of the 1960s, Bockris and Drazic, [1962] investigated the kinetics of the Fe/Fe^{2+} electrode in acidic solution using different iron samples. The kinetic data

obtained differed from those of Bonhoeffer and Heusler. The anodic Tafel slope of about 40 mV and the reaction order of about one (1) were observed. Therefore, they adopted the noncatalytic consecutive dissolution mechanism for their interpretation. According to this mechanism, $(FeOH)_{ads}$ enters in a noncatalytic one-electron transfer step by which it is oxidized to $FeOH^+$ after the initial hydrolysis of step;

$$Fe + H_2O \Leftrightarrow (FeOH)_{ads} + H^+ + e^- \tag{2.4}$$

$$(FeOH)_{ads} \rightarrow FeOH^+ + e^- \quad (rds) \tag{2.5}$$

$$FeOH^+ + H^+ \Leftrightarrow Fe^{2+}_{aq} + H_2O \tag{2.6}$$

Later many other authors reinvestigated the kinetics of the Fe/Fe^{2+} system under various experimental conditions, but mainly two different sets of kinetic data can be observed depending on the microstructure of the electrode materials. For a long time, the controversy about the validity of these mechanisms remained based on kinetic criteria drawn from true steady state and the Tafel slope and reaction order with respect to OH^- are two main parameters taken into consideration.

In fact, it is a very common experience that corrosion is deeply influenced by the metallurgical state of the material (e.g., cold working, annealing, grain size, boundaries, twinning, and segregation). The contribution to this field is mainly due to Hilbert, F. Y., et al. [1971], who claimed in their papers that the catalytic mechanism of iron dissolution is favored on highly active material, i.e., iron with a high density of crystal imperfections and dislocations produced by cold working. On the contrary, Hilbert, F. Y., et al. [1971] also observed that the consecutive mechanism would likely take place preferentially on relatively inactive, annealed, or single crystal samples. Table 2-2 shows the theoretical and experimental values of the steady state kinetic parameters for both mechanisms according to Hilbert, F. Y., et al. [1971].

Table 2-2 Kinetic data for Iron dissolution at 298 K [Hilbert, F. Y., et al. 1971]

	Catalytic mechanism		Consecutive mechanism	
	calculated	experimental	calculated	experimental
Tafel slope (mV)	29.6	30 ± 2	39.4	40 ±2
Reaction order/OH^-	2	2 ±0.3	1	1 ±0.1

Hilbert, F. Y., et al. [1971] as well as Schweickert, H. et al. [1980] also proposed the modified catalytic mechanism involving OH^- ions. The apparently unacceptable participation of hydroxyl ions in the reaction at these low pH values can be related to the strong dissociative power of transition metals with respect to water, an assumption supported for Fe by experimental evidence in ultra high vacuum [Ishikawa, Y., et al., 1991] and it is now generally accepted that anodic dissolution involves the existence of intermediate surface bonds between the metallic state and the solution species. Both groups of mechanisms stem from a common initial hydrolysis step assumed to be at equilibrium such as Eq.(2.4) According to the modified catalytic mechanism, $(FeOH)_{ads}$ enters in a catalytic sequence of dissolution at the end of which $(FeOH)_{ads}$ is regenerated and Fe is dissolved as $(FeOH)^+$:

$$Fe + (FeOH)_{ads} \Leftrightarrow Fe(FeOH)_{ads} \tag{2.7}$$

$$Fe(FeOH)_{ads} + OH^- \rightarrow FeOH^+ + (FeOH)_{ads} + 2e^- \quad \text{(rds)} \tag{2.8}$$

Iron atoms at kinks, Fe_k, shifted to the next neighboring atom, denoted Fe', in the dissolving edge:

$$Fe'(Fe_kOH)_{ads} + OH^- \rightarrow FeOH^+ + (Fe'_k\,OH)_{ads} + 2e^- \tag{2.9}$$

Finally, $FeOH^+$ is assumed to react with solution protons:

$$FeOH^+ + H^+ \Leftrightarrow Fe^{2+}_{aq} + H_2O \tag{2.10}$$

An elaborated interpretation of the catalytic role played by FeOH in the catalytic mechanism was more recently proposed by Heusler et al. [1982]. According to this model, FeOH is associated with a kink or half-crystal atom on a dissolving edge of terrace (or ledge). If one atom is removed from such a position, the active site for dissolution is simply transferred onto the next atom on the ledge. In other words, FeOH is self-regenerated and can be regarded as a catalyst, a single entity being able to dissolve a very large numbers of atoms. Figure 2-4 shows the shift of the active site for dissolution from one atom to the next one. Annihilation of kinks takes place by collision of two kinks of opposite sign, and generation of new kinks occurs at the corner position, the intersection of steps.

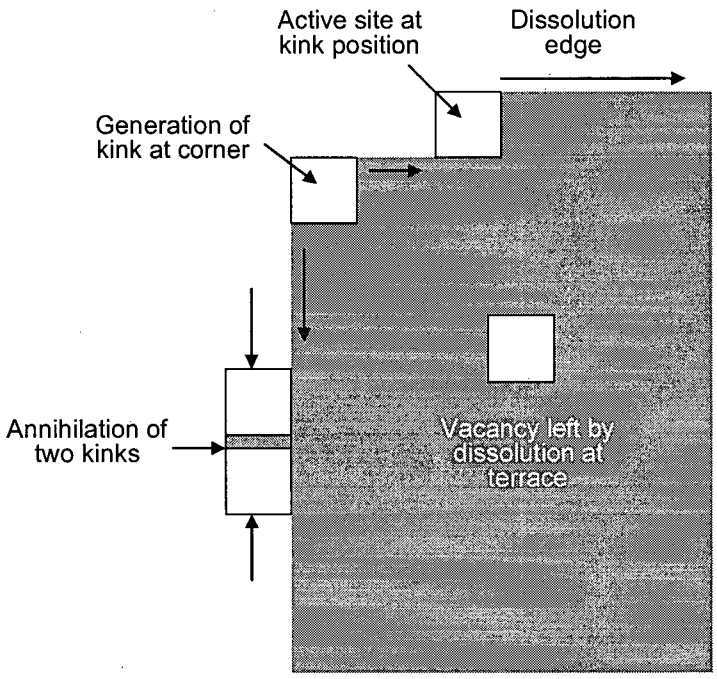

Figure 2-4 Schematic of two-dimensional lattice kinks at steps (edges or ledges), corners and terrace position [Heusler, K. E., 1982].

Anodic dissolution of iron was also elaborated by an atomistic description with a successful issue. Starting in the middle of the 1970s, Allgaier, W. and Heusler, K. E., [1979] and Folleher, B. and Heusler, K. E., [1984] had developed in a series of papers an experimental and modeling approach aimed at giving a crystallographic basis to the catalytic mechanism. It was demonstrated that a strong correlation existed between the kinetics and the atomistic structures of the electrode surface vicinal to {211} of iron single crystals in acidic solutions. The surface concentration of kinks strongly depends on the electrode potential, while the step density is determined by the pH of the solution. However, the problem remains of understanding the pH dependence of the step nucleation probability [Folleher, B. and Heusler, 1984].

Further investigation of iron dissolution by impedance analysis [Bechet, B., et al., 1977: Keddam, M., et al., 1981] has proved that both catalytic and consecutive mechanisms are operative with a relative contribution depending on the electrode potential and solution pH. A systematic analytic screening of all possible 40 reaction schemes in which three (3) Fe-containing surface species are involved completed by a numerical simulation finally led to selecting the reaction pattern shown below. They combined the catalytic and consecutive mechanisms in a parallel reaction scheme:

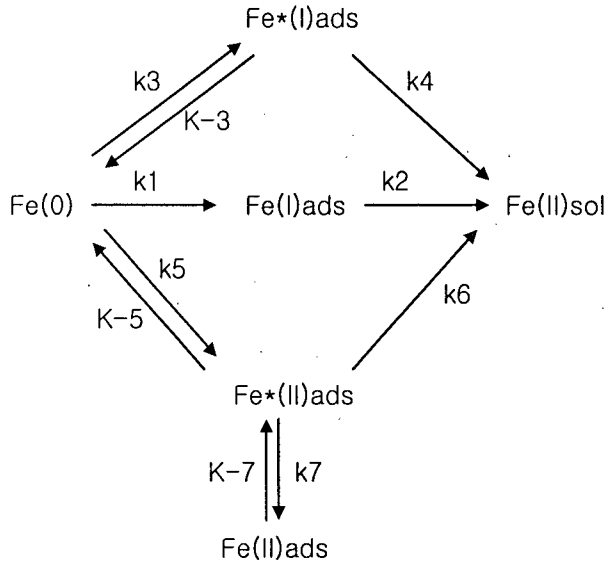

(2.9)

The three coverages determining the impedance properties in the active and transition domains are related to $Fe^*(I)_{ads}$, $Fe^*(II)_{ads}$ and $Fe(II)_{ads}$. The superscript (*) indicates species involved in catalytic dissolution paths.

In this scheme, the formation of $Fe(I)_{ads}$ from Fe(0) corresponds to chemisorption of OH^- according to Eq.(2.4), and k1, k2 path is the consecutive mechanism established early by impedance measurements bounded to the hertz range and covering low pH and low current density [Epelboin, I. and Keddam, M, 1970]. The dissolution of Fe^{2+}_{sol} via active sites, $Fe^*(I)_{ads}$, can be identified with the catalytic mechanism. At the active site $Fe^*(II)_{ads}$, two OH were believed to be adsorbed. Thus the iron in these sites is formally divalent. The second catalytic path leading to Fe^{2+}_{sol} was introduced in order to explain the number of inductive loops and the behavior in the transition and prepassivation ranges. $Fe(II)_{ads}$ is a precursor of the passive film. Using scheme (2.9), the ac behavior was simulated in good agreement with the experimental results [Keddam, M., et al., 1981]. However, the kinetic parameters used were mostly unrealistic, e. g. asymmetric electrochemical charge transfer coefficients being nearly one or zero, moreover a calculated steady state Tafel slope of 60 mV at T = 298 K is not in agreement with the experimental results (see Table 2-2).

The interpretation of the electrochemical testing (e.g., dc polarization and ac impedance measurements), morphological, and other results in terms of an iron dissolution mechanism is still controversial. Obviously, it deserves further theoretical and experimental efforts.

Cobalt (Co)

To date the studies for an anodic dissolution mechanism of cobalt are still lacking. Kravtsov, V. I. [1959] first reported the kinetic data for cobalt in a 0.5 M H_2SO_4 solution. He observed that the steady state polarization curve of cobalt followed Tafel lines and the anodic Tafel slope was $b \leq 30$ mV at 298 K. Later, Heusler, K. E. [1967] also investigated cobalt in perchlorate solutions at pH 1.3 and 3.3. As shown in Figure 2-5, the steady state polarization curves at 298 K also followed the Tafel line and the Tafel slope was $b = 29 \pm 5$ mV. From the

pH dependence of the anodic current density at constant electrode potential, a reaction order $y(OH^-) = 2.0 \pm 0.3$ with respect to hydroxyl ions was calculated, which was in agreement with Iofa, Z. A. and Wei Pao-ming, [1962] and Schwabe, K. and Voigt, C. [1966].

Thus, from the previous observations for anodic Tafel slope and reaction order for OH^- of pure Co, it is considered that a catalytic mechanism is more favorable than a non-catalytic consecutive mechanism assuming the similar electrochemical nature of Co and Fe.

Active dissolution behavior of cobalt was also observed by Mottern, M. M. and Myers, J. R. [1969] in 1 N, 5 N, and 10 N H_2SO_4 solutions as well as by Tomlinson, W. J. and Linzell, C. R. [1988] in 0.01 M H_2SO_4 + 0.99 M Na_2SO_4 solution (pH 2.55) without detailed information for kinetic parameters.

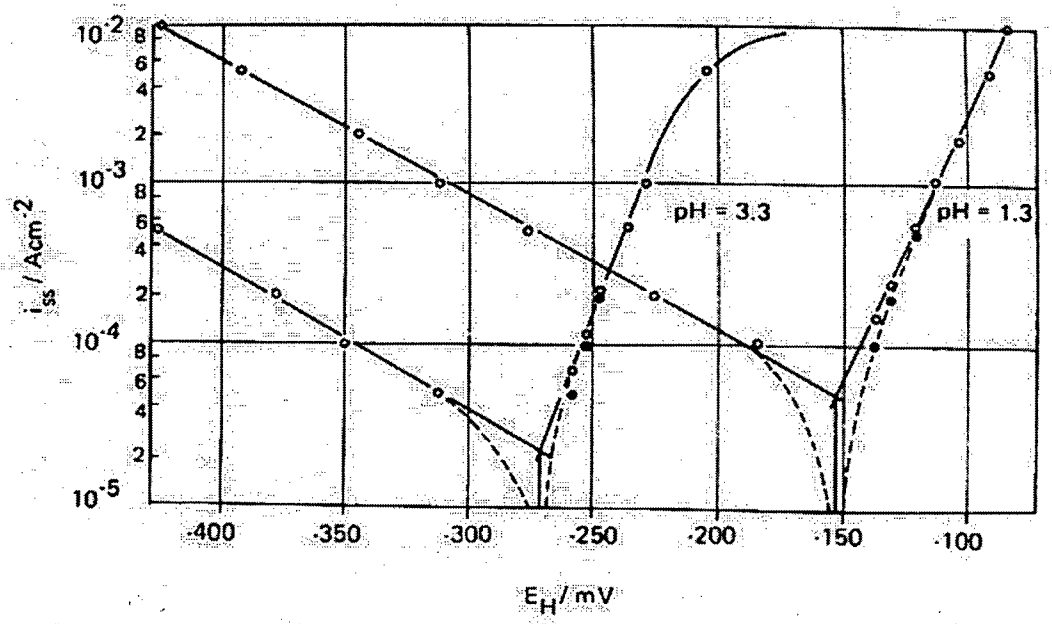

Figure 2-5 Steady-state polarization curves for Co in x M $NaClO_4$ + y M $HClO_4$, x+y = 0.5, pH=1.3 and 3.3 at 298K [Heusler, K. E. 1967]

Recently, in-situ electrochemical scanning tunneling microscopy (STM) has been applied to the study of the anodic dissolution process of metals at the atomic level. Satoru A. et al. [1997] investigated the morphological evolution during the anodic process of single crystal Co (0001) in 0.05 M Na_2SO_4 solution at pH of 3 using in-situ STM. They found that single Co (0001) structure was observed on the atomically flat terrace and the anodic dissolution process proceeded in the layer-by-layer mode, in which corrosion is initiated exclusively at step-edge as well as kink, but at terraces in the early stage of anodic dissolution. They also found that the anisotropic step lines are not atomically straight indicating that the step lines include various kink sites, and they argued that apparently, the anodic dissolution took place preferentially at step sites. Based on their observations, it is hard to tell however what mechanism (i.e., catalytic or non-catalytic) is more preferable because the motion of kinks along the steps is perhaps too fast to be detected by conventional in-situ STM, which typically has the image acquisition time in the order of a few seconds up to several minutes. In their experimental details, each frame for an image was recorded with a 10 seconds interval during the anodic dissolution process at constant anodic potential applied. It was however reported that for active metal dissolution, the ionization was a very fast process and characteristic time was estimated to less than 10 μs [Eigen, M., 1957: Foley, R. T. and Trzaskoma, 1978]. Therefore, it was possible that a very fast dynamic process of removal/addition of atoms at kink sites could not be detected by their observation.

Most recently, Magnussen O. M. et al. [2001] studied the fundamental atomic scale processes during active dissolution of single Cu (111) crystals in 0.01 M HCl by more advanced in-situ STM. By employing high speed video STM technique, capable of acquiring up to 25 atomic resolution images per second, and they found that metal Cu dissolution proceeded at a single type of structurally well-defined kinks which was consistent with a catalytic mechanism. The kinks nucleated at outer terraces corners and condensed into larger facets, resulting in an apparent collective local dissolution or growth of terraces. They also observed pronounced local dissolution/redeposition fluctuation at the individual kink even at the onset of dissolution with average kink propagation and reaction rate at kink in the range of 10^3 and 10^5 atoms per second, respectively.

Thus, the use of the advanced in-situ STM is necessary to identify the anodic dissolution mechanism of Co as well as the electrochemical measurements (i.e., the anodic Tafel slope and the reaction order, $y(OH^-)$).

2.1.3.3 Passivity of Co

Many electrochemical investigations have been reported on active dissolution and passivation of Co in neutral and alkaline pH ranges where various high stability cobalt oxides and hydroxides can be formed on the metal during anodization. However, the exact composition and the thickness of the passive film produced on the surface of Co at different potentials have been the subject of much controversy. For example, El-Wakkad and Hickling [1950] found three different electrochemical oxidation stages of Co in galvanostatic transients of anodic oxidation of Co in alkaline solutions which they assigned to the formation of CoO, Co_2O_3 and CoO_2, respectively, while Cowling and Riddiford [1969] reported only two stages and ascribed these to the formation of $Co(OH)_2$ and its subsequent oxidation to $Co(OH)_3$.

Sato and Ohtuska [1978] identified the composition of passive film on Co tested in a borate buffered solution at pH of 7 to 11 using in-situ Ellipsometry. They defined three regions of oxide passive layers (region I through III). Region I was reported to consist of a hydrated oxide of CoO; region (II) a bilayered oxide of CoO/Co_3O_4; and region (III) a bilayered oxide of CoO/Co_2O_3, respectively. It was also reported that the film thickness of the regions (I), (II) and (III) were 25 Å, 15 to 50 Å, and 15 to 35 Å, respectively. Recently, using X-ray photoelectron spectroscopy, Ismail and Badawy [2000] confirmed the presence of $Co(OH)_2/CoO$, Co_3O_4, and CoOOH upon increasing the applied potential of the passive film on cobalt. The authors suggested that the surface film formed on cobalt in alkaline solution consisted of two layers: the inner layer consisted of α-$Co(OH)_2$ and CoO and the outer layer consisted of Co(III) (CoOOH) compounds. The thickness of the passive film was found to be greater than 40 Å.

More recently, Foelske and Hans-Henning [2000, 2002] also examined the structure of the passive layer using X-ray photoelectron spectroscopy. They concluded that cobalt formed two different passive layers depending on the potentials. The primary passive film consisted of Co(II) oxide and Co(II) hydroxide at low potential. At high potential, a secondary passive film consisted of Co(II)/Co(III) mixed oxides.

2.1.3.4 Effect of P Alloying on Corrosion Behavior

Phosphorus (P) has been shown to have both detrimental and beneficial effects on the corrosion properties of alloys. For stainless steel, the detrimental effect of P is mainly due to the enhanced susceptibility to intergranular corrosion and stress-corrosion cracking (SCC) in strong oxidizing media due to P segregation along the grain boundary [Armijo, J. S. 1968: Briant, C. L. 1980]. The presence of P in solid solution and segregation to the grain boundary also prevented the formation of a passive layer on Fe, if its local concentration is higher than 2-3 at. % in hot nitrate solution [Kupper, J., et al. 1981]. In this reference, an even higher susceptibility of steels to intergranular SCC was detected after an annealing treatment that was long enough to establish equilibrium for P segregation at temperatures between 400 ^{o}C and 800 ^{o}C. This finding was closely correlated to the increased P concentration in the grain boundary and confirmed by Auger electron spectroscopy (AES). In particular, the electrodeposited Ni-2.9 wt% P (no grain size given) exhibited higher dissolution rates than that of pure Ni [Flis, J. 1985] and the electrodeposited Co-4.7 wt% P (no grain size given) [Gao, X. and Kowaka, M. 1991] also showed higher passivation current density compared to that of pure Co in an alkaline solution (1 M NaOH).

However, Krautschick, H. J., et al. [1988] observed the reduced anodic current densities for Fe-2wt % P in 1 N Na_2SO_4 (pH = 2) solution compared with pure Fe, while P accelerated the anodic dissolution rate in 5 N NH_4NO_3 solution. Using XPS investigation, they concluded that these effects could have originated from the different species of P in the corrosion products formed in the different electrolyte. After potentiostatic treatment in the anodic range, phosphate $(PO_4)^{3-}$ and $P^{\delta-}$ in a negatively charged binding state as in phosphide

or elemental P, dissolves in Fe in a Na_2SO_4 solution, while only phosphate in nitrate solution was formed.

The effect of P alloying to Co metal on the corrosion properties has been known to be beneficial in sulfuric acidic solution [Krolikowski, 1988; Yukimi et al, 1987]. For example, an increase of P content from 4 to 23 at % resulted in the increase of corrosion resistance gradually whether as a crystalline or amorphous structure as shown in Figure 2-6. The author speculated that an improvement of the resistance for phosphorous rich films could be expected.

In the case of amorphous alloys with a high P content, a beneficial effect of P was typically observed. Previous investigations have indicated that, with the addition of P, amorphous alloys exhibited better resistance to aqueous corrosion than unalloyed pure metals in acid solution [Krolikowski, A., 1988: Helfand, M. A. et al. 1992: Diegle, R. B. 1986: Demaree, J. D., 1993]. This was due to both their structural homogeneity, either the absence of grain boundaries and other crystalline imperfections or their chemical composition. The limited dissolution of P-rich amorphous alloys was mainly associated with formation of that an anodic film inhibited anodic processes. A study for amorphous Co-20 at% P alloy clearly showed the decrease of anodic dissolution rate as compared to pure Co in deaerated 0.2 N H_2SO_4 or 0.2 N HCl solution as shown in Figure 2-7 [Helfand, M. A. et al. 1992]. In this Figure, it is noticeable that lower anodic dissolution rate for pure Co metal in 0.2 N HCl solution than in 0.2 N H_2SO_4 solution, indicating different electrochemical reactivity of Co in sulphate and chloride containing solutions.

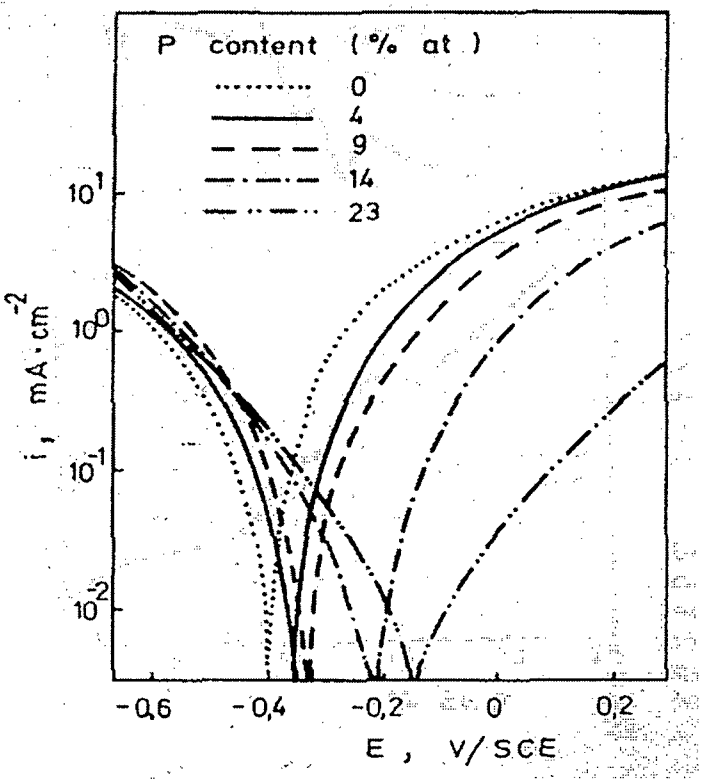

Figure 2-6 Potentiodynamic polarization curves of electrodeposited Co-P films in 0.1 N H_2SO_4 [Krolikowski, 1988]

Through XPS analysis, this anodic film formed on the surface of amorphous alloys was determined to be composed of hypophosphite anion (P^+)and phosphate (P^{+5}) in Co-20 at % P [Helfand, M. A. et al., 1992] and Ni-20 at% P [Diegle, R. B,. 1986] alloys, and Cr (or Fe) phosphate (P^{5+}) in Fe-Cr-P alloys [Demaree, J. D., 1993]. Also, some studies on these Ni-P alloys have proposed that the preferential dissolution of Ni occurred from these alloys. Anodic dissolution and XPS data showed that, with a consequent formation of an elemental P layer on the surface, a diffusion barrier for further Ni dissolution was formed [Habazaki, H., et al., 1989: Kawashima, A., et al. 1984].

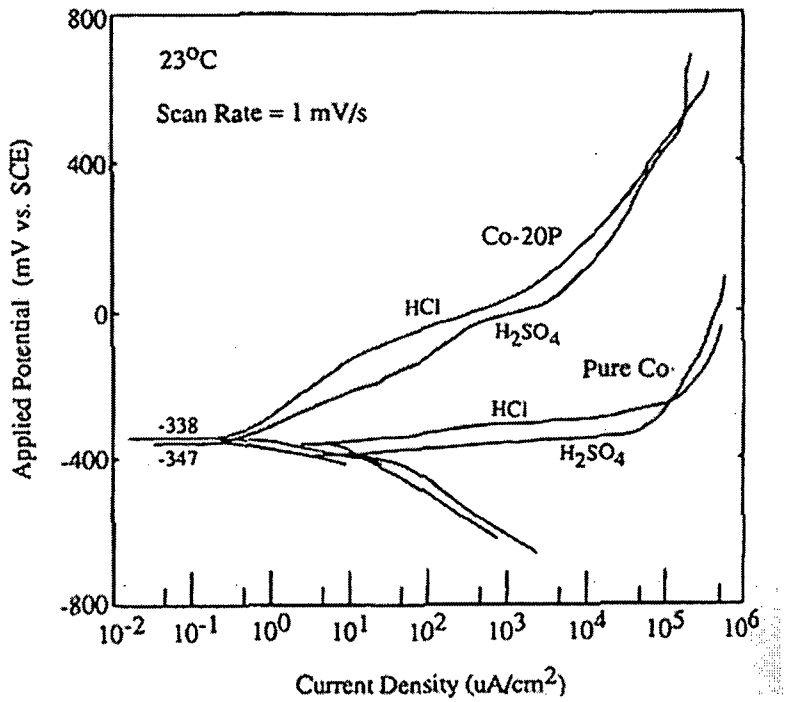

Figure 2-7 Potentiodynamic polarization curves of pure polycrystalline Co and amorphous Co-20 at% P alloy in deaerated 0.2 N H_2SO_4 and 0.2 N HCl [Helfand, M. A. et al. 1992]

2.2 Nanocrystalline Materials

In 1981, Gleiter initially proposed the synthesis of nanocrystalline materials containing large volume fractions of interface [Gleiter, H. 1981]. An extensive review of nanocrystalline materials was published in 1989 by Gleiter, which outlines some of the properties displayed by nanocrystalline materials as a consequence of their ultra-fine structure [Gleiter, H. 1989]. The increase in overall quantity of intercrystalline volume fraction in nanocrystalline materials can affect the physical, mechanical, chemical and magnetic/electrical properties. Many reports showed unique and often enhanced properties, which arise from their extremely small grain size. For example, nano-processing was found to have the most significant effect on mechanical properties such as yield strength and hardness as mentioned earlier in Chapter 1. From these improved properties of nanocrystalline materials, there are several emerging applications for nanocrystalline materials, including those which demanded corrosion and wear resistance, catalysts, in-situ repair of failed steam generator tubing in the nuclear industry, recording heads and, soft magnetic materials [Erb, U., et al. 2001].

2.2.1 Characteristic Structures of Bulk Nanocrystalline Materials

Nanocrystalline materials represent a novel class of materials with grain sizes less than 100 nm resulting in significant increases in grain boundary and triple junction volume fractions. The microstructure consists of well ordered crystallites with larger free volumes or less ordered areas associated with the grain boundaries and triple junctions. Figure 2-8 is a 2-dimensional schematic of nanocrystalline material showing a large fraction of atoms in the grain boundaries and triple junctions [Gleiter, H., 1989]. Many of the studies showed strong agreement with the notion that grain boundaries in nanocrystalline materials are not unlike those in polycrystalline materials. For instance, the grain boundary width in nanocrystalline Pd produced by inert gas condensation technique was observed to be 0.7 to 1.1 nm which corresponds well with what had been observed previously in polycrystalline materials. [Mutschele, T. and Kirchheim, R., 1987: Thomas, G. J., et al. 1989].

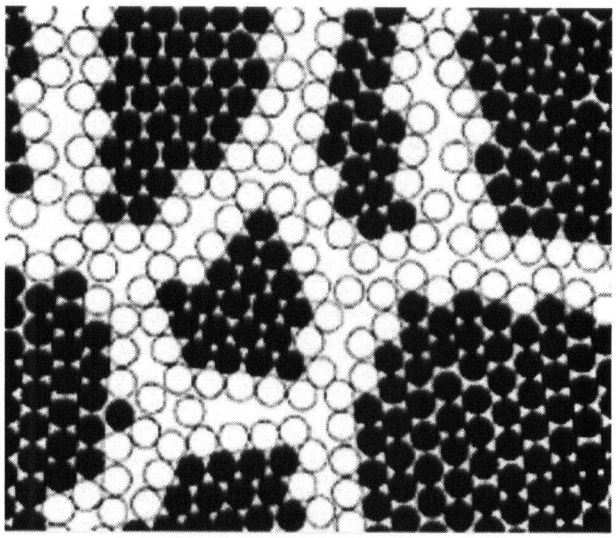

Figure 2-8 Schematic diagram of a nanocrystalline material consisting of atoms in the grain interior (•) and the atoms in the intercrystalline regions (O) [Gleiter, H., 1989]

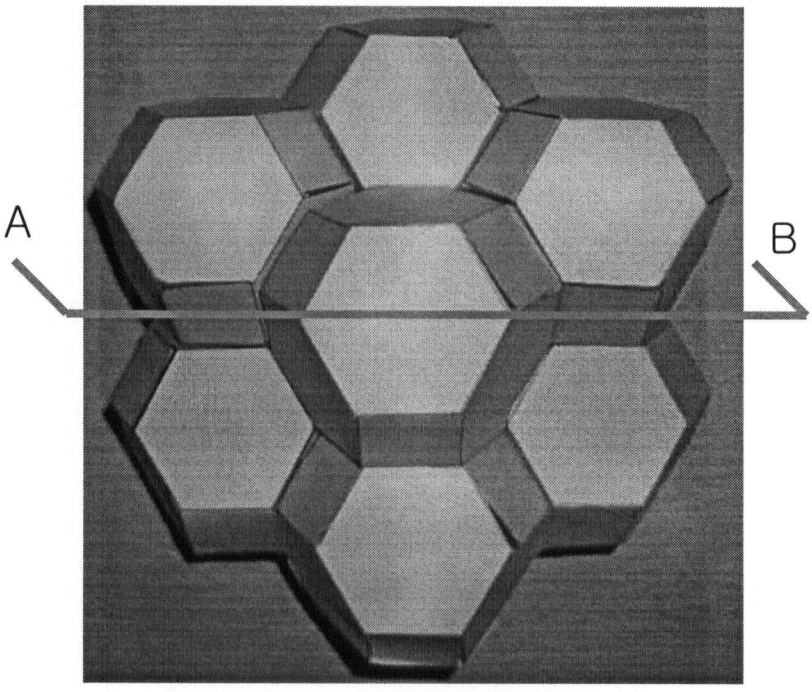

Figure 2-9 Three(3)-dimensional space filling 14-sided tetrakaidecahedrons used the model grains of an equiaxed polycrystalline materials where 14 sides and 36 edges represent grain boundary and triple junction, respectively.

Previously, Palumbo, G., et al. [1990] evaluated the volume fraction of intercrystalline components such as grain boundaries and triple junctions depending on the grain size by considering a regular 14-sided tetrakaidecahedron as the grain shape (Figure 2-9). The result showed that the volume fraction of the grain boundary component was assessed as

$$V_{gb} = \frac{3\Delta(d-\Delta)^2}{d^3} \tag{2.12}$$

where Δ is the average grain boundary thickness and d is the average grain diameter assumed a grain boundary thickness, Δ of 1 nm. The volume fraction associated with triple junction is also given by

$$V_{tj} = 1 - \frac{(d-\Delta)^2(d+2\Delta)}{d^3} = V_{ic} - V_{gb} \tag{2.13}$$

where V_{ic} is the volume fraction of the total intercrystalline components. All of the above equations are valid only for $d > \Delta$.

Figure 2-10 shows the variation of the volume fractions as a function of the grain size according to Eq. (2.12) and (2.13). This figure shows the negligible intercrystalline volume fraction for conventional polycrystalline materials; for example, less than 0.03 % of the materials with grain sizes greater than 10 μm. However, with decreasing grain size, the fraction increases rapidly and becomes comparable to that of crystalline volume fraction with a grain size of <10 nm. Based on this calculation, the volume fraction of atoms in the interfacial components can be as much as 51 % for a grain size of 5 nm decreasing to about 28 % for 10 nm, 3 % for 100 nm, and 0.3 % for a 1000 nm grain size.

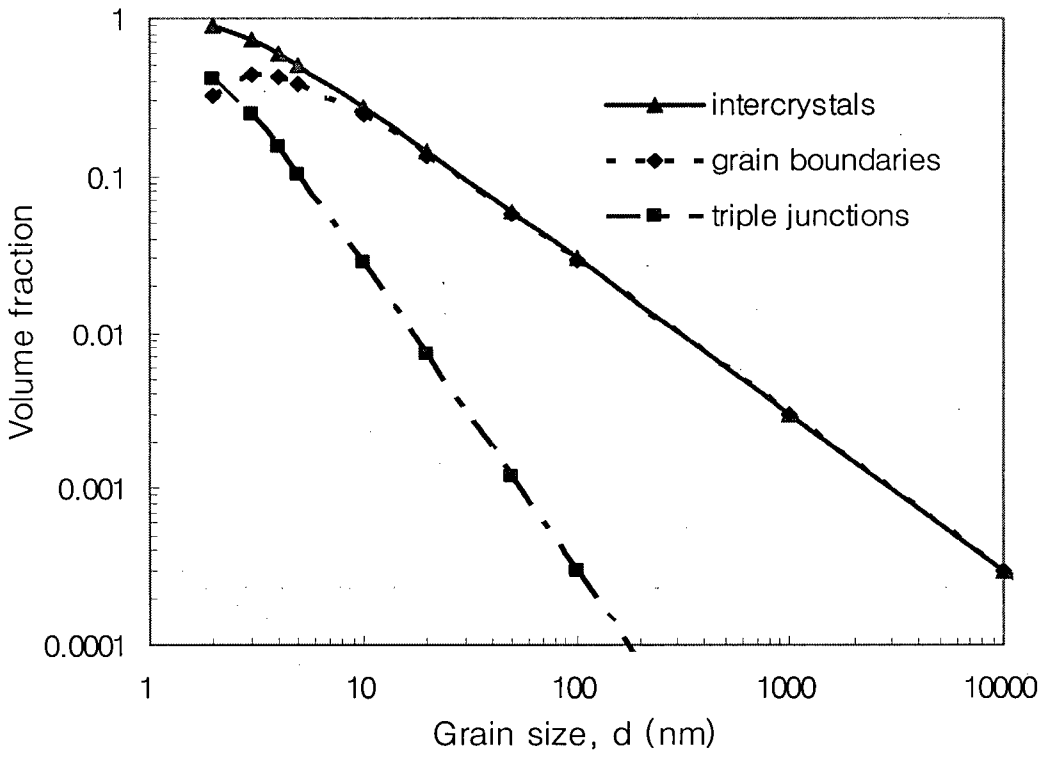

Figure 2-10 Effect of grain size on the calculated volume fractions for intercrystalline regions, grain boundaries and triple junctions assuming a grain boundary thickness (Δ) of 1 nm [Palumbo, G, et al. 1990].

Considering a cross-section along the A-B plane of the tetrakaidecahedral grains showin in Figure 2-9, Wang [1997] attempted to calculate the intercrystalline surface area fraction depending on the grain size. The detailed analysis of the surface fractions of intercrystalline components is shown in Figure 2-11, where a is the edge length of the tetrakaidecahetron, D is the mean caliper diameter of crystal and Δ is the grain boundary width.

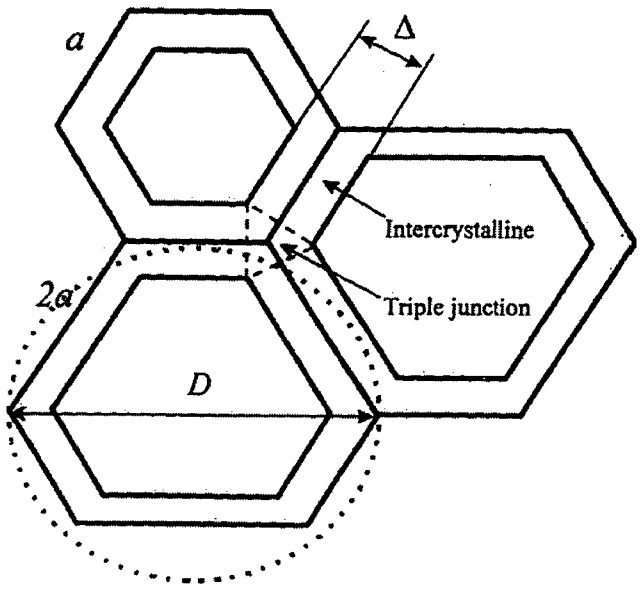

Figure 2-11 Schematic surface profile representing the interfacial region on the free surface using the cross section (A-B) in Figure 2-9, where a is the edge length of the tetrakaidecahedron, D is the grain size and Δ is the grain boundary width. [Wang, 1997]

Based on the geometry of this crystallographic model, the surface fractions of the intercrystalline components were given by the following relationships and the resultant relationships

$$S_{ic} = 1 - \left(1 - \frac{\sqrt{3}\Delta}{d}\right)^2 \tag{2.14}$$

$$S_{tj} = \left[1 - \left(1 - \frac{\sqrt{3}\Delta}{d}\right)^2\right]\left(\frac{\sqrt{3}\Delta}{2d - \sqrt{3}\Delta}\right) = S_{ic} - S_{gb} \tag{2.15}$$

where S_{ic} , S_{gb} and S_{tj} are the surface area fractions of the total intercrystalline components, grain boundary components, and triple junction components, respectively. Assuming a grain boundary thickness Δ of 1 nm, similar grain size dependence between the surface area fraction and the volume fraction was found. In Figure 2-12, a reduction of grain size from 10 μm to 5 nm leads to an increase in the intercrystalline surface area fraction from 0.02 % to

38 %. Kirchheim, R. et al [1992] postulated a special chemical potential of the atoms in the grain boundaries, which is significantly higher in comparison to the chemical potential of atoms in a single crystal. Thus, it is expected that a significant increase of the intercrystalline surface area in nanocrystalline material may result in the increase of the anodic dissolution rate due to its higher reactivity compared to coarse grained polycrystalline counterparts.

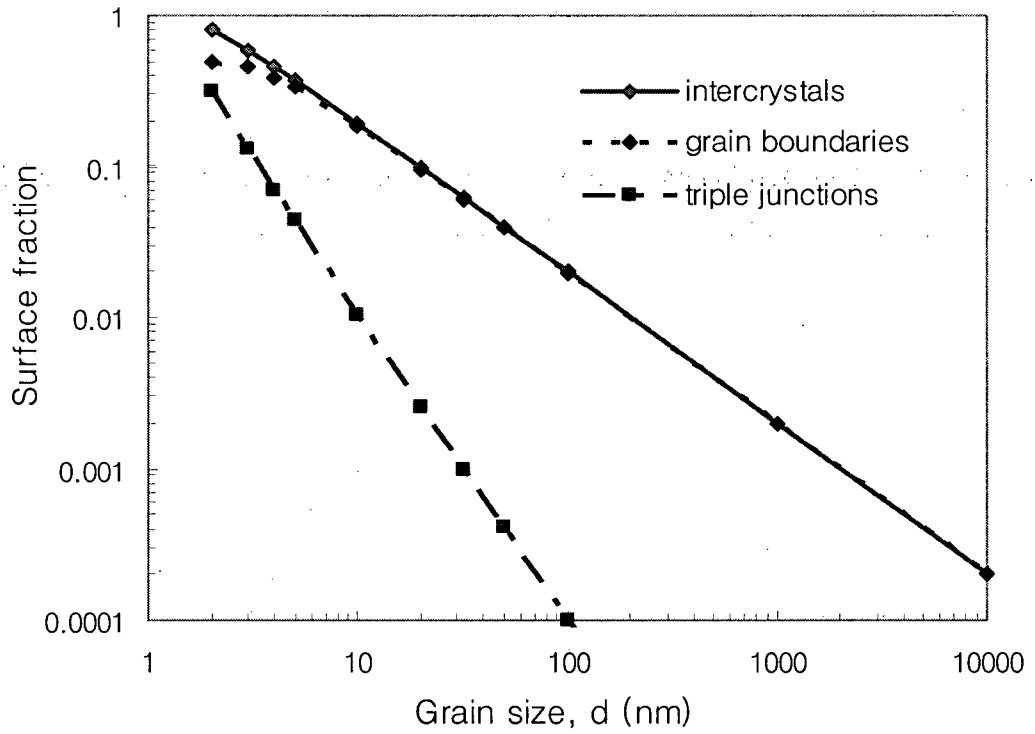

Figure 2-12 Effect of grain size on the calculated surface area fractions for intercrystalline regions, grain boundaries and triple junctions assuming a grain boundary thickness (Δ) of 1 nm[Wang, 1997].

2.2.2 Morphological Model

Since the intercrystalline defects (e.g., grain boundaries and triple junctions) are considered as preferential dissolution sites [Kirchheim, R., et al., 1992], the intercrystalline surface area fraction may be closely related to the corrosion properties.

If the intercrystalline surface area fraction is directly related to the cathode to anode area ratio (the grains play the role of the cathode and the grain boundaries play the role of the anode), higher intercrystalline surface area fraction (lower cathode to anode area ratio) in nanocrystalline materials may show better performance against localized corrosion than its polycrystalline counterpart [Fontana, M. G., 1986]. This situation may be particularly beneficial to nanocrystalline materials when the corrosion process has been occurring at two distinct sites on the same surface under no imposed external potential.

Consider that corroding metal is equivalent to a short-circuited energy-producing cell in which the energy is dissipated during the consumption of a cathodic reagent and the formation of corrosion products in a isolated system, i.e., there are no external source or sinks of electrons as shown in Figure 2-13. To maintain a mass balance, the amount of cathodic reagent consumed must be equal to the amount of the corrosion product formed, therefore the total current flowing into the cathodic reaction must be equal to the current flowing out of the anodic dissolution reaction of the metal as follows,

$$\Sigma I_a = -\Sigma I_c \text{ or } \Sigma i_a A_a = -\Sigma i_c A_c \tag{2.16}$$

where i_a and i_c are the anodic and the cathodic current density, A_a and A_c are the area for anodic and cathodic site, respectively. If the area of the anodic and cathodic site varies significantly like in a coarse grained polycrystalline material, while the anodic and cathodic currents must be equal, the respective current densities need not be equal. Therefore, as shown in Figure 2-13a, the anodic current density can be much larger than the cathodic current density by absolute value due to the higher cathode-to-anode area ratio. However, in case of the same surface area between anodic and cathodic sites, as is the case in a nanocrystalline material shown in Figure 2-13b, the anodic current density can equal the cathodic current density in absolute value.

Therefore, the reduction of grain size and uniformity of defect sites distribution may reduce the penetration current density in nanocrystalline materials.

In addition, nanocrystalline materials fabricated by electrodeposition (e.g., nanocrystalline Co) have been shown to have a narrow grain size distribution (see Figure 4-

2). These characteristics observed in nanocrystalline materials give a better localized corrosion resistance resulting from the highly distributed corrosion current.

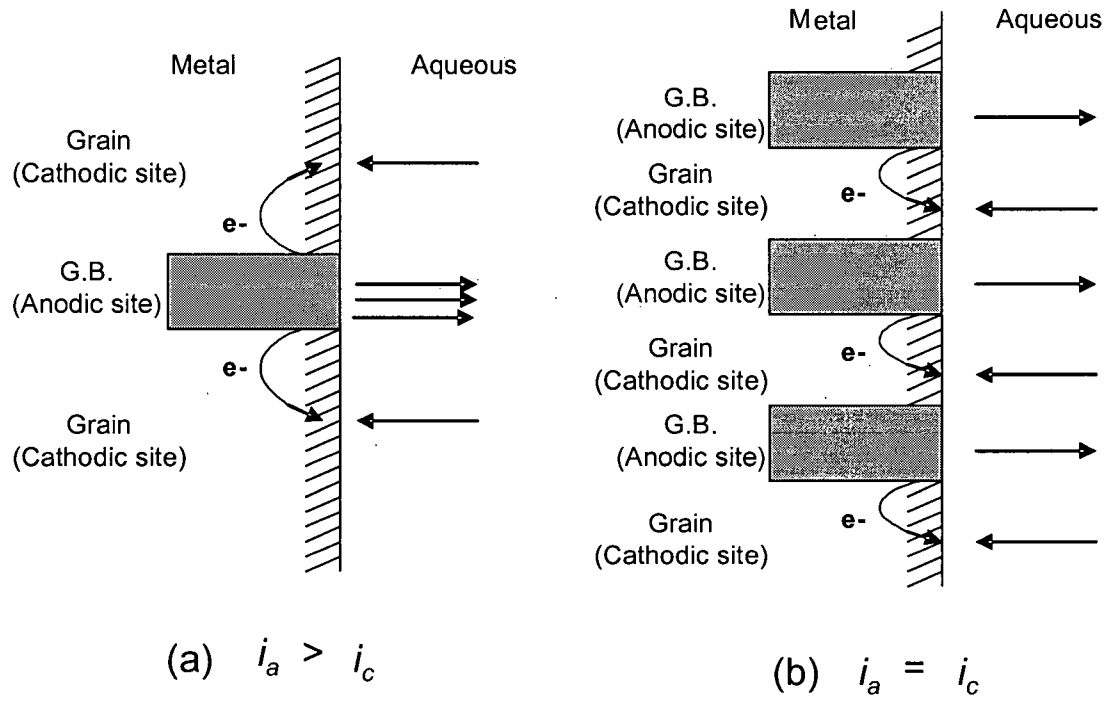

Figure 2-13 Schematic illustration of the effect of; (a) large cathode-to-anode area ratio and (b) same cathode-to-anode area ratio on the cathodic and anodic current density

2.2.3 Corrosion Behaviors of Nanocrystalline Materials

The corrosion properties of nanocrystalline structures have been studied for a variety of metal and alloy systems under various electrochemical conditions. However, although a thorough understanding of the effects of grain size and chemical composition on the corrosion behavior of nanocrystalline materials is crucial for their future industrial applications, the overall research efforts in this area to date have been rather limited. Therefore, the corrosion phenomena of nanocrystalline materials in the literature are reviewed along with the synthesis methods of nanocrystalline materials such as crystallization from amorphous state, electrodeposition, mechanical alloying, gas phase coating and other methods. The following review will be made to present the main differences in the corrosion properties of nanocrystalline materials compared with conventional coarse grained polycrystalline and/or amorphous counterparts.

2.2.3.1 Nanocrystalline Materials Obtained by Crystallization from Amorphous Precursor

Nanocrystalline alloys can be produced through controlled crystallization, starting from amorphous precursors. [Gleiter, H., 1981; Erb, U. 2001] This technology is based on the low-temperature conventional or impulse annealing of metallic glasses. By modifying heat treatment procedures, ultrafine grains can be partially or completely obtained within the amorphous matrix. The basic condition to obtain a material with extremely fine grains by crystallization can be attributed to slow growth rate and nucleation, which are characteristics of solid amorphous materials. Thus, a controlling of the solidification rate of amorphous materials results in a homogeneous and random distribution of the nanocrystalline metal particles and precipitates in the amorphous matrix.

Diegle and Slater [1976] first reported, to our knowledge, the anodic polarization behavior of two different amorphous alloys, i.e. Alloy 2826 ($Fe_{40}Ni_{40}P_{16}B_4$) and Alloy 2826A ($Fe_{24}Cr_{15}Ni_{40}P_{16}B_4$) in 1 N H_2SO_4 containing 0.1 and 1 M NaCl compared with nanocrystalline counterparts (grain size, 20 nm) after the crystallization process. In their

study, nanocrystalline alloys exhibited much increased active and passive current densities compared to amorphous states both with and without adding NaCl.

This deterioration by crystallization was also observed by Naka et al. [1980]. They found a rapid deterioration of the corrosion resistance by crystallization of amorphous Fe-10Cr-13P-7C and Fe-36Ni-14Cr-12P-6B in 1 N HCl as shown in Figure 2-14. They reasoned that an increase in the anodic and passive current densities in the polarization curves was attributed to the compositional fluctuations such as precipitation, segregation and other composition gradients in the nanostructured materials (grain size, 50 nm) which can behave as dominant active sites with respect to corrosion.

Other studies also showed the similar deterioration of amorphous materials by crystallization (e.g. Cr-16~29Ni-14P alloy in 6 M HCl [Asami et al., 2001], $Nd_{14}Fe_{80}B_6$ and $Nd_{12}Dy_2Fe_{73.2}Co_{6.6}Ga_{0.6}B_{5.6}$ magnet in 0.1M H_2SO_4 [El-Moneim, A. A. et al., 2002]).

In contrast, Thorpe et al. [1988] reported an improvement in the corrosion resistance of Metglass 2826A ($Fe_{32}N_{46}Cr_{14}P_2B_6$) alloy by crystallization treatment. The amorphous alloy was annealed for long term periods at 423 K and transferred the nanosized crystalline with a grain size of 2 to 15 nm. As shown in Figure 2-15, the nanocrystalline alloy showed a decrease of anodic dissolution rate in the amount of about an order smaller than amorphous state in 1 M NaCl (pH=3). The authors reasoned that this improved corrosion resistance was due to the presence of a thicker passive film and a greater Cr enrichment of the surface film due to rapid diffusion through the interfaces.

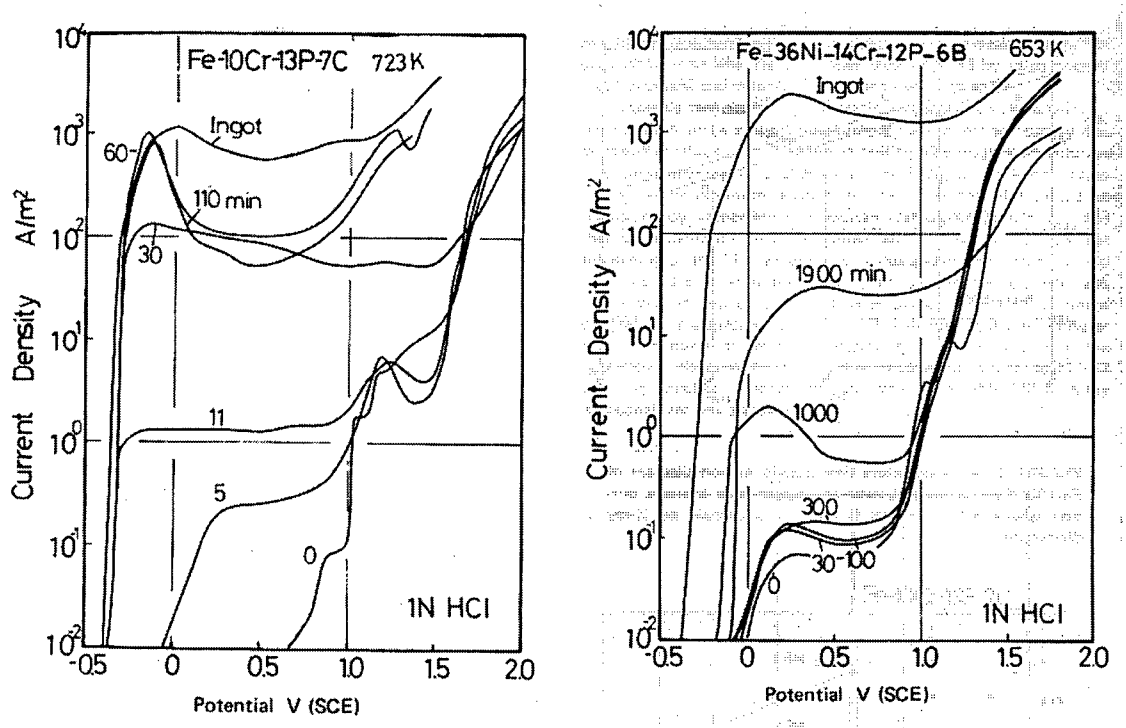

(a) (b)

Figure 2-14 Changes in polarization curve of amorphous (a) Fe-10Cr-13P-7C alloy with time of heat treatment at 723 K, and (b) Fe-36Ni-14Cr-12P-6B alloy with time of heat treatment at 653 K in 1 N HCl [Naka, M. et al., 1994]

Sousa and Kiminami [1997] also observed an enhanced corrosion resistance for nanocrystalline Fe-Cu-Nb-Si-B alloys with the grain size of α -Fe(Si) crystallite 14.4 ~ 15.5 nm by mass loss measurements in 0.1 M H_2SO_4 solution compared with the amorphous state. The result shows that the presence of nanocrystalline grains leads to a decrease of the mass loss values when compared to those in the as-cast (amorphous) state, indicating that nanocrystallization improved corrosion resistance. The author suggested that the higher corrosion resistance of nanocrystalline alloys could be attributed to a higher diffusion rate which leads to a higher deposition rate of Si in the surface, and growth of a more continuous, thicker and protective SiO_2 film. The decrease of corrosion resistance of the sample with 2.5 at% Si with the nanocrystallization was probably related to low Si content that was not

enough to ensure the formation of a protective SiO_2 film, and the effect of increasing corrosion prevailed due to the presence of corrosion preferential sites caused by nanocrystallization.

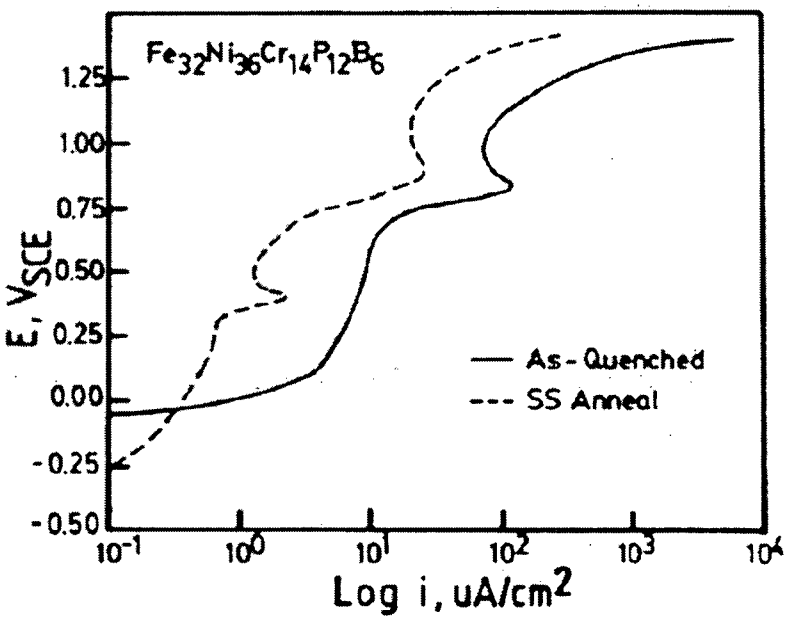

Figure 2-15 Potentiodynamic polarization curves for Alloy 2826A in the as-quenched (amorphous) and the annealed (nanocrystalline) in 0.1 M NaCl + 0.1 M Na_2SO_4 solution (pH=3) [Thorpe et al., 1988]

2.2.3.2 Nanocrystalline Materials Obtained by Electrodeposition

Electodeposition has been identified to be a technologically feasible and, for many applications, economically superior technique for the production of nanocrystalline pure metals and alloys. Nanocomposites can also be electrodeposited with grain size less than 100 nm [Benea, L. et al., 2002]. A variety of methods such as D.C plating, pulse plating and electroless plating have been utilized for this purpose. Fundamentally, electrodeposition will result in nanostructured materials when electrodeposition parameters (e.g. plating bath compositions, pH, temperature, overpotential, etc) are chosen such that electrocrystallization results in massive nucleation and reduced grain growth [Erb, U. et al. 1996].

Rofagha et al. [Rofagha, R. et al., 1991] first explored the corrosion behavior of electrodeposited nanocrystalline Ni in 2 N H_2SO_4 solution using potentiodynamic and potentiostatic testing. The average grain size of the nanocrystalline sample under investigation was 32 nm and its potentiodynamic polarization curves were compared to those for polycrystalline Ni with an average grain size of 100 μm as shown in Figure 2-16.

The polarization curves for both nanocrystalline and polycrystalline Ni samples exhibited the active-passive-transpassive transitions. However, differences are evident in passive current density and corrosion potential. First, the passivation current density for nanocrystalline Ni was about 10 times higher than that of the polycrystalline Ni sample. The authors rationalized this higher current density in terms of the amount of grain boundary and triple junction present in nanocrystalline materials. As can be seen in Figure 2-10, the intercrystalline volume fractions for the samples were calculated to be 0.02 % for the 100 μm polycrystalline Ni and 6 % for 32 nm nanocrystalline Ni. Therefore it was suggested that the increased electrochemical response for the nanocrystalline materials was due to the higher dissolution rate by the enhanced intercrystalline (grain boundaries and triple junctions) region which provides sites for electrochemical activity. However, the differences in passivation current density between poly- and nanocrystalline Ni samples became negligible at high potentials (e.g. 1100 mV_{SCE}). Second, a positive shift of the corrosion potential for the nanocrystalline Ni (E_{corr} = 7 mV_{SCE}) as compared to that of 100 μm grain sized Ni (E_{corr} = -170 mV_{SCE}) was observed. This was interpreted to be the result of enhanced catalysis of the hydrogen reduction reaction due to large quantity of intercrystalline contents.

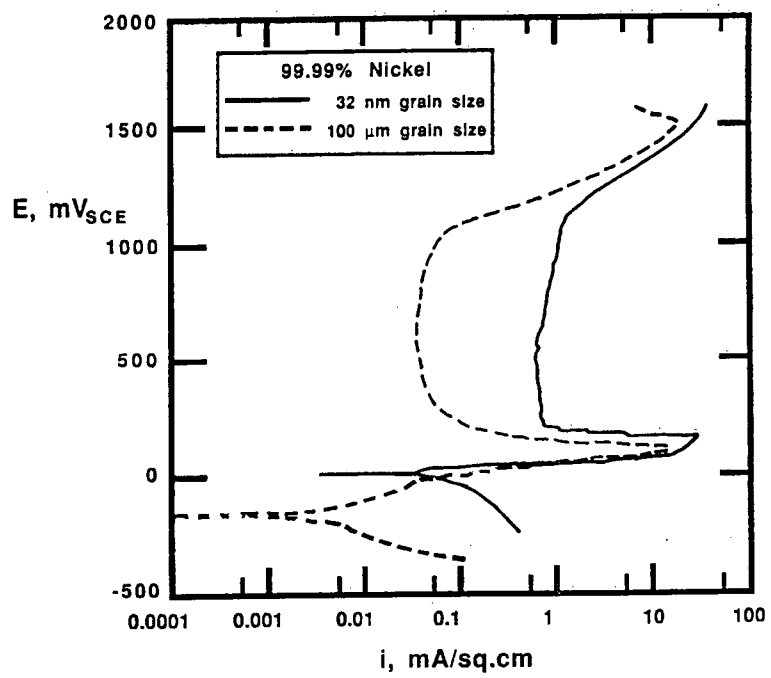

Figure 2-16 Potentiodynamic anodic polarization curves for nanocrystalline (32nm grain size) and polycrystalline (100μm grain size) 99.99% Ni in 2N H_2SO_4 at 293 K obtained using a potential scan rate of 0.5 mV/s [Rofagha et al. 1991]

Figure 2-17 shows the scanning electron micrographs of 100 μm and 32 nm grain size Ni samples following anodic polarization at 1200 mV_{SCE} for 2000 seconds. Both Ni samples exhibited extensive corrosion but nanocrystalline Ni was more uniformly corroded while the specimen with 100 μm grain size showed extensively localized attack along the grain boundaries and triple junctions. A follow up study using XPS on the corroded samples revealed that decreasing grain size of the Ni samples resulted in the formation of more defective passive film while the thickness of the passive layer was the same on both samples [Rofagha, et al, 1994]. The higher defective passive film on the nanocrystalline sample than the polycrystalline sample allows for a more uniform breakdown of the passive film which in turn leads to a more uniform corrosion. Therefore it was concluded that nanoprocessing might be advantageous to the overall corrosion performance of nickel in an environment where localized attack would be expected.

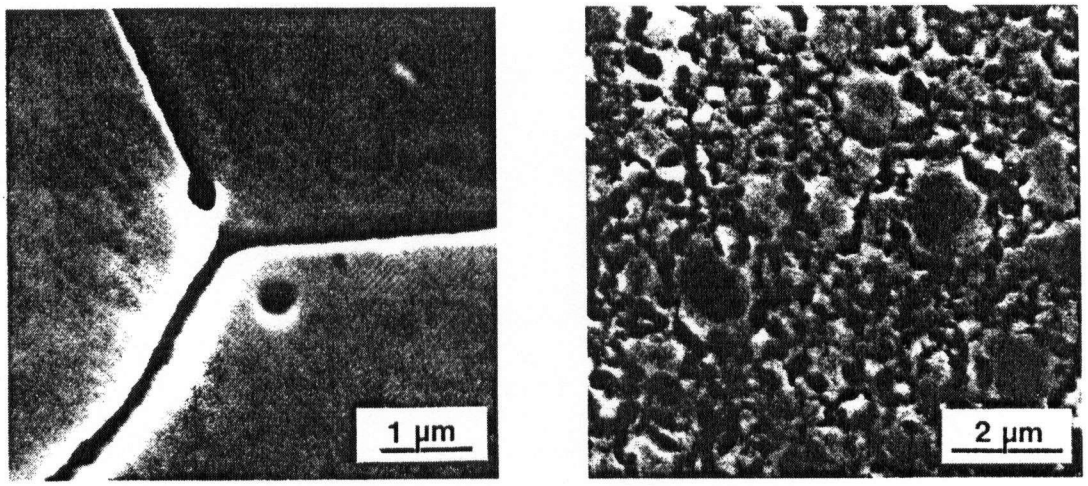

(a) (b)

Figure 2-17 Scanning electron micrographs of (a) 100 μm (b) 32 nm grain size Ni following anodic polarization at 1200mV_{SCE} in 2N H_2SO_4 for 2000s [Rofagha et al. 1991]

Recently, Mishra, R. and Balasubramaniam, R. [2004] reported a similar result on the corrosion behavior of nanocrystalline Ni synthesized by pulsed current electrodeposition technique using a Watt's bath both with and without saccharine addition. Nanocrystalline Ni samples having different grain sizes (8 ~ 28 nm) showed an increase in the passivation current densities and more noble corrosion potentials in 1 M H_2SO_4 compared to coarse grained Ni counterpart (grain size, 61 μm) as shown in Figure 2-18, while showed lower localized corrosion tendency. They reasoned that the decreased corrosion resistance was due to the defective nature of passive film formed on nanocrystalline Ni samples.

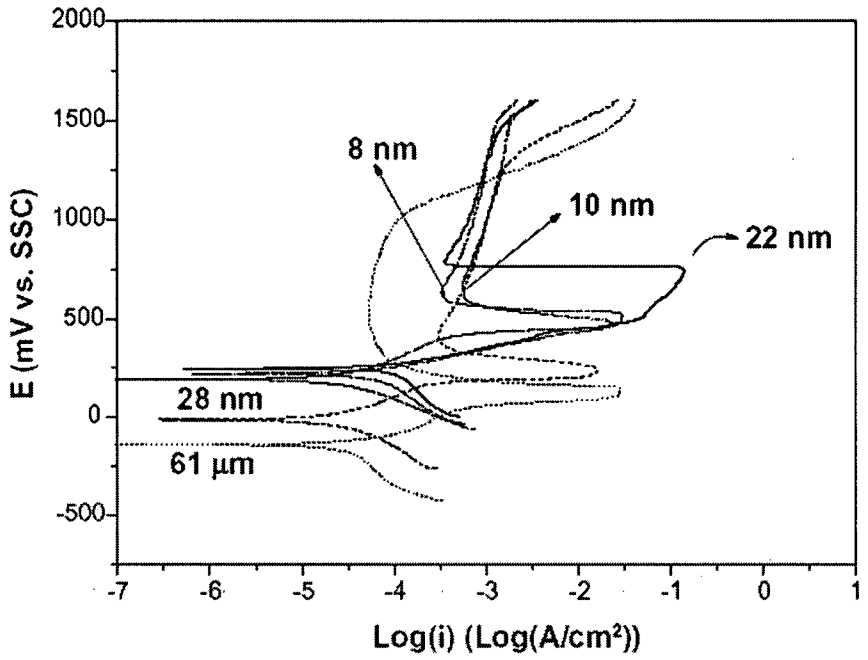

Figure 2-18 Potentiodynamic polarization curves of poly- and nanocrystalline Ni in 1 M H_2SO_4 at scan rate of 0.5 mV/s [Mishra, R. and Balasubramaniam, R., 2004].

For the potential use of nanocrystalline Ni in Ni batteries, electrocatalysts and fuel cells, Wang et al. [1995] investigated the corrosion behavior of electrodeposited nanocrystalline Ni in 30 % KOH. They found that the dissolution current density of nanocrystalline Ni (grain size, 32 nm) was higher than that of polycrystalline Ni (grain size, 52 μm) in the passive regions. The authors then summarized the corrosion behavior of electrodeposited nanocrystalline Ni in alkaline solution as follows. In the low anodic over potential range, corrosion attack is initiated more easily at grain boundaries and triple junctions which control the dissolution mechanism. With an increase in anodic polarization, the corrosion becomes less structure dependent as was observed in the case of acidic solutions.

Kim, S. H. et al. [2003] investigated the effect of grain size on the corrosion characteristics of electrodeposited nanocrystalline Co with an average grain size of 13 ~ 15 nm in 0.25 M Na_2SO_4 solution (pH=6.5) and 0.1 M NaOH solution (pH=13) by anodic polarization tests. For the 0.25 M Na_2SO_4 solution, they found that the overall shape of the

anodic polarization curve for nanocrystalline Co was very similar to that of its coarse grained polycrystalline Co counterpart, including a similarity in both the obtained E_{corr} value and lack of clear evidence of passivation. They concluded that the corrosion behavior of Co was not greatly affected by nanoprocessing, in fact, a slightly enhanced anodic dissolution current was observed for nanocrystalline Co. (Figure 2-19a). However, the nanocrystalline Co showed more uniform corrosion, which means, a higher resistance to intergranular corrosion which was consistent with the previous observation for Ni electrodeposits. For the 0.1 M NaOH solution, potentiodynamic polarization tests have been shown that the grain size refinement does not affect the passivasion characteristics of Co as shown in Figure 2-18b.

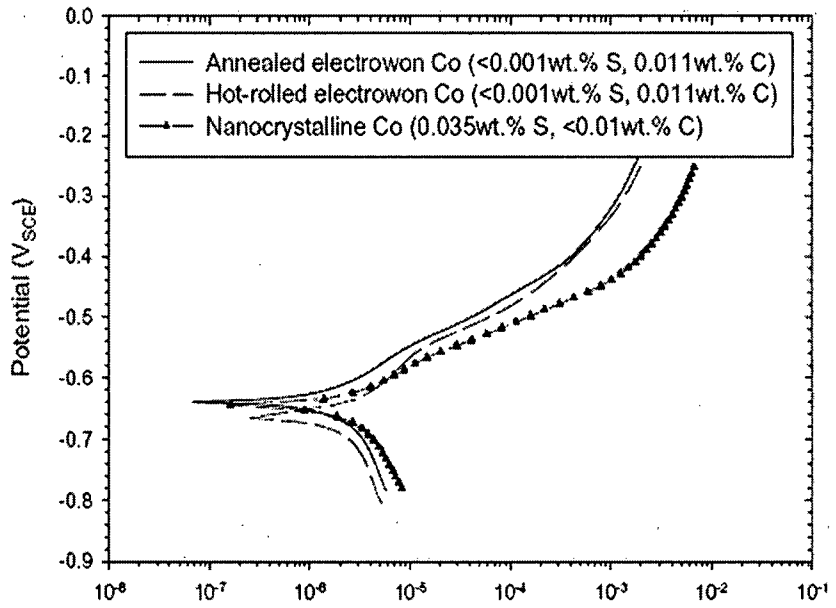

(a)

Figure 2-19 Potentiodynamic Polarization curves obtained from poly- and nanocrystalline Co in deaerated (a) 0.25 M Na_2SO_4 (pH=6.5) and (b) 0.1 M NaOH (pH=13) at 298 K (scan rate: 0.2 mV/s) [Kim, S. H., et al., 2003]

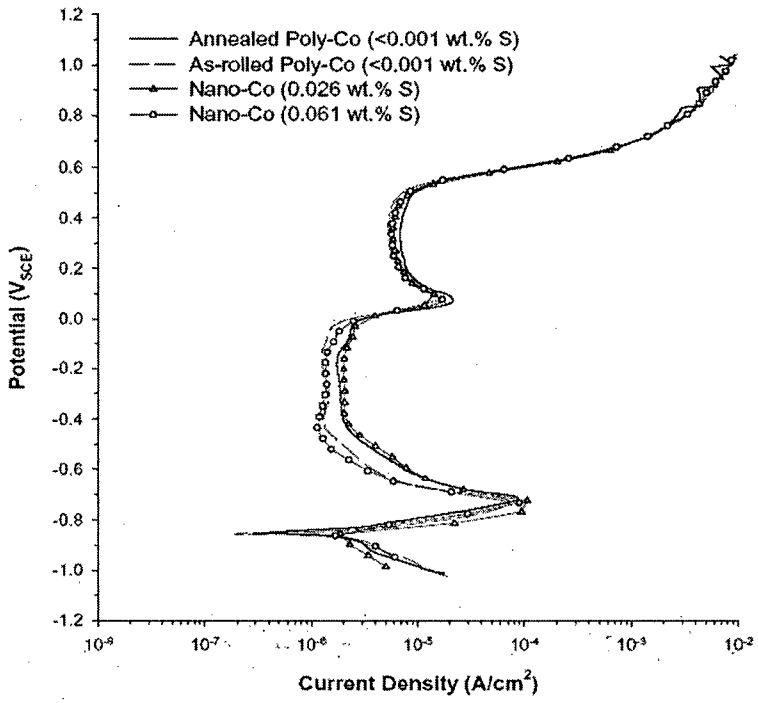

(b)

Figure 2-19 (continued)

The corrosion behavior of nanocrystalline Zn (grain size, 56 nm) in comparison with electrogalvanized (EG) steel (grain size, 10 μm) in deaerated 0.5 M NaOH solution was investigated using potentiodynamic polarization tests and impedance measurements [Youssef, Kh. M. S., et al., 2004]. The results showed that the estimated corrosion rate of nanocrystalline Zn was found to be about 60 % lower than that of EG steel and the passive current densities for the nanocrystalline Zn were lower than that of EG steel as shown in Figure 2-20. The authors reasoned that the enhanced corrosion resistance of nanocrystalline Zn can be related to the good nature of passive film formed on the nanocrystalline Zn surface due to higher diffusion rate of elements in nanocrystalline material.

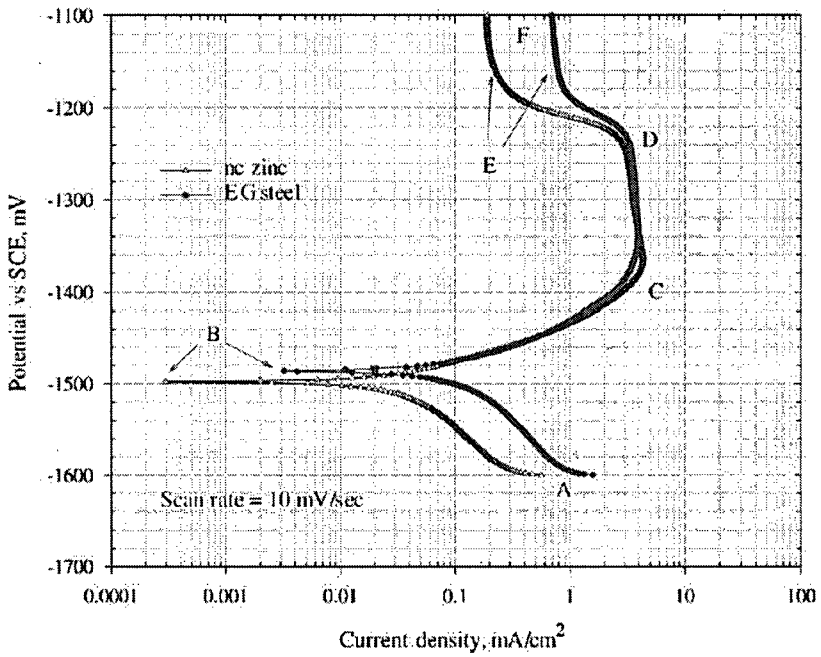

Figure 2-20 Polarization curves of nanocrystalline Zn and EG steel in deaerated 0.5 N NaOH [Youssef, Kh. M. S., et al., 2004]

The corrosion behavior of nanocrystalline Ni-1.4 and 1.9 wt% P alloys prepared by electrodeposition (grain sizes of 8.4 nm and 22.6 nm, respectively) in 0.1 M H_2SO_4 was assessed using a potentiodynamic polarization test compared to amorphous Ni-6.23 wt% P and coarse-grained polycrystalline Ni (grain size, 100 μm) [Rofagha, R., et al., 1993]. As shown in Figure 2-21, the increase of anodic dissolution rate for nanocrystalline materials over the coarse grained polycrystalline Ni was observed. The authors reasoned that this behavior was due to mainly the phosphorus content and, to a lesser extent, the high volume fraction of grain boundaries and triple junctions which resulted in the formation of non-protective surface films.

Splinter et al. [1996] further examined the corrosion films formed on nanocrystalline and amorphous Ni-P alloys in 0.1 M H_2SO_4 using XPS and found an enrichment of elemental P compared to Ni content at the surface of both materials, suggesting that Ni was preferentially dissolved during anodic polarization. The authors suggested that the P atoms served to prevent the formation of a passive film by blocking primary OH^- adsorption sites,

the precursor to passive film formation. The defective films on nanocrystalline Ni also facilitated atom dissolution and oxidation of surface P atoms from hypophosphite to soluble phosphate anions.

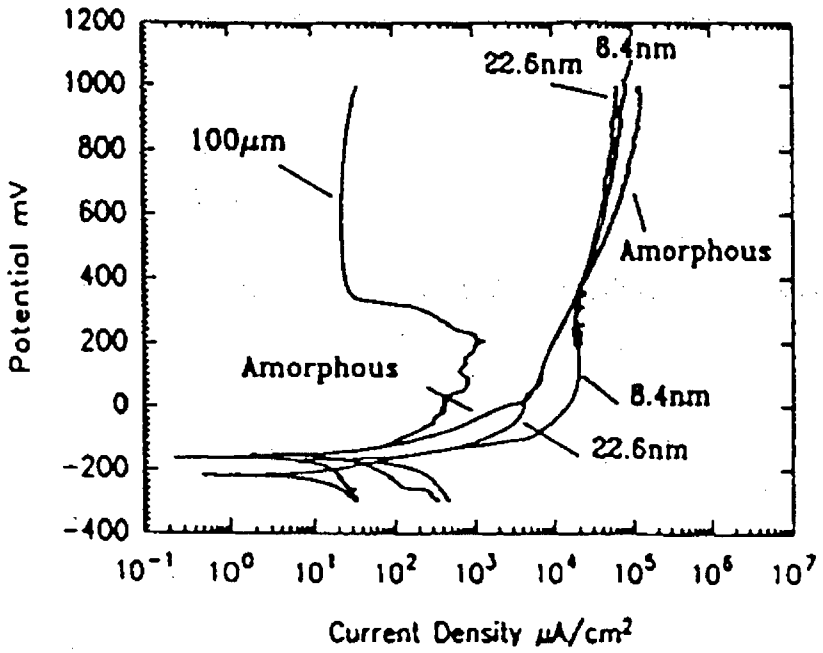

Figure 2-21 Anodic polarization curves for Ni-P alloys and pure Ni in 0.1 M H_2SO_4, scan rate= 1mV/sec [Rofagha et al. 1993]

A study for the corrosion properties of nanocrystalline Co-P (grain size of 50 nm, no bulk P concentration given) also demonstrated the detrimental effect of P alloying compared with nanocrystalline Co (grain size, 67 nm) in 0.25 M Na_2SO_4 solution (pH=10.5) [Aledresse and Alfantazi, 2004]. As shown in Figure 2-22, nanocrystalline Co-P showed higher corrosion current density and anodic dissolution rate than nanocrsyatlline Co without clear evidence of passivation for both samples.

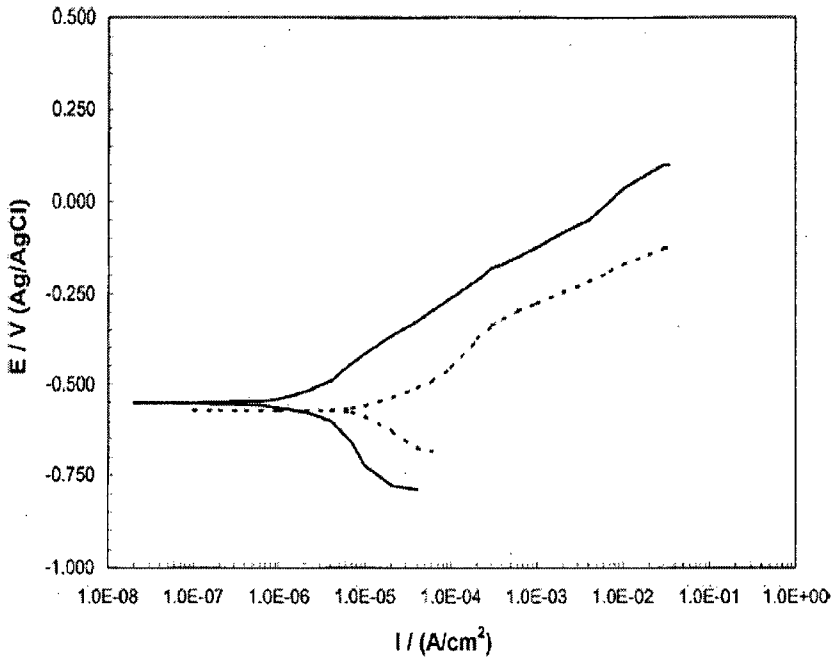

Figure 2-22 Potentiodynamic polarization curves for nanocrystalline Co-P (-------) and conventional polycrystalline Co (——) [Aledresse and Alfantazi, 2004]

Due to their high wear resistance and the low cost of ceramic powder, Ni-SiC composites have been investigated to the greatest extent. Recently, Benea et al. [2002] synthesized the nanostructured Ni-SiC composite by electroplating using nanometer size of SiC (mean diameter, 20 nm) as shown in Figure 2-23. They also investigated the corrosion properties of the composite comparing pure Ni coatings in 0.5 M Na_2SO_4 (pH=5.7). In their observations, E_{corr} of nanostructured Ni-SiC composite shifted more noble potential in the amount of 90 mV than that of pure Ni and the polarization resistances of the composite were much higher than those obtained from pure Ni coatings both without and with a normal sliding load of 30 N as shown in Figure 2-24a and b, respectively.

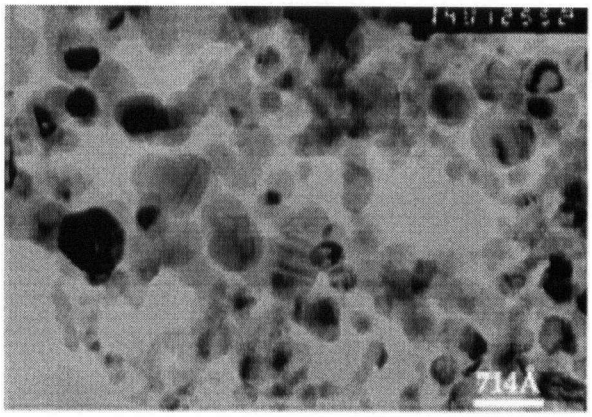

Figure 2-23 TEM image of nano-SiC particles [Benea et al. , 2002]

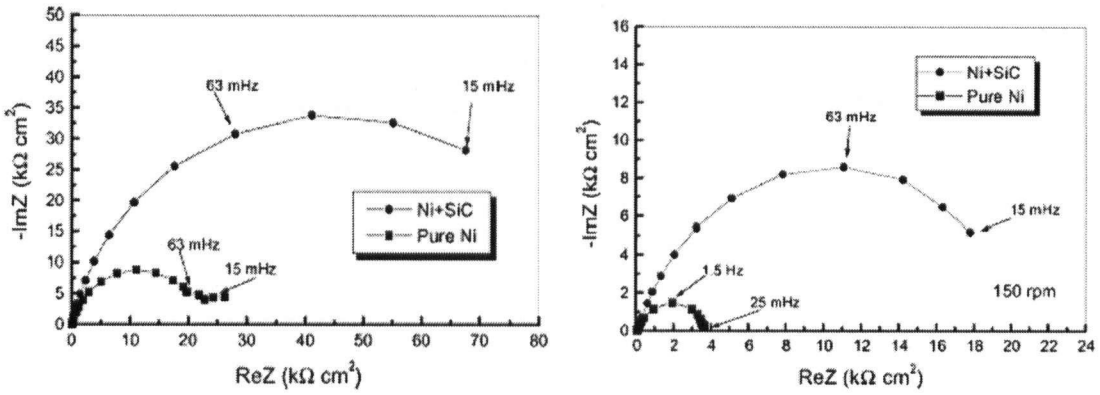

(a) (b)

Figure 2-24 Impedance diagrams of nanostructured Ni-SiC composites and pure Ni coatings performed in 0.5 M Na_2SO_4 at 150 rpm of cylinder (a) without a normal load and (b) with a normal sliding load of 30 N [Benea et al. , 2002]

2.2.3.3 Nanocrystalline Materials Obtained by Gas Phase

New alloys have been developed by using new metastable materials produced by passing from the gas state directly to the solid state [Hadjipanayis, G. C. and Siegel, R. W., 1993; Michael Nastasi et al, 1991; David L. Bourell 1996]. It is generally preferable to synthesize nanophase materials from atomic or molecular precursors in order to gain the greatest control over a variety of microscopic aspects of the condensed ensemble. Various

techniques such as sputtering, pulsed-high-energy-density plasma (PHEDP), and thermal spraying, etc have been developed to improve the surface properties of materials.

Zeiger et al.[1995] studied the anodic dissolution of nanocrystalline Fe-8 wt% Al (grain size, 40 nm) prepared by magnetron sputtering methods in deaerated 0.1 M Na_2SO_4 at pH 1 and 6 compared with polycrystalline counterpart (grain size, 200 ~ 300 μm). In strong acidic solution (pH=1), both samples dissolved actively without passivation (Figure 2-25a). In the case of nanocrystalline Fe-8 wt% Al, E_{oc} was shifted to more negative potential and the anodic current density was higher than that of polycrystals due to higher defect density (e.g. grain boundaries). In comparison, in weakly acidic solution (pH=6), E_{oc} of nanocrystalline material was shifted to more positive potential and the anodic and passivation current densities were clearly lower than those found in their polycrystalline counterparts as shown in Figure 2-25b. They reasoned that a faster dissolution and diffusion of Al through the grain boundaries in nanocrystalline sample promoted more protective passive film formation resulting in Al-rich passive oxide layer.

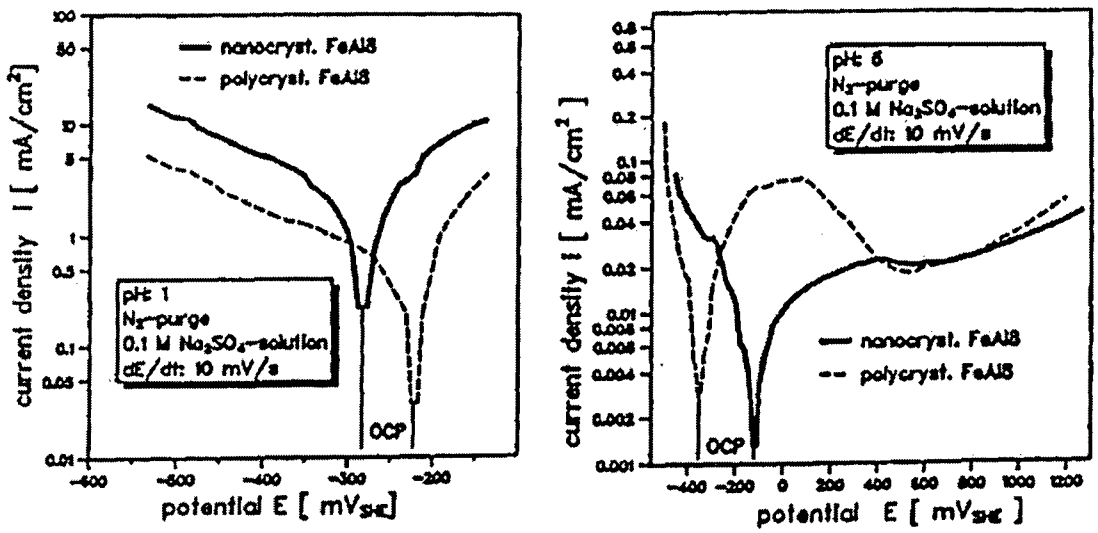

(a) (b)

Figure 2-25 Potentiodynamic polarization curves of poly- and nanocrystalline Fe-8 wt% Al in deaerated 0.1 M Na_2SO_4 at (a) pH=1 and (b) pH=6 [Zeiger et al., 1995]

Inturi et al. [1992] studied the corrosion behavior of sputter-deposited nanocrystalline 304-type stainless steel film with a grain size of 25 nm by potentiodynamic polarization tests in 0.3 wt% NaCl solution at 23 °C. They observed that the breakdown potential of the nanocrystalline stainless steel films was approximately 850 mV higher than that of conventional material (grain size, 30 μm) of the same composition as shown in Figure 2-26. They reasoned that this enhanced localized corrosion resistance of the nanocrystalline materials was attributed to the large number of uniformly distributed defects in the passive film which are primarily located at the grain boundaries. In comparison to coarse-grained materials, the chloride concentration at each of the defects of nanocrystalline materials was greatly reduced. Therefore localized enrichment of chlorides and subsequent acidification at each defect on the grain boundary site required a greater driving force (more positive potential) for stable pit growth. Also, the authors pointed out that the presence of second phases (probably γ-Fe_2O_3 and Fe_3O_4) at the grain boundaries did not deteriorate the enhanced localized corrosion resistance of the nanocrystalline materials.

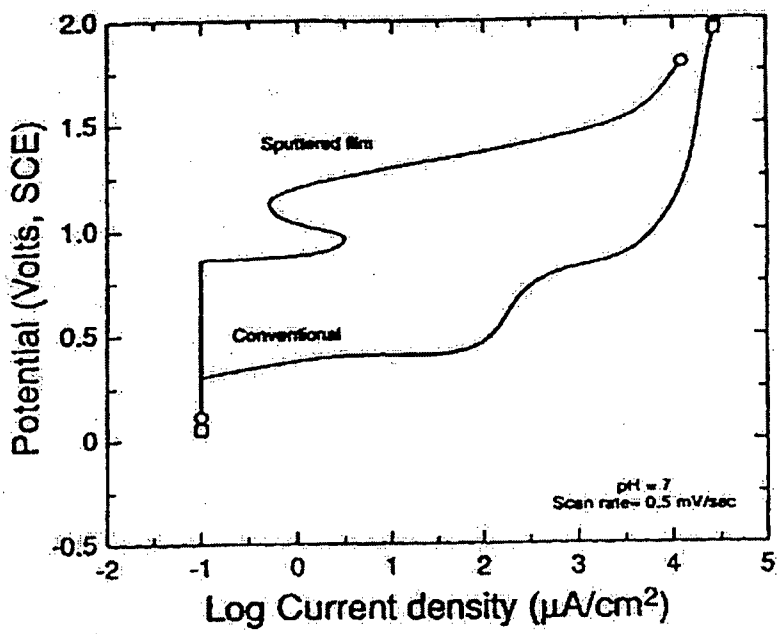

Figure 2-26 Anodic polarization curves for nano- and conventional polycrystalline 304 type stainless steel in aerated 0.3wt% NaCl [Inturi, 1992]

Nanocrystalline Co-Cr coatings (grain size, 21 nm) was prepared by plasma spraying and their corrosion performance was compared to conventional Co-Cr (ASTM F75) alloys (grain size was estimated to the order of tens micrometer) in Hank's solution (composed of mainly NaCl) at pH of 7 as shown in Figure 2-27 [Cheng, D. et al., 2001]. The nanocrystalline coatings showed a lower anodic and passivation dissolution rate and less localized damage than that of the conventional one, demonstrating better performance for application potential for orthopedic implants. They explained the enhanced corrosion resistance may be due to i) reduced grain boundary segregation, ii) the presence of residual strain and iii) different repassivation kinetics in nanocrystalline materials.

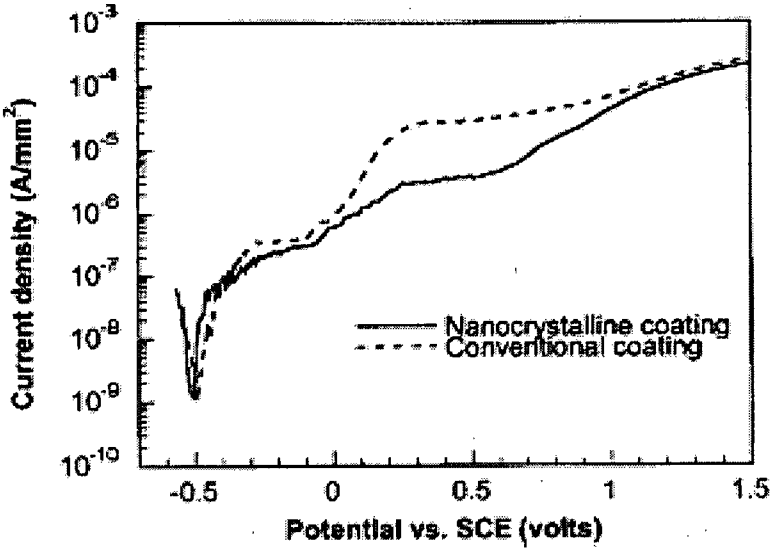

Figure 2-27 Current densities of conventional Co-Cr alloys and nanocrystalline coatings during the first sweeping cycle in Hank's solution [Cheng, D. et al., 2001]

The Pulsed-High-Energy-Density-Plasma (PHEDP) has been applied for surface modification of stainless steel. In this modification, the surface of the stainless steel was heated up to about 1500 °C very quickly, then the surface was cooled down rapidly. In particular, the quenching process was accompanied by the implantation of active plasma particles containing TiCN, c-BN, or AlN. Wei Kun et al. [1999] produced AlN film on

stainless steel by PHEDP methods and investigated their corrosion resistance in 2 % NaCl solution compared with unmodified stainless steel. The formed films are composed of nanocrystalline-structured AlN phase (crystal size, ~10 nm). They found that the nanocrystalline-structured AlN films clearly contributed to the improvement of the corrosion resistance of the modified steel, whose corrosion rate reduced by ten times compared to that of the unmodified stainless steel.

2.2.3.4 Nanocrystalline Materials Obtained by Mechanical Alloying

Mechanical alloying is a well known solid state reaction technique to synthesize alloys with nanometer-scale crystallites and to obtain extended solid solutions.

Schneider, M. et al. [2000] and Elkedim et al. [1996] investigated the corrosion behavior of nanocrystalline Ni produced by ball milling in 1 N H_2SO_4 and 0.1 M H_2SO_4 solutions, respectively. According to their test results using potentiodynamic polarization as well as impedance measurements, both groups observed a decrease of corrosion resistance for nanocrystalline Ni compared with coarse grained polycrystalline counterpart, i.e., higher passivation current density due to more defective passive film formed on nanocrystalline Ni surface. It is in agreement with Rofagha et al. [1991] and Mishra, R. and Balasubramaniam, R. [2004] who reported similar results for nanocrystalline Ni synthesized by different method, i.e., electrodeposition (see section 2.2.3.2.).

The corrosion behavior of nanocrystalline Fe (grain size, 28 nm) obtained by ball milling and hot compaction in comparison with polycrystalline Fe (grain size, 7 μm) was investigated in a 0.5 M H_2SO_4 solution [Elkedim et al., 2002]. The results showed that the corrosion resistance parameters (peak active current density, active domain, width of passivation) of ball-milled nanocrystalline Fe were lower than that of polycrystalline Fe as shown in Figure 2- 28.

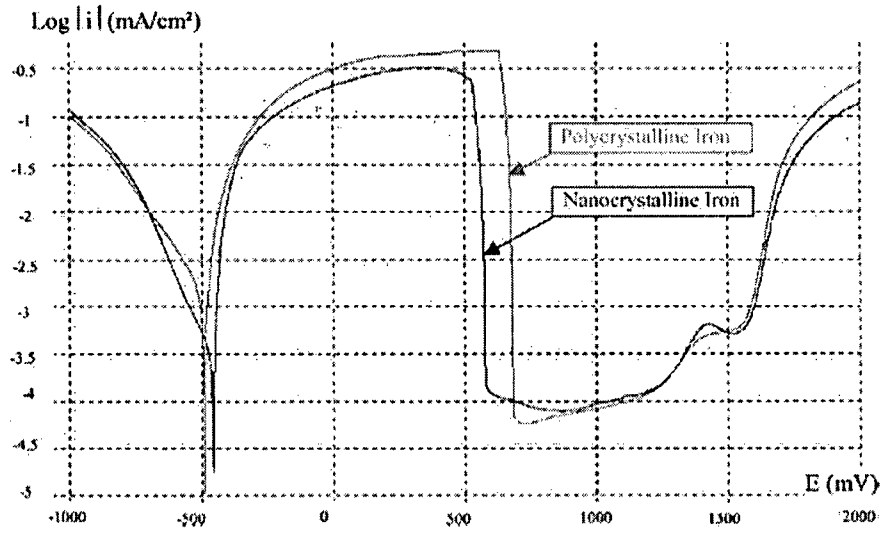

Figure 2-28 Potentiodynamic polarization curves of poly- and nanocrystalline Fe prepared by ball-milling in 0.5 M H_2SO_4 [Elkedim et al., 2002]

A few studies have also reported the improved corrosion resistance of nanocrystalline pure metals synthesized by ball milling methods. For example, nanocrystalline Mg in borate buffered solution (pH=8.4) and KOH (pH=14) [Zidoune, M. et al., 2004], nanocrystalline Ru in 1 M NaOH [Roue, L. et al., 1998] and nanocrystalline Cu in 1 M NaOH [Elkedim, et al., 1998] exhibit better corrosion resistance than their polycrystalline counterparts in terms of nobler corrosion potential and smaller passivation current density.

This enhancement of corrosion resistance may be supported by Grake et al. [1998] and Wurschum, R. [2002] who argued that the grain boundaries and dislocation act as easy diffusion paths and thus lead to rapid formation of the protective film.

On the other hand, Co-35 ~50 at% Cu mechanical alloyed powders (grain size, ~ 20 nm) in borate solution [Lopez-Hirata, V. M. and Arce-Estrada, 1997] and $Cu_{90}Ni_{10}$ alloys (grain size, 21 nm) in neutral solution containing chloride [Barbucci, A. et al. 1999], produced by ball milling process, the nanoprocessing has a rather negative effect on the corrosion resistance. This may be due to the same reason, i.e. faster atomic diffusion at the grain boundaries leading to a higher anodic dissolution rate of the metal by either a direct reaction to a bare metal surface or via a defective passive layer. It is also noted that the

surface defects, e.g. adatoms, vacancies, microclusters, grain boundaries, etc. play an important role as superactive sites for various surface electrochemical processes [Burke, L. D. et al. 2001].

2.2.3.5 Summary

Due to their unique microstructural characteristics (i.e. comparable volume and surface area fraction of intercrystalline defects), nanocrystalline materials have a strong tendency of high electrochemical reactivity compared to that of coarse grained polycrystalline materials. Thus, an increased driving force for electrochemical reaction can lead to the higher anodic dissolution rate of nanocrystalline materials (e.g., the electrodeposited nanocrystalline Co (Figure 2-19a), nanocrystalline Fe-8 % Al prepared by the sputtering method (Figure 2-25a), mechanical alloyed nanocrystalline Co-Cu [Lopez-Hirata and Arce-Estrada, 1997] and ball milled nanocrystalline Cu-Ni [Barbucci, A. et al, 1999]).

On the other hand, an increased reactivity can allow a more protective passive layer to form via easy or rapid atomic diffusion along the large fraction of grain boundaries in nanocrystalline pure metals. Many nanocrystalline pure metals having a clear passivation region (e.g. electrodeposited nanocrystalline Zn (Figure 2-20)), ball-milled nanocrystalline Fe (Figure 2-28), ball-milled nanocrystalline Mg [Zidoune, M. et al, 2004], ball-milled nanocrystalline Ru [Roue, L. et al, 1998], and mechanical processed ultra fine grained Cu [Vinogradov et al, 1999]) clearly showed the increase of corrosion resistance i.e. smaller passivation current. It is noticeable that the synthesis route was not crucial in the corrosion performance for these types of nanocrystalline pure metals. Furthermore, a higher homogeneity due to their fine grain size in nanocrystalline material allows a better distribution of defect area, thus resulting in reduced localized corrosion attack (Figure 2-17). The beneficial effects of grain size reduction are also found in binary or multi-composition alloy systems. For example, several binary systems such as nanocrystalline Fe-8 % Al prepared by sputtering method (Figure 2-25b), plasma-sprayed nanocrystalline Co-Cr (Figure 2-27), and mechanical alloyed nanocrystalline $Fe_{53}Al_{47}$ [El-Kedim, 2004] showed higher corrosion resistance due to i) microstructural homogeneity and ii) more protective passive

layers enriched Al or Cr via rapid diffusion of Al or Cr atoms along the grain boundaries compared to that of coarse grained polycrystals. An increased corrosion resistance by nanoprocessing was also observed in the multi-composition alloys such as nanocrystalline stainless steel prepared by sputtering (Figure 2-28), nanocrystalline 304 stainless steel prepared by sand blasting [Wang and Li, 2002], $Fe_{32}Ni_{36}Cr_{14}P_{12}B_6$ (Figure 2-15) and Fe-Cu-Nb-Si-B [Sousa and Kiminami, 1997] also showed higher corrosion resistance.

However, conflicting results have been observed among the passivating nanocrystalline pure metals regarding corrosion resistance. A study of nanocrystalline Co in alkaline solution showed a comparable corrosion resistance compared to that of its' polycrystalline Co counterpart (Figure 2-19b). In the case of nanocrystalline Ni, several studies clearly showed the decreased corrosion resistance regardless of synthesis methods (Figure 2-16 and Figure 2-18). In earlier studies, such a nanoprocessing by the crystallization from an amorphous precursor most likely led to the deterioration of the corrosion resistance of amorphous such as Alloy 2826 (40Fe-40Ni-16P-4B) and Alloy 2826A (24Fe-15Cr-40Ni-16P-4B) [Diegle and Slater, 1976] and Fe-10Cr-13P-7C (Figure 2-14). This inferior corrosion resistance of the nanocrystalline state was mainly due to i) the presence of intercrystalline defects and ii) segregation, precipitation and other compositional gradients inducing galvanic corrosion [Diegle and Slater, 1976; Naka et al, 1980]. However, as mentioned above, $Fe_{32}Ni_{36}Cr_{14}P_{12}B_6$ (Figure 2-15) and Fe-Cu-Nb-Si-B [Sousa and Kiminami, 1997] showed an improved corrosion resistance. By considering very similar chemical composition and corrosion environments, conflicting results are not currently understood. The corrosion studies for nanocrystalline Ni-P (Figure 2-21) and nanocrystalline Co-P (Figure 2-22) clearly demonstrated a detrimental effect of P alloying on corrosion resistance compared to that of conventional polycrystalline Ni and Co, respectively. However, both studies did not include the comparative corrosion properties of the coarse grained polycrystalline counterpart containing the same or similar P content. Thus, the effect of grain size reduction alone on the corrosion properties can not be evaluated separately with respect to the P alloying. In spite of numerous opinions for the effect of grain size and alloying elements as well as synthesis methods on the corrosion properties of nanocrystalline materials, there is still a lack of fundamental understanding of the corrosion mechanism in such materials.

3 Research Objectives

The purpose of this study is to investigate the corrosion properties of electrodeposited nanocrystalline Co and Co-P alloys by using various dc polarization and ac EIS techniques coupled with surface analysis (e.g., SEM, EDX and XPS). In contrast, the previous corrosion studies of nanocrystalline Co and Co-P alloys were carried out by using conventional polarization techniques. The research objectives of the proposed work are as follows:

(1) To obtain a greater understanding of the corrosion properties of nanocrystalline Co and Co-P alloys (grain sizes of 7 to 20 nm) in a wide range of solution pH ranging from 1 to 13.

(2) To investigate the effects of grain size on the anodic and cathodic reaction rates.

(3) To explore the anodic dissolution mechanism of poly- and nanocrystalline Co by measuring anodic Tafel slopes and other kinetic paramenters in acidic solution and to compare these results to surface analysis.

(4) To determine the effects of P alloying (1.1 and 2.1 wt %) on the anodic dissolution and passivation phenomena as well as to identify the electrochemical reaction mechanisms for these alloys.

(5) To perform, to my knowledge, the only experiments investigating the influence of chloride ions on nanocrystalline Co and Co-P alloys in 3.56 wt% NaCl solution to simulate exposure to sea water environments.

(6) To evaluate the stability of the passive film formed on poly- and nanocrystalline Co and nanocrystalline Co-P alloys in alkaline solution and to estimate the thickness of the passive film as well as identify the chemical composition of this film by using EIS and XPS analysis.

4 Experimental

4.1 Materials

4.1.1 Coarse Grained Polycrystals

In the current study, the electrodeposited polycrystalline Co with a purity of >99.95 wt% sample was used as the reference material and referred to as "polycrystalline Co". The sample was received from Falconbridge Ltd. with 25 mm cut squares (1"x1") as shown in Figure 4-1. Table 4-1 shows the typical analysis of polycrystalline Co, containing low concentration of impurities (e.g., <10 ppm of S). This grade is used by virtually every industry sector.

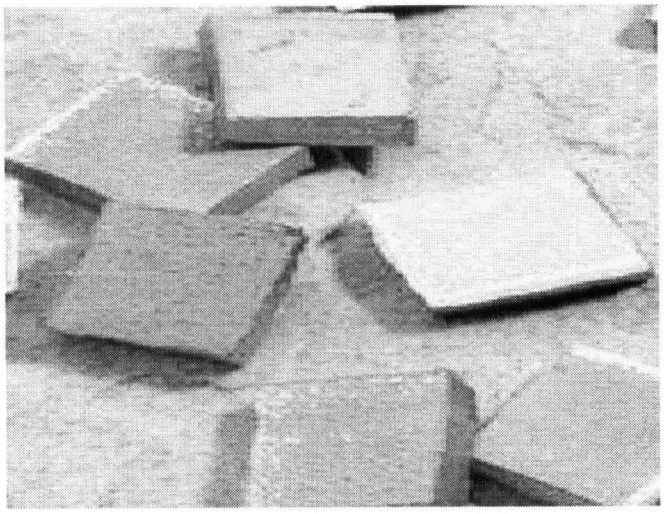

Figure 4-1 Conventional polycrystalline Co electrodeposits

*Table 4-1 Typical analysis of polycrystalline Co (wt%) used in the current study**

Co	C	Cu	S	Fe	Pb	Ni	Zn	N_2	H_2	O_2
99.95	0.0020	0.0005	<0.0010	0.001	0.0002	0.03	0.0002	0.0001	0.0005	0.005

* Data from Falconbridge Ltd. (http://www.falconbridge.com/)

Another set of polycrystalline Co electrodeposits with purity of >99.95 % containing 370 ppm of S (annealed at 950 °C for 2hrs in Ar gas and quenched in water) were also utilized to investigate the effect of sulfur (S) impurities on the corrosion properties and referred to as "annealed polycrystalline Co". This sample was also provided by Falconbridge Ltd. with thin broken pieces of approximately 25 mm. Table 4-2 also shows the typical analysis of annealed polycrystalline Co.

*Table 4-2 Typical analysis of annealed polycrystalline Co (wt%) used in the current study**

Co	C	Cu	S	Fe	Pb	Ni	Zn
99.95	0.0015	0.0005	0.037	0.001	0.0002	0.05	0.0001

* Data from Falconbridge Ltd. (http://www.falconbridge.com/)

4.1.2 Nanocrystals

In case of nanocrystalline Co samples referred to as "nanocrystalline Co", a sheet of sample with purity >99.95 wt% (0.2 mm thick) was pulse-plated from a bath containing cobalt sulfate, sodium chloride, boric acid and varying amounts of saccharin onto a titanium cathode using a patented technology (US Patent #5,352,266) by Integran Technologies Inc. of Toronto. The grain size of nanocrystalline Co was controlled by optimizing the electrodeposition parameters such as bath composition, pH, temperature, current density, etc. After plating to the desired thickness, the sheet was mechanically peeled off the substrate. Leco CS (Infrared absorption) analysis revealed that the nanocrystalline Co samples contained 200 or 300 ppm of S by weight. The source of the high levels of S in the nanocrystalline Co was likely saccharin ($C_7H_5NO_3S$) which was added to the electroplating bath as a grain refiner.

Nanocrystalline Co-P samples were also produced using a pulse electrodeposition technique (US Patent #5,433,797) by Integran Technologies Inc. of Toronto. The amount of P co-deposited with Co was controlled by the phosphoric concentration in the plating bath. The bulk concentrations of P in nanocrystalline Co-P alloys used in the current studies were

1.1 and 2.1 wt% and these are referred to as "nanocrystalline Co-1.1P" and "nanocrystallineCo-2.1P", respectively. The bulk concentration of P was determined by Energy Dispersive X-ray Spectroscopy (EDX). To investigate the effects of grain size refinement and P alloying in nanocrystalline Co-P alloys, some as-deposited nanocrystalline Co-1.1P and 2.1P alloys were annealed to induce grain growth at 350 °C for 4 hrs or at 800 °C for 2 hrs in Ar gas flow and quenched in water and referred to as "annealed nanocrystalline Co-1.1P" and "annealed nanocrystalline Co-2.1P", respectively. Based on the similar thermal stability bahavor (i.e., slow changes of heat flow and heat peak at ~ 470 °C) between nanocrystalline Co-1.1P in the current study and nanocrystalline Co-0.6 wt % P electrodeposits in the reference [Choi, Pyuck-Pa, 2003], the annealing temperature (i.e., 350 °C or 800 °C) was determined by direct comparison of two thermogram curves as shown in Figure A-7a and b (see more details in section 5.1.3.2). All tested samples in the current study are summarized in Table 4-3.

Table 4-3 Summary of all tested samples used in the current study

Samples (S or P concentration in weight)	Condition
Polycrystalline Co (<10 ppm of S)	- As-deposited electrowon
Annealed polycrystalline Co (370 ppm of S)	- Annealed at 950 °C for 2hrs in Ar gas and quenched in water
Nanocrystalline Co (200 ppm of S)	- As-deposited
Nanocrystalline Co (300 ppm of S)	- As-deposited
Nanocrystalline Co-1.1P (1.1 wt% P)	- As-deposited
Nanocrystalline Co-2.1P (2.1 wt% P)	- As-deposited
Annealed nanocrystalline Co-1.1P and 2.1P at 350 °C (1.1 and 2.1 wt % P, respectively)	- Annealed at 350 °C for 4hrs in Ar gas and quenched in water
Annealed nanocrystalline Co-1.1P and 2.1P at 800 °C (1.1 and 2.1 wt % P, respectively)	- Annealed at 800 °C for 2hrs in Ar gas and quenched in water

4.2 Materials Characterization

4.2.1 Transmission Electron Microscope (TEM)

The grain size and structure of nanocrystalline samples were characterized using dark field image and diffraction patterns in a Hitachi H800 Transmission Electron Microscope at 200 kV. TEM samples were prepared by jet polishing in 20% perchloric acid plus 80% methanol (by volume) electrolyte at a temperature -15 °C and an electropolishing voltage of 30 V dc.

Figure 4-2a and b show a typical TEM darkfield image and the corresponding selected area diffraction pattern (SADP) for nanocrystalline Co containing 200 ppm of S, respectively. The grains are uniformly distributed and ultra-fine, confirming a narrow grain size distribution typically observed in nanocrystalline Co [Kim, S. H., 2003; Karimpoor, A. A., 2002; Hibbard, G., 2001]. The mean grain size of about 20 nm with a standard deviation of 7.6 was determined by measuring 275 grains from the darkfield image over a representive area and the corresponding grain size distribution is shown in Figure 4-2c. The analysis of the corresponding electron diffraction pattern revealed that the rings corresponded to those characteristic diffraction patterns of a HCP Co structure with the first five rings corresponding to the {100}, {002}, {101}, {102} and {103} planes.

A microstructure found for a nanocrystalline Co-1.1P is given in Figure 4-3a and b which show a darkfield TEM image and the corresponding SADP, respectively. The microstructure of nanocrystalline Co-1.1P also shows an ultra-fine equiaxed grain structure and a narrow grain size distribution (Figure 4-3c) which is similar to that of nanocrystalline Co. The mean grain size was determined to be about 10 nm with a standard deviation of 3.4 by measuring 115 grain diameters from the darkfield image. The rings from the SADP also corresponded to the characteristics of a HCP Co structure without clear evidence of cobalt-phosphide precipitates in as-deposited state despite the low phosphorous solubility in cobalt (e.g., 0.63 at %, see Appendix A-1.), suggesting that nanocrystalline Co-1.1P is a single-phased solid solution supersaturated with phosphorous. Considerable extension of the solid solubility was previously observed in other nanocrystalline materials such as Ni-P

[McMahon, G. and Erb, U., 1989], Co-W [Osmola, et al., 1993] and Zn-Ni [Alfantazi, A., and Erb, U., 1996] due to their unique microstructures.

4.2.2 Optical Microscopy

For coarse grained Co samples, metallographic analysis of a polished and etched specimen revealed that both polycrystalline Co and annealed polycrystalline Co showed mainly equiaxed grains with some black holes resulting from the over etching as shown in Figure 4-3a and b, respectively. The average grain sizes for both samples were about 16 μm and 27 μm, respectively, measured by line intercept method.

As shown in Figure 4-4c and d, both annealed nanocrystalline Co-1.1P and 2.1P alloys at 800 °C, the morphologies exhibited different sizes of precipitates mainly along the grain boundaries and the grain sizes were increased up to about 2 and 1 μm, respectively, per line intercept methods.

For etching solution, a mixture of 15 ml nitric acid, 15 ml acetic acid, 60 ml HCl and 10 ml water was used for all etched samples.

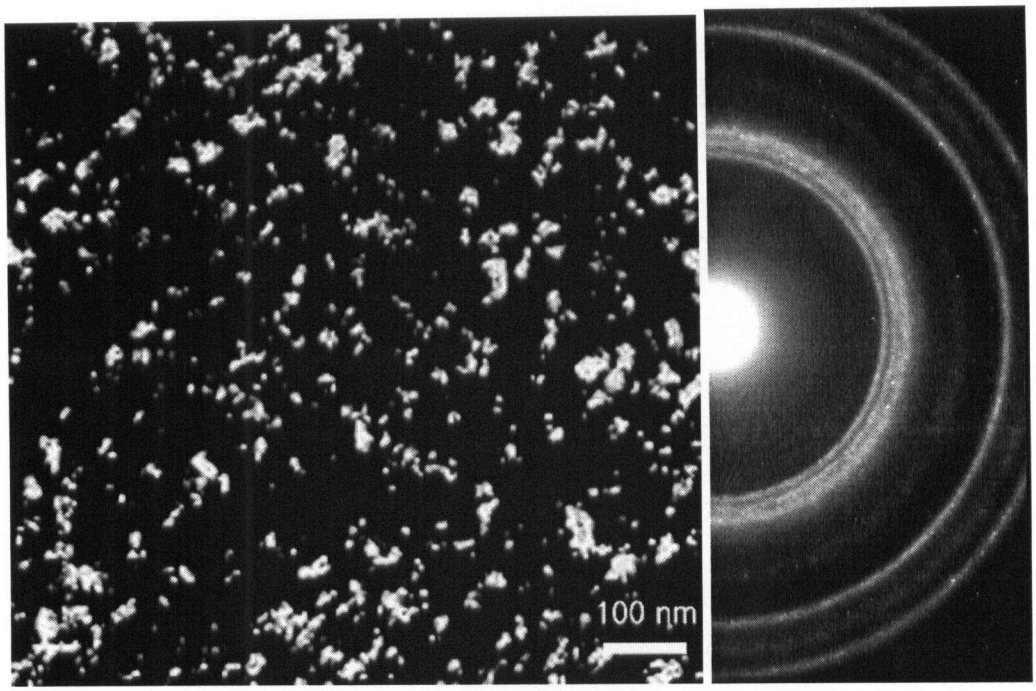

(a) (b)

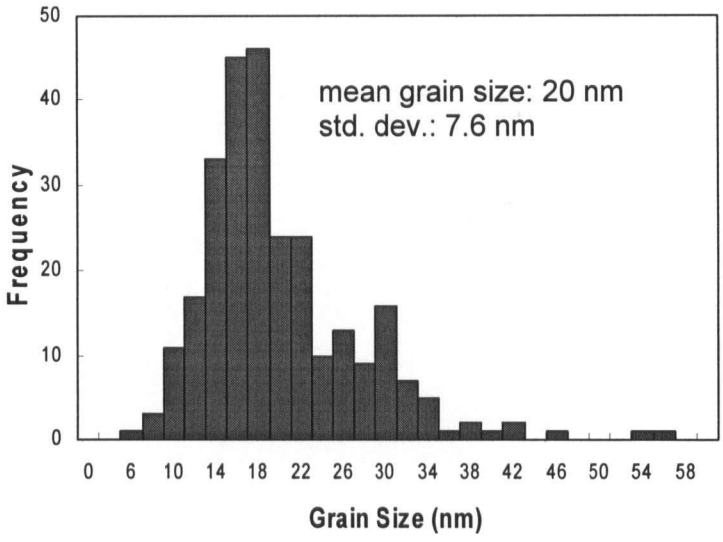

(c)

Figure 4-2 TEM dark field image (a) as well as selected area diffraction pattern (b) and corresponding grain size distribution (c) for nanocrystalline Co.

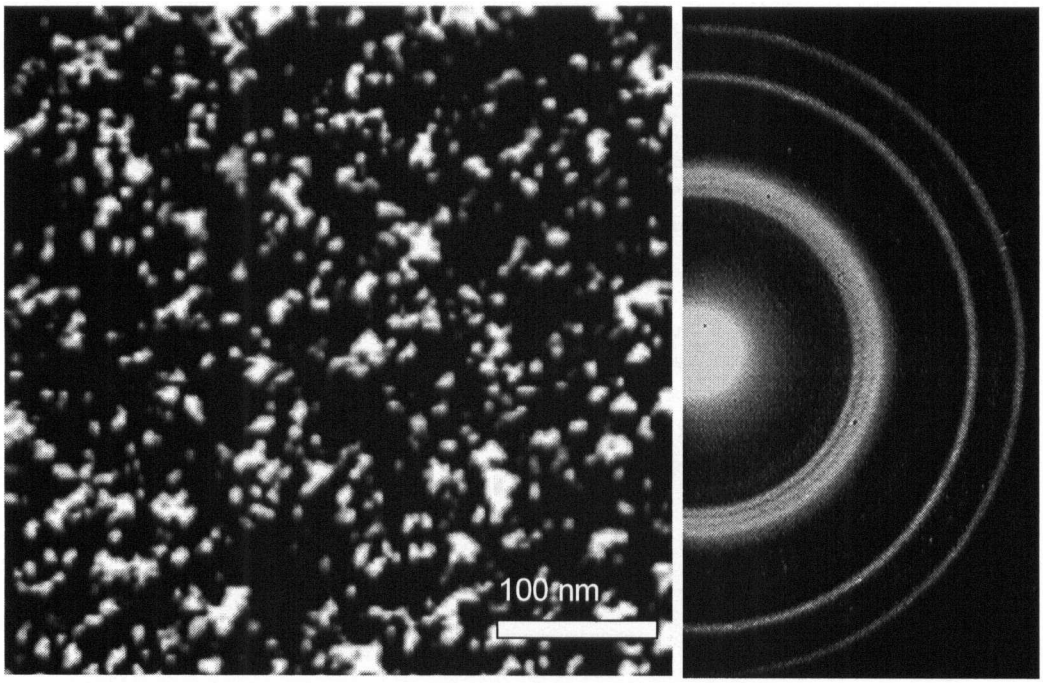

(a) (b)

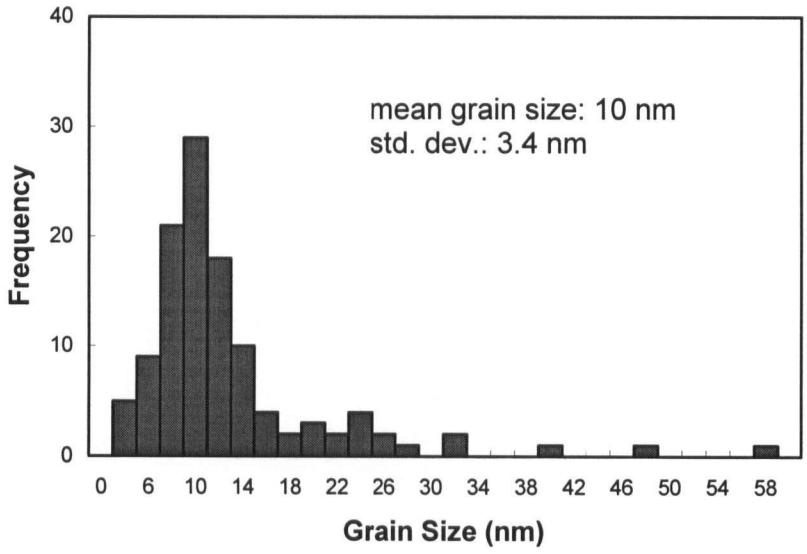

Figure 4-3 TEM dark field image (a) as well as selected area diffraction pattern (b) and corresponding grain size distribution (c) for nanocrystalline Co-1.1P.

(a)

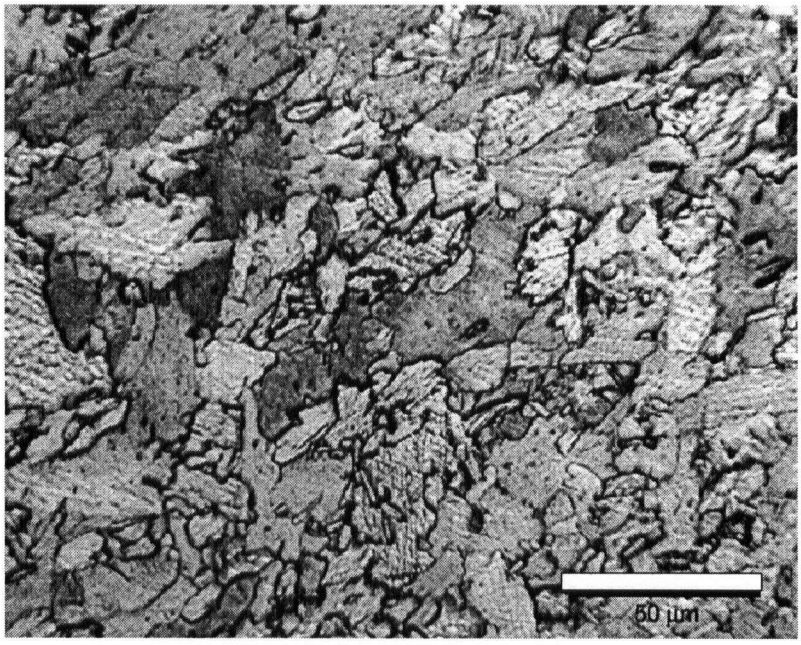

(b)

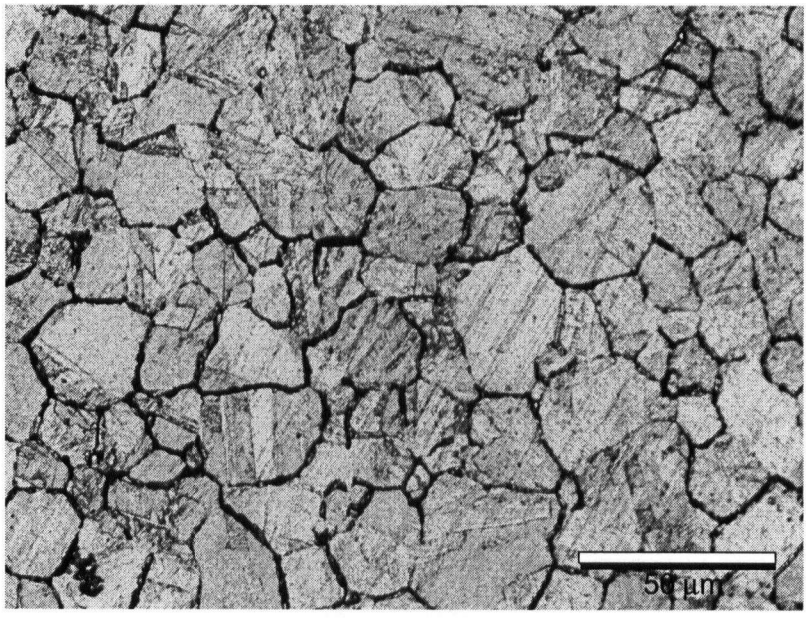

Figure 4-4 Optical micrographs showing the microstructure of (a) polycrystalline Co, (b) annealed polycrystalline Co, (c) annealed nanocrystalline Co-1.1P at 800 °C and (d) annealed nanocrystalline Co-2.1P at 800 °C.

(c)

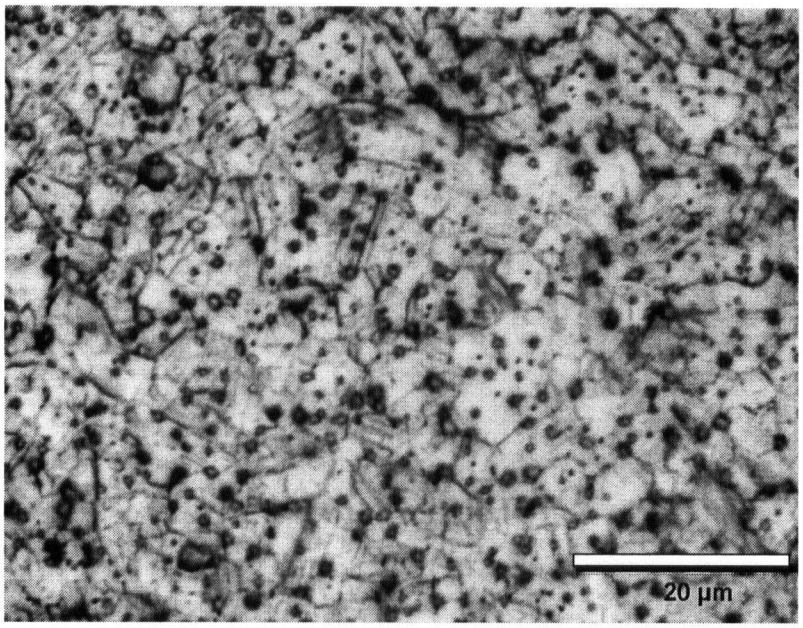

(d)

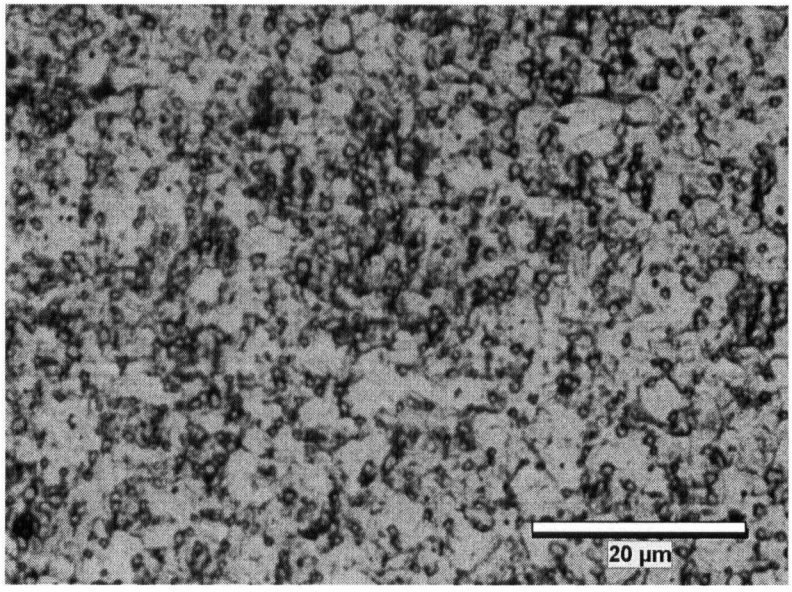

Figure 4-4 (continued)

4.2.3 X-ray Diffraction (XRD)

All Co and Co-P samples were also characterized by means of XRD using CuKα radiation (λ = 1.5418 Å) on a standard Siemens D5000 diffractometer at a scan rate of 0.04°/sec. The measured XRD patterns are presented in Figure 4-5 along with the standard peaks for α-Co (hexagonal close packed, HCP) [JCPDS-PDF, No.5-727] and ε-Co (face centered cubic, FCC) [JCPDS-PDF, No.15-806].

For all Co and Co-P samples (except annealed nanocrystalline Co-1.1P and 2.1P at 800 °C as shown Figure 4-6c and 4-7c, respectively) used in this study, the observed peaks are matched well with those corresponding to HCP Co in the range of 2θ = 35° ~ 102°. However, the peaks positioned at 44.70°, 76.01° and 94.83° could be due to the diffraction from either the HCP or the FCC phase. Although a clear analysis for each phase is not possible, based on these peaks, the FCC phase would also show the peaks from {200} and {222} planes positioned at 51.56° and 97.75°. From the absence of these peaks, it is concluded that all observed samples shown in Figure 4-4 consist mainly of the HCP phase. It is noteworthy that the X-ray diffraction patterns of as-deposited nanocrystalline Co and Co-P samples show considerable line broadening which is a result from the ultra fine grain size [Cullity, 1978]. By direct calculation from the line broadening equations, so called, Scherrer's formula [Cullity, 1978], the grain sizes of nanocrystalline Co and Co-P samples were also determined. This method is well suited to detect grain diameters of less than 100 nm (see Appendix A-2).

Figure 4-6 and 4-7 show XRD patterns of annealed nanocrystalline Co-1.1P and 2.1P samples, respectively, in comparison with as-deposited states. For annealed nanocrystalline Co-1.1P at 350 °C shown in Figure 4-6, the measured peaks are well matched with those corresponding to HCP Co structure and have a strong basal {002} texture similar to as-deposited state. The XRD patterns also show considerable line broadening, indicating the ultrafine grain size. In the case of the annealed nanocrystalline Co-1.1P at 800 °C, however, the observed peaks have been sharpened and FCC Co phase and Co_2P phase [JCPDS PDF. No.6-595] have also been identified from the peak positioned at 51.5° and 40.5°, respectively. These peaks from FCC Co phase and Co_2P phase are more pronounced in annealed

nanocrystalline Co-2.1P at 800 °C. Table 4-4 summarizes the crystal structures and average grain sizes of all tested Co and Co-P samples used in the current study.

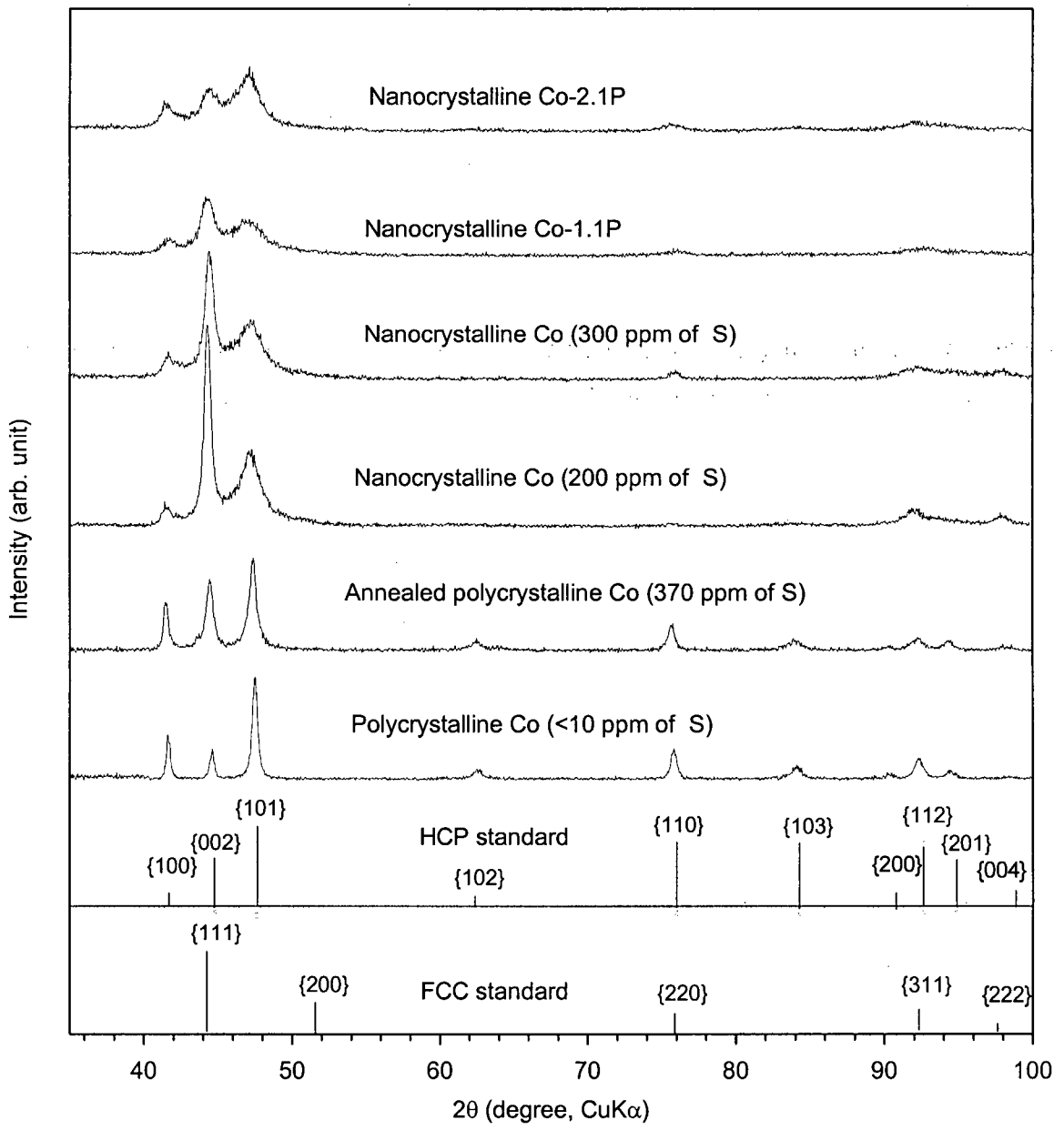

Figure 4-5 XRD patterns of Co and Co-P samples along with the standard peaks for α-Co (hexagonal close packed, HCP) [JCPDS-PDF, No.5-727] and ε-Co (face centered cubic, FCC) [JCPDS-PDF, No.15-806].

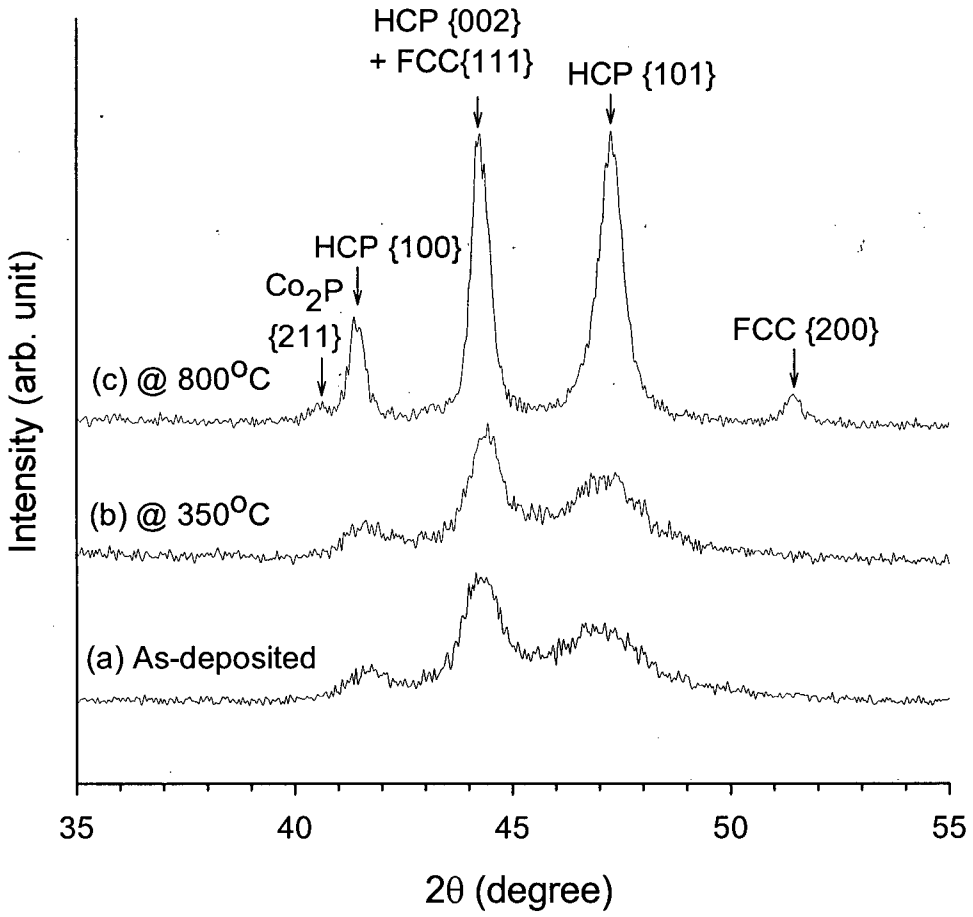

Figure 4-6 XRD patterns for different types of nanocrystalline Co-1.1P alloys: (a) as-deposited, (b) annealed at 350 °C for 4 hrs, and (c) annealed at 800 °C for 2 hrs.

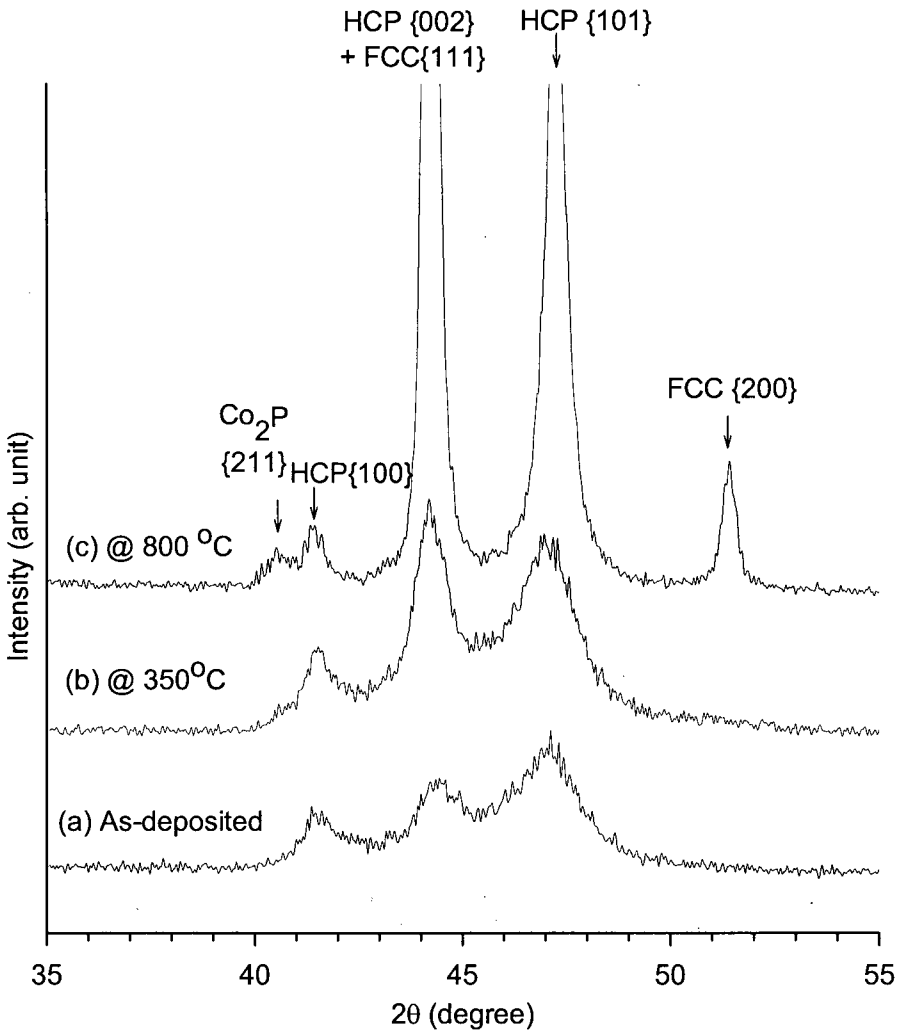

Figure 4-7 XRD patterns for different types of nanocrystalline Co-2.1P alloys: (a) as-deposited, (b) annealed at 350 °C for 4 hrs, and (c) annealed at 800 °C for 2 hrs.

Table 4-4 Crystal structures and average grain sizes of all Co- and Co-P samples used in the current study

Samples	Crystal Structure	Ave. Grain Size
Polycrystalline Co (<10 ppm of S)	HCP	16 μm*
Annealed polycrystalline Co (370 ppm of S)	HCP	27 μm*
Nanocrystalline Co (200 ppm of S)	HCP	20 nm#, 17 nm+
Nanocrystalline Co (300 ppm of S)	HCP	13 nm+
Nanocrystalline Co-1.1P	HCP	10 nm#, 8 nm+
Nanocrystalline Co-2.1P	HCP	7 nm+
Annealed nanocrystalline Co-1.1P at 350 °C	HCP	12 nm+
Annealed nanocrystalline Co-2.1P at 350 °C	HCP	9 nm+
Annealed nanocrystalline Co-1.1P at 800 °C	HCP+FCC+Co_2P	2 μm*
Annealed nanocrystalline Co-2.1P at 800 °C	HCP+FCC+Co_2P	1 μm*

* Measured by line intercept method in optical micrographs

+ Estimated by line broadening equations according to Eq. (A-1) and (A-2)

Measured from TEM dark field images

Note: The grain sizes estimated by line broadening equations for nanocrystalline Co (200 ppm of S) and nanocrystalline Co-1.1P were typically smaller than those measured from TEM dark field images in the amount of 2~3 nm. These differences, i.e., smaller grain sizes determined by XRD technique, may be due to contributions to the peak broadening other than grain boundaries, for instance, from conceivable crystal imperfections such as internal tensions, twin, and stacking faults [Barton, S. F., 1967].

4.3 Electrochemical Testing

4.3.1 Electrolytes

All tested solutions were prepared from reagent grade chemicals and the distilled and de-ionized water (having an electrical resistivity of ~1MΩ). The various electrolytes used for the current study are listed in Table 4-5. The pH of solution was measured to ±0.1 pH units by a sensitive pH-meter. The first and second acidic solutions were selected to compare the anodic dissolution rates of Co samples and to investigate the anodic dissolution mechanism by comparing the anodic Tafel slopes and reaction order for hydroxyl ions. For practical application in a sea water environment, a chloride containing solution was used. Lastly, the alkaline solution was also employed to study the passivation characteristics depending on the grain size and level of P alloying of Co and Co-P alloys.

Table 4-5 List of test solutions for the current study

Test Solution	pH at 298 K
0.1 M H_2SO_4	1.0 ± 0.1
0.5 M Na_2SO_4 + small amount of concentrated H_2SO_4	3.0 ± 0.1
3.56 wt.% by weight NaCl	6.2 ± 0.1
0.1 M NaOH	13.0 ± 0.1

4.3.2 Electrochemical Test Cell and System

For electrochemical measurement, a polarization cell similar to the one described in ASTM G5 (Figure 4-8) was used. The electrolyte test cell consisted of a commercially available one-liter glass cell (Princstion Applied Research, Model G0096), a platinum (Pt)

mesh counter, an external saturated calomel reference electrode, SCE (Princstion Applied Research, Mode, K0077), the working electrode, and a nitrogen gas purge tube.

The working electrode was mounted in a Tefzel® Dupont fluorocarbon electrode holder (Figure 4-9) and the crevice-free teflon washer exposes ~0.9 cm^2 of the specimen to the test solution. The SCE was interfaced to the test solution via a salt bridge filled with the test solution. The bridge was connected to a Luggin probe with a Vycor tip®(porous glass) that terminated ~2 mm from the working electrode surface. The tip was designed specifically to provide ultra low liquid leakage rates and minimum IR drop through the tip. If required, corrections were made for ohmic drop (iR) effect due to solution resistivity between the Luggin capillary and the working electrode.

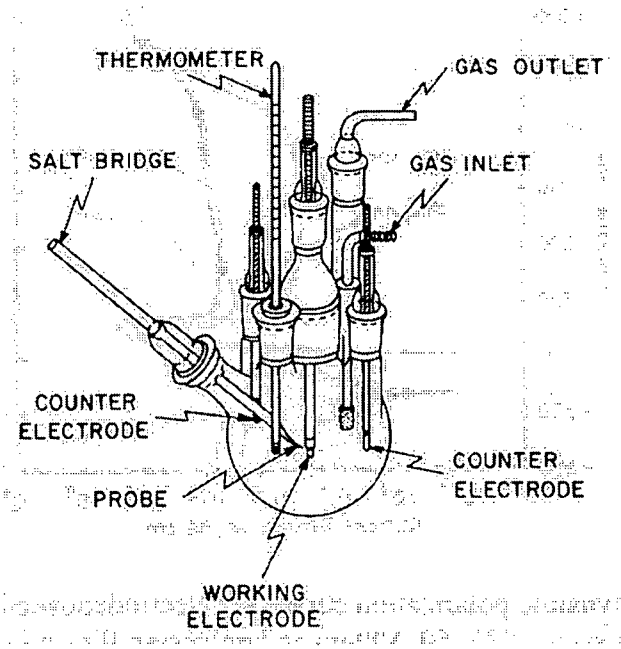

Figure 4-8 Schematic diagram of the polarization cell used in the ASTM G5 Test

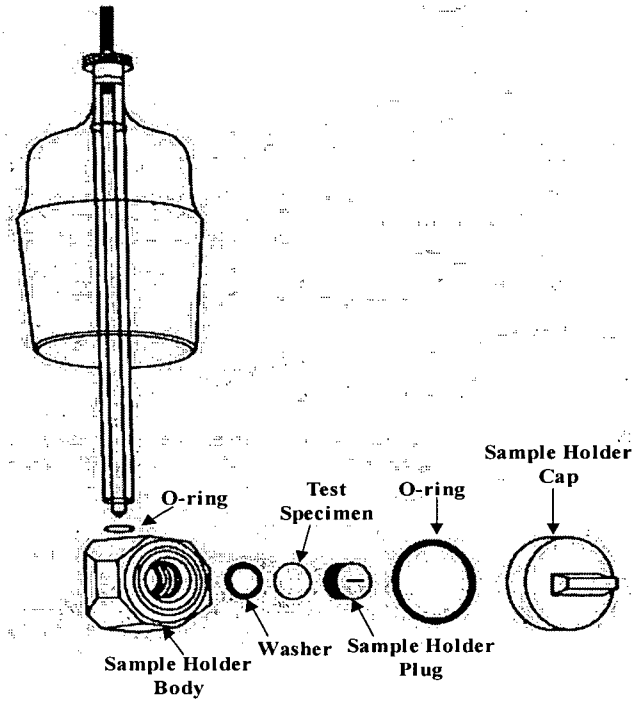

Figure 4-9 Schematic of electrode holder used in the electrochemical tests

The potentiostatic and (cyclic) potentiodynamic polarization experiments were conducted using an Electrochemical Interface (Solartron Model 1286) with built in General Purpose Interface Bus Board (GPIB) controlled by a personal computer via a commercial software package called CorrWare™ for Windows as shown in Figure 4-10. This potentiostat has a DC potential range ± 12.8 V and a current range of ± 2.0 A with max resolution of 100 μV and 1 nA, respectively. The CorrWare™ (Scribner Associates, ver.2.7) software is designed to provide potentiostat control, data acquisition, and on-screen real time graphics. The CorrView™ (Scribner Associates, ver.2.7) software was used for post test data analysis and charting.

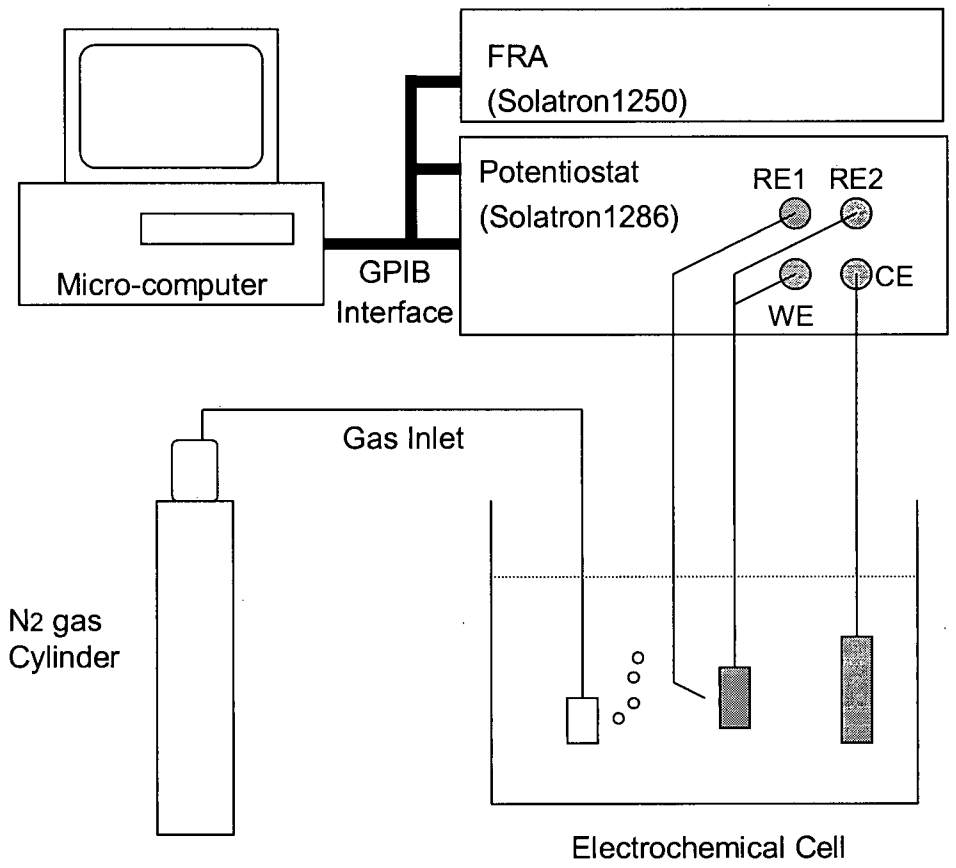

Figure 4-10 Schematic diagram of the electrochemical measurement system for testing.

The electrochemical impedance spectroscopy (EIS) measurements were performed with a combination of a Solartron 1286 Electrochemical Interface and a Solartron 1250 Frequency Response Analyzer (FRA). The voltage and current signals were transferred to a FRA, which generated and recorded the electrochemical impedance data. An ac excitation voltage signal generated by a FRA was then added to the internal dc polarization voltage set by the potentiostat, thereby providing the perturbation to the electrochemical system. The electrochemical impedance software ZPlot™ (Scribner Associates, ver.2.7) and ZSimpWin™ (PAR, ver3.10) were employed to control the measurement and analyze the impedance data.

4.3.3 Electrochemical Procedure

4.3.3.1 Specimen and Test Solution Preparation

The working electrode were mechanically ground to grit size #1200 SiC paper and degreased with acetone and cleaned untrasonically in ethyl alcohol within 1 hour before electrochemical testing.

For the electrochemical testing in acidic (pH=1.0 and 3.0) and alkaline (pH=13.0) solutions, the testing solutions were deaerated by pre-purified N_2 through the cell for 30 minutes prior to testing to reduce the oxygen level of the solution, and throughout the corrosion testing. During the test, the solution was magnetically stirred to minimize concentration effects. On the other hand, the neutral solution containg 3.56 % by weight NaCl was open to air to simulate a sea water environment.

4.3.3.2 Polarization Tests

After the specimen was transferred to the test cell, the open circuit potential (E_{oc}) was monitored to allow the working electrode to reach a steady state. Potentials were measured with respect to an external saturated calomel electrode (SCE) interfaced to the test solution. In this thesis, all potentials except E-pH diagrams are reported with respect to the SCE via the conversion:

$$E(V, SCE) = E(V, SHE) - 0.241\ V \qquad (4.1)$$

Three types of polarization tests were used in the present study. First, a potentiodynamic polarization test was usually used. In this test, the scan was started from the cathodic potential ranges to reduce the air formed oxides on the electrode surface and then the scan was continued in the positive direction until a pre-selected upper threshold potential was reached at a scan rate of 0.5 mV/s in acidic (pH=1 and 3) and 1 mV/s in both 3.56 % NaCl and 0.1 M NaOH solutions to keep a state of equilibrium during the polarization scan.

Second, a potentiostatic polarization test was performed in 0.1 M H_2SO_4 and 0.1 M NaOH solution. The preselected potential was directly applied to the working electrode and the current was measured as a function of time.

Third, a cyclic potentiodynamic polarization technique was also used to investigate the pitting susceptibility in 3.56 % NaCl solution. After stabilizing the open circuit potential, the test starts at -0.6 V_{SCE}, then the potential is increased in a positive direction at a scan rate of 1 mV/s up to 0.5 V_{SCE}. The potential scan is then reversed to the negative direction. The test is completed when the potential scans back to 50 mV lower than the initial corrosion potential. During the backward scan, the occurrence of localized corrosion on the surface can be characterized through an anodic current hysteresis loop. The rest potential (E_{rest}) can also be determined from the polarization curve.

After each test, the specimen was washed with de-ionized water and dried. All tests were carried out at room temperature. Most electrochemical measurements were repeated at least twice to confirm the reproducibility and the validity of the results (see Appendix Figure A-3~A-6 for reproducibility on various potentiodynamic polarization curves and EIS curves). In the work of this thesis, the ohmic resistance was obtained from the EIS data at the higher frequency limit. The resistance was then used to correct the potentiodynamic data before analysis.

4.3.3.3 Electrochemical Impedance Spectroscopy (EIS)

EIS has been now established as a powerful tool in describing the electrochemical interface at steady state. The technique was first used by Randles and Somerton in 1952 [Macdonal, J. R., 1987]. The greatest strength of this tool stems from the fact that it is essentially a steady state and non-destructive method, which employs a very small external voltage or current perturbation to drive the electrode/environment interface not far from the steady state, and then detects interfacial relaxation covering a wide range of relaxation times over many orders of magnitude [Macdonald, D. D., 1990].

Ohm's law defines resistance in terms of the ratio between voltage and current (R=E/I). Electrochemical interfaces are not simply resistive. The electrochemical double layer adds a capacitive term to the transfer resistance. Other electrode processes such as adsorption and diffusion are also frequency (and time) dependent and influence the impedance responses. Therefore a more practical circuit parameter, referred to as impedance, is essential to describe the ability of an electrical circuit to resist the flow of electrical current.

The response of any linear system to a perturbation of arbitrary form may be described by a transfer function:

$$H(s) = \overline{E}(s) \Big/ \overline{I}(s) \tag{4.2}$$

where s is the Laplace frequency, and $\overline{E}(s)$ and $\overline{I}(s)$ are Laplace transformation of voltage and current signals in time domain, respectively [Creason, S. C. and Smith, D. E., 1972]. In the case of the steady state sinusoidal frequency domain, the transfer function becomes:

$$H(j\omega) = F\{\overline{E}(t)\} \Big/ F\{\overline{I}(t)\} = E(j\omega) \Big/ I(j\omega) = Z(j\omega) \tag{4.3}$$

where F signifies the Fourier transform, E(jω) and I(jω) are the frequency dependent sinusoidal voltage and current [Macdonal, D. D., 1990]. Since the impedance is a complex number, it can be written in the form:

$$Z(j\omega) = Z' - jZ'' \tag{4.4}$$

where $j = \sqrt{-1}$, Z' and Z" are the frequency dependent real part and the frequency dependent imaginary part in Cartesian coordinates. Also the magnitude and the phase of the impedance in the polar form are as follows:

$$|Z(j\omega)| = \sqrt{(Z')^2 + (Z'')^2} \ , \ \tan\phi = -Z'' \Big/ Z' \tag{4.5}$$

where ϕ is the phase angle. Alternatively the complex impedance may be expressed as:

$$Z(j\omega) = |Z|e^{j\phi} \tag{4.6}$$

There are two common methods to display the impedance data according to the mathematical forms by Eq.(4.5) and (4.6). One is named as the Nyquist plot or complex plane, presented as –Z" vs. Z' and the other is the Bode plot, presented as log|Z| and ϕ vs. logf, where f is frequency. Each of these two plots has specific adavantages. The Nyquist plot is more useful for mechanistic study since the number of relaxations and their mechanistic implication (charge transfer resistance, adsorption, diffusion process, etc) are often more apparent.

The electrochemical impedance at the electrode interface can be measured using various instruments and techniques, ranging from a simple oscilloscope display to a Fast Fourier Transform (FFT) analyzer. The usual instrument used is a frequency response analyzer. A generator provides a sinusoidal voltage or current at a given frequency and the response of an electrical circuit at that frequency is measured. The measurement is then repeated at another frequency.

Most impedance measurements are analyzed by fitting the impedance spectra to an equivalent circuit. Therefore the aim of the impedance measurement is often to find which equivalent circuit fits best and to determine the values of its elements. Unfortunately, there is no unique solution to the question of which equivalent circuit best fits the experimental data. Any number of electrical circuits that could yield the same impedance response could be conceived. Furthermore, the fit can be improved by adding more adjustable circuit elements to the model. Therefore, one should be cautioned that a good agreement between the experimental data and the impedance fitted for an equivalent circuit model does not necessarily mean that the model is correct. Some elements in those circuit models do not possess an appropriate physical meaning in terms of the electrochemical reactions at the electrode interface. Therefore, the concept employed in this thesis to reduce the model to small number of reasonable models as shown in Figure 4-11.

In Figure 4-11a, one is the simplest models of the electrochemical interface which is that of Randle's type with a parallel combination of a resistance R_2, and a capacitance C in

series with another resistance R_1 and can be described as $R_1(CR_2)$ according to the nomenclature of Boukamp [Boukamp, B. A., 1993].

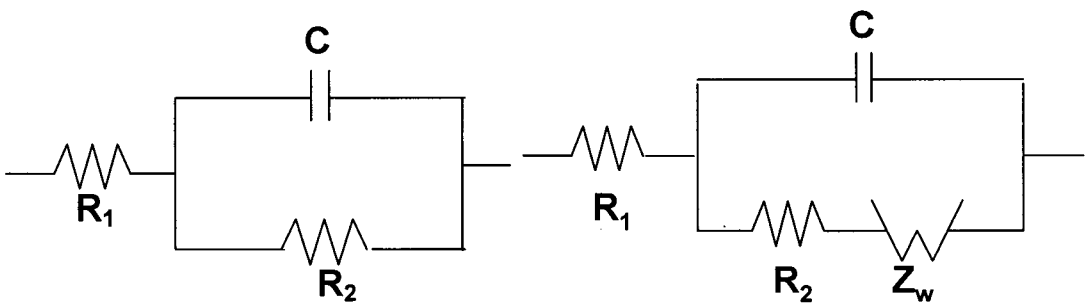

Figure 4-11 Equivalent circuits used for the evaluation of impedance spectra of the electrode in present study showing the resistance (R), capacitance (C) and Warburg impedance (Z_w)

An example of the response for a corroding electrode is rarely of simple Randle characteristics. Contributions from processes such as diffusion or adsorption add extra elements, resulting in further semicircles and irregularities in the Nyquist plot. In case, a charge transfer is influenced by diffusion to and from the electrode (e.g. vacancy transport across the passive film), the Warburg impedance (Z_w) can be seen in the impedance plot. The Warburg element is easily recognized by a line with an angle of $\leq 45^{\circ}$ in the lower frequency region. The equivalent circuit of the electrochemical cell is shown in Figure 4-11b and described as $R_1(C[R_2W])$ by the Boukamp code. The bracket shows that the enclosed elements are parallel.

For the impedance measurement, in this study, the amplitude of the ac-signal was low enough to ensure that the response of the electrochemical cell behaved linearly. Thus a small amplitude (±5mV) sinusoidal potential perturbation superimposed over the dc polarization potential is applied such that an impedance measurement can be obtained without (or negligibly) affecting the equilibrium condition of the electrode surface. To achieve a steady state, the electrode was held at the assigned potential for 10 minutes.

In a real electrochemical cell, the impedance spectrum may be distorted due to nonidealities such as surface roughness. Thus constant phase element (CPE) is formally employed instead of a perfect (ideal) capacitor [Macdonald, J. R., 1987]. The impedance of such a non-ideal element, CPE, is represented by:

$$Z_{CPE} = {}^{-j}\!/_{(\omega Q)^n} \tag{4.7}$$

For an ideal capacitor, Q is equal to C and n=1. Usually n has a value between 0.5 and 0.99.

By replacing the ideal capacitance to CPE for fitting and simulation purpose, a good fitting result was achieved as shown in Figure 4-12 using non-linear least square fitting (NLLS) method. In this Figure, the Nyquist plots for both measured data and the calculated curve illustrate the validity of the model.

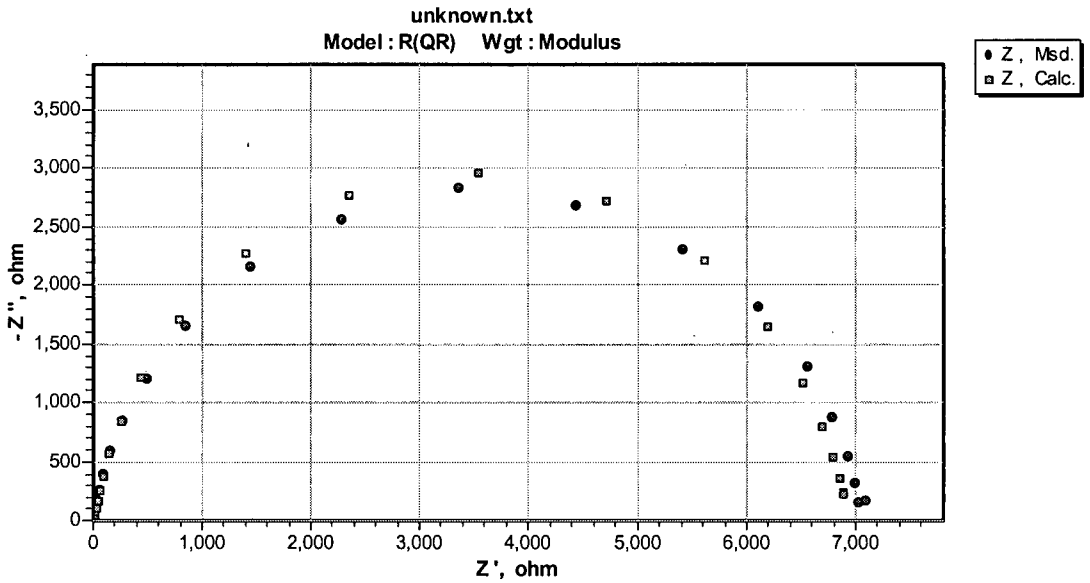

Figure 4-12 Experimental impedance data obtained for nanocrystalline Co-2.1P in 0.1 M H_2SO_4 solution after 90 minutes immersion at E_{oc} and calculated curve using R(QR) circuit

4.4 Surface analysis

The surface morphology of the specimens was characterized by scanning electron microscopy (SEM) using a Hitachi S-2300 scanning electron microscope. Chemical composition of the Co surface was determined using a Kevex energy dispersive X-ray spectroscopy (EDS) system attached to the SEM.

The chemical composition, oxidation state and thickness of the passive film also examined by X-ray Photoelectron Spectroscopy (XPS) experiments using a Leybold model MAX 200 with a MgK_{α} ($h\nu$=1253.6 eV) anode X-ray source operated normally at 15 kV and an emission current intensity of 20 mA. Owing to disturbing Auger signals and high differences in the chemical shift of Co(II) and Co(III), a less intense Co $2p_{1/2}$ signal was used for evaluation [Foelske and Strehblow, 2000]. The binding energies of the XPS signals of all species have been corrected by assuming the C 1s signals of all at 284.4 eV.

5 Results and Discussion

5.1 Corrosion in Acidic Solution

5.1.1 Pure Co

In this section, the effects of bulk S impurity and grain size on the corrosion properties as well as anodic dissolution mechanism of Co are discussed.

5.1.1.1 Polarization Behavior

Figure 5-1 presents typical potentiodynamic polarization curves for all Co samples in deaerated 0.1 M H_2SO_4 solution. Experimental parameters including kinetic data are summarized in Table 5-1.

All samples exhibited active dissolution without any distinctive transition to passivation up to -0.1 V_{SCE}. The non-passivating behavior of pure Co in acidic solution is expected based on the thermodynamics as seen in the E-pH diagram for the Co-water system (see Figure 2-1). It was also seen in previous studies [Heusler, K. E. 1962; Motten, M.M., 1969; Tomlinson, W. J., 1988; Krolikowski, A., 1988; Helfand, M. A., 1992; Badawy, W. A., 2000]. However, a study showed the passivation of polycrystalline Co with a high passivation current density, i.e., > 10 mA/cm^2 and passivation potential ranges were not well-defined in deaerated Na_2SO_4 (concentration was not given) at pH=0, 0.3 and 1.5 [Tikkanen et al, 1964] as well as in aerated 0.1 M H_2SO_4 [Tadeusz Blaszczyk et al, 2000]. This passivation may be attributed to different material properties in term of impurities, textures, and volume fraction of fcc/hcp phase and different ionic activities in the solution and possibly mass transfer effects at high anodic potential ranges.

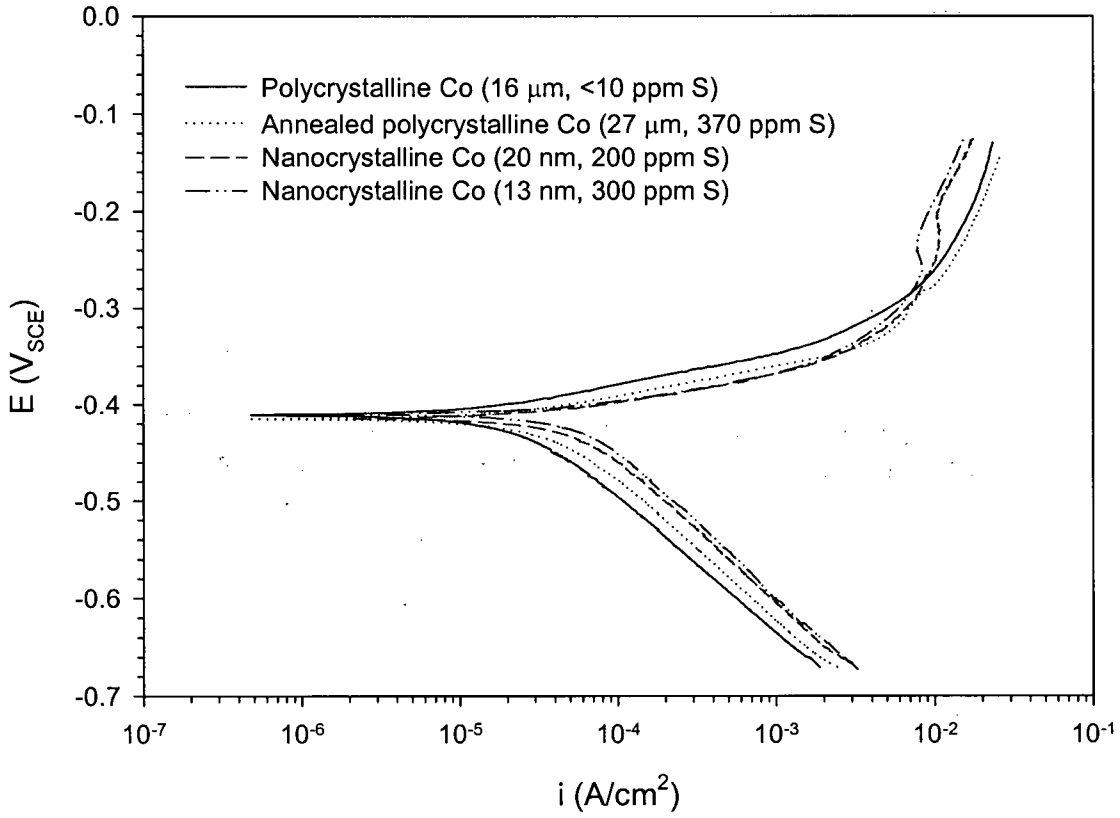

Figure 5-1 Potentiodynamic polarization curves of pure Co samples in deaerated 0.1 M H_2SO_4 (pH=1)(iR-corrected assumed ohmic resistance equals 8 Ωcm^2, scan rate=0.5mV/s).

In the low anodic potential range including corrosion potential, an annealed polycrystalline Co containing 370 ppm of S showed a slightly higher anodic dissolution rate than that of polycrystalline Co containing <10 ppm of S. An increased current density due to surface element S on Ni and Ni-Fe single crystals with well-controlled coverage of radioactive S has been reported on many occasions [Oudar, J. 1979; Marcus, P. A., 1984]. In the reference by Oudar, J. [1979], it was clearly demonstrated that the adsorbed S on the metal surface accelerated the anodic dissolution of the metals comparing to S free case and the adsorbed S on the metal surface was highly stable. They reasoned that the acceleration effect was due to a weakening of the metal-metal bonds induced by adsorbed S, which leads to a lowering of the activation energy barrier for the passage of metal atom from the surface

to the solution. In the current study, if we put forward a similar interpretation regardless of homogeneity of S distribution on the metal surface, it can be speculated that the catalytic effect of S on the anodic dissolution of metal Co is due to a weakening of Co-Co metal bonds induced by the S impurity in the Co matrix. Indeed, the bond strength of Co-Co (168 kJ/mole) is smaller than that of S-S (428 kJ/mole) and Co-S (331 kJ/mole) [CRC Handbook, 2004-05]. The existence of a dipole $Co^{\delta+}$-$S^{\delta-}$ associated with the presence of S and cobalt sulfide can also promote the anodic dissolution.

Table 5-1 Corrosion potential (E_{corr}), anodic Tafel slope (b_a), cathodic Tafel slope (b_c) and corrosion current density (i_{corr}) taken from polarization data.

Sample	E_{corr} (V_{SCE})	b_a* (V/decade)	b_c* (V/decade)	i_{corr}^{+} ($\mu A/cm^2$)	$i_{0,H+/H2}^{\#}$ ($\mu A/cm^2$)
Polycrystalline Co (<10 ppm S)	-0.411	0.033	0.142	28	5.8
Annealed polycrystalline Co (370 ppm S)	-0.416	0.031	0.144	33	6.0
Nanocrystalline Co (200 ppm of S)	-0.415	0.029	0.146	48	9.0
Nanocrystalline Co (300 ppm of S)	-0.409	0.030	0.148	52	10.0

* iR-corrected value assumed ohmic resistance equals 8 Ωcm^2.

+ Estimated by extrapolation of the Tafel slopes (Stern method).

Estimated by extrapolation of the cathodic Tafel slope to the equilibrium potential for hydrogen evolution reaction at pH=1 ($E_{H^+/H_2} = -59mV_{SHE}$).

In the case of both nanocrystalline Co samples, the anodic dissolution rates were higher than that of annealed polycrystalline Co. An increased dissolution rate in the anodic potential range as well as non-passivation was also observed on the nanocrystalline Co (grain

size, 13 nm) containing 350 ppm of S in deaerated 0.25 M Na_2SO_4 solution at pH of 6.5 compared with polycrystalline Co (<10 ppm of S) (see Figure 2-19a).

Since the amount of S impurity in annealed polycrystalline Co (370 ppm of S) and nanocrystalline Co samples (200 or 300 ppm of S) in the current study were almost at the same level, it is considered that these further increases are mainly due to the extremely fine grain size. Through the theoretical calculation assuming grain boundary thickness of 1 nm in ref. [Palumbo, G.. et al., 1990], the surface area fraction of intercrystalline components (e.g., grain boundaries and triple junctions) in a crystalline material increase from a value of 0.008 % at a grain size of 27 μm to about 10 and 15 % at grain sizes of 20 and 13 nm, respectively (see Figure 2-12). Therefore, it is likely that a significant increase of intercrystalline surface area fraction resulted in the increased dissolution kinetics acting as active dissolution sites without a passive layer.

An explanation for the increased dissolution kinetics of nanocrystalline Co can be approached in terms of the reduced activation energy for metal dissolution due to much higher surface area fraction of intercrystalline defects in the ultra-fine grain sized crystalline materials. Because significant intercrystalline surface area in nanocrystalline materials represents a region of stored excess free energy with respect to a conventional polycrystalline material, there is a significant driving force for anodic dissolution considering that the intercrystalline defects are preferential dissolution sites.

Recently, Tromans, D. and Meech, J. A., [2001] made an attempt to estimate the dissolution kinetics of mechanically activated minerals in terms of a decreased acitivation energy due to a high dislocation density. By applying a similar approach to our system, a theoretical estimation of the dissolution rate ratio between poly- and nanocrystalline Co for comparison can be deduced. Based on Arrhenius rate law behavior, the resulting dissolution rate, *k*, is given by Eq. (5-1):

$$k = \vec{k} - \overleftarrow{k} = A[\exp(\frac{-\Delta\vec{G}}{RT}) - \exp(\frac{-\Delta\overleftarrow{G}}{RT})] \qquad (5\text{-}1)$$

where $\vec{k}$ and $\overleftarrow{k}$ are rates for the anodic dissolution and the cathodic reduction of the metal, respectively, A is a rate constant, and R is the gas constant. The activation energy for dissolution and reduction is denoted $\Delta\vec{G}$ and $\Delta\overleftarrow{G}$, respectively. In the case of anodic dissolution, it can be considered that $\Delta\overleftarrow{G}$ is larger than $\Delta\vec{G}$ ($\Delta\vec{G} < \Delta\overleftarrow{G}$), the second exponential term may be ignored with respect to the first term, so that Eq.(5-1) becomes:

$$k \approx \vec{k} = A\exp(\frac{-\Delta\vec{G}}{RT}) \tag{5-2}$$

The free energy profiles of conventional polycrystalline and nanocrystalline materials under conditions where the rate controlling process is activation or charge transfer control across the aqueous double layer are shown schematically in Figure 5-2. In the case of nanocrystalline materials, the molar activation energy of metal dissolution is decreased from $\Delta\vec{G}_{poly}$ to $\Delta\vec{G}_{nano}$ with excess free energy (G^{xs}) due to a significant increase of intercrystalline defects (e.g., grain boundaries and triple junctions), whereas $\Delta\overleftarrow{G}$ remain unchanged. From Eq.(5-2) the dissolution rates for polycrystalline and nanocrystalline materials, k_{poly} and k_{nano}, respectively, become:

$$k_{poly} \approx A\exp(\frac{-\Delta\vec{G}_{poly}}{RT}) \tag{5-3}$$

$$k_{nano} \approx A\exp(\frac{-\Delta\vec{G}_{nano}}{RT}) \approx A\exp(\frac{G^{xs} - \Delta\vec{G}_{poly}}{RT}) \tag{5-4}$$

The resulting dissolution rate ratio $\frac{k_{nano}}{k_{poly}}$ is obtained from Eq.(5-3) and (5-4):

$$\frac{k_{nano}}{k_{poly}} \approx \exp(\frac{G^{xs}}{RT}) \tag{5-5}$$

The excess free energy (G^{xs}) stored in the intercrystalline defects can be separated into the excess enthalpy (H^{xs}) and the excess entropy (S^{xs}) contributions associated with

significant amounts of intercrystalline defects:

$$G^{xs} = H^{xs} - TS^{xs} \qquad (5\text{-}6)$$

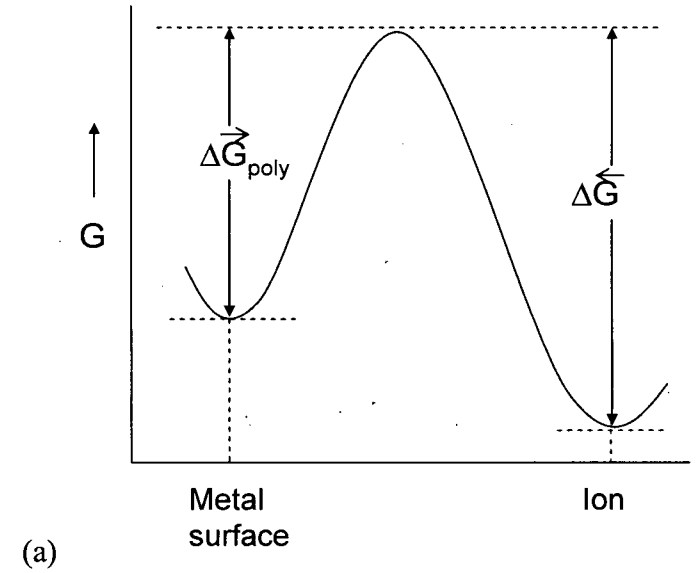

(a)

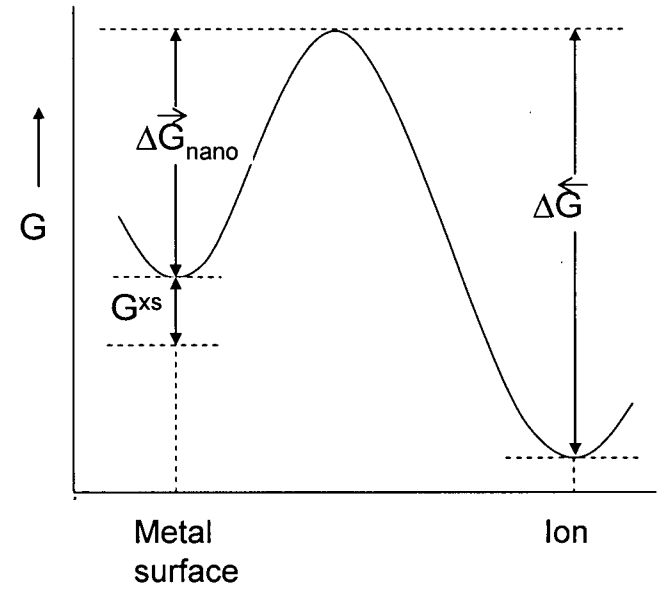

(b)

Figure 5-2 Schematic energy profiles showing changes in activation energy of dissolution: (a) conventional polycrystalline material with activation energy of dissolution $\Delta\vec{G}_{poly}$ *and (b) nanocrystalline material with decreased activation energy of* $\Delta\vec{G}_{nano}$.

From the theoretical calculation [Fecht, H. J., 1990] and experimental measurements using DSC and DTA [Tschope, A. and Birringer, 1993], the excess entropy contribution to the excess free energy was rather small. For example, the excess entropy contribution (0.109 J/m^2) of nanocrystalline Pt (mean grain sizes between 12 and 18 nm) was only 4% of the excess enthalpy of 2.6 J/m^2 at 300 K, so Eq.(5-6) may be expressed to Eq.(5-7) and Eq.(5-5) substitutes to Eq.(5-8):

$$G^{xs} \approx H^{xs} \tag{5-7}$$

$$\frac{k_{nano}}{k_{poly}} \approx \exp(\frac{H^{xs}}{RT}) \tag{5-8}$$

Therefore, the dissolution rate ratio between poly- and nanocrystalline materials can be calculated if the excess enthalpy is known.

Recently, G.. Hibbard et al. [2001] investigated the thermal stability of electrodeposited nanocrystalline Co (grain size of 20 nm) using DSC (differential scanning calorimeter) and they found that the excess interfacial enthalpy of its material due to the increased intercrystalline volume fraction was estimated to be 1.1 J/m^2.

Suppose that the excess interfacial enthalpy of nanocrystalline materials is concentrated in the grain boundaries and the contribution of triple junction to the total intercrystalline volume fraction is sufficiently small when the grain size is 20 nm (see Figure 2-12), the total excess interfacial enthalpy may be written as:

$$\Delta H_{total} = A_{gb}\gamma_{gb} = H^{xs} \tag{5-9}$$

where A_{gb} is the total grain boundary area with $A_{gb} = 2gV_m/d$, where g is the dimensionless geometrical factor depending on grain shape, assigned as 1.67 by A. Tschope et al. [1992], V_m is the molar volume of Co (6.7×10^{-6} m^3/mol), d is the grain size (20 nm), and γ_{gb} is the specific grain boundary free energy (J/m^2) and the resultant excess interfacial enthalpy can be estimated about 1.231 kJ/mole.

By substitution of the estimated value of total excess interfacial enthalpy to Eq.(5-8), the relative dissolution rate ratio is calculated as 1.64 at 298 K. If the relative dissolution rate ratio can be represented directly in terms of the anodic current density ratio between annealed polycrystalline Co and nanocrystalline Co, the anodic dissolution rate (anodic current density) of nanocrystalline Co (grain size of 20 nm) may have to be 1.64 times higher than that of annealed polycrystalline Co (grain size of 27 μm).

By direct calculation of the ratios using the measured anodic current densities in low anodic overpotential region taken from the iR corrected anodic polarization curves of those samples, it was found that the value of the average ratio (1.67) was very close to the estimated value (1.64) as shown in Table 5-2.

Table 5-2 Measured anodic current density ratios between nanocrystalline Co (grain size of 20 nm) and annealed polycrystalline Co (grain size of 27 μm) taken from Figure 5-1.

Potential (V_{SCE})	-0.40	-0.38	-0.36
Anodic Current Density Ratio	1.48	1.92	1.62
($i_{\text{nano Co (20nm)}} / i_{\text{annealed poly Co (27 μm)}}$)	(Average 1.67)		

It can be concluded that the enhanced anodic dissolution rate of nanocrystalline Co compared to that of annealed polycrystalline Co has been clearly attributed to significant increase of intercrystalline defects by nanoprocessing resulted in the reduced activation energy barrier of dissolution due to excess free energy stored in intercrystalline defects.

For all Co samples, the anodic Tafel slopes of 31 ± 2 mV were observed as shown in Table 5-1. Similar value of 29 ± 2 mV for pure Co was previously found in perchlorate solution at pH of 1.3 (see Figure 2-5) and in sulphate solution [Iofa Z. A. and Wei Pao-ming, 1962]. The anodic Tafel slopes observed in the current study suggests that the anodic

dissolution of poly- and nanocrystalline Co at pH of 1 proceeds more favorably via the catalytic mechanism rather than the non-catalytic consecutive mechanism on steady state polarization as described in section 2.1.3.2. To clarify either catalytic or non-catalytic mechanism in acid solution, the determination of the reaction order with respect to the hydroxyl ion is needed and will be described in section 5.1.1.2.

As the anodic potential was increased, the differences in the anodic current densities became smaller and eventually the dissolution rates of both nanocrystalline Co samples have been smaller than those of both polycrystalline counterparts above approximately -0.27 V_{SCE}. In order to investigate this difference in more detail, the potentiostatic polarization at -0.1 V_{SCE} was performed in the same solution. The resulting current densities as a function of time are shown in Figure 5-3 with showing the effect of stirring-off.

As shown in this Figure, the steady state current density of nanocrystalline Co was 1.48 times smaller than that of polycrystalline Co and this was consistent with the potentiodynamic polarization curves (Figure 5-1). For both samples, switching the stirrer off indicated "Quiescent" on Figure 5-3 caused a decrease in the anodic current density and switching the stirrer on again returned to the steady state current density. Solution velocity clearly affected the dissolution rate. Therefore, at this potential, it is certain that the anodic reaction of both Co samples is under mixed control of anodic mass transport and charge transfer. While the displacement of current density by stirring-off for polycrystalline Co was ~3.7 mA/cm^2, the value of nanocrystalline Co was much smaller (~0.8 mA/cm^2). The different degree of displacement may be due to the different degree of an inhibition effect to the anodic dissolution rate by corrosion products. Therefore, it would be expected that the corrosion product formed on the surface of nanocrystalline Co can provide better corrosion protection compared to that of polycrystalline Co.

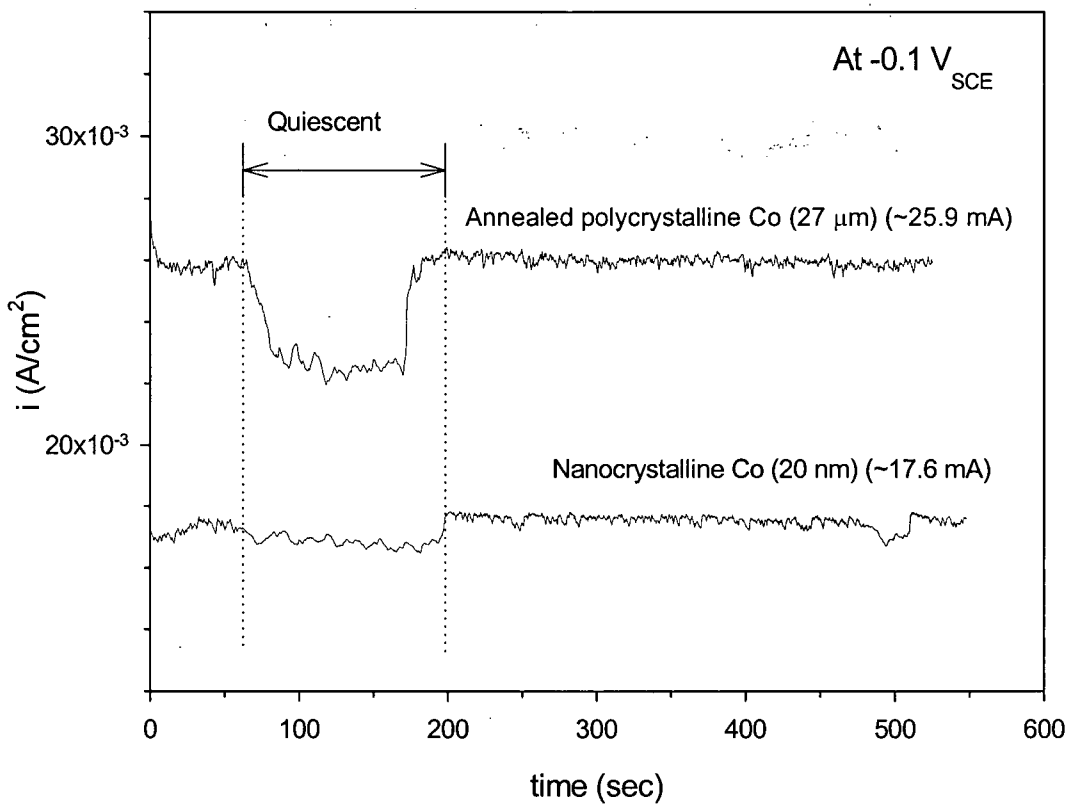

Figure 5-3 Current densities of annealed poly- and nanocrystalline Co samples measured at a potentiostatic polarization of -0.1 V_{SCE} with showing the effect of stirring-off in deaerated 0.1 M H_2SO_4 (pH=1).

In the cathodic overpotential region, nanocrystalline Co usually demonstrated higher cathodic reaction rate having a similar cathodic Tafel slope as shown in Figure 5-1 and Table 5-1. Increased H_2 evolution reaction of the nanocrystalline Ni in 0.1 N NaOH was previously reported by Doyle *et al.* [Doyle, D. M., 1995]. They found that the exchange current density of nanocrystalline Ni with grain size of 20 nm was about 6 times higher than that of the annealed Ni (~50 μm of grain size).

In fact, nanocrystalline Co showed a slightly higher $i^{\circ}_{H^+/H_2}$ in comparison with a conventional polycrystalline Co and the exchange current density for nanocrystalline Co was about 1.8 times higher than that of the polycrystalline counterpart similar to the value of

anodic dissolution case (Ave. 1.67). Even though the increase of the exchange current density in our study was less remarkable than 6 times due to the differences in the material used (Ni vs. Co) and different ionic species and activity in alkaline solution, it is possible to put forward a similar interpretation in the current study, namely, the reduced activation energy for hydrogen evolution on nanocrystalline Co.

5.1.1.2 Effect of Solution pH

Figure 5-4 presents the potentiodynamic polarization curves of annealed poly- and nanocrystalline Co in deaerated 0.5 M Na_2SO_4 at pH of 3 adjusted by addition of concentrated H_2SO_4 solution. Experimental parameters including kinetic data are also summarized in Table 5-3.

Both samples demonstrate very similar polarization behavior without an evident passivation regime up to -0.05 V_{SCE} and the cathodic and anodic reaction rates of nanocrystalline Co were slightly higher than that of annealed polycrystalline Co. The increased electrochemical reaction rate can be also considered to be the result of the increased active sites of nanocrystalline Co due to much higher surface fraction of intercrystalline defects. The corrosion potential, E_{corr}, shifts to a more active value and the dissolution rate at a constant potential increases with increasing pH of the solution from 1 to 3 (see Figure 5-1).

By selecting respective (partly extrapolated) log i values corresponding to the same potential from the Tafel lines in Figure 5-1 and 5-4, a straight line with a slope dlogi/dpH = 1.85 is obtained. According to the catalytic charge transfer mechanism for anodic dissolution of pure Co, the electrochemical reaction order $y(OH^-)^+ = 2.0 \pm 0.3$ with respect to hydroxyl ions was usually observed [Heusler, K. E., 1962; Iofa Z. A., 1962]. The calculated reaction order of 1.85 in the current study is closer to the value of 2 rather than 1, indicating a catalytic mechanism (see Table 2-2).

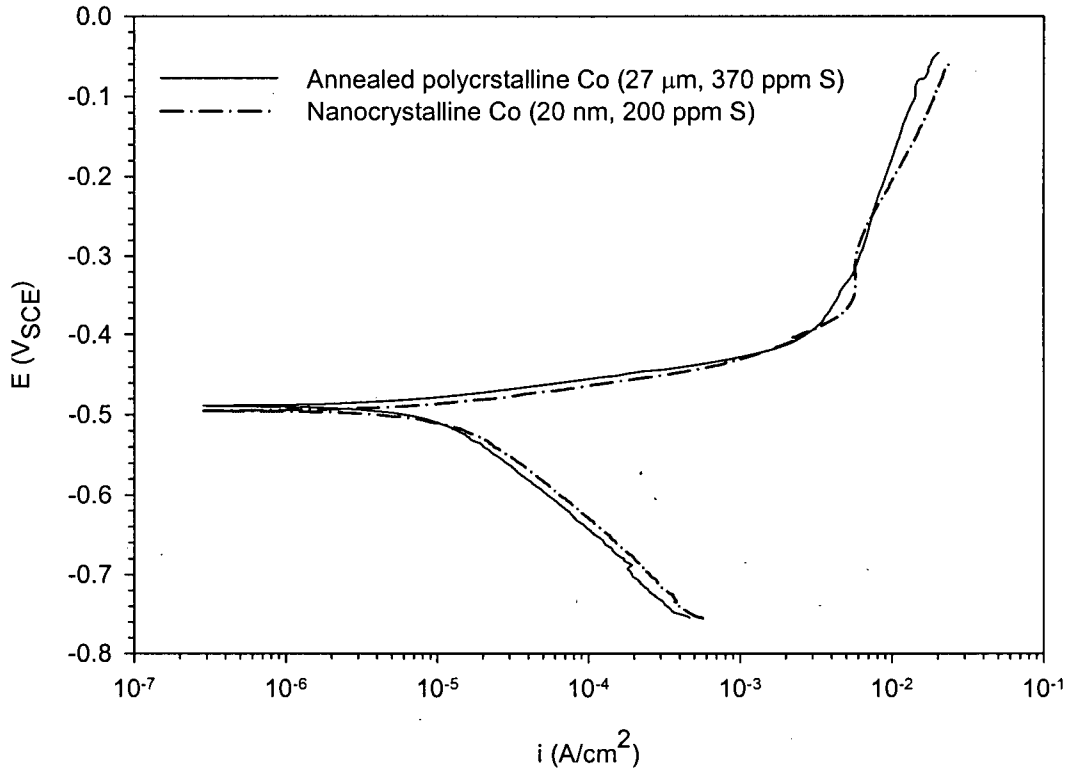

Figure 5-4 Potentiodynamic polarization curves of annealed poly- and nanocrystalline Co in deaerated 0.5 M Na_2SO_4 (pH=3) (iR-corrected assumed ohmic resistance equals 10 Ωcm^2, scan rate=0.5mV/s).

Table 5-3 Kinetic parameters taken from polarization data at pH of 3.

Sample	E_{corr} (V_{SCE})	b_a (V/decade)	b_c (V/decade)	i_{corr}^{*} ($\mu A/cm^2$)	$i_{0,H+/H2}^{\#}$ ($\mu A/cm^2$)
Annealed polycrystalline Co (27 μm)	-0.490	0.028	0.156	15	0.12
Nanocrystalline Co (20 nm)	-0.495	0.030	0.159	18	0.15

[+] Estimated by extrapolation of the Tafel slopes (Stern method).

[#] Estimated by extrapolation of the cathodic Tafel slope to the equilibrium potential for hydrogen evolution reaction at pH=3 ($E_{H^+/H_2} = -177mV_{SHE}$).

From the pH dependence of anodic dissolution rate, i.e., reaction order $y(OH^-)^+$ = 1.85 and the anodic Tafel slopes of 31 ± 2 and 29 ±1 mV at pH of 1 and 3, respectively, it is possible that the anodic dissolution rates for poly- and nanocrystalline Co in the current study are determined by the catalytic mechanism.

Assuming that the anodic dissolution behavior of Co is analogous to that of Fe in terms of the surface active sites, i.e., kinks on the surface lattice (see Figure 2-4), the dissolution process can be described as follows:

From the initial hydrolysis step at equilibrium, i.e., a initial water dissociation, the intermediate products, $(CoOH)_{ads}$ with simple Langmuir adsorption behavior can be formed as follows:

$$Co + H_2O \Leftrightarrow (CoOH)_{ads} + H^+ + e^- \qquad (5\text{-}10)$$

According to the catalyzed mechanism, $(CoOH)_{ads}$ enters in the catalytic sequence of dissolution starting from an active site, i.e., kink sites, and Co dissolve as $CoOH^+$:

$$Co_k + (CoOH)_{ads} \Leftrightarrow Co(Co_kOH)_{ads} \qquad (5\text{-}11)$$

$$Co(Co_kOH)_{ads} + (OH)^-_{ads} \rightarrow CoOH^+ + (Co_kOH)_{ads} + 2e^- \qquad (5\text{-}12)$$

where, Co_k denotes Co atoms at kink site. Assuming step (5-10) in fast equilibrium, i.e., the concentration of $(CoOH)_{ads}$ proportional to $[OH]^-$ and time independent, step (5-12) is rate-determining.

Finally, $CoOH^+$ is assumed to react with solution proton, and then transfers to cobaltous ion:

$$CoOH^+ + H^+ \rightarrow Co^{2+}_{aq} + H_2O \qquad (5\text{-}13)$$

The subscripts "ads" and "aq" indicate the species adsorbed at the Co surface and dissolved in the aqueous solution, respectively.

5.1.1.3 Electrochemical Impedance Spectroscopy (EIS) measurements

Electrochemical impedance spectroscopy measurements were performed in order to gain a better understanding of the corrosion behaviour in terms of anodic dissolution rate and dissolution mechanism of annealed polycrystalline Co and nanocrystalline Co.

In Figure 5-5, diagram (a) was measured at -0.6 V_{SCE} in the cathodic potential range and shows only one capacitive loop for both Co samples disregarding unstable impedance responses in low frequency ranges (<1 Hz). Very active hydrogen evolution was observed on both Co samples as gas bubbles on the surface were clearly visible. The hydrogen evolution rate of nanocrystalline Co was higher than that of annealed polycrystalline Co by a factor of 2.0. This was found by measuring the diameter of the capacitive loop. Therefore, it is speculated that the hydrogen evolution reaction on both Co samples have a common mechanism at this potential and the intercrystalline defects also play a significant role in the hydrogen evolution reaction.

After 30 minutes immersion at E_{oc}, the impedance spectra demonstrate two time constants, namely a capacitive loop in high and medium frequency ranges and a inductive loop in low frequency range (mHz ranges) as shown in Figure 5-5b. The capacitive loop is due to the double layer capacity in parallel with the charge transfer resistance and the low frequency relaxation is due to the slow reaction by adsorbed reaction intermediate $(Co_kOH)_{ads}$ during the Co metal dissolution process according to Eq.(5-12) considering very small degree of surface coverage of adsorbed hydrogen at open circuit potential according to the hydrogen permeation experiments on Fe [Dafft, E. G. et al., 1979]. Besides the observed electrochemical parameters (see Table 5-1), the appearance of an inductive loop also supports the fact that the anodic dissolution of Co can proceed via catalytic mechanism. Schweickert, H., et al. proved theoretically [1978] as well as experimentally [1980; 1981] that the observed inductive loops in the iron in deaerated acid solution could not be explained by the non-catalytic consecutive mechanism.

By definition of the polarization resistance (R_p), the value of the real part impedance when $f \rightarrow 0$, R_p could be estimated by the extrapolation from the low frequency inductive loop (10 mHz) up to the four decades below (0.001 mHz) using Kramers-Kronig relation and

resultant values of R_p for annealed polycrystalline Co and nanocrystalline Co were found to be about 280 and 208 Ωcm^2, respectively. The ratio of $1/R_p$ for those two values is 1.35, which is very close to the value of corrosion current density ratio between annealed polycrystalline Co and nanocrystalline Co (1.45) (see Table 5-2). Thus, on the basis of the catalytic mechanism, it can be concluded that the corrosion rate of both Co samples is closely related to the amount of intercrystalline defects on the metal surface.

Following potentiostatic polarization at -0.3 V_{SCE} for 10 minutes, the impedance spectroscopy measurements were conducted. The resultant impedance spectra are presented in Figure 5-5c. Both Co samples exhibited three loops; a capacitive loop at high frequency, an inductive loop at medium frequency (~1 Hz) and a second capacitive loop at low frequency. This medium frequency inductive loop is related to the adsorbed reaction intermediate and the comparison of the diagrams at E_{oc} revealed that the lower frequency inductive loop transformed into a capacitive loop. Although the origin of this second capacitive loop is not clear at present, it may be related to the corrosion product such as Co hydroxide and/or oxide. This lower frequency capacitive loop was usually observed in the anodic to passive transition ranges of Fe in acid solution and attributed to the formation of Fe oxide species $Fe(O)_{ads}$ [Keddam, M., et al, 1981; Schweickert, H., et al, 1981]. The charge transfer resistance of nanocrystalline Co by measurement of the diameter of the first capacitive loop was slightly smaller than that of annealed polycrystalline Co.

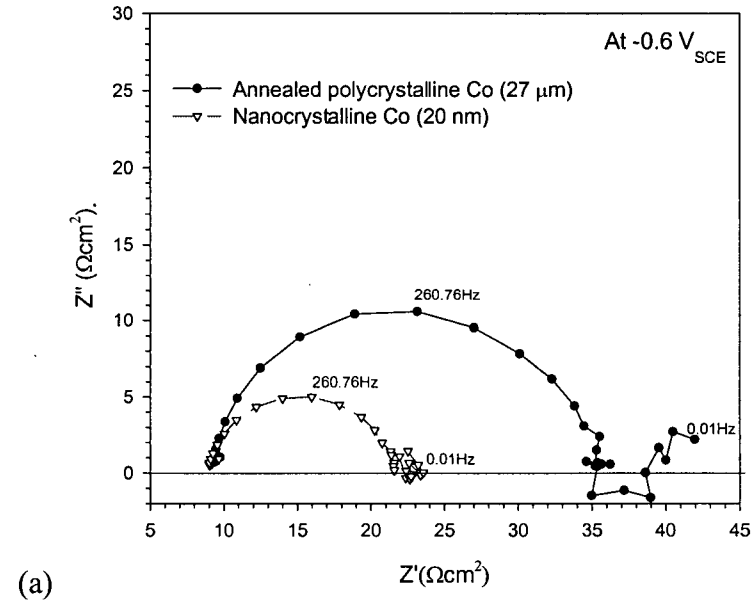

(a)

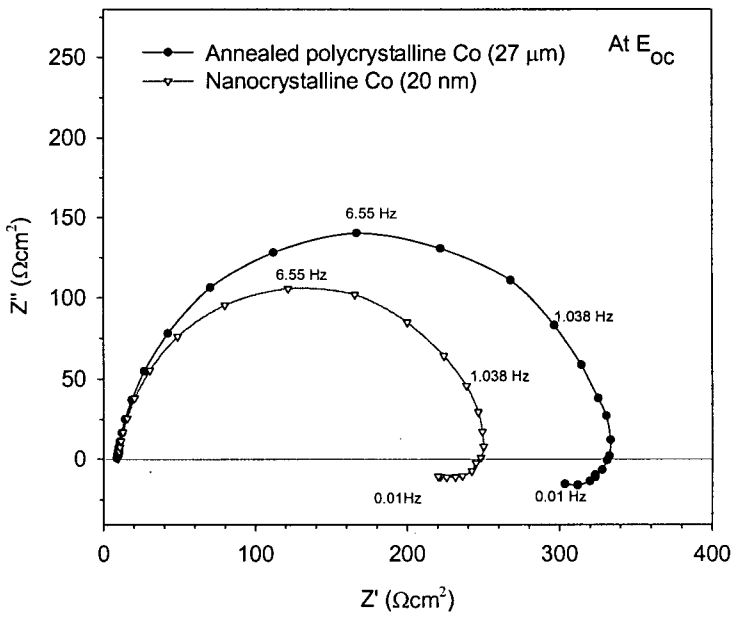

(b)

Figure 5-5 Nyquist plots of electrochemical impedance spectra recorded on poly- and nanocrystalline Co samples at (a) -0.6, (b) E_{oc}, and (c) -0.3 V_{SCE} in deaerated 0.1 M H_2SO_4 (pH=1).

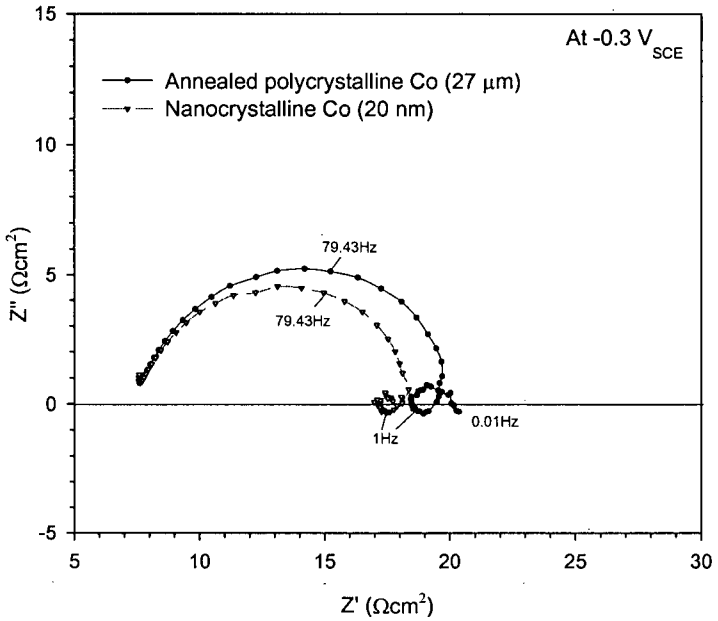

(c)

Figure 5-5 (continued)

5.1.1.4 Corrosion Morphologies

Figure 5-6 shows SEM micrographs of the typical corroded surfaces of Co samples after potentiostatic polarization treatment at -0.3 and -0.1 V_{SCE} for 10 minutes in deaerated 0.1 M H_2SO_4.

Polycrystalline Co containing <10 ppm of S corroded rather uniformly having a weak grain boundary attack at low anodic overpotential as shown in Figure 5-6a. An increase in the anodic overpotential up to -0.1 V_{SCE} lead to more rough morphologies (Figure 5-6b). The corroded surface exhibited clearly different crystallographic orientations and the macroscopic steps and kinks appeared on the crystal faces.

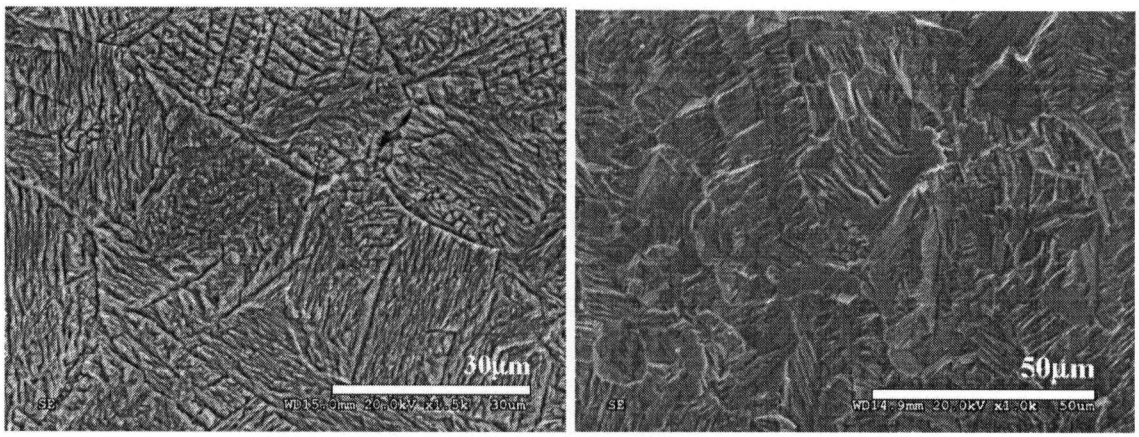

(a) -0.3 V_{SCE} (b) -0.1 V_{SCE}

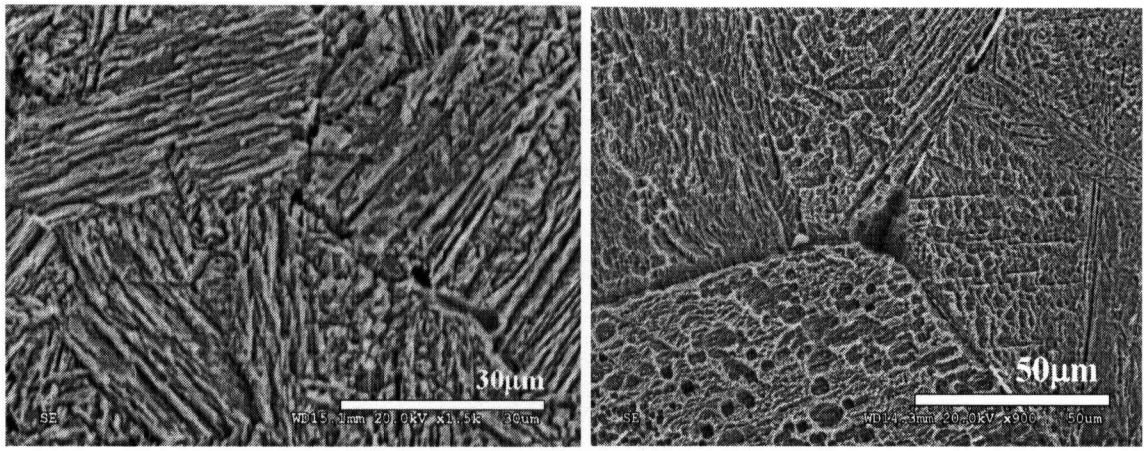

(c) -0.3 V_{SCE} (d) -0.1 V_{SCE}

Figure 5-6 SEM images showing typical corrosion morphologies of polycrystalline Co (16 μm, <10 ppm of S) after potentiostatic polarization at (a) -0.3 V_{SCE}, (b) -0.1 V_{SCE} ; annealed polycrystalline Co (27 μm,. 370 ppm S) after potentiostatic polarization at (c) -0.3 V_{SCE}, (d) -0.1 V_{SCE} ; nanocrystalline Co (20 nm, 200 ppm S) after potentiostatic polarization at (e) -0.3 V_{SCE}, (f) -0.1 V_{SCE} in deaerated 0.1 M H_2SO_4 (pH=1).

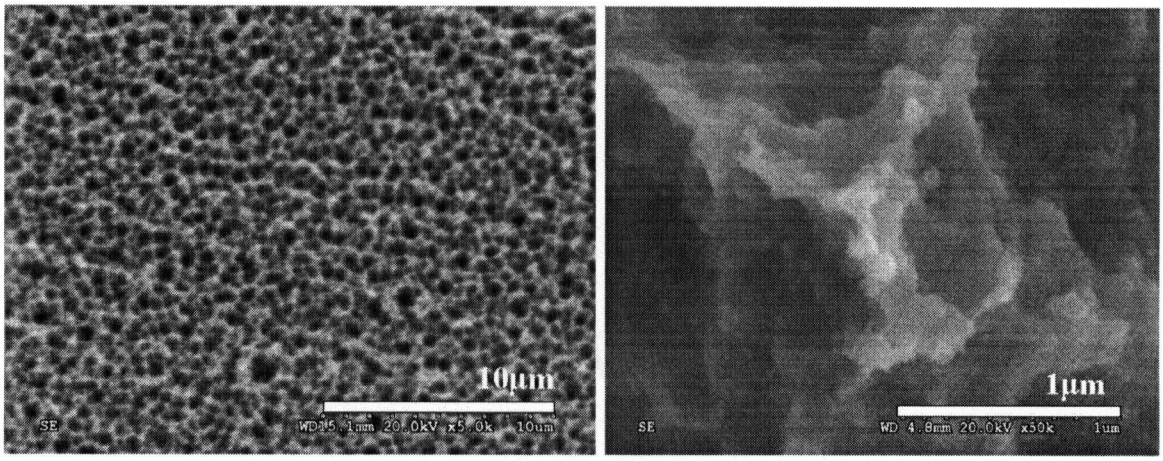

(e) -0.3 V_{SCE} (f) -0.1 V_{SCE}

Figure 5-6 (continued)

In the case of annealed polycrystalline Co containing 370 ppm of S after potentiostatic polarization at -0.3 V_{SCE}, the corroded surface was similar to that of polycrystalline Co (Figure 5-6c), while the surface experienced significant preferential corrosion attack along triple junctions and grain boundaries leaving the cobalt sulfide resides (white pieces within the grain boundaries) at -0.1 V_{SCE} (Figure 5-6d). During annealing process (at 950 °C for 2 hrs), the local sulfur concentration along grain boundaries can increase and lead to precipitation of different multiple phases (see Appendix A-3) which would act as anodic sites with respect to the grain interior. By careful examination, one can find very regular shaped steps and kinks along the edges of each plateau.

On the other hand, nanocrystalline Co exhibited uniform pitting corrosion. Although the surface showed many small sized pits (much less than 1 μm) as shown in Figure 5-6e, the detrimental preferential grain boundary attack was largely eliminated by the nanoprocessing. At a magnification of 50 times higher in Figure 5-6f, nanocrystalline Co was also found to display a series of steps and kinks which were stepped downward gradually to the bottom of the pit implying that the anodic dissolution process took place by a catalytic mechanism via active sites such as kinks and step edges.

All the poly- and nanocrystalline Co samples investigated showed macroscopic steps and kinks on the corroded surface at relatively high anodic overpotential range. This finding may support that the anodic Co dissolution process in the current study takes place by catalytic charge transfer mechanism via active sites, i.e. kinks. For the detailed understanding of crystallographic structures such as steps and kinks or other surface defects, further examinations to atomistic morphologies should be followed. A detailed mechanism for structural changes on the Co surface is currently lacking.

5.1.2 Co-P Alloy

5.1.2.1 Open Circuit Potential Behavior

The open circuit potential (E_{oc})-time behavior of nanocrystalline Co and Co-P samples were recorded and presented in Figure 5-7. For nanocrystalline Co, E_{oc} decreased continuously during the first 5 minutes, which could be attributed to the anodic dissolution of the air-formed native oxide film [Pourbaix, M., 1966], and reached the values of -0.422 V_{SCE} after 30 minutes. In the case of nanocrystalline Co-1.1P and nanocrystalline Co-2.1P, E_{oc} increased sharply during the first 200 seconds and reached a much more noble value than that of nanocrystalline Co in the amount of 57 and 62 mV, respectively. The significantly nobler E_{oc} value for nanocrystalline Co-P alloys illustrates the positive effect of P alloying on the corrosion resistance of Co.

5.1.2.2 Potentiodynamic Polarization Behavior

Figure 5-8 shows the potentiodynamic polarization curves for nanocrystalline Co-1.1P and nanocrystalline Co-2.1P alloys in deaerated 0.1 M H_2SO_4 (pH=1) at room temperature. For comparison, the polarization curve for nanocrystalline Co is also shown in this figure.

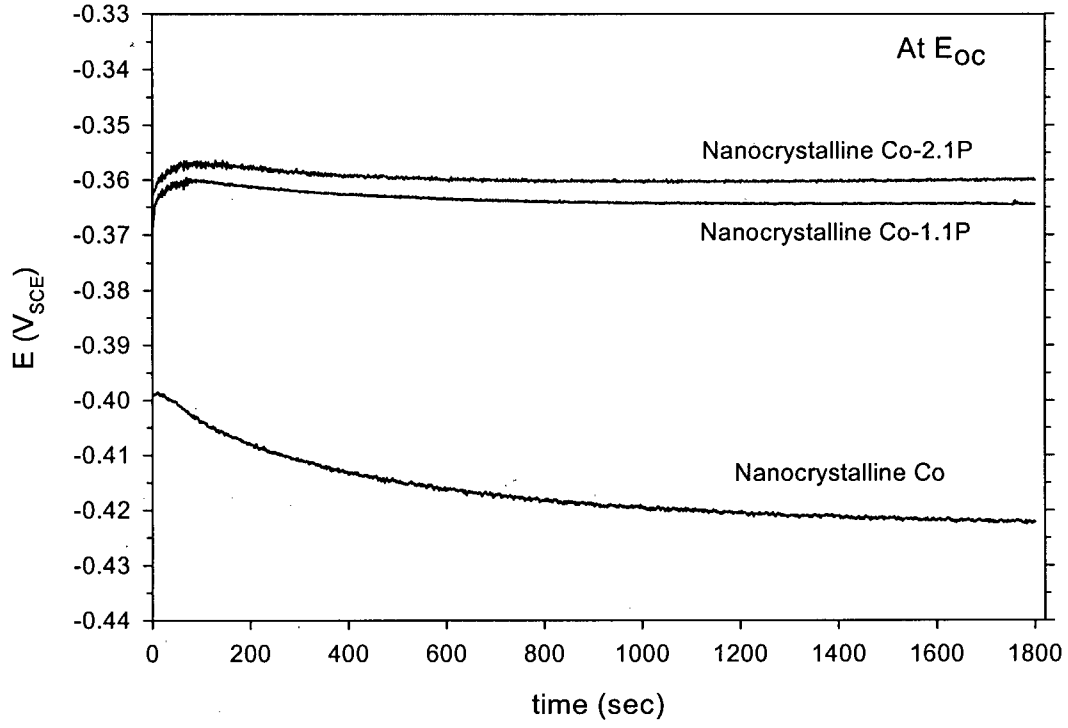

Figure 5-7 Typical E_{oc}-time behavior of nanocrystalline Co, nanocrystalline Co-1.1P and 2.1P alloys in deaerated 0.1 M H_2SO_4 at room temperature.

The anodic polarization curves of nanocrystalline Co-1.1P alloy shifted to a more positive value of potential and significantly reduced the anodic dissolution rates as compared to that of nanocrystalline Co. This nobler shift was more evident in nanocrystalline Co-2.1P. The anodic polarization regimes of both nanocrystalline Co-1.1P and nanocrystalline Co-2.1P alloys in general displayed two regions that may be differentiated by the slope, dE/di, of the potentiodynamic curve. First, at potentials from E_{corr} to about -0.3 and -0.28 V_{SCE} which may be defined to the critical potentials (E_{crit}) for nanocrystalline Co-1.1P and nanocrystalline Co-2.1P, respectively, anodic dissolution is kinetically limited due to their high values of slope, dE/di (equal 54 and 57 mV/decade for 1.1P and 2.1P, respectively).

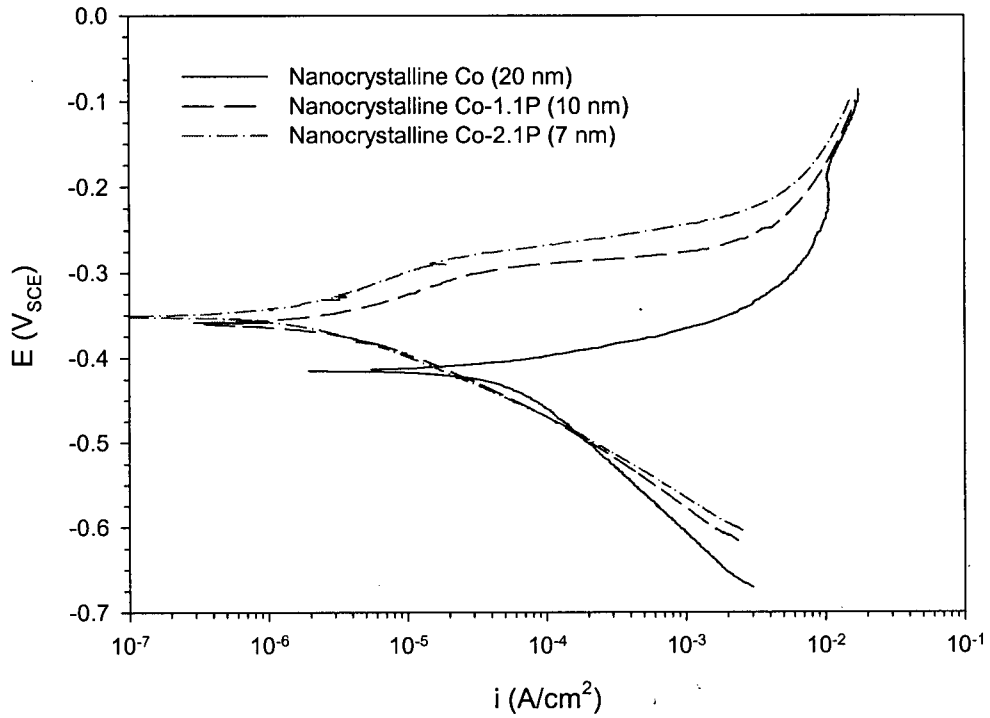

Figure 5-8 Potentiodynamic polarization curves of nanocrystalline Co-1.1P and 2.1P alloys in deaerated 0.1 M H_2SO_4 (pH=1) at room temperature (scan rate=0.5mV/s).

Second, at potentials above E_{crit}, both alloys begin to dissolve rapidly at rates that substantially exceed those in the lower potential region, which is similar to the onset of pitting corrosion due to the breakdown of passive film to a degree. Upon anodic polarization to E_{crit}, both nanocrystalline Co-1.1P and nanocrystalline Co-2.1P alloys retained their surface finish and remained visually intact, while nanocrystalline Co was observed to dissolve rapidly and uniformly at potentials just above E_{corr}. However, the metal surface of nanocrystalline Co-P alloys became black quickly above E_{crit}. Thus it can be postulated that the anodic dissolution mechanism of nanocrystalline Co-P alloys changed from anodic inhibition, i.e., limited kinetics but thermodynamically favorable in the potential regions below E_{crit} to accelerated anodic dissolution above E_{crit}. Helfand, M. A. *et al*, [1992] also observed similar behavior, i.e., two different slopes on the anodic polarization curve for

glassy Co-20 at% P alloy during anodic potentiodynamic polarization in 0.2 N H_2SO_4 electrolytes.

However, it is worthy to note that the presence of critical potential, i.e., different slopes, was not usually apparent in conventional polycrystalline Co-P alloys containing low level of P content (< 4 wt% P), for example, Co-4 wt% P in 0.1 M H_2SO_4 [Krolikowski, A., 1988] and Co-0.8, 2.1, 3.0 and 3.84 wt% P in HCl [Yukimi et al, 1987]. The anodic inhibition effect in nanocrystalline Co-1.1 and nanocrystalline Co-2.1P alloys below the critical potential is peculiar. This difference could be due to high electrochemical reactivity originating from the highly disordered structures of nanocrystalline materials.

The overpotential for H_2 evolution also decreased and the cathodic reaction rates increased very fast upon increasing the cathodic potential from the result of P alloying. The decrease of overpotential and high hydrogen evolution reaction activities of low P content alloys were previously reported for Ni-P alloys [Krolikowski, A. and Wiecko, A., 2002]. They observed that the cathodic Tafel slope of Ni-7 at% P was much lower than that of pure Ni in 0.1 M H_2SO_4 electrolyte. Therefore, it can be concluded that the effects of P for nanocrystalline Co-1.1P and nanocrystalline Co-2.1P on the hydrogen evolution reaction are more significant than grain size reduction.

This is also consistent with the anodic behavior. By considering the relatively smaller grain sizes of nanocrystalline Co-1.1P (10 nm) than that of nanocrystalline Co (20 nm), higher anodic dissolution rates of nanocrystalline Co-1.1P could be expected due to a higher surface area fraction of intercrystalline defects than nanocrystalline Co, however, an addition of P leads to reduced kinetics and the corrosion resistance of nanocrystalline Co-P alloys further increased with a higher P level of 2.1 wt%. Therefore, we may conclude that P content plays a more important role than grain size reduction in the corrosion behavior of nanocrystalline Co-1.1P and nanocrystalline Co-2.1P alloys. The beneficial effects in corrosion resistance of alloying transition metals with small amounts of P have been observed previously in electrodeposited polycrystalline Co-4 at % P alloys in 0.1 N H_2SO_4 solutions [Krolikowski, A., 1988] and polycrystalline Fe-2 wt% P in 1 N Na_2SO_4 (pH=2) [Krautschick, H., J., et al., 1988]. As the anodic potential was increased, the differences in

the anodic current densities became smaller and eventually similar at higher anodic potentials. This shows that the dissolution kinetics at higher anodic potentials is less dependent on crystalline defects and P.

5.1.2.3 Corrosion Morphologies

Figure 5-9 presents the corrosion morphologies observed in the SEM following the potentiodynamic polarization scan up to -0.1 V_{SCE}.

The corrosion morphology following Co metal dissolution of nanocrystalline Co was characterized by a uniform corrosion having lots of shallow pits (Figure 5-9a), which was almost identical to the corrosion morphologies after the potentiostatic polarization test (Figure 5-6e) and same interpretation described in section 5.1.1.4 can be applied to this morphology.

In the case of both nanocrystalline Co-1.1P and nanocrystalline Co-2.1P samples, however, the corroded surfaces were found to be covered by a non-protective blackish colored film after the potentiodynamic polarization scan. While the pitting corrosion was prevalent on the surface of nanocrystalline Co-1.1P and a few microcracks were also observed as shown in Figure 5-9b, cracks aligned mainly along the polishing direction as well as more or less random directions were observed on the corroded surface of nanocrystalline Co-2.1P (Figure 5-9c).

When the corroded surface of the both alloys was analyzed with EDX, the intensity of the P peak was significantly increased (not shown here). Although a quantitative analysis of the exact surface concentration of P is difficult due to the unknown accurate size of interaction volume in the EDX analysis, a comparison with the EDX spectrum before the polarization test clearly showed that there was a considerable enrichment of P on the surface.

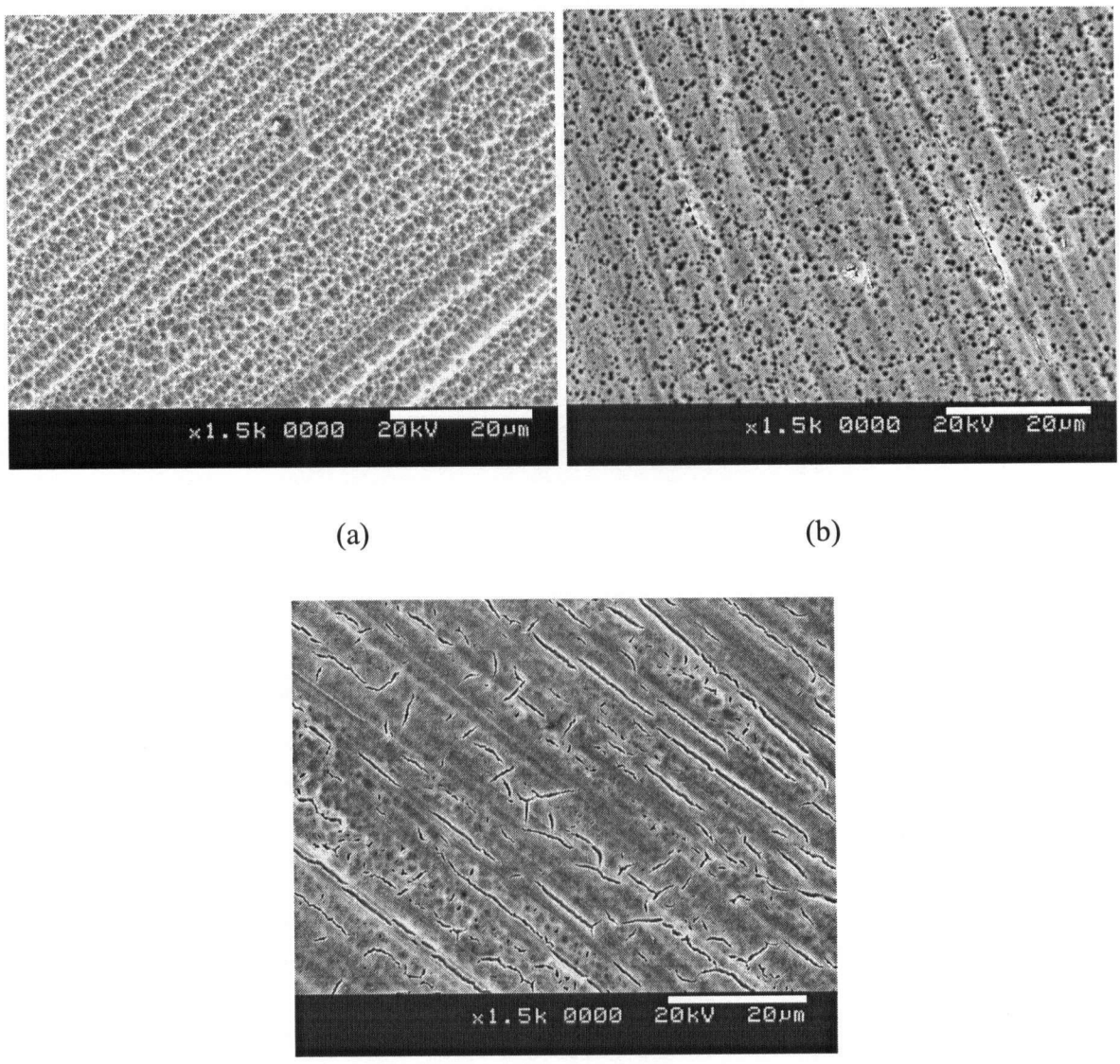

(a) (b)

(c)

Figure 5-9 SEM images showing typical corrosion morphologies for; (a) nanocrystalline Co, (b) nanocrystalline Co-1.1P and (c) nanocrystalline Co-2.1P after potentiodynamic polarization scan up to -0.1 V_{SCE} in deaerated 0.1 M H_2SO_4 (pH=1) (scan rate=0.5 mV/s).

However, no P peak inside the pits and the cracks was often observed. Thus, the Co metal on the substrate was therefore exposed to the solution without the benefit of P alloying within these pits and cracks. Therefore, it can be concluded that the excellent corrosion

resistance of nanocrystalline Co-P alloys in low anodic overpotential ranges was deteriorated by localized corrosion at high anodic overpotential ranges, i.e., above E_{crit}, and this was closely related to the enrichment of P on the surface.

The localized corrosion attack (i.e., pitting and cracking) and the increase of the surface P concentration observed in the current study are very analogous to the dealloying phenomena. During the dealloying process in the binary system, alloy is parted by selective dissolution of less noble element, for example, Zn from brass, Al from bronze, Ag from Au-Ag alloy [Pickering, H. W., 1983; Newman, R. C. and Sieradzki, K., 1994; Erlebacher, J., et al., 2001] and Ni from Ni-P alloys [Flis, J. and D. J. Duquette, 1985; Longfei, Z., et al., 1988]. When selective dissolution occurs, in general, the topmost layers of the alloy surface are depleted of the active component, and preferentially enriched in the more noble component of alloy. Further dissolution process eventually results in the formation of porous structure, i.e., pits and/or cracks composed almost entirely of the more noble alloy constituent in the potential region above E_{crit} [Pickering, H. W. and Y. S. Kim, 1982; Pickering, H. W., 1983; Li, R and K. Sieradzki, 1992].

Therefore, a similar dissolution process (i.e., selective dissolution of Co) may be also applicable to the localized corrosion of nanocrystalline Co-P alloys in the current study considering a significant increase of P content on the metal surface and very porous structure.

5.1.2.4 Potentiostatic Polarization Behavior

In order to investigate the selective dissolution process in more detail, potentiostatic polarization tests for nanocrystalline Co and Co-P samples were conducted at -0.3 V_{SCE} for 10 minutes in deaerated 0.1 M H_2SO_4.

As shown in Figure 5-10, the current density variations with time for nanocrystalline Co-P alloys significantly differ from that for nanocrystalline Co. While the current density of nanocrystalline Co (20 nm) increased very rapidly within <30 seconds as polarized and reached steady state after about 120 seconds, the current densities of both nanocrystalline Co-

1.1P and 2.1P deceased until about 40 and 80 seconds, respectively, and then the current densities increased continuously up to 10 minutes. Although the current densities of nanocrystalline Co-P alloys did not reach steady state after 10 minutes, the current densities of nanocrystalline Co-1.1P and nanocrystalline Co-2.1P were lower than that of nanocrystalline Co by a factor of 0.19 and 0.02, respectively. An increase of elemental P concentration to 2.5 times on the surface of nanocrystalline Co-1.1P after 30 minutes immersion at E_{oc} was confirmed by XPS analysis (see Figure 5-11 and 5-12) compared to that of an etched clean surface. The gradual decrease of current densities during initial periods could be attributed to the inhibition effects due to surface P enrichment by blocking of the anodic dissolution site of Co, however, further dissolution of Co facilitates the compositional changes in the vicinity of the alloy surface and thus results in a non-protective porous structure containing pits by phase separation process (spinodal decomposition) [Erlebacher, J., et al., 2001] and/or cracks by plastic deformation due to surface stress [Heusler K. E., 1997] as shown in Figure 5-9b and c.

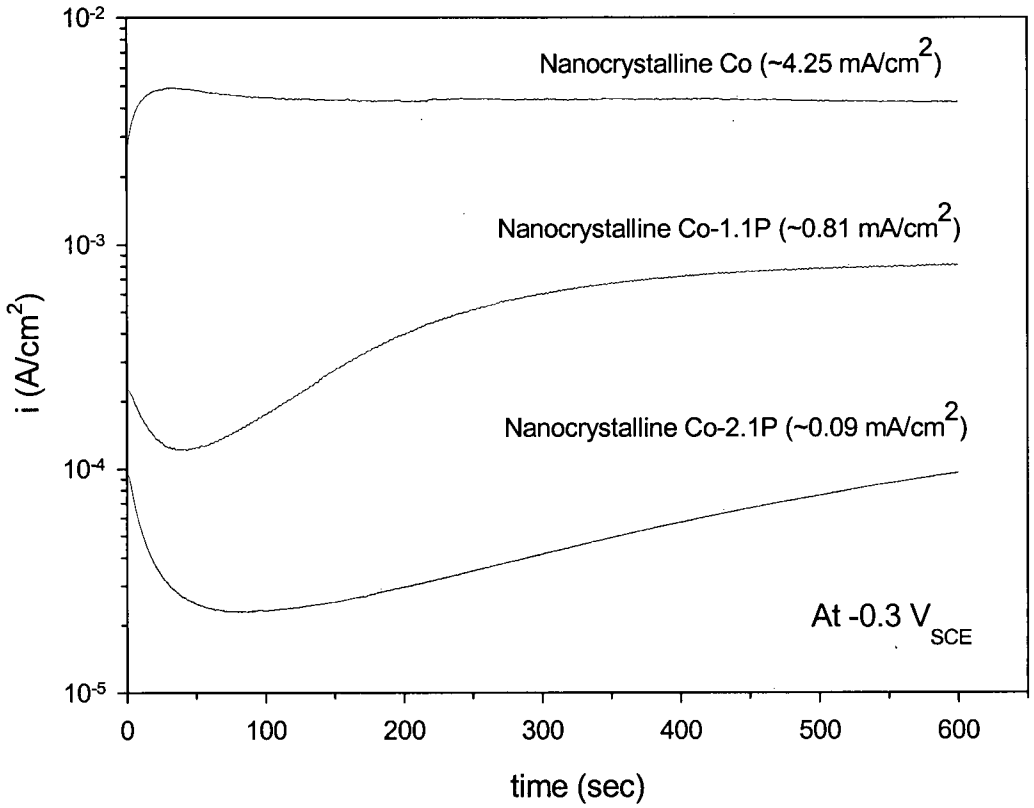

Figure 5-10 Typical current densities of nanocrystalline Co and Co-P alloys at potentiostatic polarization of -0.3 V_{SCE} for 10 minutes in deaerated 0.1M H_2SO_4 solution (pH=1). The values of current density indicated on the figure are the measured values after 10 minutes.

5.1.2.5 X-ray Photoelectron Spectroscopy (XPS)

To elucidate the nature of the corroded surface of nanocrystalline Co-P alloys, XPS analysis was conducted. Figure 5-11 shows the XPS spectra of P 2p, Co 2p and O 1s obtained from the corrosion film formed on the nanocrystalline Co-1.1P specimen following immersion at E_{oc} for 30 minutes and potentiostatic polarization treatment at -0.3 V_{SCE} for 10 minutes compared to that of the etched clean surface.

The P 2p spectra consist of a doublet from elemental P (P^0) at 129.6 eV and two singlets at 132.0 eV and 133.7 eV corresponding to hypophosphite (P^+) and phosphate (P^{5+}), respectively [Helfand, M. A., et al., 1992; Diegle, R. B., et al., 1986; Kawashima, A., et al., 1984]. The Co 2p spectra show the presence of metallic 2p contributions (Co^0) at 793.1 eV

and the oxidized Co species, cobaltic (Co^{3+}) and cobaltous (Co^{2+}) cations were found at 794.8 and 796.6 eV, respectively [Wagner C. D., 1979].

Only O 1s spectra after potentiostatic polarization treatment at -0.3 V_{SCE} for 10 minute was also observed. However, due to binding energy overlap between various forms of oxidized P and oxidized Co, for example H_2O at 533.9 eV, OH^- at 531.3 eV, O^{2-} at 529.5 eV, $H_2PO_2^-$at 530.9 eV, and $H_2PO_4^-$ at 531.9 eV [Diegle, R. B. and N. R. Sorensen, 1988; Foelske, A. and H. H. Strehblow, 2000], the O1s data are not conclusive.

The peak area ratios of the P 2p and Co 2p signals in Figure 5-11 are plotted in Figure 5-12 and compared with results obtained from an ion etched nanocrystalline Co-1.1P (2.2 at% P) substrate. The measured P/Co atomic ratio shows an increase in surface P of about 2.5 and 55 times for the samples following immersion at E_{oc} for 30 minutes and at -0.3 V_{SCE} for 10 minutes, respectively.

Since there are no appreciable peaks for oxidized P and oxidized Co after immersion at E_{oc}, it is evident that the increased elemental P on the surface played a major role in enhancing the corrosion resistance by hindering further dissolution of Co following an initial selective dissolution of Co. An accumulation of a more noble component on the surface of binary alloys was typically observed. For example, J. E. Holliday and H. W. Pickering [1973] reported that the amount of elemental Cu in the surface layer of Cu-30 at% Zn alloys increased by a factor of max. 2.4 at a constant potential in acidic sulfate solution, and that the average thickness of the layer at steady state was on the order of 10^{-6} cm using XPS analysis.

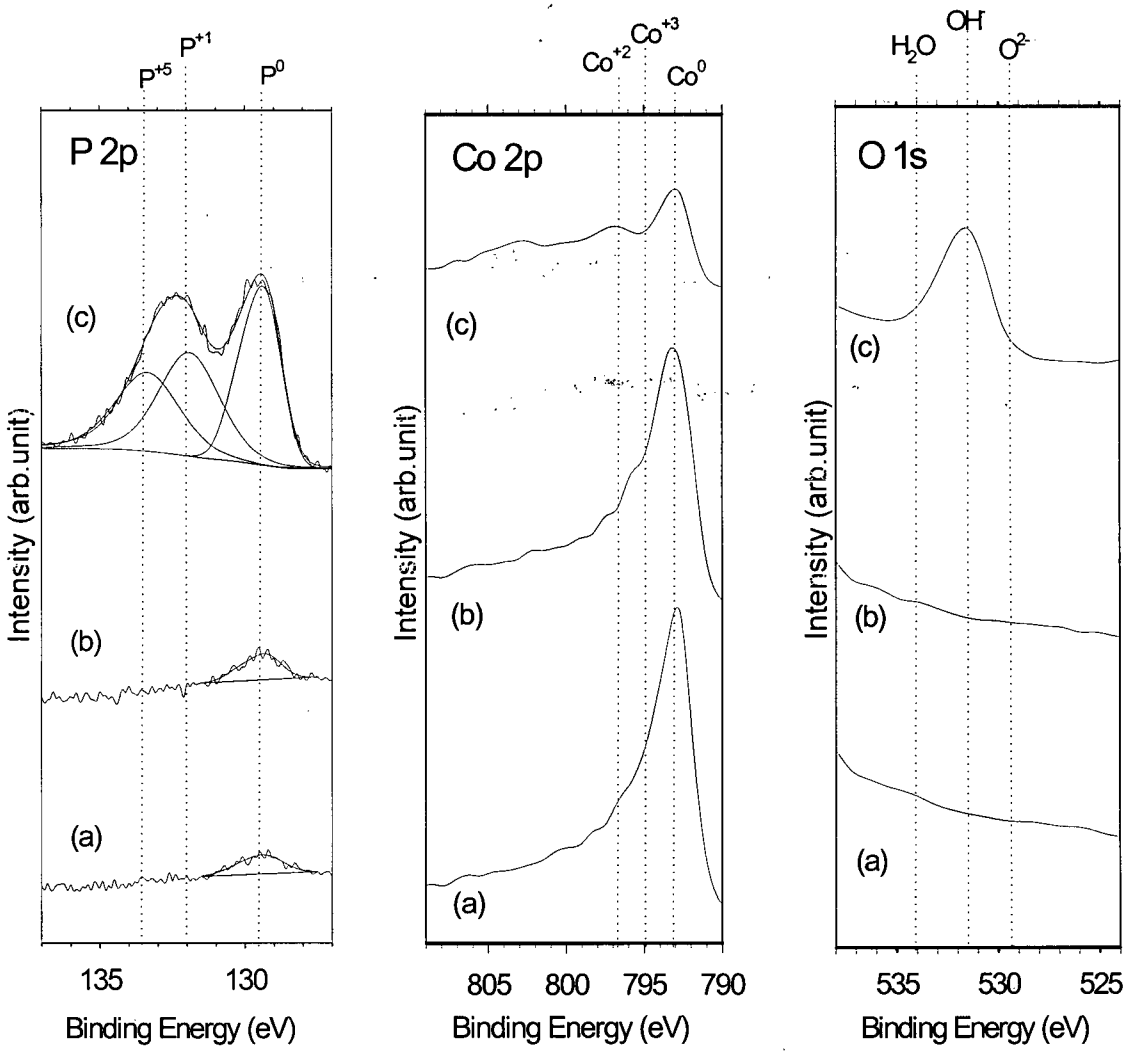

Figure 5-11 P 2p, Co 2p and O 1s spectra obtained from the surface of nanocrystalline Co-1.1P following: (a) ion-etched clean surface, (b) after immersion at E_{oc} for 30 minutes, and (c) after potentiostatic polarization at -0.3 V_{SCE} for 10 minutes in deaerated 0.1 M H_2SO_4 (pH=1).

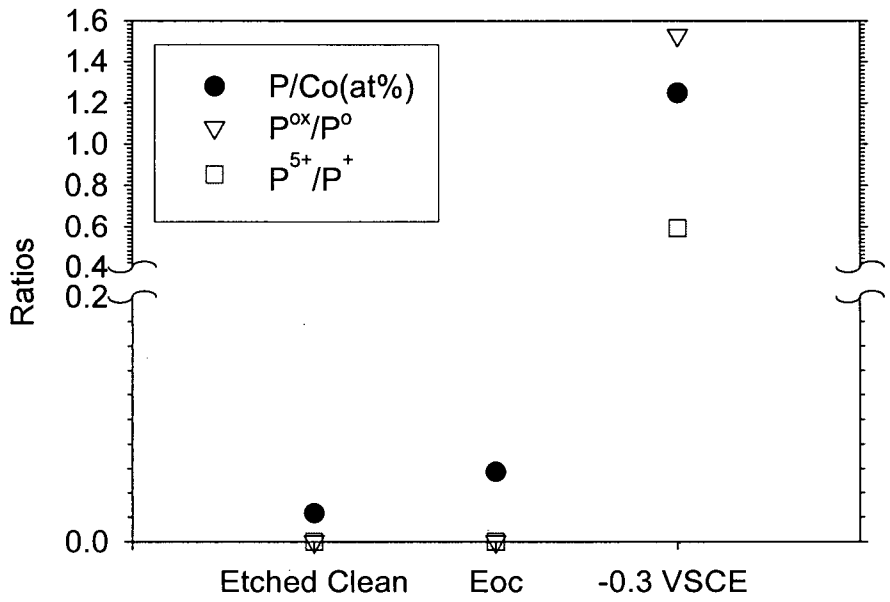

Figure 5-12 Peak area ratios of P 2p and Co 2p spectra obtained from Figure 5-11.

Upon polarization at -0.3 V_{SCE} for 10 minutes, the oxidation of this alloy resulted in a significant increase in elemental P in addition to considerable oxidized P signals and the ratio of oxidized P to elemental P (P^{ox}/P^{o}) was 1.56. According to the E-pH diagram for the P-water system (see Figure 2-2), hypophosphite can be formed by reaction of water with P and further oxidized to phosphate from hypophosphite at high anodic potentials:

$$P + 2H_2O \rightarrow H_2PO_2^- + 2H^+ + e^- \qquad (5\text{-}14)$$

$$H_2PO_2^- + 2H_2O \Leftrightarrow H_3PO_4 + 3H^+ + 4e^- \qquad (5\text{-}15)$$

Previous investigations have indicated that with the addition of P, amorphous alloys exhibited better resistance to aqueous corrosion than unalloyed pure Co in acidic solution (see Figure 2-7). The limited dissolution of P rich amorphous alloys was mainly associated with an anodic film formation inhibiting anodic dissolution processes. Through XPS analysis, this film was determined to be composed of hypophosphite anion (P^+) and

phosphate (P^{5+}) in Co-20 at% P [Helfand, M. A. et al., 1992] and Ni-20 at% P [Diegle, R. B., et al., 1986] alloys and Cr (or Fe) phosphate (P^{5+}) in Fe-Cr-P alloys [Demaree, J. D., at al., 1993]. On the contrary, in the case of nanocrystalline material containing a low level of P content, Splinter, S. J., et al. [1986] observed that an enrichment of P for nanocrystalline Ni-1.9 wt% P leads to an enhancement of the anodic dissolution rate having no clear passivation compared to that of pure Ni in acid solution (see Figure 2-21). They reasoned that the detrimental effect of P on Ni passivation was attributed to the formation of a porous, non-protective film consisting of mainly soluble phosphate, hypophosphite, and elemental P. When the corroded surface was examined by SEM, the well developed pits were also observed.

Therefore, in the current study, even greater enrichment of elemental P was observed at -0.3 V_{SCE} than obtained at E_{oc}, it followed that an enrichment of elemental P did not provide effective inhibition for the anodic dissolution of Co compared to that achieved at E_{oc}. It was also considered that the contribution to inhibition of oxidized P species, i.e., hypophosphite and phosphate, was not significant. These conclusions can be drawn by the fact that a higher dissolution rate and pitting were observed.

5.1.2.6 Electrochemical Impedance Spectroscopy (EIS)

Figure 5-13a shows the impedance spectra of nanocrystalline Co-P alloys measured at E_{oc} after immersion for 30 minutes. Impedance responses of the alloys have been remarkably changed in term of both the shape and the size of the semicircle compared to that of nanocrystalline Co. The resulting Nyquist plots present a capacitive loop for both nanocrystalline Co-1.1P and 2.1P without clear evidence of an inductive loop up to 10 mHz.

The size of semicircles of nanocrystalline Co-1.1P and 2.1P increased significantly compared to that of nanocrystalline Co by a factor of about 19 and 21, respectively. Thus it can be expected that the addition of P increases the resistance of the alloys against corrosion, as expected in accordance with the results of potentiodynamic polarization tests. Since the inhibition effect on the anodic dissolution of Co as well as the increase of surface P

concentration was observed, this enhancement should be attributed to the electrochemical changes on the electrode surface due to elemental P enrichment.

Following potentiostatic polarization at -0.3 V_{SCE} for 10 minutes, the impedance spectra of nanocrystalline Co-P alloys clearly exhibited two inductive loops at low frequency ranges as shown in Figure 5-13b. As the corroded surface of nanocrystalline Co-P alloys was examined by SEM morphology and XPS analysis, these inductive loops were closely related to adsorption-relaxation of Co intermediates i.e., $(Co_kOH)_{ads}$ as described in section 5.1.1.3 and/or adsorbed P intermediates i.e., hypophosphite or phosphate according to Eq.(5-14) and Eq.(5-15), respectively, formed during anodic dissolution process.

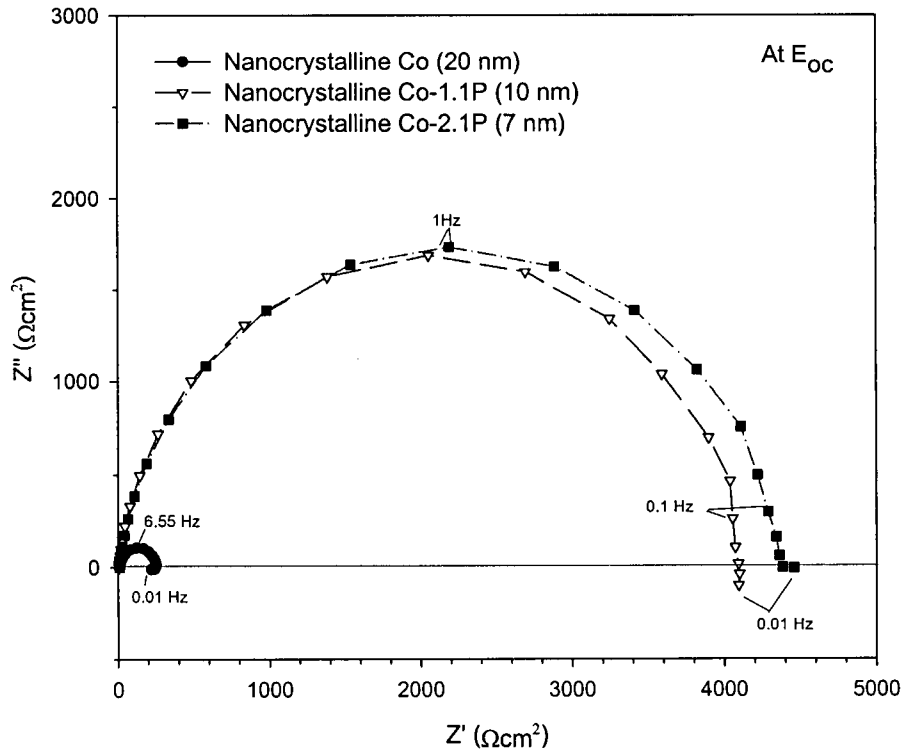

(a)

Figure 5-13 Nyquist plots of electrochemical impedance spectra recorded on nanocrystalline Co-1.1P and nanocrystalline 2.1P samples obtained at (a) E_{oc} and (b) -0.3 V_{SCE} in deaerated 0.1 M H_2SO_4 (pH=1).

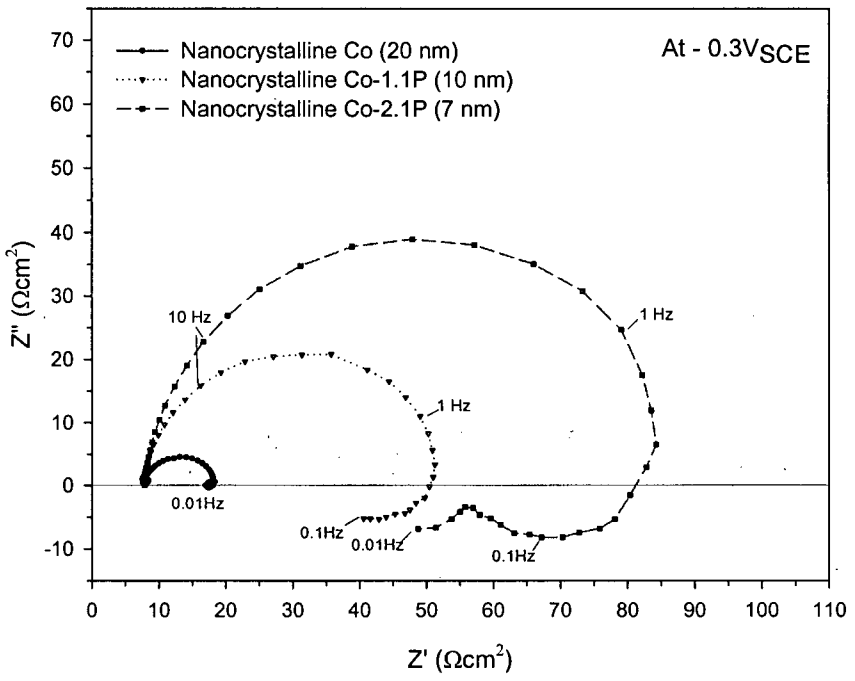

(b)

Figure 5-13 (continued)

The charge transfer resistance of nanocrystalline Co-1.1P and nanocrystalline Co-2.1P increased 5.6 and 10 times, respectively, compared to that of nanocrystalline Co in terms of the size of the capacitive loop in diameter, suggesting that a porous layer consisting of elemental and oxidized P species still provides a kinetic barrier to further dissolution.

In order to further investigate the effect of alloying P on the corrosion rate, the variation of the impedance of nanocrystalline Co-1.1P and 2.1P at E_{oc} was recorded by a function of the immersion time (t) as shown in Figure 5.1.14. All impedance plots exhibited a slightly depressed semicircle and the size of the semicircles increased gradually with the immersion time for both alloys.

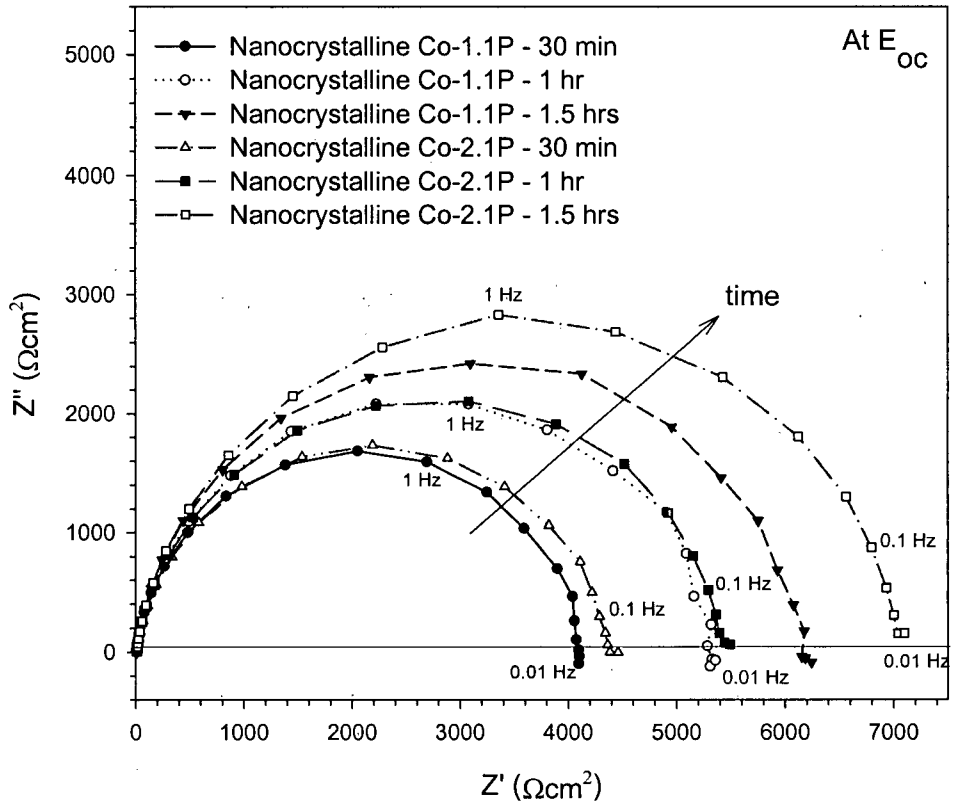

Figure 5-14 Nyquist plot of electrochemical impedance spectra as a function of immersion time recorded on nanocrystalline Co-1.1P and 2.1P alloys at E_{oc} in deaerated 0.1 M H2SO4 (pH=1).

In the Bode plot, the maximum phase angle value increased slightly and the log|Z| against log f linearity in a broad frequency range indicating relatively insulating and protective properties of the surface film in all cases and there was no clear evidence of inductive loop up to low frequency ranges. Therefore, a simple Randle's circuit consisting of interfacial resistance in parallel with an equivalent capacitance was applied to estimate the parameters (see Figure 4-11a). The electrolyte resistance was omitted since it was found to be in the order of 8 Ωcm2, which is negligible in comparison with the impedance values shown in Table 5-4.

Table 5-4 Impedance parameter values and the P enriched layer thickness of nanocrystalline Co-P alloys as a function of the immersion time measured at E_{oc}

Immersion time (minutes)	Q_e (F/cm^2)	R_i (Ωcm^2)	δ_L (nm)
Nanocrystalline Co-1.1P			
30	4.18×10^{-5}	4042	4.5
60	4.06×10^{-5}	5234	4.8
90	4.01×10^{-5}	6055	4.9
Nanocrystalline Co-2.1P			
30	6.00×10^{-5}	4298	2.2
60	5.91×10^{-5}	5328	2.3
90	5.78×10^{-5}	6924	2.4

In this equivalent electrical circuit, it was considered that a capacitance is the combination of the double layer capacitance and the P enriched layer capacitance. The interfacial resistance also contains two components, namely, the charge transfer resistance and the P enriched layer resistance. In Table 5-4, the equivalent capacitance (Q_e) is the magnitude of CPE (constant phase element) which is formally introduced only for impedance data fitting to meet the requirements (see Eq.(4.7)) [Macdonald, J. R., 1987]. In the present case, n is 0.90 ~0.92 which is close to the value for an ideal capacitor behavior (n=1).

The interfacial resistances (R_i) for both alloys increased continuously with immersion time, whereas its equivalent capacitance decreased. In particular, the interfacial resistance has been increased along with the increase of bulk P concentration. This finding can be explained in term of the increase of the accumulation of P on the surface followed by

the preferential dissolution of Co assuming same anodic dissolution mechanism during the immersion time.

As an approximation, the equivalent capacitance (Q_e) may be related to a series connection between the double layer capacitance (Q_{dl}) and the P enriched layer capacitance (Q_L) according to the usual expression:

$$\frac{1}{Q_e} = \frac{1}{Q_{dl}} + \frac{1}{Q_L} \tag{5-16}$$

If the P enriched layer thickness (δ_L) can be estimated by utilizing the equation applied to usual capacitor, the thickness may be expressed as follows:

$$\delta_L = \frac{\varepsilon\varepsilon_o A}{Q_L} \tag{5-17}$$

where ε is the dielectric constant of the P enriched layer, and ε_o is the permittivity of free space (8.85×10^{-12} F/m), and A is the surface area (0.9 cm^2). Taking Q_{dl} = 100 $\mu F/cm^2$ [Awad, G. H., 1985] and ε = 4.1 for element P [CRC Handbook, 2004-05], the P enriched layer thicknesses for nanocrystalline Co-1.1P and nanocrystalline Co-2.1P were calculated as a function of immersion time and listed in Table 5-4.

Since Q_L diminishes with increasing δ_L according to Eq.(5-17), Q_e should decrease with increasing δ_L in agreement with the results given in Table 5-4 and illustrated in Figure 5-15. The P enriched layer thickness (Q_L) for both alloys continuously increases with immersion time.

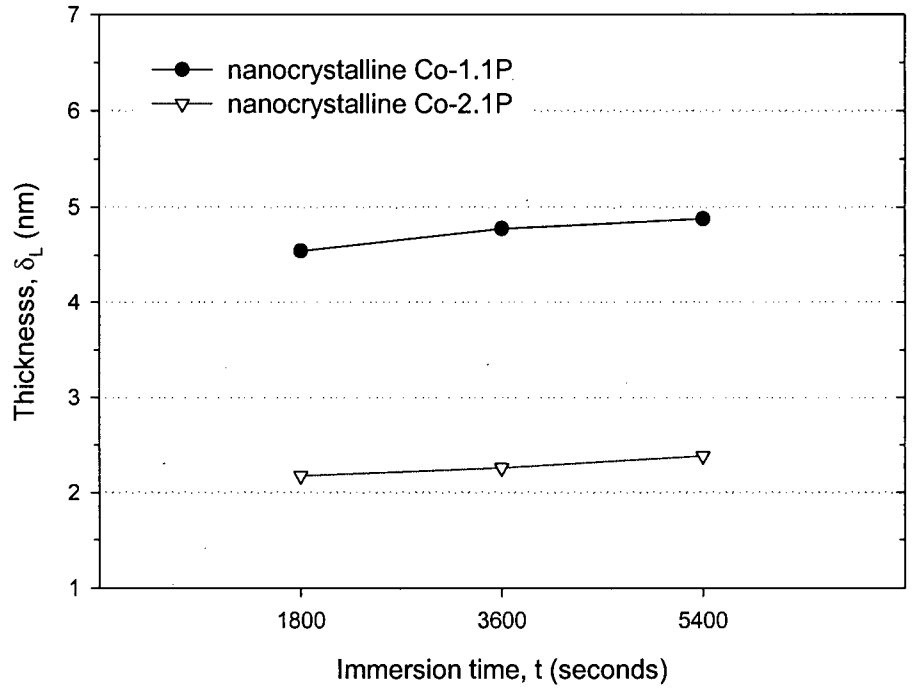

Figure 5-15 Comparison of the P enriched layer thickness on nanocrystalline Co-1.1P and 2.1P as a function of immersion time at open circuit potential in deaerated 0.1M H_2SO_4 (pH=1).

A thickening of the surface layer consisted of a more noble component on binary alloys was also observed in the previous studies. Experimental measurement using Auger depth profiling on binary alloys of Cu-30Au and Ag-30Pd [Laurent, J. and D. Landolt, 1991], and Cu - (5 ~ 30 at %) Pd [Gniewek, J., et al., 1978] polarized below E_c revealed gradual enrichment of the layer with the more noble component towards the alloy surface. The thickness and the extent of enrichment of this layer (i.e., the concentration profile of the more noble component within this layer) increased with the time and magnitude of polarization and typical thickness of the layer range from 5 to 20 nm, corresponding to about 25 to 100 atom layers, as determined from the measured depth-profile curves. In the current study, the thickness of the P enriched layer ranged from 2 to 5 nm was a little smaller than that observed in the previous studies. This difference may be due to different bulk concentration of the more noble component, i.e., a much smaller bulk P concentration in the current study.

Another finding is that the P enriched layer formed on nanocrystalline Co-2.1P is thinner than that of nanocrystalline Co-1.1P. A decrease of the layer thickness indicates that the P enriched layer on nanocrystalline Co-2.1P is more protective, i.e., more compact than that obtained from nanocrystalline Co-1.1P, resulting in higher interfacial resistance of nanocrystalline Co-2.1P. In the reference [Gniewek, J., et al., 1978], it was found that the concentration gradient was correspondingly steeper for the lower concentration of alloy having a thicker layer with the enriched more noble component.

To illustrate the different thickness of the P enriched layer between nanocrystalline Co-1.1P and nanocrystalline Co-2.1P alloys, a simple physical model has been suggested as shown in Figure 5-16. In this binary system, the active component (Co) and the noble component (P) are represented to the empty circle and the solid circle, respectively.

In the anodic dissolution process, the active component (Co) dissolves preferentially while the dissolution of the more noble component (P) is rather limited. Since the more noble component is enriched close to the alloy surface, further dissolution of the active component in the alloy is inhibited by the protective layers of the more noble component (P) enriched layer. Finally, the thickness of the P enriched layer may be constant after reaching to the steady state sometime. The thickness of the P enriched layer is also dependent on the bulk P concentration as observed previously (see Figure 5-15). From this physical model, it is easily observed that the thickness (δ_L) on the nanocrystalline Co-2.1P is smaller than that of nanocrystalline Co-1.1P due to their higher probability of surface P atoms at the steady state. Thus the interfacial resistance of the nanocrystalline Co-2.1P could be higher due to a more protective nature by higher P concentration on the surface.

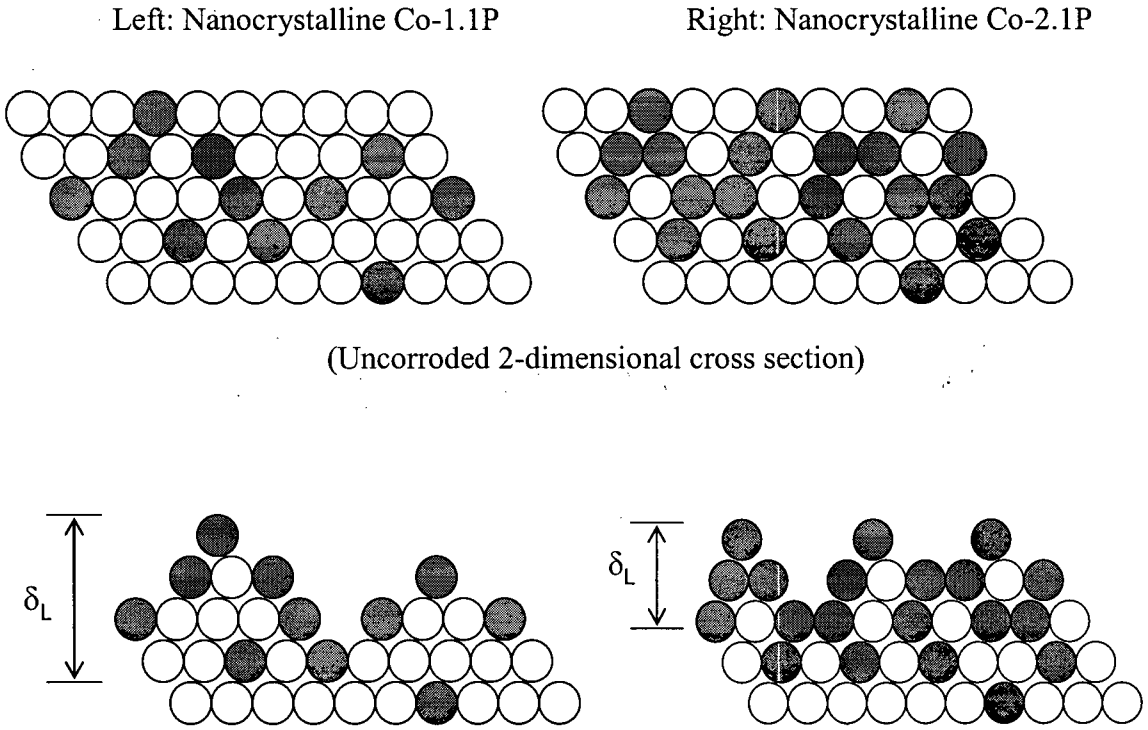

Figure 5-16. Schematic of simple physical models showing different thicknesses (δ_L) of the P enriched layer for nanocrystalline Co-1.1P (left) and nanocrystalline Co-2.1P (right) with active component of Co (O) and noble component of P (•) in anodic dissolution process. (The number of P atoms in the figure does not indicate exact concentration of bulk P contents in the above mentioned Co-P alloys.)

5.1.3 Effect of Heat-Treatment on the Corrosion Behavior of Nanocrystalline Co-P alloy

In this section, the effects of chemical heterogeneity and grain growth by heat-treatment on the corrosion properties of nanocrystalline Co-1.1P alloy are discussed.

5.1.3.1 Open Circuit Potential Behavior

The open circuit potential (E_{oc})-time behavior of all investigated samples were recorded and shown in Figure 5-17. The open circuit potentials for both nanocrystalline Co-

1.1P samples annealed at 350 °C and 800 °C decreased significantly as compared to that of as-deposited state and reached the values of -0.390 and -0.403 V_{SCE} after 30 minutes, respectively. It is indicated that the corrosion resistance could be deteriorated by heat treatment.

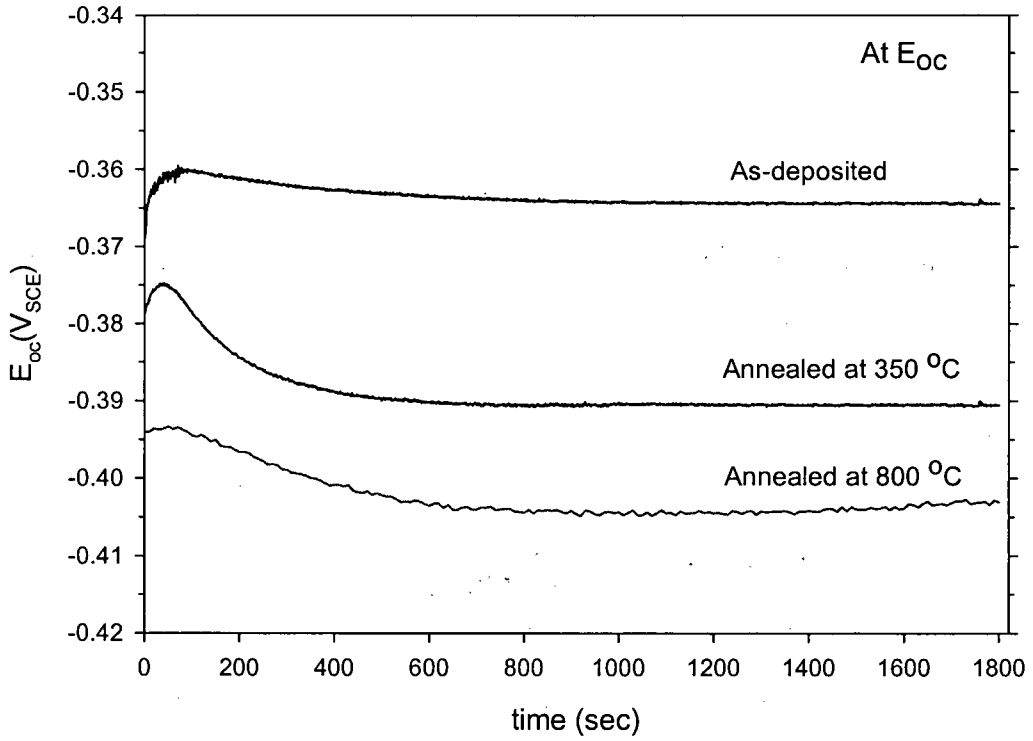

Figure 5-17 E_{oc}-time behavior of as-deposited and annealed nanocrystalline Co-1.1P alloys as indicated on the graph in deaerated 0.1 M H_2SO_4 (pH=1).

5.1.3.2 Potentiodynamic Polarization Curves

Figure 5-18 presents typical potentiodynamic polarization curves for the tested samples in deaerated 0.1 M H_2SO_4 solution. It is evident that an enhanced corrosion resistance of as-deposited nanocrystalline Co-1.1P, however, was remarkably deteriorated by heat-treatment at elevated temperatures. Both anodic polarization curves for annealed nanocrystalline Co-1.1P samples shifted to a more negative potential and increased anodic dissolution rates. Also, the anodic inhibition effect in low anodic potential ranges of the as-

deposited state was eliminated. Recently, Choi, Pyuck-Pa [2003] investigated P distribution within nanocrystalline structures using 3-D Tomographic Atom Probe (TAP) and other analytical techniques. The author observed that the grain size of as-plated Co-1.2 at % P (7.9 nm) increased to 11.4 nm after being annealed at 400 °C with the grain boundaries saturated with segregated P atoms. Further annealing at 480 °C resulted in both the formation of P precipitates (Co_2P and CoP) in the grain boundaries and substantial grain growth (50.3 nm). Indeed, our annealed nanocrystalline Co-1.1P samples demonstrated similar thermal stability, i.e., a small increase of grain size annealed at 350 °C and Co precipitates (Co_2P) and significant grain growth annealed at 800 °C as shown in Figure 4-4 & 4-6 and Table 4-3.

As typically observed in passivating systems, the detrimental effect of P was mainly ascribed to P segregation along the grain boundaries which is believed to result in a non-protective passive layer as discussed in section 2.1.3.4. Even if our as-deposited nanocrystalline Co-1.1P did not show a clear passivation region, the reduced corrosion resistance of the annealed samples could be due to a higher degree of P segregation in the grain boundaries and the formation of P precipitates rather than grain size effect. As the anodic potential was increased above -0.2 V_{SCE}, the differences in the anodic current densities became smaller and eventually similar at higher anodic potentials.

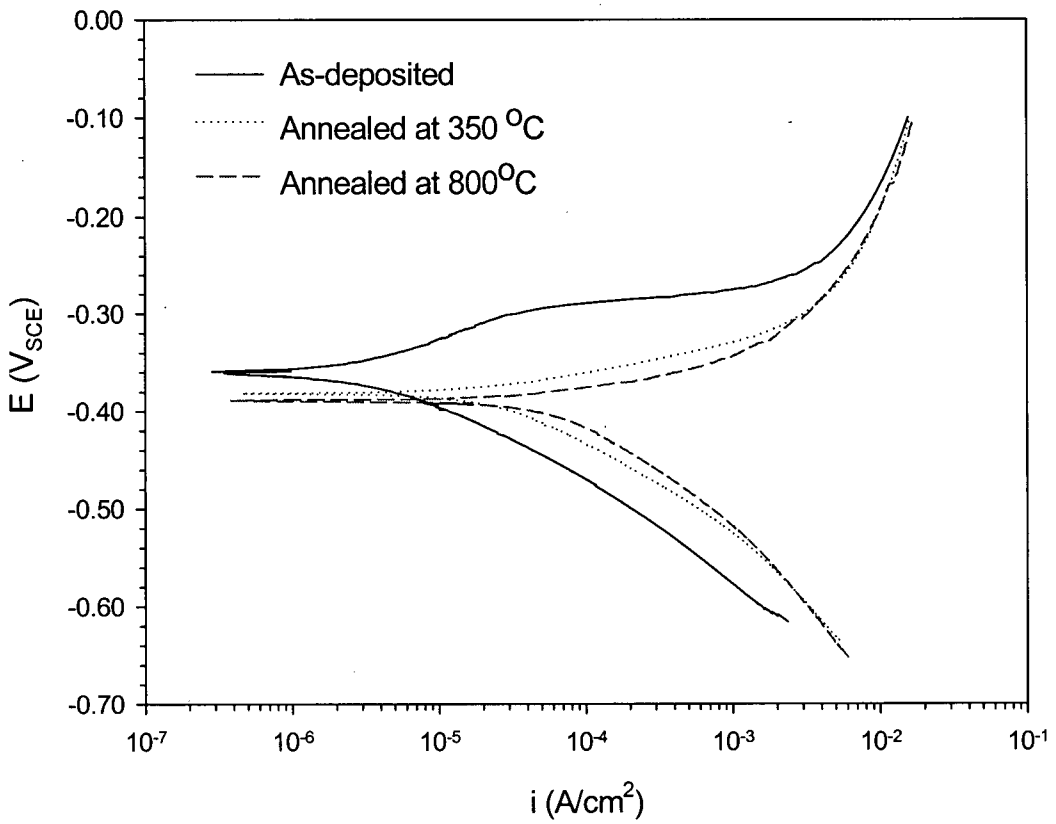

Figure 5-18 Typical potentiodynamic polarization curves of as-deposited and annealed nanocrystalline Co-1.1P alloys as indicated on the graph in deaerated 0.1 M H_2SO_4 (pH=1) (scan rate=0.5mV/s).

5.1.3.3 Electrochemical Impedance Spectroscopy (EIS) Measurement

Figure 5-19a shows Nyquist impedance plots of as-deposited nanocrystalline Co-1.1P and annealed nanocrystalline Co-1.1P measured at E_{oc} after 30 minutes immersion.

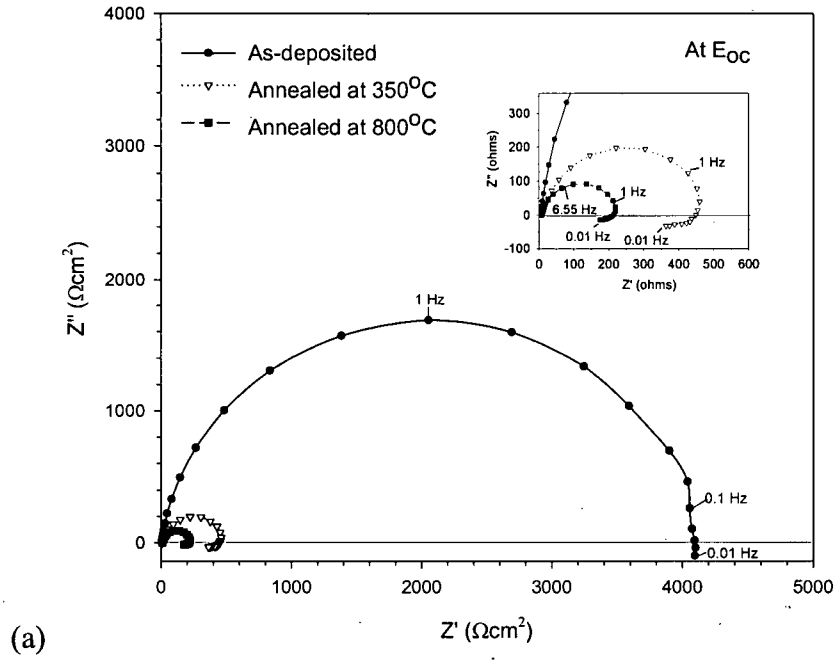

(a)

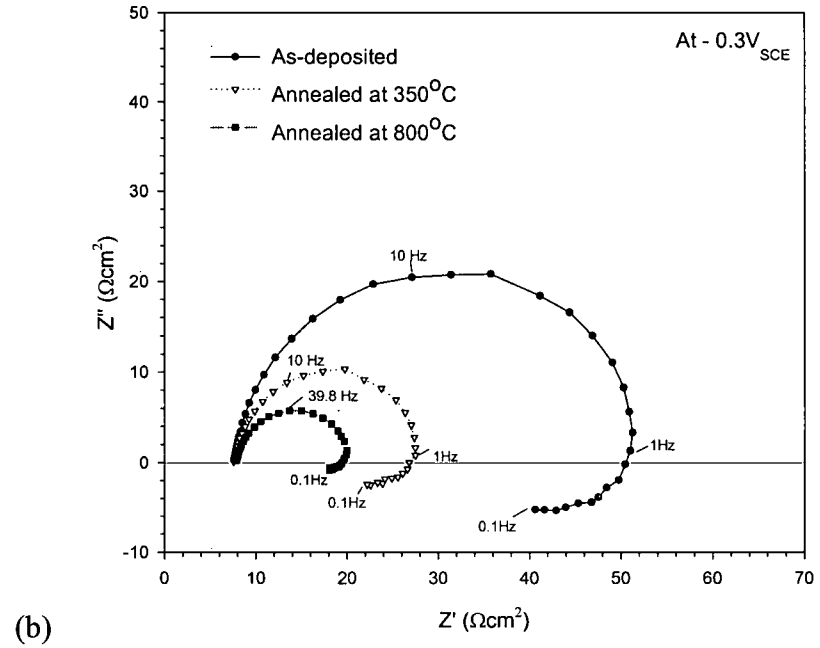

(b)

Figure 5-19 Nyquist plot of electrochemical impedance spectra recorded on as-deposited and annealed nanocrystalline Co-1.1P alloys at (a)E_{oc}, (b) -0.3 V_{SCE} and (c) -0.25 V_{SCE} in deaerated 0.1 M H_2SO_4 (pH=1).

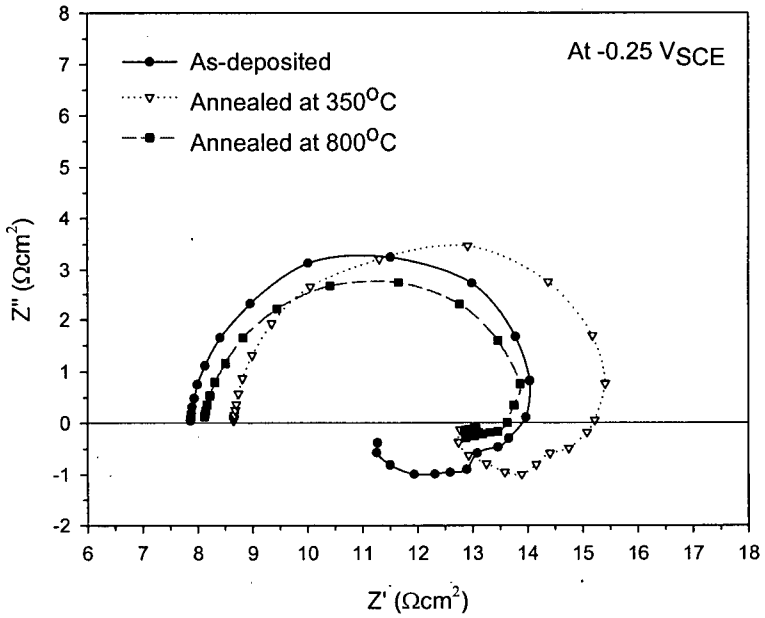

(c)

Figure 5-19 (continued)

In contrast to the as-deposited state, in the case of both annealed nanocrystalline Co-1.1P samples, the inductive loops in the low frequencies were clearly visible and, in addition, tremendous decreases of the size of the capacitive loop were observed. Therefore, the corrosion rates of the annealed samples could be increased.

Following potentiostatic polarization at -0.3 V_{SCE} for 10 minutes, impedance spectroscopy measurements were conducted. These impedance spectra are presented in Figure 5-19b. For the nanocrystalline Co-1.1P annealed at 350 °C, the shape of the impedance diagram was very similar to that of the as-deposited state showing one capacitive loop at high frequency and more than two inductive loops in the low frequencies. Actually an almost identical electrochemical response between as-deposited and annealed samples was found at -0.25 V_{SCE} as shown in Figure 5-19c. From this similarity, it can be suggested that both as-deposited nanocrystalline Co-1.1P and nanocrystalline Co-1.1P annealed at 350 °C samples retain very similar anodic dissolution processes at -0.3 V_{SCE} and -0.25 V_{SCE} while

the annealed one exhibited a smaller charge transfer resistance than the as-deposited case in the low anodic potential range.

However, in the case of nanocrystalline Co-1.1P annealed at 800 °C, the low frequency response was much different and seemed very similar to nanocrystalline Co.

5.1.3.4 Corrosion Morphologies

Figure 5-20 compares the corroded surfaces of three different Co-1.1P samples after potentiostatic treatment at -0.3 V_{SCE} for 10 minutes in 0.1 M H_2SO_4.

As shown in Figure 5-20a, as-deposited nanocrystalline Co-1.1P exhibited pitting corrosion similar to the corroded surface after the potentiodynamic polarization scan (see Figure 5-9b). In the case of nanocrystalline Co-1.1P annealed at 350 °C, the corroded surface shows numerous smaller pits as well as micro-fissures and appears more porous than the as-deposited case. This more defective film formed on the annealed sample could be responsible for increased anodic dissolution rate compared to the as-deposited one.

This is well consistent with the results observed during potentiodynamic polarization testing and impedance measurements. As discussed above regarding P segregation easiness by the annealing process, it is believed that the increased anodic dissolution rate and the more defective corrosion morphologies of nanocrystalline Co-1.1P annealed at 350 °C are due to higher chemical heterogeneity, i.e., the degree of P segregation in the grain boundaries and rearrangement/regrouping of P atoms during the annealing process.

In contrast to the above two samples covered by the P enriched surface film, the corroded surface of nanocrystalline Co-1.1P annealed at 800 °C was quite different, i.e., it consisted of Co metal and different sizes of Co phosphide precipitates (mainly Co_2P) along the grain boundaries. In particular, the area near these precipitates was more severely corroded due to galvanic corrosion originating from the potential difference between these precipitates and the adjacent Co matrix.

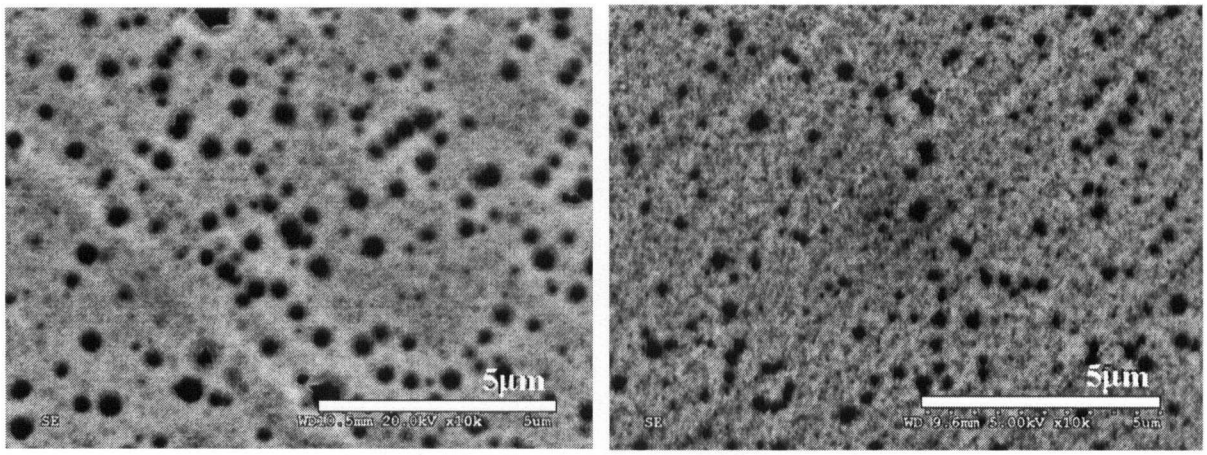

(a) (b)

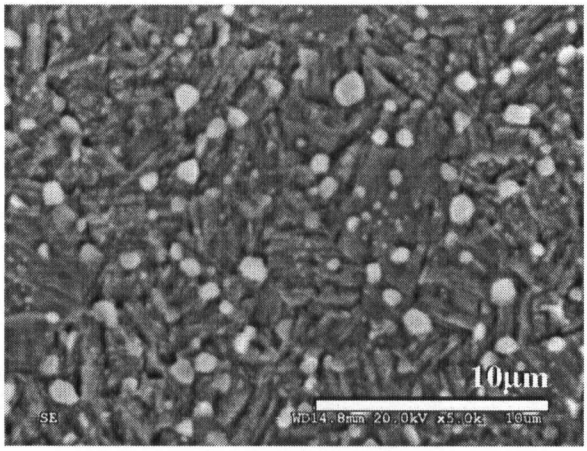

(c)

Figure 5-20 SEM images comparing the corrosion morphologies for; (a) as-deposited nanocrystalline Co-1.1P, (b) and (c) nanocrystalline Co-1.1P annealed at 350 °C and 800 °C, respectively, after potentiostactic polarization at -0.3 V_{SCE} for 10 minutes in deaerated 0.1 M H_2SO_4 (pH=1).

5.1.3.5 X-ray Photoelectron Spectroscopy (XPS)

Figure 5-21 shows the XPS spectra of P 2p and Co 2p obtained from the corrosion film formed on three different Co-1.1P samples following potentiostatic treatment at -0.3 V_{SCE} for 10 minutes in deaerated H_2SO_4. The peak area ratios of the P 2p and Co 2p signals in Figure 5-21 are plotted in Figure 5-22.

Upon polarization at -0.3 V_{SCE} for 10 minutes, the oxidation of all tested samples results in a significant increase in elemental P as well as considerable amounts of oxidized P components. In the case of nanocrystalline Co-1.1P annealed at 350 °C, the concentration of P contents on the corroded surface was smaller than that on the as-deposited alloy. An increased Co^{2+} peak from multiple sources such as cobalt hydroxide/oxide, cobalt hypophosphite and cobalt phosphate was also observed while the Co^0 peak decreased. Although it is not clear what the relationship is between the two different P/Co atomic ratios at the present time, it may be originated from the different chemical heterogeneity of P distribution due to heat treatment, resulting in different degree of pitting corrosion.

In the case of nanocrystalline Co-1.1P annealed at 800 °C, both the amounts of P^0 and oxidized P species decreased and Co^{2+} increased further compared to those of the annealed one at 350 °C. As can be seen in SEM morphologies (Figure 5-20c), the cobalt phosphides could be a main contribution to the P^0 peak which is not from elemental P in the solid solution.

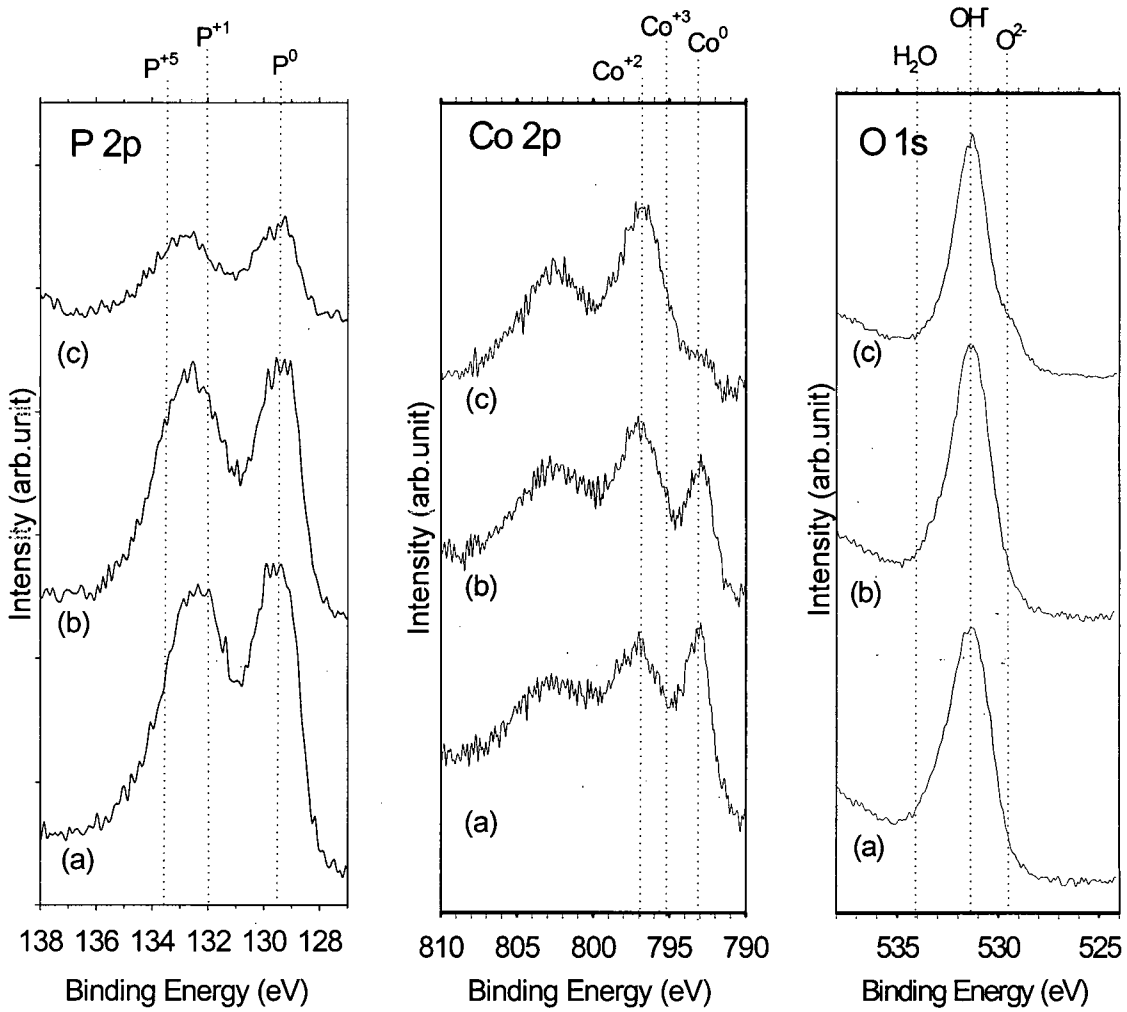

Figure 5-21 P 2p, Co 2p and O 1s spectra obtained from the surface of three different types of nanocrystalline Co-1.1P samples after potentiostatic treatment at -0.3 V_{SCE} for 10 minutes in deaerated 0.1 M H_2SO_4 (pH=1); (a) as-deposited (b) annealed at 350 °C and (c) annealed at 800 °C.

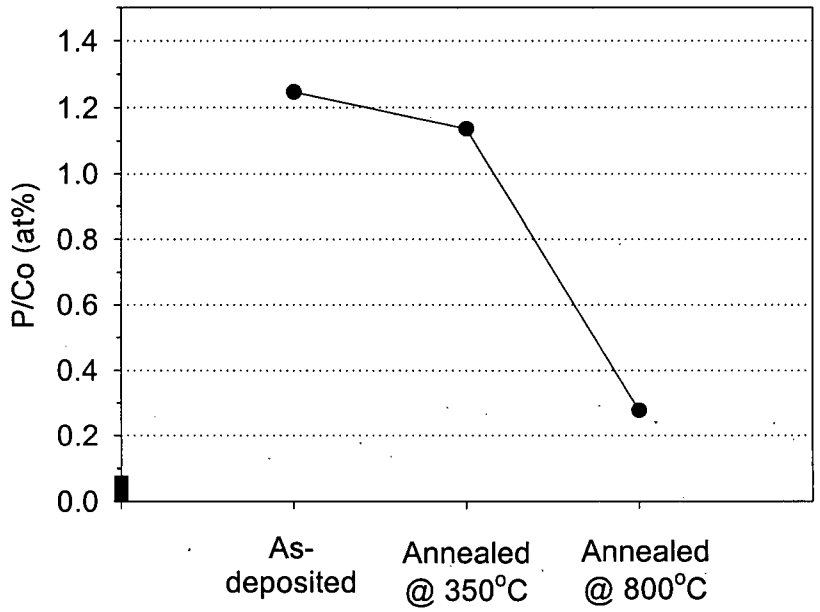

Figure 5-22 Peak area ratio of P 2p and Co 2p spectra obtained from Figure 5-21.

5.1.4 Summary

1. All tested Co and Co-P samples exhibited active dissolution without clear evidence of passivation in acidic solutions at pH of 1 and 3. At both solution pHs, nanocrystalline Co showed higher anodic and cathodic reaction rates compared to polycrystalline Co while detrimental localized corrosion was remarkably reduced. The better localized corrosion resistance of nanocrystalline Co was explained by a morphological model, which considered different penetration current densities due to a different cathode-to-anode area ratio between coarse grained and ultra fine grain sized crystals.

2. An enhanced electrochemical reaction rate for nanocrystalline Co was due to a significant increase of intercrystalline defects (e.g., grain boundaries and triple junctions) by nanoprocessing which resulted in the reduced activation energy barrier for electrochemical reaction due to the excess free energy in nanocrystalline Co.

3. In an attempt to elucidate the anodic dissolution process of poly- and nanocrystalline Co, a catalytic charge transfer mechanism has been identified as a more favorable route than the non-catalytic consecutive charge transfer mechanism by examining i) electrochemical kinetic parameters (i.e., anodic Tafel slopes and the electrochemical reaction order with respect to hydroxyl ion), ii) the low frequency relaxation process due to adsorption in impedance spectra showing inductive loops and iii) macroscopic steps and kinks on the corroded surface.

4. Addition of P leads to a significant increase in the corrosion resistance, i.e. an ennoblement of corrosion potential and a reduced anodic dissolution rate as well as a much higher charge transfer resistance at the open circuit potential for nanocrystalline Co-P alloys. By using XPS analysis, it was concluded that an enhanced corrosion resistance of nanocrystalline Co-P alloys is due to the increased elemental P concentration on the corroded surface at the open circuit potential, providing an inhibition effect to further dissolution of Co following an initial selective dissolution of Co.

5. The thickness of the P enriched layer formed on nanocrystalline Co-1.1P and nanocrystalline Co-2.1P alloys during dealloying continuously increased with immersion time at the open circuit potential and this thickness was dependant on the bulk P concentration, i.e., thinner on nanocrystalline Co-2.1P than on nanocrystalline Co-1.1P. A simple physical model was proposed to explain the formation of the P enriched layer depending on the bulk P concentration.

6. However, at higher anodic overpotential ranges, the superior corrosion resistance of nanocrystalline Co-P alloys did not last due to the formation of a non-protective surface film consisting of mainly hypophosphite and phosphate as well as elemental P. Pitting corrosion was detected at these potentials.

7. It was clearly demonstrated that P concentration plays a more important role than grain size reduction in the anodic dissolution reaction of the nanocrystalline Co-P alloy system.

8. The excellent corrosion resistance of nanocrystalline Co-P alloys deteriorated when they were exposed to heat-treatment at elevated temperatures. This reduced corrosion resistance could be due to higher chemical heterogeneity (e.g., different degree of P segregation and second phase precipitates).

5.2 Corrosion in 3.56% NaCl Solution

In this section, the corrosion properties of poly- and nanocrystalline Co and Co-P alloys in an aerated chloride containing solution are described. For practical applications, a 3.56 % by weight NaCl solution was used to simulate sea water.

5.2.1 Cyclic Polarization Behavior

Figure 5-23 presents typical cyclic polarization curves for nanocrystalline Co and nanocrystalline Co-1.1P alloy in an aerated 3.56 % NaCl solution. The results clearly demonstrate the differences in their corrosion potentials (E_{corr}), rest potentials (E_{rest}), anodic current densities and cathodic current densities. A current-potential hysteresis loop with a relatively large area was shown in nanocrystalline Co, while the polarization curves for both forward and reverse scan were almost identical in nanocrystalline Co-1.1P.

5.2.1.1 Forward Scan

Both samples displayed anodic dissolution up to 0.5 V_{SCE} without clear evidence of passivation. In the case of nanocrystalline Co-1.1P, the polarization curve was shifted to a more negative value of potential and higher anodic current density compared to that of nanocrystalline Co. In particular, this detrimental effect of P alloying on the corrosion resistance at low anodic overpotential was opposite to the beneficial effect of P alloying in sulfuric acid solution as shown in section 5.1. It is rather complex to identify the different effects of P in neutral sodium chloride and sulfuric acid solutions and it seems somewhat improper to compare them directly because these two sets of test results were obviously performed in different solutions at different pH and at different concentrations of dissolved O_2. However, the introduction of the different adsorption properties of chloride and sulfate ion on the metal surface may help gain insight into the possible effects of P.

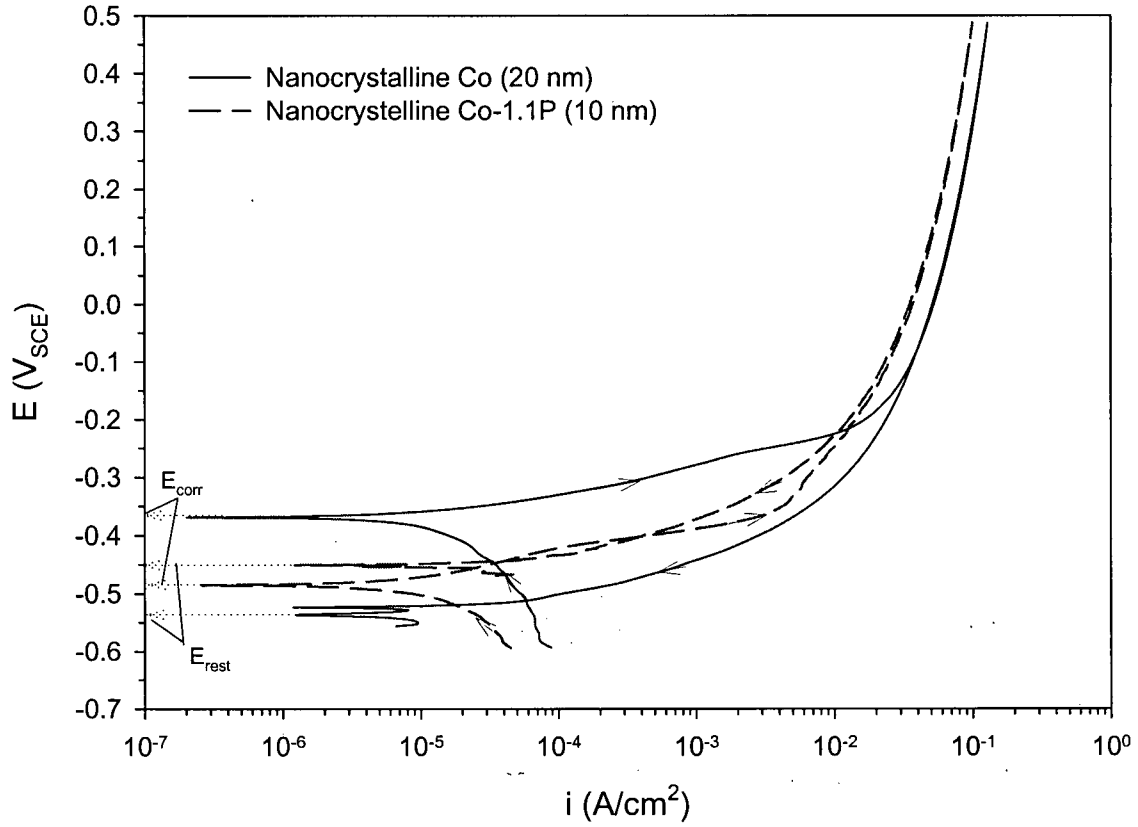

Figure 5-23 Typical cyclic polarization curves of nanocrystalline Co and nanocrystalline Co-P alloys in aerated 3.56 % NaCl solution at pH of 6.2 (scan rate=1mV/s).

There were a few studies performed on the influence of different types of anions on the electrochemical responses of pure Co. In early the 1960s, Z. A. Iofa et al. observed that halogen anions were chemisorbed on the surface of Co and inhibited the electrochemical reactions both in anodic oxidation and cathodic reduction. The solutions under consideration were 1 and 5 N H_2SO_4, containing I^-, Br^-, and Cl^-. Inhibition effects increased with increasing concentrations of halogen anions. [Z. A. Iofa, et al, 1964]. It was also reported that the dissolution rate of pure Co was slower in hydrochloric acid than in sulfuric acid [N. Pangachiev, et al, 1960; Helfand, et al, 1992].

Recently, G. Horanyi [2004] investigated the specific adsorption properties of Cl^- and $HSO_4^-(SO_4^{2-})$ ions on Co and Fe by radiotracer technique in perchlorate solution. According to his study, it was found that the adsorption strength of Cl^- on the Co surface was much higher than that of SO_4^{2-} at pH of 5. This similar behavior, i.e., stronger adsorption of Cl^- than that of HSO_4^- or $H_2PO_4^-$ ions, was also reported on Pt [G. Horanyi, 1998] and Rh [G.. Horanyi and M. Wasberg, 1996]. In summary, from the previous studies, it was clearly demonstrated that the chloride ions have a strong adsorption tendency on the surface of Co and the adsorbed chloride ions provide an inhibition effect on the anodic dissolution of Co.

The adsorption properties of P with chloride ions are not well known and, to our knowledge, the published experimental data is not available at present. However, by comparing the degree of electronegativity for Co, P and Cl, we might get an idea of the effect of P on the electrochemical responses of Co-P alloys in a chloride containing solution. The electronegativity of Co, P and Cl are 1.88, 2.19 and 3.16, respectively [CRC, 85th ed.]. Considering these values, Cl is more attracted to Co than P, in other words, P may be repulsive to Cl due to their similar electronegativity. This repulsive nature of P to Cl may reduce the amount of adsorption area of Cl^- on the Co-P surface. Therefore, the total Cl^- adsorption will be decreased as the surface fraction of P is increased. This reduced area can lead to a reduced inhibition effect by adsorbed Cl^- as mentioned above.

Identification of corrosion products is also important. Co and P may react with adsorbed Cl^- and can form $CoCl^+$, $CoCl_2$, PCl_4, and PCl_5. Their corresponding Nernst Equations at $[Cl^-]=0.6$, $[Co]=[P]=[CoCl_2]=1$, and 25 ^{0}C are as follows:

For $CoCl^+$:

$$Co + Cl^- = CoCl^+ + 2e^- \qquad (5\text{-}18)$$

$$E_{Co/CoCl^+} = 0.30 + \frac{0.059}{2}\log\left(\frac{[CoCl^+]}{[Cl^-]}\right) V_{SHE} \qquad (5\text{-}19)$$

$E_{Co/CoCl+}$ = -0.115 and 0.666 V_{SCE} at $[CoCl^+] = 10^{-6}$ and 1, respectively.

For $CoCl_2$:

$$Co + 2Cl^- = CoCl_2 + 2e^- \quad (5\text{-}20)$$

$$E_{Co^{2+}/CoCl_2} = 0.280 + \frac{0.059}{2}\log\left(\frac{1}{[Cl^-]^2}\right) V_{SHE} \quad (5\text{-}21)$$

$E_{Co2+/CoCl2} = 0.052\ V_{SCE}$.

For PCl_4:

$$P + 4Cl^- = PCl_4 + 4e^- \quad (5\text{-}22)$$

$$E_{P/PCl_4} = 0.462 + \frac{0.059}{4}\log\left(\frac{1}{[Cl^-]^4}\right) V_{SHE} \quad (5\text{-}23)$$

$E_{P/PCl4} = 0.234\ V_{SCE}$.

$$P + 5Cl^- = PCl_5 + 5e^- \quad (5\text{-}24)$$

$$E_{P/PCl_5} = 0.686 + \frac{0.059}{5}\log\left(\frac{1}{[Cl^-]^5}\right) V_{SHE} \quad (5\text{-}25)$$

$E_{P/PCl5} = 0.458\ V_{SCE}$.

After calculation of the equilibrium potential of possible chloride complexes of Co and P, it is clear that these equilibrium potentials are higher, i.e., more anodic than those of low anodic potentials (about -0.45 to -0.25 V_{SCE}) in nanocrystalline Co-1.1P as shown in Figure 5-23. Therefore, from the thermodynamic standpoint, these corrosion products do not contribute to an increase of anodic dissolution of Co-P alloys at low overpotential ranges. Finally, it can be concluded that the increase in the anodic dissolution rate of nanocrystalline Co-1.1P at low anodic potentials compared to that of nanocrystalline Co is due to the reduced adsorption area of chloride anions on the electrode surface.

In the high anodic overpotential range, the anodic dissolution rate of nanocrystalline Co-1.1P is lower than that of nanocrystalline Co. The enhanced corrosion resistance of nanocrystalline Co-1.1P could be due to the formation of oxidized P products as can be seen in the E-pH diagrams for P-water (see Figure 2-3 and 2-4). Furthermore, the adsorption properties of chloride ions on Co and P may be changed to a reduced adsorption strength by the formation of cobalt chloride and phosphorous chloride complexes at higher applied anodic potentials.

5.2.1.2 Reverse Scan

When the scan was reversed at 0.5 V_{SCE} in the cathodic direction, a hysteresis loop with a large area was produced in nanocrystalline Co. The rest potential, E_{rest}, was more negative than the corrosion potential E_{corr}.

In the case of nanocrystalline Co-1.1P, the anodic polarization curve for the reverse scan was almost identical to the forward scan and E_{rest} was more noble than E_{corr}. This enhanced corrosion resistance can be due to the oxidized P, i.e., hypophosphites and/or phosphates formed at high anodic potentials during the forward scan.

5.2.2 Potentiodynamic Polarization Curves

Figure 5-24 presents potentiodynamic polarization curves of annealed poly- and nanocrystalline Co and nanocrystalline Co-1.1P and 2.1P alloys in an aerated 3.56 % NaCl solution. The electrochemical parameters taken from the polarization curves are listed in Table 5-5.

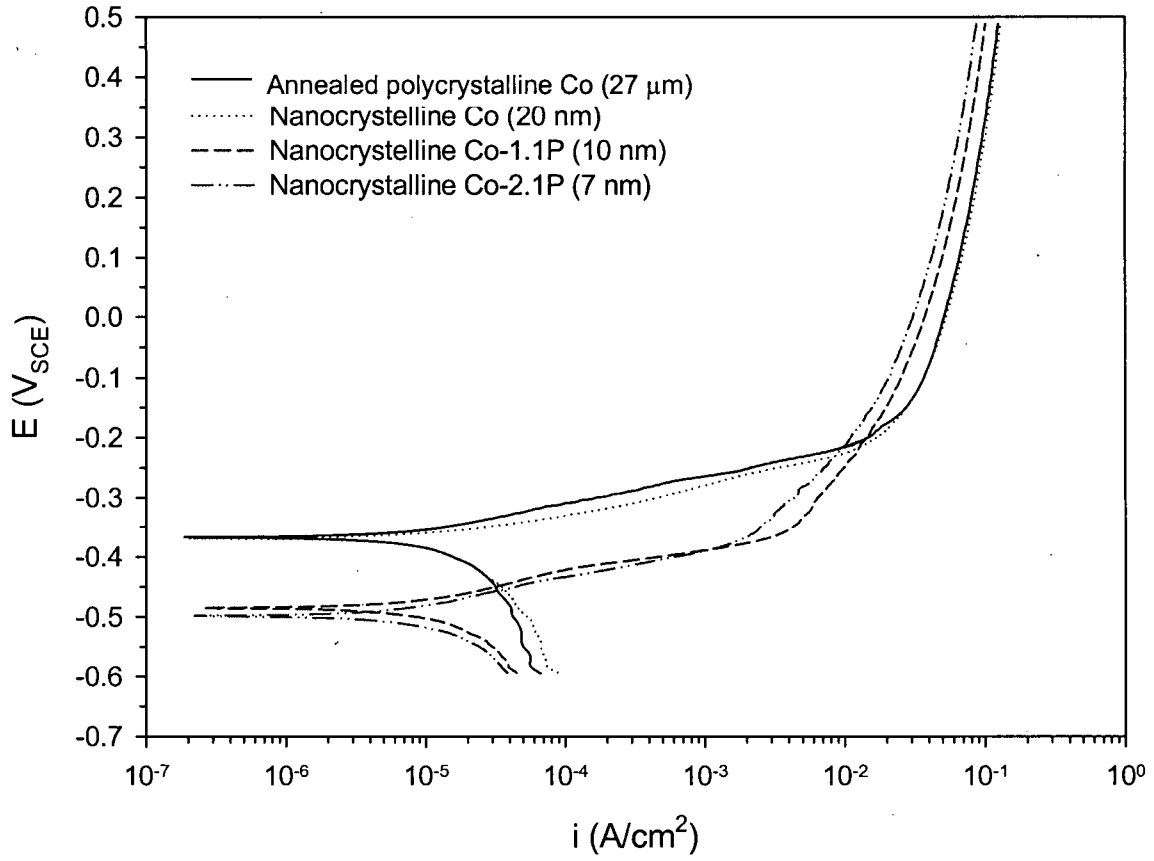

Figure 5-24 Typical potentiodynamic polarization curves of annealed annealed poly- and nanocrystalline Co and nanocrystalline Co-1.1P and 2.1P alloys in aerated 3.56 % NaCl solution at pH of 6.2 (scan rate=1mV/s).

Annealed polycrystalline Co has very similar anodic and cathodic curves to those of nanocrystalline Co. Thus, it is reasonable to predict that the electrochemical reaction would proceed along the same mechanism. However, the value of the anodic and cathodic current densities for nanocrystalline Co-1.1P was smaller than for nanocrystalline Co. A lower electrochemical reaction rate of coarse grained Co compared to nanosized crystalline Co was also observed in sulfuric acid solution as mentioned in section 5.1.

In the case of nanocrystalline Co-P alloys, the polarization curves are shifted to less noble potentials and higher anodic current densities in the low anodic potential region. In the

high anodic potential region, lower anodic current densities than nanocrystalline Co are observed. This shift was more pronounced as bulk P content increased.

In the aerated 3.56 % NaCl solution, dissolved oxygen reduces to water according to Eq.5.2.9 and the corresponding Nernst equation is as follows:

$$O_2 + 4H^+ + 4e^- = H_2O \qquad (5\text{-}26)$$

$$E_{O_2/H_2O} = 1.229 - 0.059pH + 0.015\log P_{O_2}\ V_{SHE} \qquad (5\text{-}27)$$

$E_{O2/H2O}$=0.618 V_{SCE} at pH =6.1 and P_{O2}=0.2 atm.

Table 5-5 Corrosion potential (E_{corr}) and exchange current density ($i_{o,O2/H2O}$) for oxygen reduction taken from polarization data.

Sample	E_{corr} (V_{SCE})	i_{corr}* (A/cm^2)	$i_{0,O2/H2O}$# (A/cm^2)
Annealed pPolycrystalline Co (27 μm)	-0.365	1.86×10^{-5}	10^{-11}
Nanocrystalline Co (20 nm)	-0.369	2.51×10^{-5}	10^{-11}
Nanocrystalline Co-1.1P (10 nm)	-0.487	1.72×10^{-5}	10^{-16}
Nanocrystalline Co-2.1P (7 nm)	-0.502	1.43×10^{-5}	10^{-17}

* Estimated by linear polarization methods in the range of ±10 mV at E_{corr}.

Estimated rigorously by extrapolation of the cathodic Tafel slope to the equilibrium potential for oxygen reduction reaction at pH=6.1 (E_{O_2/H_2O} = 0.859 V_{SHE}).

By rigorous estimation of the exchange current density using extrapolation of the cathodic Tafel region to the equilibrium potential of the oxygen reduction reaction (0.618

V_{SCE}), it is found that the exchange current densities of nanocrystalline Co-P alloys are much lower than those of pure Co as shown in Table 5-5.

This reduced exchange current density of Co-P alloys can shift E_{corr} to more negative potentials and lower i_{corr} in keeping with the mixed potential theory. Considering the reduced corrosion current density of Co-P alloys compared to pure Co, it is possible to conclude that, in an aerated NaCl solution, the corrosion rate is controlled by the oxygen reduction reaction rather than the anodic dissolution reaction. Because of the low solubility of oxygen in water (8~10 ppm), it was observed that diffusion of dissolved oxygen to the interface became cathodic current limiting at about 10^{-4} A/cm^2.

5.2.3 Effects of Heat Treatment on Polarization Behavior of Nanocrystalline Co-P alloy

Figure 5-25 and 5-26 present potentiodynamic polarization curves of the as-deposited and annealed nanocrystalline Co-1.1P and 2.1P, respectively, in aerated 3.56 % NaCl solution (pH=6.2).

Both anodic polarization curves of annealed nanocrystalline Co-1.1P and 2.1P shifted to a more positive value of potential and decreased anodic dissolution rates at lower anodic potential. These different responses were more evident as the bulk P content increased.

According to the results from XRD tests of the samples (Figure 4-6 and 4-7) and a study for thermal stability of nanocrystalline Co-0.6 wt% P prepared by electrodeposition [Choi, Pyuck-Pa, 2003], it is considered that there was the increased chemical heterogeneity (i.e., degree of P segregation along the grain boundaries and rearrangement/regrouping of P atoms during annealing) and precipitation of cobalt phosphides (Co_2P) resulted from the annealing process at elevated temperatures.

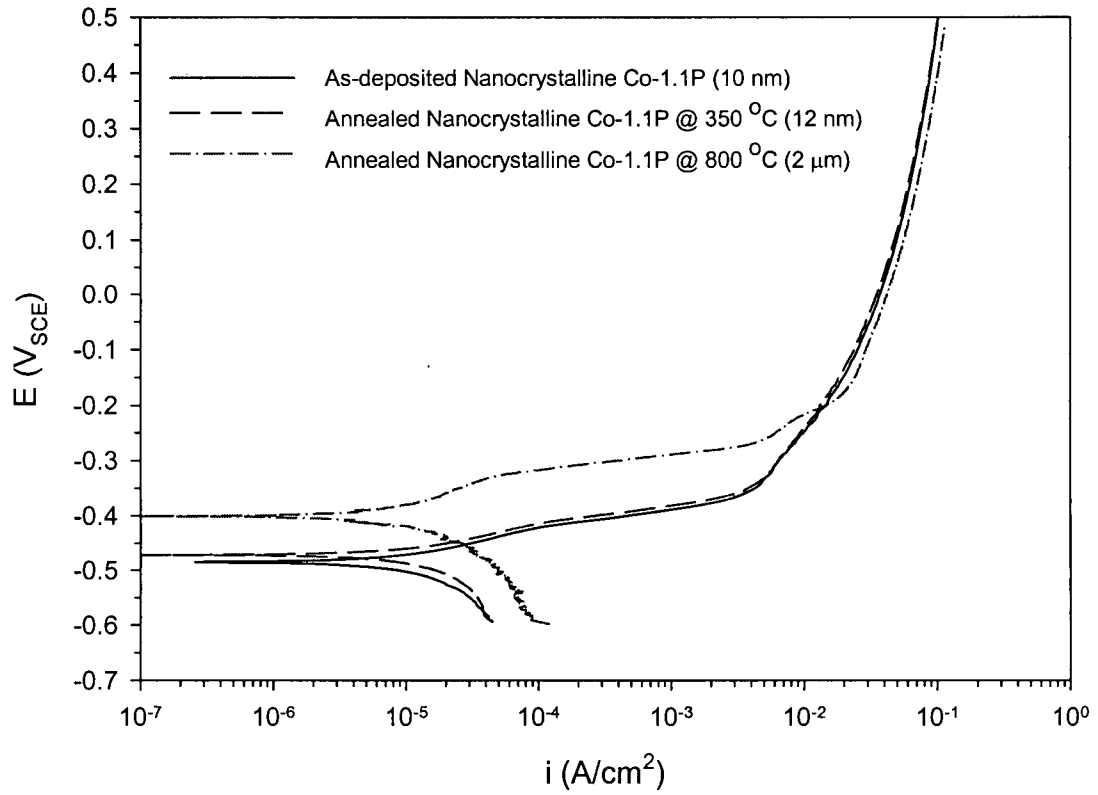

Figure 5-25 Typical potentiodynamic polarization curves of as-deposited and annealed nanocrystalline Co-1.1P in aerated 3.56 % NaCl solution at pH of 6.2 (scan rate=1mV/s).

Changes in the degree of P segregation and precipitation can affect the adsorption properties of chloride ions on the electrode surface. In a simple physical model, shown in Figure 5-27, increased P segregation after annealing at 350 °C can provide a higher likehood of Cl^- adsorption to Co atoms due to the decreased interaction area of repulsive P than in the case of the as-deposited nanocrystalline Co-1.1P. Higher adsorption area by Cl^- can result in the increase of the inhibition effect previously mentioned. In the case of the samples annealed at 800 °C, the possibility of Cl^- adsorption to Co atoms increase further due to a further increased area taken by Co atoms on the metal surface. It is also expected that the dissolution of cobalt phosphides would be difficult due to the relatively strong nature of their covalent bonding. Therefore, the anodic dissolution of Co could be further restricted by the inhibition effect of Cl^-.

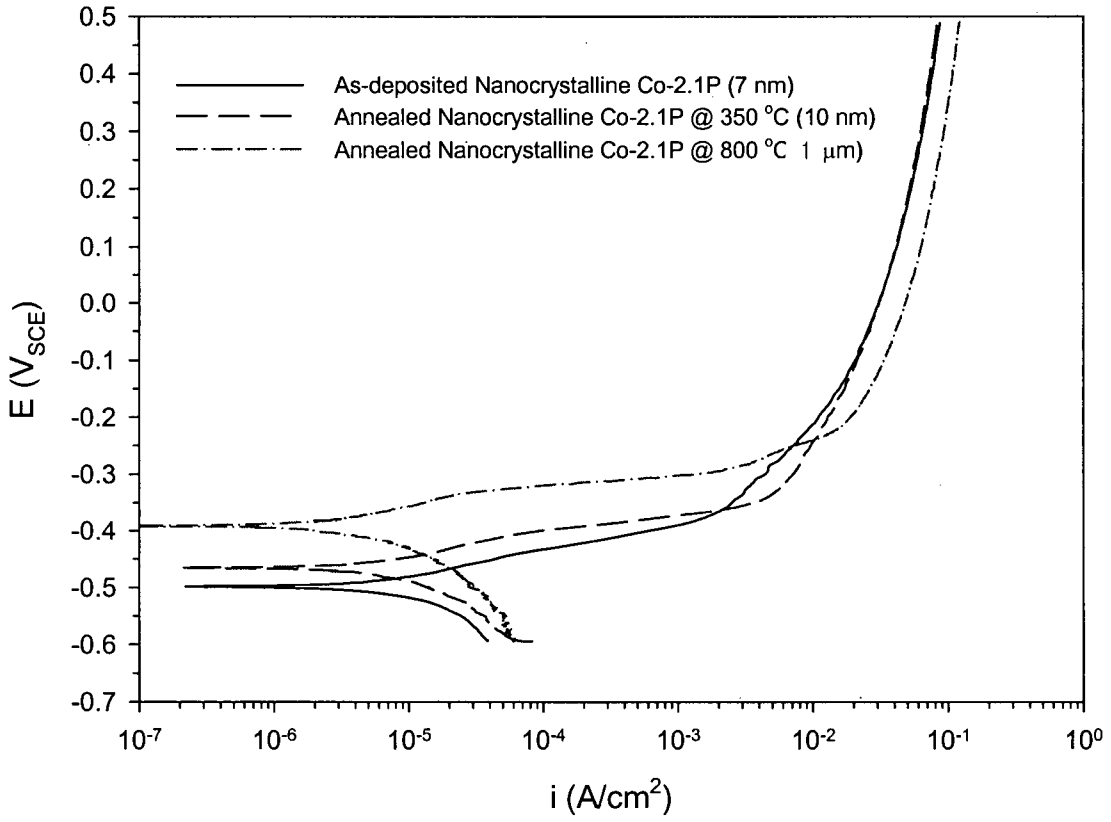

Figure 5-26 As-deposited and annealed nanocrystalline Co-2.1P in aerated 3.56 % NaCl solution at pH of 6.2 (scan rate=1mV/s).

A similar explanation along the lines of the different adsorption properties of Cl^- ions can also apply to cathodic reactions. In an aerated Cl^- containing solution, dissolved oxygen reduces to water or hydroxyl ion while consuming protons and electrons.

According to Coulomb's law, Cl^- ions can attract protons which are positively charged. Thus more adsorption of Cl^- on the surface can accelerate cathodic reaction. Moreover, negatively charged hydroxyl ions could be quickly removed from the surface because they carry the same charge as Cl^-. Thus, a higher concentration of adsorbed Cl^- on the surface can speed up the oxygen reduction reaction. This is the reason why higher O_2 reduction exchange current densities are observed on pure Co than on Co-P alloys, as shown in Table 5-5. In a suggested simple adsorption/reaction model, assumptions are made as

follows: first, the relative reactivity of adsorbed and dissolved oxygen and water on the surface are not changed or only changed insignificantly so as not to affect overall reaction rates; second, the surface defects (i.e., grain boundaries and triple junctions, etc.) and other possible variables on the surface are not considered.

It is clear that the grain size refinement results in increasing larger intercrystalline surface fractions. These intercrystalline defects can serve as an active site for the anodic dissolution of Co as shown in section 5.1. Therefore, nanocrystalline Co-P alloys, having a smaller grain size (10 nm), may exhibit higher dissolution rates than nanocrystalline Co (grain size of 20 nm) in the anodic dissolution regimes. This may not be true in a passivating system.

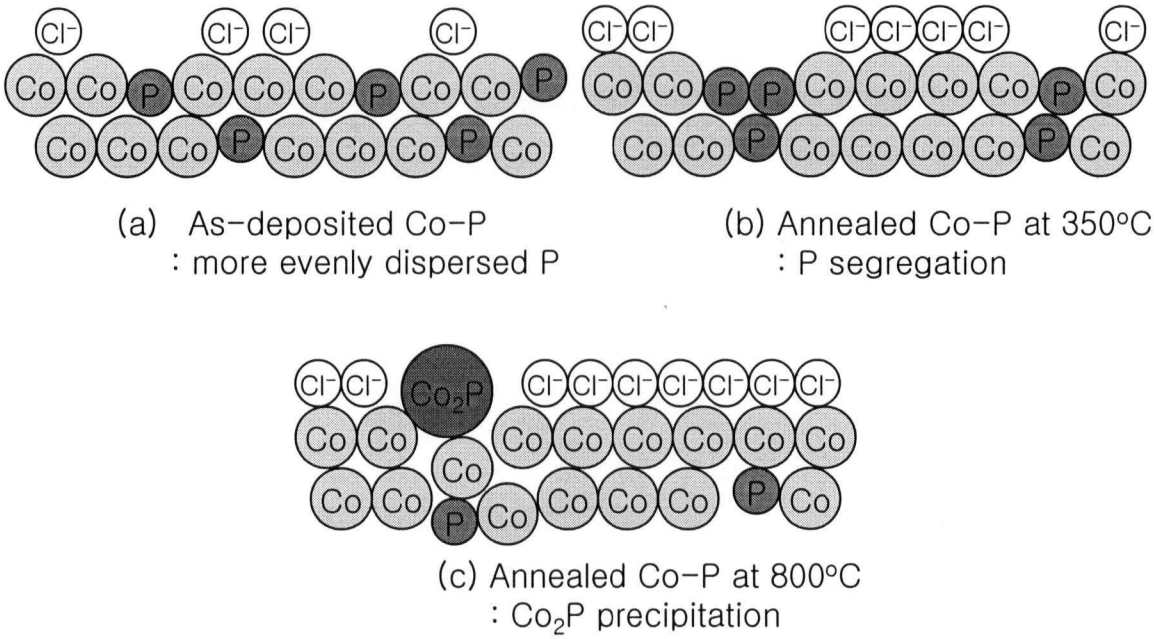

Figure 5-27 Schematic of physical models showing different adsorption characteristics of Cl⁻ ions due to different degrees of P segregation and precipitation in anodic dissolution process.

5.2.4 Summary

1. Both poly- and nanocrystalline Co displayed active dissolution behavior without clear passivation up to 0.5 V_{SCE}. Nanocrystalline Co has a very similarly shaped anodic curve to its polycrystalline Co counterpart, but the anodic current densities for nanocrystalline Co were higher than for polycrystalline Co. This finding was in agreement with the observations in acidic solution.

2. Nanocrystalline Co-P alloys, the polarization curves were shifted to more negative potentials and higher anodic current ranges than the curves for nanocrystalline Co. This indicated that alloying with P led to a decreased overall corrosion resistance. Based on previous experimental observations by other researchers and on the electronegativity of Co, P and Cl, it was considered that the increase in the anodic dissolution rate of nanocrystalline Co-P alloys is likely due to the reduced adsorption area of chloride anions on the electrode surface.

3. However, it was found that nanocrystalline Co-P showed a lower corrosion rate than that of nanocrystalline Co due to much smaller cathodic exchange current density for the oxygen reduction.

4. In the case of nanocrystalline Co-P alloys annealed at 350 °C and 800 °C, anodic polarization curves shifted to the more positive potentials and smaller current density ranges compared to the as-deposited state, indicating enhanced corrosion resistance by heat treatment. This response was more evident in nanocrystalline Co-2.1P than in nanocrystalline Co-1.1P.

5. This different response was explained through a physical model by considering the different adsorption properties of chloride ions on the electrode surface which resulted from the changes in the degree of P segregation in the nanocrystalline Co-P alloys.

5.3 Corrosion in Alkaline Solution

5.3.1 Potentiodynamic Polarization Behavior

5.3.1.1 Pure Co

Figure 5-28 presents typical potentiodynamic polarization curves obtained from pure Co samples in deaerated 0.1 M NaOH solution at room temperature.

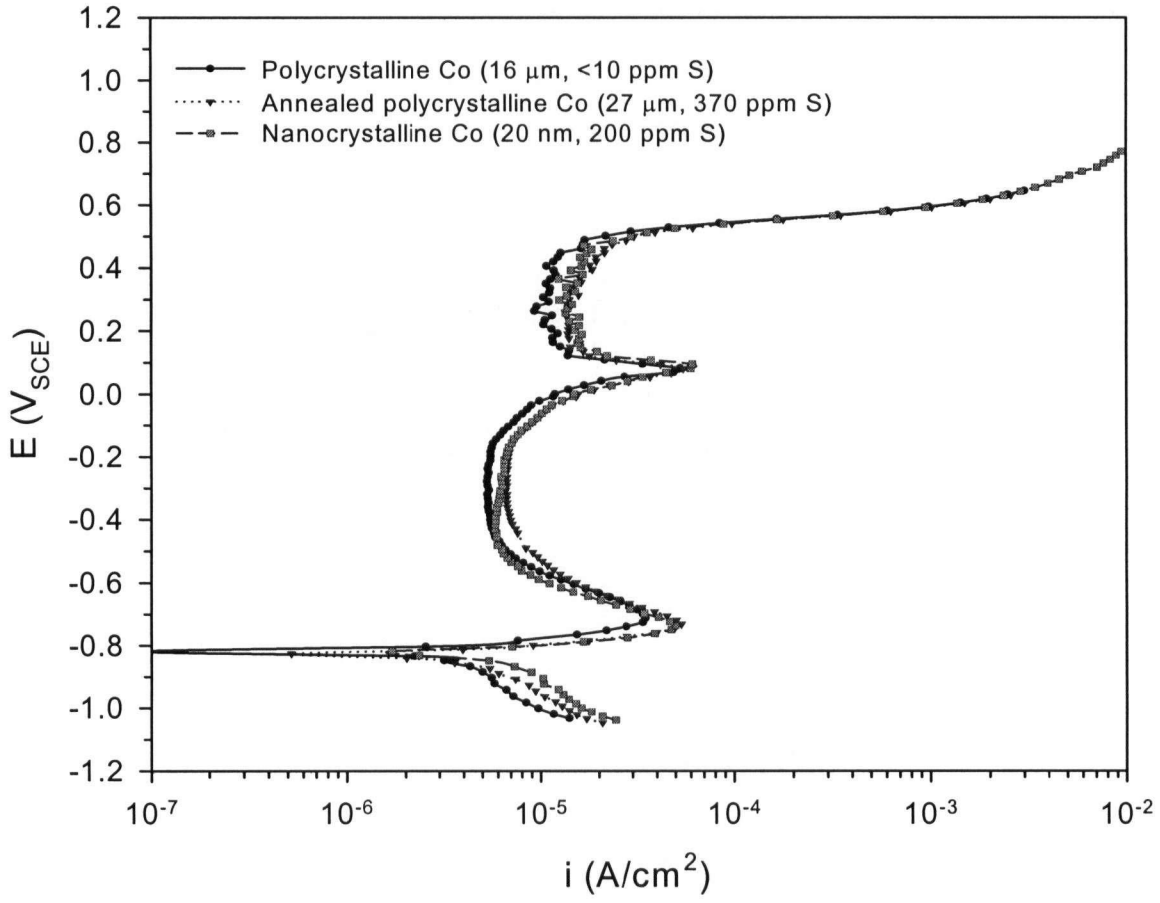

Figure 5-28 Anodic polarization curves of pure Co samples in deaerated 0.1 M NaOH solution at pH of 13 (scan rate=1mV/s).

These curves have qualitatively very similar behavior. Since the corrosion tests were conducted in deaerated solution, the only possible cathodic reaction is H_2 evolution from water reduction in the cathodic regions.

In the anodic regions, all tested samples showed classical active-passive-transpassive behavior with the onset of clear primary and secondary passivations occurring at -0.75 V_{SCE} and 0.07 V_{SCE}, respectively. These values are in good agreement with the findings reported by Tikkanen and Tuomine [1968] and Foelske, A. and Strehblow, H-H. [2000] observed in an anodic polarization study on conventional polycrystalline Co in Na_2SO_4 (pH=13.6) and 0.1 N NaOH, respectively, and also by Kim, S. H., et al [2003] for nanocrystalline Co in 0.1 M NaOH (see Figure 2-19b).

In the low anodic potential range, Co dissolution rate increased as the overpotential increased until the equilibrium solubility of Co^{2+} and/or $HCoO_2^-$ was reached in the solution. At the onset of primary passivation at the potential of -0.75 V_{SCE}, it is believed that the surface Co metal was covered with cobalt salts such as cobalt hydroxides and/or cobalt oxides that caused a drop in the dissolution rate at slightly higher potentials. The value of -0.75 V_{SCE} suggests that the drop in the dissolution current density is due to either or both of the following equilibrium reactions and the corresponding Nernst equations at pH=13 and 25 ^{o}C:

$$Co + 2H_2O = Co(OH)_2 + 2H^+ + 2e^- \quad (5\text{-}28)$$

$$E = +0.095 - 0.059\ pH = -0.672\ V_{SHE} = -0.913\ V_{SCE} \quad (5\text{-}29)$$

$$Co + H_2O = CoO + 2H^+ + 2e^- \quad (5\text{-}30)$$

$$E = +0.166 - 0.059\ pH = -0.601\ V_{SHE} = -0.842\ V_{SCE} \quad (5\text{-}31)$$

Considering the calculated equilibrium potentials for the formation of $Co(OH)_2$ and CoO, which is more negative than that of the primary passivation potential, these corrosion products can contribute to a significant reduction of the anodic dissolution rate. Since the hydroxide form has a more negative equilibrium potential than the oxide from, the formation

of $Co(OH)_2$ is to be the thermodynamically more favorable and this species is therefore likely to be the largest constituent of the passive film.

When the potential increased beyond these potential regions (e.g., -0.913 V_{SCE} or -0.842 V_{SCE}), $Co(OH)_2$ and CoO can be oxidized according to the following reactions and the corresponding Nernst equations at pH 13 and 298 K:

$$3Co(OH)_2 = Co_3O_4 + 2H_2O + 2H^+ + 2e^- \quad (5\text{-}32)$$

$$E = +0.993 - 0.059\ pH = +0.226\ V_{SHE} = -0.015\ V_{SCE} \quad (5\text{-}33)$$

$$3CoO + H_2O = Co_3O_4 + 2H^+ + 2e^- \quad (5\text{-}34)$$

$$E = +0.777 - 0.059\ pH = +0.01\ V_{SHE} = -0.231\ V_{SCE} \quad (5\text{-}35)$$

Even though no clear current peak was observed at the calculated potential values, it is expected that the oxidation process would form Co_3O_4 oxides. In the oxidation reactions of Eq.(5-32) and (5-34), the oxidation number of Co_3O_4 is 2.67, i.e., this oxide has a mixed valence state of Co^{+2} and Co^{+3} [Pourbaix, M., 1966].

At E = 0.07 V_{SCE}, a second current peak was observed. This is due to a further oxidation of the passive film leading to $Co(OH)_3$ and/or Co_2O_3 for which the possible equilibrium reactions are as follows:

$$Co_3O_4 + 5H_2O = 3Co(OH)_3 + H^+ + e^- \quad (5\text{-}36)$$

$$E = +1.018 - 0.059\ pH = +0.251\ V_{SHE} = 0.01\ V_{SCE} \quad (5\text{-}37)$$

$$Co(OH)_2 + H_2O = Co(OH)_3 + H^+ + e^- \quad (5\text{-}38)$$

$$E = +1.002 - 0.059\ pH = +0.233\ V_{SHE} = -0.008\ V_{SCE} \quad (5\text{-}39)$$

$$2Co_3O_4 + H_2O = 3Co_2O_3 + 2H^+ + 2e^- \quad (5\text{-}40)$$

$$E = +1.018 - 0.059\ pH = +0.251\ V_{SHE} = 0.01\ V_{SCE} \quad (5\text{-}41)$$

Above the transpassive potential (~0.52 V_{SCE}), the anodic current density was increased rapidly due to oxygen evolution as well as the formation of CoO_2 as follows:

$$4OH^- = O_2 + 2H_2O + 4e^- \quad (5\text{-}42)$$

$$E = +1.229 - 0.059\ pH = +0.776\ V_{SHE} = 0.526\ V_{SCE} \quad (5\text{-}43)$$

$$Co(OH)_3 = CoO_2 + H_2O + H^+ + e^- \quad (5\text{-}44)$$

$$E = +1.477 - 0.059\ pH = +0.71\ V_{SHE} = 0.469\ V_{SCE} \quad (5\text{-}45)$$

In summary, the overall shape of the potentiodynamic polarization curves for nanocrystalline Co is very similar to those of the other two polycrystalline Co samples including the corrosion potentials (E_{corr} = -0.82 V_{SCE}), primary and secondary passivation potentials, and the transpassive potential (E_{trans} = 0.52 V_{SCE}) as well as their two current peaks, i.e., about 50 and 70 $\mu A/cm^2$ at -0.75 V_{SCE} and 0.07 V_{SCE}, respectively, and the passivation current densities. Therefore, it is clear that the corrosion behavior of Co is not greatly affected by the grain size reduction.

5.3.1.2 Co-P alloys

Figure 5-29 presents potentiodynamic polarization curves for nanocrystalline Co-1.1P, nanocrystalline Co-2.1P and nanocrystalline Co in deaerated 0.1 M NaOH solution. The electrochemical parameters taken from the polarization curves are listed in Table 5-6.

Similar to nanocrystalline Co, nanocrystalline Co-P alloys exhibited active, passive, and transpassive polarization behavior, having the primary and secondary passivations. However, the passivation current densities in the primary and secondary passivation regimes increased gradually as the concentration of P content increased, indicating the less protective nature of the passive layers formed on the nanocrystalline Co-P alloys.

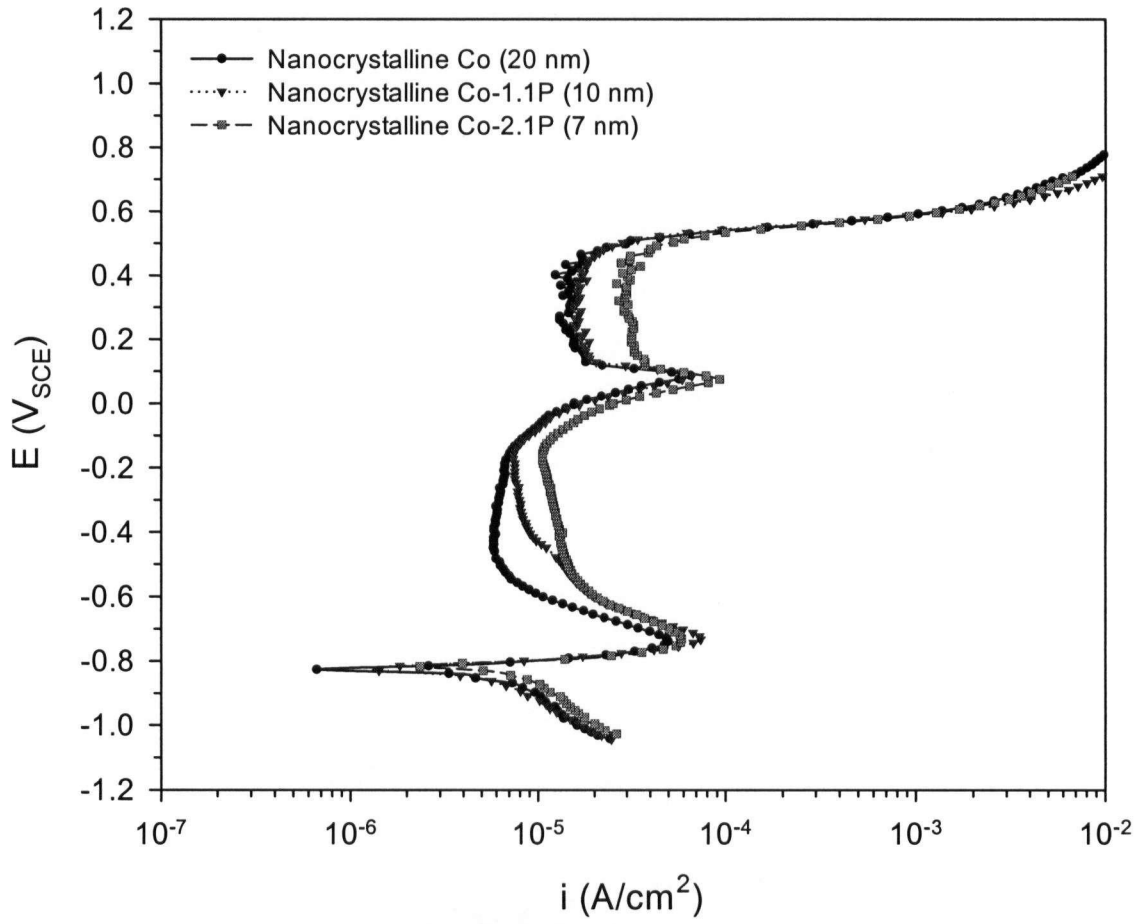

Figure 5-29 Potentiodynamic polarization curves of Nanocrystalline Co-1.1P and 2.1P alloys in deaerated 0.1 M NaOH solution at pH of 13 (scan rate=1 mV/s).

Table 5-6 Corrosion potential (E_{corr}) and corrosion current density (i_{corr}) taken from polarization data.

Sample	E_{corr} (V_{SCE})	i_{corr}*(A/cm^2)
Nanocrystalline Co (20 nm)	-0.824	6.67×10^{-6}
Nanocrystalline Co-1.1P (10 nm)	-0.820	8.10×10^{-6}
Nanocrystalline Co-2.1P (7 nm)	-0.814	1.56×10^{-5}

*Estimated by linear polarization methods in the range of ±10 mV at E_{corr}.

A similar effect of P alloying on passivation of nanocrystalline materials was previously reported by Rofagha, R. et al.[1993] (see Figure 2-20). They reasoned that P atoms served to prevent the formation of a protective passive film by blocking primary OH^- adsorption, the precursor to passive film formation. In an alkaline solution, the detrimental effects of P alloying were also observed in the electrodeposited Ni-2.9 wt% P [Flis, J., 1985] and the electrodeposited Co-4.7 wt% P [Gao, X. and Kowaka, M. 1991]. In these studies, both alloys showed higher passivation current densities than their pure metal counterparts.

In the current study, it is clear that P alloying to nanocrystalline Co leads to a higher passivation current and deteriorates the resistance of the passive films. This may be due to the same reasons mentioned above, i.e., the hindering role of surface P atoms in the formation of a protective passive film by blocking OH^- adsorption on the metal surface. As the P content increased, the corrosion current density increased and the corrosion potential shifted more positive potential as seen in Table 5-6. These different responses of nanocrystalline Co-P alloys are due to a higher cathodic reaction rate by the catalytic effect of P content on H_2 evolution reaction as explained in section 5.1.2.2.

5.3.2 Passive Film Characterization

5.3.2.1 Electrochemical Impedance Spectroscopy (EIS) Measurement

The passive film was characterized using impedance measurements at the primary and secondary passivation potentials. Figure 5-30a and b show the impedance spectra of all tested samples after potentiostatic polarization at -0.4 V_{SCE} and 0.3 V_{SCE} for 10 minutes, respectively.

In the case of poly- and nanocrystalline Co samples after potentiostatic polarization at -0.4 V_{SCE} as shown in Figure 5-30a, the spectra exhibited a partially resolved semicircle at high frequencies and Warburg type impedance with a straight line with the slope of about 45° at low frequencies.

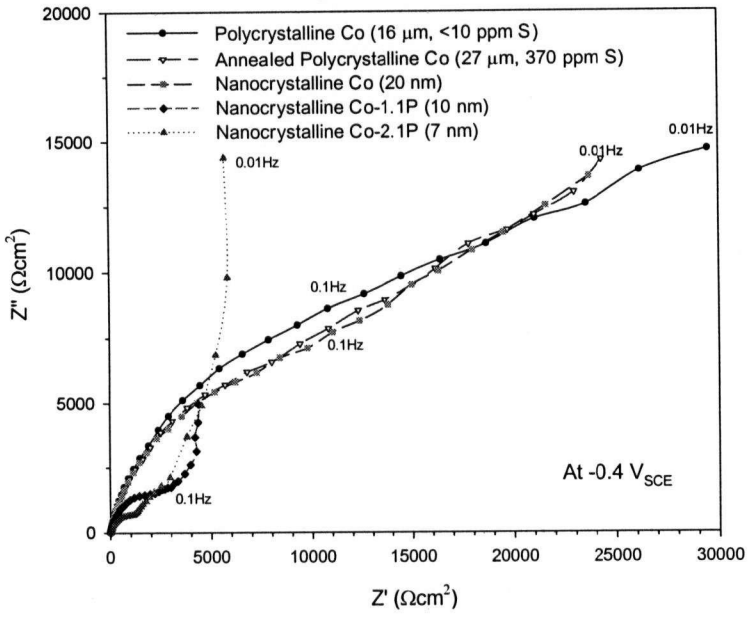

(a)

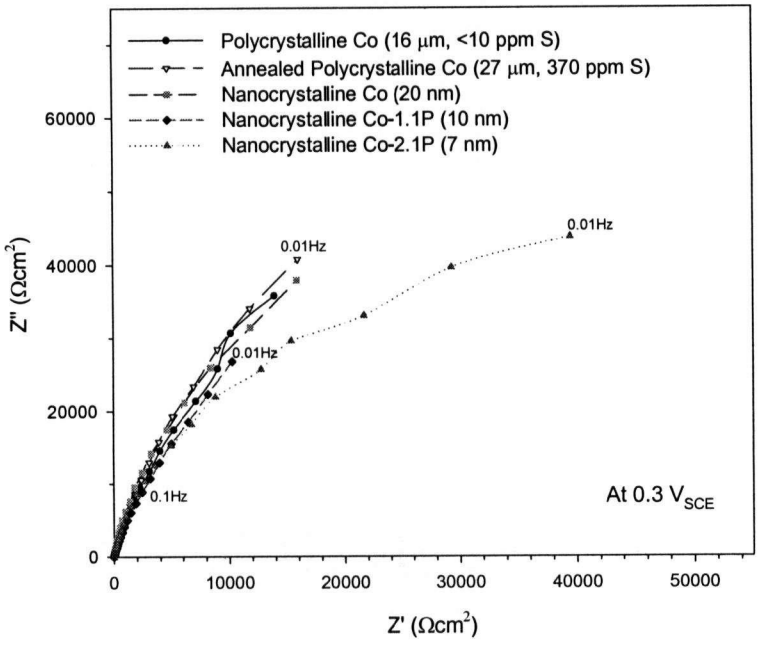

(b)

Figure 5-30 Nyquist plots of electrochemical impedance spectra recorded on all tested samples after potentiostatic polarization at (a) -0.4 V_{SCE} and (b) 0.3 V_{SCE} for 10 minutes.

Similar spectra were also observed for passive films on Ni and Type 304 stainless steel in borate (pH=8.7) and phosphate (pH=9.1) buffer solutions by Chao et al. [1982]. They argued that the semicircle at high frequencies was associated with the film-solution interface impedance as predicted by Armstrong and Edmondson [1973] and the Warburg-type impedance was apparently also associated with vacancy transport across the passive film.

However, Macdonald, D. D. [1990] has claimed that the contribution to the impedance from the reactions at the film-solution interface was negligible at frequencies above $\sim 10^{-10}$ Hz and, under these circumstances, the impedance at high frequencies arose entirely from the charge transfer reactions occurring at the metal-film interface and the impedance at low frequencies was associated with the movement of vacancies through the film.

Therefore, in the current study spectra were fit to a Randle's type circuit consisting of a passive film capacitance, Q_F in parallel with a passive film resistance, R_F, and Warburg impedance, Z_w (both in series)(see Figure 4-11b). The resultant values are listed in Table 5-7. In this electrical circuit, the passive film resistance includes both the metal-film interface impedance and the film-solution interface impedance. The passive film capacitance is mainly due to the space charged layer within the passive film.

Table 5-7 Impedance parameter values after potentiostatic polarization treatment for 10 minutes at -0.4 V_{SCE}.

Samples	Q_F (F/cm^2)	R_F ($k\Omega cm^2$)	σ ($k\Omega/s^{1/2}$)
Polycrystalline Co (16 μm)	6.12×10^{-5}	12.9	8.4
Annealed polycrystalline Co (27 μm)	6.24×10^{-5}	11.9	8.1
Nanocrystalline Co (20 nm)	6.53×10^{-5}	11.5	7.3
Nanocrystalline Co-1.1P (10 nm)	7.88×10^{-5}	2.3	1.2
Nanocrystalline Co-2.1P (7 nm)	1.03×10^{-4}	1.0	0.8

As shown in Table 5-7, the values of passive film resistance for the three different types of poly- and nanocrystalline Co samples are not much different and the resistance of nanocrystalline Co is smaller than those of the other two samples.

In the case of nanocrystalline Co-1.1P and nanocrystalline Co-2.1P, the size of the semicircles at high frequencies decreased remarkably compared to that of nanocrystalline Co and the passive film resistances reduced by a factor of 5 and 10 times, respectively. The different low frequency response, i.e., an almost vertical line or bending towards the negative real part, also indicates a porous film. This effect has been observed earlier in the case of Fe-Cr alloys in sulfuric acid solution and has been related to the pre-passivation process (i.e. a negative slope in the polarization curve) [Keddam, M. et al, 1986].

Therefore, it is clear that the P content on the metal surface deteriorates the protectiveness of the passive film formed on nanocrystalline Co-P and that this detrimental effect of P content on the passivation process is consistent with the results from potentiodynamic polarization tests.

A quantitative analysis of the Warburg impedance at low frequencies has been extensively studied by Chao et al. [1982] and Smedley, S. and D. D. Macdonald [1989] based upon the proposed point defect model for the growth of passive films. In this model, under certain conditions, the Warburg impedance was found to have the form as follows:

$$Z_W = \sigma\omega^{-1/2}(1-j) \qquad (5\text{-}46)$$

where the Warburg coefficient is $\sigma = \frac{\sigma_M \sigma_o}{\sigma_M + \sigma_o}$ (σ_M and σ_o : the Warburg coefficients for the movement of metal cation vacancies and oxygen anion vacancies, respectively), the angular frequency is $\omega = 2\pi f$ and j is the complex number, $\sqrt{-1}$.

By plotting the measured Z' against $\omega^{-1/2}$ for all tested samples, the Warburg coefficient, σ (defined as $dZ'/d\omega^{-1/2}$) can be obtained from the slope of the line as shown in

Figure 5-31 and the resultant values of the Warburg coefficient for all tested samples are listed in Table 5-7.

As shown in this Table, the values of the Warburg coefficient for poly- and nanocrystalline Co samples are similar, but, the Warburg coefficient decreased significantly with increasing P contents by a factor of 5 and 8 times for nanocrystalline Co-1.1P and 2.1P, respectively compared to that of nanocrystalline Co. Therefore, it is apparent that the high diffusion barrier resistances of poly- and nanocrystalline Co are deteriorated by the addition of P content due to the reduced Warburg coefficient.

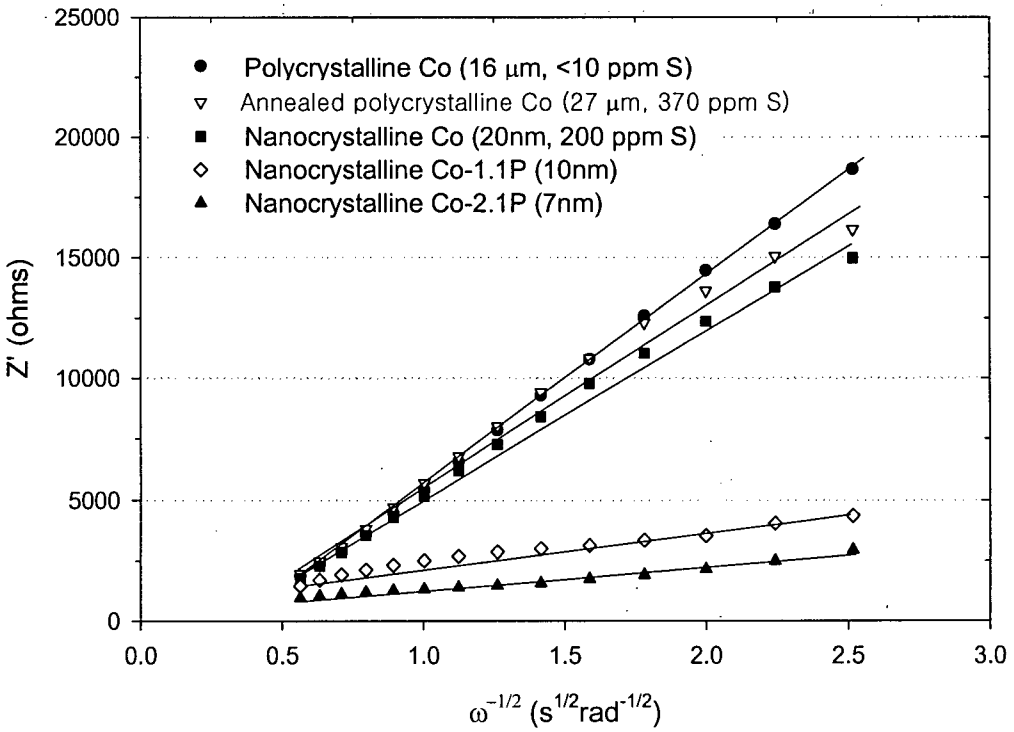

Figure 5-31 Dependence of Z' on $\omega^{-1/2}$ for all tested samples after potentiostatic polarization treatment for 10 minutes at -0.4 V_{SCE}.

Following potentiostatic polarization at 0.3 V_{SCE} for 10 minutes, the impedance spectra of all tested samples exhibited a large sized semicircle at high frequencies without clear evidence of Warburg impedance up to 10 mHz as shown in Figure 5-30b. Thus, the

simple Randle's circuit consisting of a passive film capacitance, Q_F in parallel with a passive film resistance, R_F was employed to fit the experimental data (see Figure 4-9a) and the resultant values are listed in Table 5-8.

Similar to the results from the impedance measurement at -0.4 V_{SCE}, the passive film resistances of poly- and nanocrystalline Co samples were higher than those of nanocrystalline Co-1.1P and nanocrystalline Co-2.1P alloys. It is also noteworthy that the measured values of the resistance at 0.3 V_{SCE} were much higher compared to those at -0.4 V_{SCE}. These different responses at -0.4 and 0.3 V_{SCE} can be due to the different nature of passive film (e.g. structure, chemical composition and thickness, etc.) formed at different potential ranges. Thus, it is expected that denser and/or thicker films can be formed at 0.3 V_{SCE} compared to the passive film formed at -0.4 V_{SCE}. According to thermodynamic calculations, corrosion products having a different valence state of cobalt such as bivalent (Co^{+2}) and trivalent (Co^{+3}) are favored at -0.4 V_{SCE} and 0.3 V_{SCE}, respectively. Compared to the density of the bulk material, the densities of more oxidized forms of cobalt oxides such as Co_3O_4 (6.1 g/cm^3) and Co_2O_3 (5.2 g/cm^3) are actually larger than that of $Co(OH)_2$ (3.6 g/cm^3) [CRC Handbook, 2004-05]. Thus, it is considered that the denser corrosion products formed at 0.3 V_{SCE} due to their larger value of density contributed to the enhanced resistances at 0.3 V_{SCE} compared to the resistance obtained at -0.4 V_{SCE}.

Table 5-8 Impedance parameter values after potentiostatic polarization treatment for 10 minutes at 0.3 V_{SCE}.

Samples	Q_F (F/cm^2)	R_F (kΩcm^2)
Polycrystalline Co (16 μm)	1.40×10^{-4}	149.6
Annealed Polycrystalline Co (27 μm)	1.59×10^{-4}	134.0
Nanocrystalline Co (20 nm)	1.69×10^{-4}	128.6
Nanocrystalline Co-1.1P (10 nm)	2.47×10^{-4}	117.2
Nanocrystalline Co-2.1P (7 nm)	2.78×10^{-4}	85.5

Since the passive film capacitance, Q_F due to the dielectric properties of the passive film is correlated to the passive film thickness (t_F) and the dielectric constant (ε) of the passive film, it can be expressed as [J. Bessone, et al., 1983]:

$$t_F = \frac{\varepsilon\varepsilon_o A}{Q_F} \tag{5-47}$$

where ε is the dielectric constant of the passive film, and ε_o are permittivity of free space (8.85×10^{-12} F/m) [CRC Handbook, 2004-05], and A is the surface area (0.9 cm^2). Taking ε = 12.9 for CoO [CRC Handbook, 2004-05] at -0.4 V_{SCE} and ε = 12.5 for Co_2O_3 [Wu, L., et al. 1983] at 0.3 V_{SCE}, the thickness of passive film formed at -0.4 V_{SCE} and 0.3 V_{SCE} was calculated and listed in Table 5.3.4.

At -0.4 V_{SCE}, the thickness for polycrystalline Co showed the highest value and the thickness decreased gradually with increasing S impurities. Further decrease of the thickness with increasing P contents was also observed on nanocrystalline Co-P alloys. As observed previously by Gudic, S. [2002], they found that the oxide resistance increased linearly with increasing the oxide thickness formed on Al and Al-Sn alloys at different anodic potential in a borate buffer solution (pH=7.8). Therefore, in the current study, the reduced thickness formed on nanocrystalline Co-P alloys contributed to the decrease of the passive film resistance assuming that the structure and chemical composition of the film for all tested samples was similar.

In the secondary passivation potential ranges, more oxidized and denser corrosion products are favored as discussed previously. In Table 5-9, it is observed that the thickness formed at 0.3 V_{SCE} is commonly smaller than that formed at -0.4 V_{SCE}. When we consider the much larger film resistance measured at 0.3 V_{SCE} compared to that measured at -0.4 V_{SCE} (see Table 5-7 and 5-8), it is clear that the passive film formed at 0.3 V_{SCE} has a more dense structure and therefore that the passive film formed -0.4 V_{SCE} is more porous. Similarly to the effects of P alloying observed at -0.4 V_{SCE}, the increase of P contents lead to a further decrease of thickness at 0.3 V_{SCE}.

Table 5-9 Thickness of the passive film for the tested samples after potentiostatic polarization treatment for 10 minutes at -0.4 and 0.3 V_{SCE}.

Samples	Thickness, t (nm)	
	-0.4 V_{SCE}	0.3 V_{SCE}
Polycrystalline Co (16 μm)	16.8	7.1
Annealed Polycrystalline Co (27 μm)	16.5	6.3
Nanocrystalline Co (20 nm)	15.7	5.9
Nanocrystalline Co-1.1P (10 nm)	13.0	4.0
Nanocrystalline Co-2.1P (7 nm)	10.0	3.6

In summary, the passive film resistances of poly- and nanocrystalline Co showed higher values than those of nanocrystalline Co-P alloys measured both at -0.4 V_{SCE} and 0.3 V_{SCE}. It was also demonstrated that the resistance measured in the secondary passivation potential ranges (e.g. 0.3 V_{SCE}) was much higher than that measured in the range of the primary passivation potential (e.g. -0.4 V_{SCE}) and that the enhanced resistance was due to different nature of the passive film, i.e. the passive film formed at 0.3 V_{SCE} was denser and thinner than the passive film formed at -0.4 V_{SCE}.

5.3.2.2 Corrosion Morphologies

Unlike at lower pH where all tested samples showed extensive surface dissolution, identifiable morphology was observed on nanocrystalline Co and nanocrystalline Co-1.1P SEM micrographs taken after potentiostatic polarization treatment for 10 minutes at -0.4 V_{SCE} as shown in Figure 5-32 at low and high magnification.

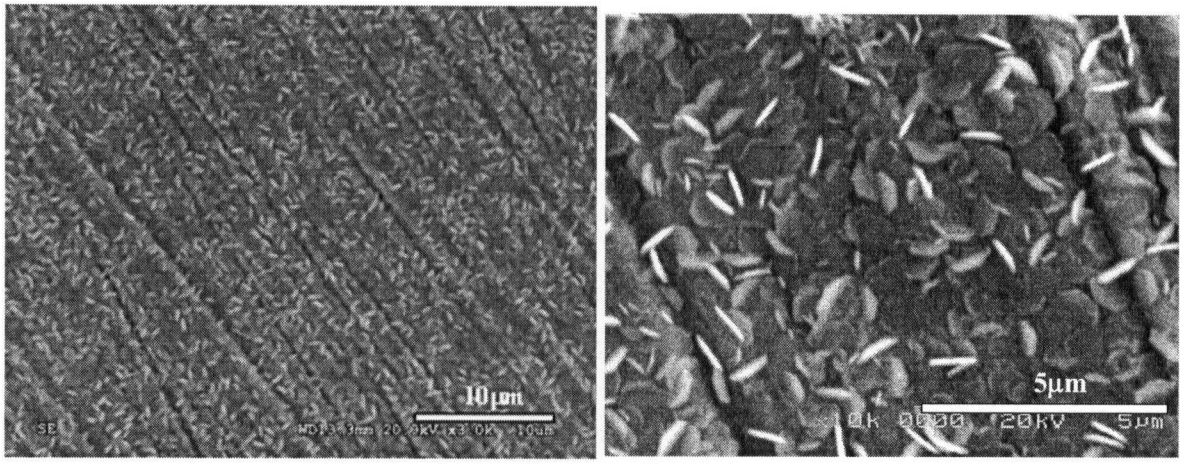

(a) (b)

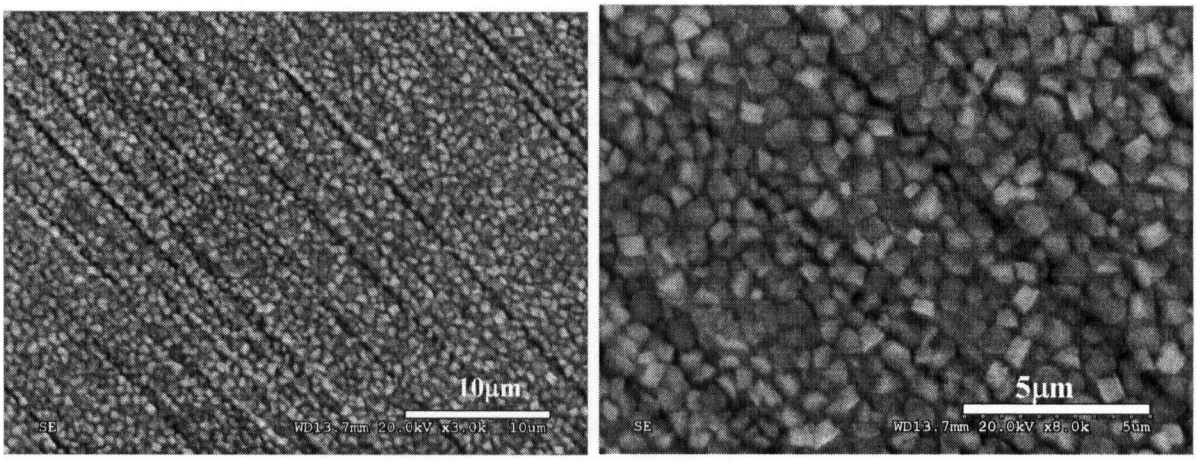

(c) (d)

Figure 5-32 Typical corrosion morphology at (a) low & (b) high magnification for nanocrystalline Co; and at (c) low & (d) high magnification for nanocrystalline Co-1.1P, taken after potentiostatic polarization treatment for 10 minutes at -0.4 V_{SCE} in deaerated 0.1 M NaOH solution.

The corroded surface for both samples contained fine reaction products which appeared to be oxide and/or hydroxide layers (in actual, confirmed by XPS analysis in the following section). The morphologies for polycrystalline Co and annealed polycrystalline Co samples were very similar to that of nanocrystalline Co (Figure 5-32a and b), however, nanocrystalline Co-P alloys were quite morphologically different.

As shown in Figure 5-32c and d at different magnifications, the corrosion products formed on the surface of nanocrystalline Co-1.1P have discontinued and irregular cylindrical shapes and the corroded surface appears porous while the corrosion morphology for nanocrystalline Co shows less porosity. These different corrosion morphologies may support the findings that the film resistance for nanocrystalline Co-P alloys was smaller than that of nanocrystalline Co due to their more defective structure.

5.3.2.3 X-ray Photoelectron Spectroscopy (XPS)

Passive layers on polycrystalline Co, nanocrystalline Co, and nanocrystalline Co-1.1P were prepared under potentiostatic polarization control in deaerated 0.1 M NaOH and examined with XPS. Figure 5-33 and 5-34 present some Co 2p and O 1s spectra obtained at -0.4 V_{SCE} and 0.3 V_{SCE} of the applied potential for 10 minutes, respectively. In particular, it is noticeable that the P 2p peak from the P content was not detected in nanocrystalline Co-1.1P.

In Figure 5-33, all measured Co 2p and O 1s spectra of the above three different samples exhibit a strong peak at 796.5 eV and 531.3 eV, respectively. These binding energies have been shown to be associated with Co^{+2} and OH^-, respectively.

As one can expect from the polarization curves as well as the thermodynamic prediction at low anodic potential, the passive layer consists of mainly cobalt hydroxide, $Co(OH)_2$ and there is no clear evidence of the formation of CoO at -0.4 V_{SCE}. This species (i.e., $Co(OH)_2$) has been observed by A. Foelske and H-H Strehblow [2002]. They found fairly similar XPS spectra for a passivated pure Co (no grain size given) in 0.1 M NaOH and

the passive layer consisted of pure $Co(OH)_2$ having a thickness of >15 nm after 5 minutes of passivation in the primary passivation potential range.

As the typical electron penetration depth of the X-ray beam ranges from 1 nm to 10 nm, it is considered that the thickness of the passive layer consisting of $Co(OH)_2$ is thicker than 10 nm because no contribution of Co^0 at 793.2 eV corresponding to the binding energy of metallic cobalt from the metal substrate was detected. This range of thickness can be partly verified by the estimated thickness from impedance measurements at the same potential (see Table 5-9).

At the secondary passivation potential (e.g., 0.3 V_{SCE}), the Co 2p spectra show a broader binding energy range which is likely due to multiplet splitting which can be resolved as having two major peaks at 794.8 eV and 796.5 eV corresponding to Co^{+3} and Co^{+2}, respectively, as well as a minor peak at 793.2 eV as shown in Figure 5-34.

The former major peak at 794.8 eV could be associated with Co_2O_3 and $Co(OH)_3$ as well as Co_3O_4. For the O 1s spectra, all three samples show two well resolved peaks at 529.5eV and 531.3 eV which can be assigned to the oxygen in O^{2-} ions and in OH^- ions, respectively, as well as $O^{2-(spin)}$ peak at 530.4 eV from Co_3O_4 spinel structure [Jean-Charles Dupin, et al., 2002, Foelske, A. and H-H Strehblow, 2002].

It is known that Co_3O_4 has a normal spinel structure in which magnetic cobaltous ions are located at the tetrahedral sites and the diamagnetic cobaltic ions at the octahedral sites [Miyatani, K. K. et al., 1966]. Considering the equilibrium reactions in the secondary passivation potentials as indicated by the above reaction equations (Eq.(5.36) and(5.40)), a further oxidation of Co_3O_4 leads to rather complex compounds consisting of Co_3O_4, Co_2O_3 and $Co(OH)_3$. The formation of a closed and protecting species such as Co_3O_4 and Co_2O_3 apparently leads to a decrease of the layer thickness by observation of an appreciable contribution of the Co^0 peak at 793.2 eV.

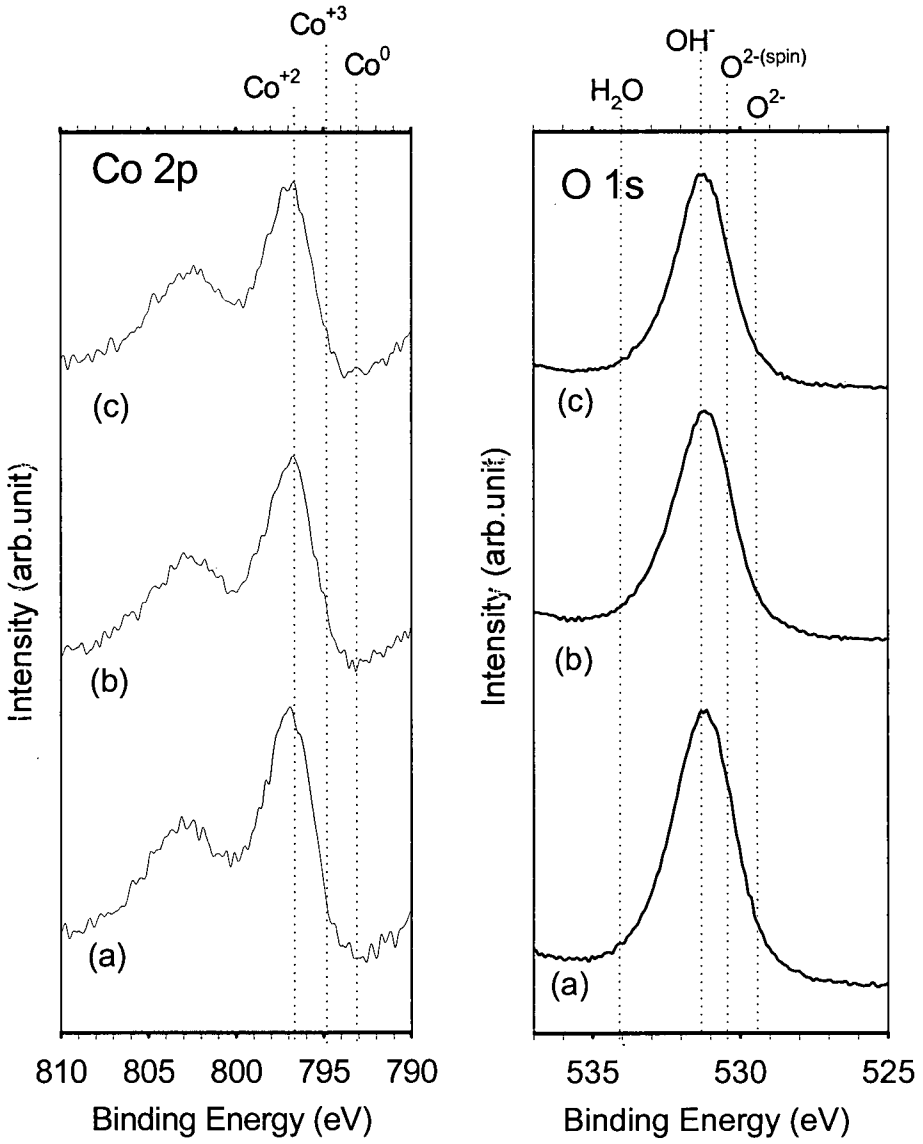

Figure 5-33 Co 2p and O 1s spectra obtained from the surface of (a) polycrystalline Co, (b) nanocrystalline Co, and (c) nanocrystalline Co-1.1P after potentiostatic polarization treatment for 10 minutes at -0.4 V_{SCE} in deaerated 0.1 M NaOH solution at pH of 13.

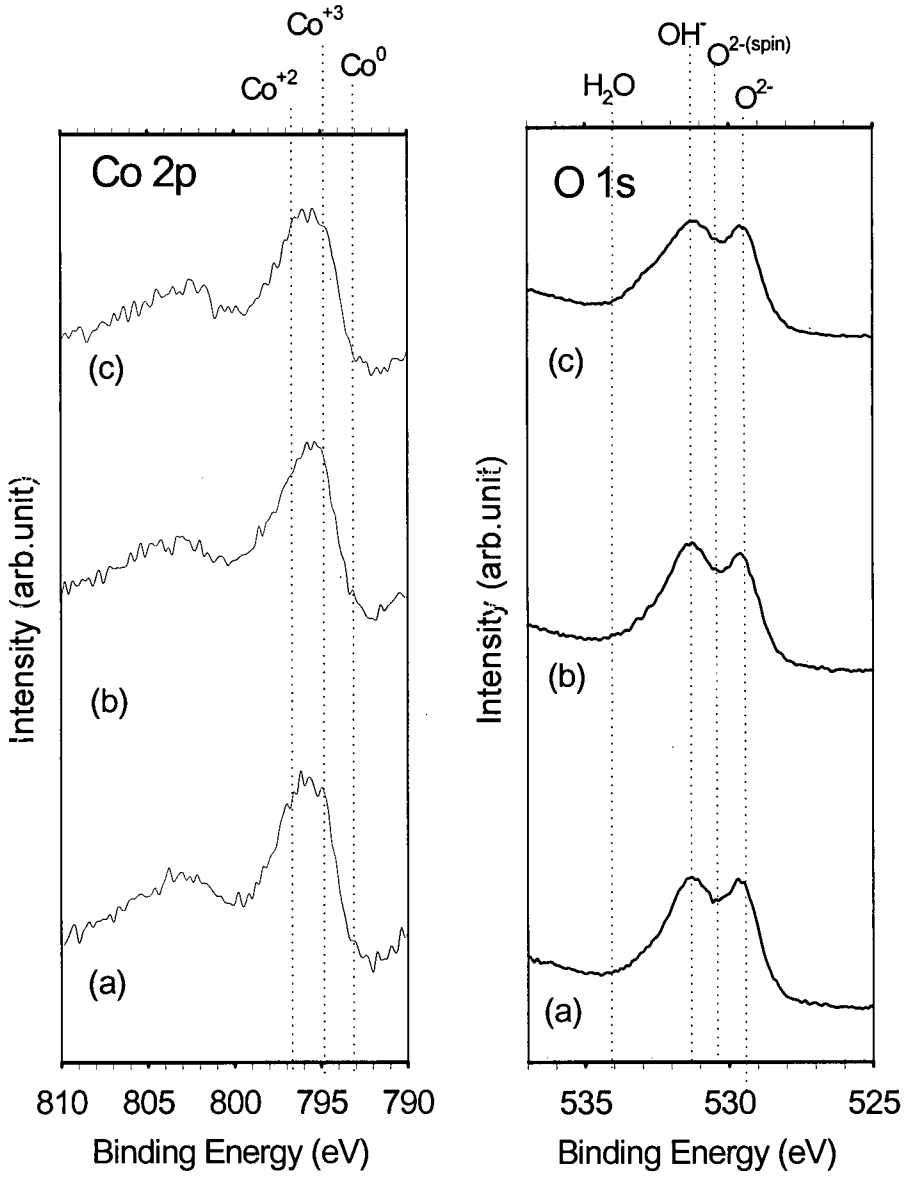

Figure 5-34 Co 2p and O 1s spectra obtained from the surface of (a) polycrystalline Co, (b) nanocrystalline Co, and (c) nanocrystalline Co-1.1P after potentiostatic polarization treatment for 10 minutes at 0.3 V_{SCE} in deaerated 0.1 M NaOH solution at pH of 13.

5.3.3 Effects of Heat Treatment on Polarization Behavior of Nanocrystalline Co-P Alloys

Figure 5-35 shows typical potentiodynamic polarization curves for as-deposited and annealed nanocrystalline Co-1.1P samples in deaerated 0.1 M NaOH solution.

Polarization behaviors of two samples annealed at 350 °C and 800 °C were not much different to that of the as-deposited state and showed classical active-passive-transpassive polarization behavior. However, both annealed samples had lower passivation current densities in the primary and the secondary passivation regions than the as-deposited sample. This different behavior of the annealed samples is correlated to different adsorption behavior due to the different degree of P segregation and precipitation resulting from the annealing treatments. Therefore, a similar explanation with respect to the different adsorption properties of Cl^- ions, as previously described in section 5.2.3, may apply to OH^- ions because they have the same charge.

In the case of the annealed sample at 350 °C, the increased P segregation can provide a higher possibility of OH^- adsorption to Co atoms on the metal surface compared to the as-deposited state. Thus, the formation of a passive film on the annealed sample at 350 °C could be easier due to a higher adsorption area of OH^-. For the annealed sample at 800 °C, the possibility of OH^- adsorption to Co atoms further increases due to an increased area fraction of Co atoms on the metal surface. This may explain the very similar ranges of the passivation current densities for both nanocrystalline Co and nanocrystalline Co-1.1P annealed at 800 °C (see Figure 5-29 and 5-35). The enhanced corrosion resistance of the annealed samples was also confirmed through impedance spectra as shown in Figure 5-36. In particular, the impedance spectra of the annealed sample at 800 °C was almost identical to the impedance spectra obtained for nanocrystalline Co (see Figure 5-30a).

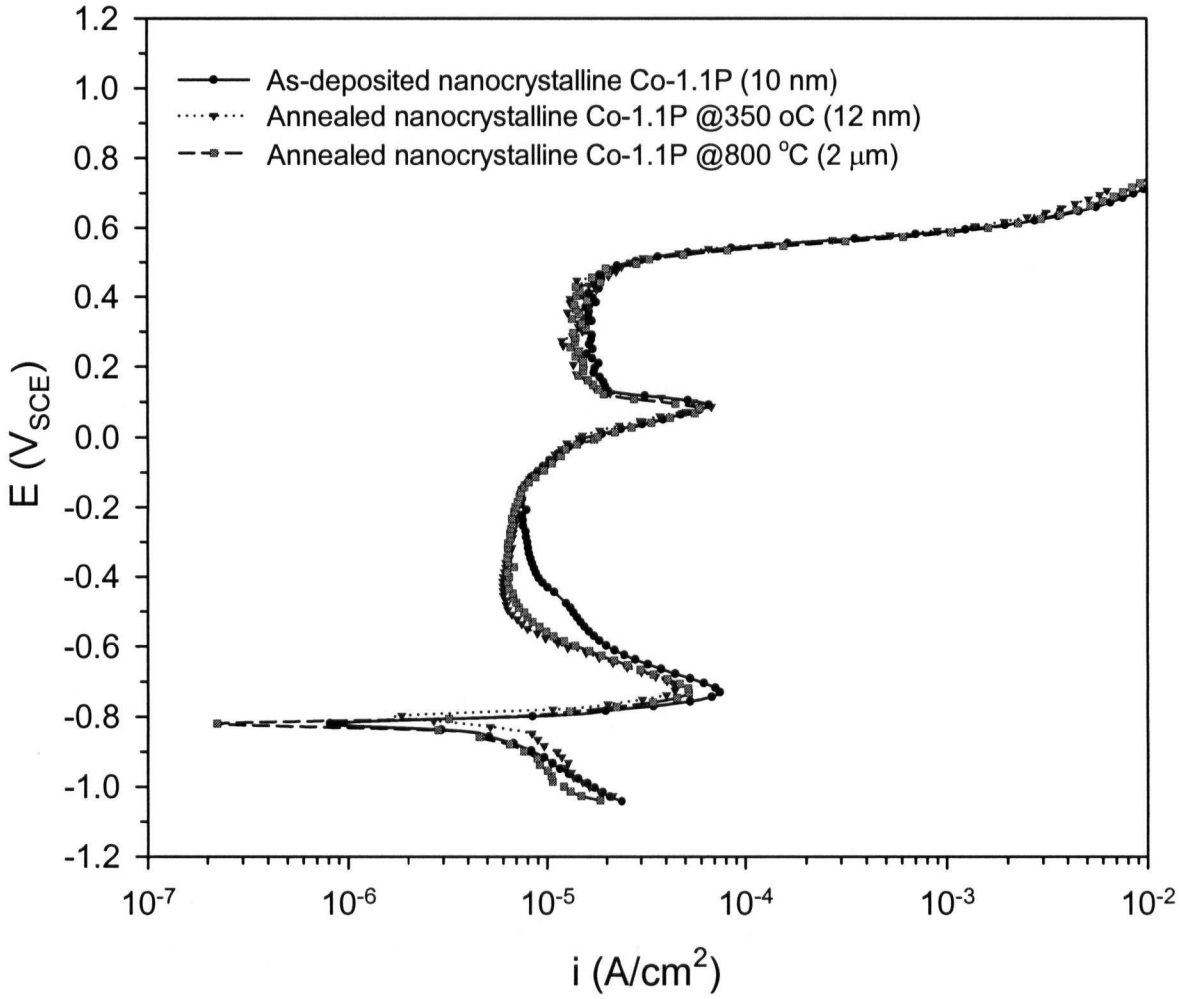

Figure 5-35 Potentiodynamic curves for as-deposited and annealed nanocrystalline Co-1.1P samples in deaerated 0.1 M NaOH solution at pH of 13 (scan rate=1mV/s).

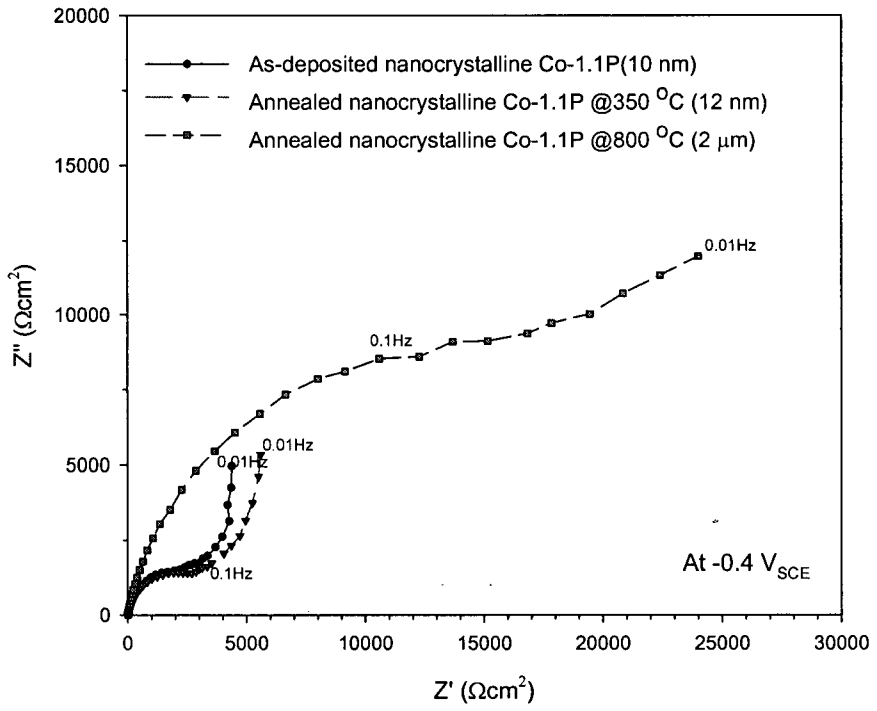

Figure 5-36 Nyquist plots of electrochemical impedance spectra recorded on as-deposited and annealed nanocrystalline Co-1.1P samples after potentiostatic polarization at -0.4 V_{SCE} for 10 minutes.

5.3.4 Summary

1. All investigated Co and Co-P samples exhibited classical active-passive- transpassive behaviors with the onset of clear primary and secondary passivation occurring at about -0.75 V_{SCE} and 0.07 V_{SCE}, respectively, in 0.1 M NaOH solution at pH of 13.

2. Anodic polarization curves of poly- and nanocrystalline Co had qualitatively very similar behavior including anodic and passive current densities. Therefore, it is evident that the corrosion behavior of pure cobalt is not greatly affected by grain size reduction.

3. However, P alloying lead to higher passivation current densities in the primary and secondary passivation ranges. By extracting the impedance parameters from a Randle's type circuit model, it was clearly demonstrated that the values of both the passive film resistance and thickness for nanocrystalline Co-P alloys were smaller than those for

poly- and nanocrystalline Co.

4. XPS analysis revealed that the passive film formed in the primary passivation range (e.g., -0.4 V_{SCE}) consisted of mainly $Co(OH)_2$ having a thickness of >10 nm and the passive film formed in the secondary passivation range (e.g., 0.3 V_{SCE}) consisted of rather complex compounds such as Co_3O_4, Co_2O_3, $Co(OH)_3$ and $Co(OH)_2$ with a thickness of <10 nm.

5. Both annealed nanocrystalline Co-P samples at 350 °C and 800 °C had lower passivation current densities in the primary and the secondary passivation regions than the as-deposited sample. This different behavior of the annealed samples is correlated to different OH^- adsorption to Co atoms on the metal surface due to the different degree of P segregation and precipitation resulting from the annealing treatments

6 Conclusions

This study was concerned with the corrosion properties of nanocrystalline Co and Co-1.1 and 2.1 wt% P alloys (grain sizes of 7 to 20 nm) prepared by electrodeposition in a wide range of solution pH ranging from 1 to 13. By using annealed nanocrystalline samples, an attempt was made to separate the effects of grain size reduction, P alloying and heat-treatment in these materials and summaried in Table 6-1. From this study, the following conclusions can be drawn.

Table 6-1 Summary of the effects of grain size reduction, P alloying and heat treatment on the corrosion properties of nanocrystalline Co and Co-P alloys

Solution (pH)	Parameter	Grain size reduction (for pure Co)	P alloying (1.1 & 2.1 wt%)	Heat-treatment @ 350 & 800°C
0.1M H_2SO_4 0.5M Na_2SO_4 (pH=1 & 3)	Anodic current density	Increased	Decreased	Increased
3.56 wt% NaCl (pH=6.2)	Anodic current density	Increased	Increased	Decreased
0.1M NaOH (pH=13)	Passivation current density	Similar	Increased	Decreased

In deaerated acidic solutions

The grain size reduction led to an increase in the anodic dissolution rate due to a significant increase of intercrystalline defects by nanoprocessing, but nanocrystalline Co showed reduced localized attack. In particular, a catalytic charge transfer mechanism for the anodic dissolution process of poly- and nanocrystalline Co has been identified as a more favorable route than the non-catalytic consecutive charge transfer mechanism. The

comparative dissolution kinetics between poly- and nanocrystalline Co were also quantified in terms of the reduced activation energy due to the stored excess free energy of nanocrystalline Co. By alloying with 1.1 and 2.1 wt% P, the corrosion resistance for nanocrystalline Co-P alloys increased significantly, i.e., an ennoblement of the corrosion potential and a reduced anodic dissolution rate due to the increased elemental P concentration on the corroded surface were observed at open circuit potential. P alloying played a more important role than grain size reduction in the anodic dissolution reaction of the nanocrystalline Co-P alloy system. After heat-treatment at elevated temperatures (e.g., 350 °C and 800 °C), the excellent corrosion resistance of nanocrystalline Co-P alloys deteriorated due to their higher chemical heterogeneity (e.g., different degree of P segregation and second phase precipitates).

In the aerated 3.56 % NaCl solution

The anodic current densities for nanocrystalline Co were higher than for polycrystalline Co, in agreement with the observations in acidic solution, and without clear passivation up to 0.5 V_{SCE}. On the contrary to the reduced anodic current density in acidic solution, addition of P led to an increase in the anodic dissolution rate due to the reduced chloride adsorption on the electrode surface. It was found however that nanocrystalline Co-P showed a lower corrosion rate than that of nanocrystalline Co due to much smaller cathodic exchange current density for the oxygen reduction. In the case of nanocrystalline Co-P alloys annealed at 350 °C and 800 °C, anodic polarization curves shifted to the more positive potentials and smaller current density ranges compared to the as-deposited state, indicating enhanced corrosion resistance by heat treatment. This different response was explained through a physical model by considering the different adsorption properties of chloride ions on the electrode surface which resulted from the changes in the degree of P segregation and 2^{nd} phase precipitates (e.g., Co_2P) in the nanocrystalline Co-P alloys.

In a deaerated alkaline solution

Potentiodynamic polarization tests showed that the corrosion behavior of pure cobalt

is not greatly affected by grain size reduction. Anodic polarization curves of poly- and nanocrystalline Co had qualitatively very similar behavior including anodic and passive current densities. However, P alloying led to higher passivation current densities in the primary and secondary passivation ranges indicating a more important role of P alloying than grain size reduction. By XPS analysis, it was revealed that the passive film formed in the primary passivation range consisted of mainly $Co(OH)_2$ having a thickness of >10 nm and the passive film formed in the secondary passivation range consisted of rather complex compounds such as Co_3O_4, Co_2O_3, $Co(OH)_3$, and $Co(OH)_2$ with a thickness of <10 nm. Both annealed nanocrystalline Co-P samples at 350 °C and 800 °C had lower passivation current densities in the primary and the secondary passivation regions than the as-deposited sample. This different behavior of the annealed samples is correlated to different OH^- adsorption to Co atoms on the metal surface due to the different degree of P segregation and precipitation resulting from the annealing treatments.

Major contributions to the related field

The effects of grain size reduction, P alloying, and heat-treatment on the corrosion properties of nanocrystalline Co and Co-1.1 and 2.1P alloys (grain sizes of 7 to 20 nm) in a wide range of solution pH were evaluated by using a variety of electrochemical measurement techniques and surface analysis. The results from this study are surely useful for the design of nanostructured materials for applications requiring wear and corrosion resistance.

Most results in the current study are essentially new. The following aspects are unique:

- Identification of the anodic dissolution and passivation mechanisms for nanocrystalline Co and Co- P alloys.
- Quantitative evaluation of the kinetics for active dissolution of poly- and nanocrystalline Co in terms of their different activation energies.
- Suggestion of several atomic physical models (dealloying process, different chloride adsorption properties, etc) as well as a morphological model (e.g., different corrosion morphologies).
- Proposition of a modified E-pH diagram for the nanocrystalline Co-water system.

7 Recommendations for Future Work

As introduced in Chapter 1, nanocrystalline Co and Co-P alloys have been identified as candidate materials for the replacement of hexavalent chromium coatings in wear and corrosion resistant applications. In particular, as the hardness of nanocrystalline Co-P alloys increased with increasing P concentration (Figure 1-2), corrosion studies for such nanocrystalline Co-P alloys containing high bulk P concentrations (e.g., $\geq$ 5.2 wt%) in a wide variety of solution pH will be essential for practical application of these materials as well as for the development of a further understanding of the corrosion behavior of nanocrystalline materials in general.

Depending on the solution, the effect of P alloying in nanocrystalline Co-P alloys has resulted in different corrosion responses. For example, alloying with P resulted in a detrimental effect in a chloride containing solution (3.56 % NaCl) while the beneficial effect were seen in acidic solutions (0.1 M H_2SO_4 and 0.5 M Na_2SO_4). As it was pointed out in section 5.2.1, it seems somewhat improper to compare these results directly because the two sets of test results were obviously performed in different solutions at different pH and at different concentrations of dissolved O_2. Therefore, corrosion tests under environments as similar as possible (e.g., 0.1 M H_2SO_4 and 0.1 M HCl) may be needed to better understand the different effects of P on the corrosion behavior of nanocrystalline Co and Co-P alloys in aqueous solutions.

In an alkaline solution, passive film characterization using XPS analysis to determine the chemical composition, structure and thickness of the film formed on poly- and nanocrystalline Co and Co-P alloys was not conclusive. Thus, AES depth profiling would be needed for a more accurate characterization.

To our knowledge, the current study is the first to present the anodic dissolution mechanism and detailed kinetics for the corrosion of nanocrystalline Co and Co-P alloys. For a further understanding of the electrochemical reactions for these advanced materials, the use of advanced in-situ STM is strongly recommended.

8 References

Aledresse, A., Alfantazi, A., J. Mater. Sci., 39 (2004) p.1523.

Alfantazi, A. and Erb., U., J. Mater. Sci. Lett. 15 (1996) p.1361

Allgaier, W. and Heusler, K. E., J. Appl. Electrochem. 9 (1979) p.155

Armijo, J. S., Corrosion, 24(1) (1968) p.24.

Armstrong, R. D. and K. Edmondson, Electrochim Acta, 18 (1973) p.937

Asami, K., B-P. Zhang, M. Mehmood, H. Habazaki and K. Hashimoto, Scripta mater., 44 (2000) p.655

ASM Handbook, Volume 3, "Alloy Phase Diagrams", ASM Materials Park, Ohio (1992)

ASM Handbook, Volume 13B, "Corrosion: Materials", ASM Materials Park, Ohio (2003)

Aus, M. J., Cheung, C., Szpunar, B. and Erb, U., J. Materials Science Letter, 17 (1998) p.1949

Awad, G. H., Proceedings of the 6th European Symposium on Corrosion Inhibitors (6SEIC) Ann. Univ. Ferrara, N. S., Sez., V, Suppl. 8, (1985) p.359

Badawy, W.A., F. M. Al-Kharafi and J. R. Al-Ajmi, J. Applied Electrochemistry, 30 (2000) p.693

Barbucci, A., Farne, G., Matteazzi, P., Riccieri, R., Cerisola, G., Corrosion Science, 41(1999) p.463

Barton, S. F., Handbook of X-Rays, McGraw-Hill, New York, (1967) 17-1 ~ 17-18

Bechet, B., Epeboin, I., and Keddam, M., J. Electroanl. Chem., 76 (1977) p.129

Benea, L, Bonora, P. L., Borello, A. and Martelli, S., Wear, 249 (2002) p.995

Bessone, J., C. Mayer, Juttner, and W.J. Lorenz, Electrochim. Acta 28 (1983) p.171

Betteridge, W., "Cobalt and its alloys", Ellis Horwood ltd., (1982)

Bockris, J. O' M, D. Drazic and A. D. Despic, Electrochim. Acta 4 (1961) p.325

Bockris, J. O' M. and Drazic, D., Electrochim. Acta. 7 (1962) p.293

Bonhoeffer, K. F. and Heusler, K. E., Phys. Chem., 61 (1957) p.122

Boukamp, B. A., Equivalent-Users Manual, Computer Assisted Electrochemical as-Impedance Data Analysis System, Univ. of Twente, April (1993)

Briant, C. L., Corrosion, 36(9) (1980) p.497.

Burke, L. D., Casey, D. P. O'Connel, A. M., Nagle, L. C., Proceedings of the 201st Meeting of the Electrochemical Society, Philadelphia, Abstract No.330, May (2001)

CRC Handbook of Chemistry and Physics, 85th ed., 2004-05

Chao, C. Y, L. F. Lin, and D. D. McDonald, J. Electrochem. Soc. 129 (1982) p.1874

Cheung, C., D. Wood and U. Erb, "Processing and properties of nanocrystalline materials", TMS (1996) p.479

Choi, Pyuck-Pa, Ph.D. Thesis, University Gottingen, (2003) Chapter 5

Cowling, R. D. and Riddiford, A.C., Electrochim. Acta, 14 (1969) p.981

Creason, S. C. and Smith, D. E., J. Electroanal. Chem., 36 App 1 (1972)

Cullity B. D. "Elements of X-Ray Diffraction" 2nd ed., Addison-Wesley Publishing Company, Inc., (1978) p.102

Dafft, E. G., K. Bonenkamp, and H. J. Engell, Corro. Sci., 19 (1979) p.591

David L. Bourell, "Synthesis and Processing of Nanocrystalline Powder", TMS (1996)

Demaree, J. D., G. S. Was, and N.R.Sorensen, J. Electrochem. Soc, 140(2) (1993) p.331.

Diegle R. B. and Slater J. E., Corrosion, 32 (1976) p.155

Diegle, R. B., N. R. Sorensen, and G. C. Nelson, J. Electrochem. Soc 133(9) (1986) p.1769

Diegle, R. B. and N. R. Sorensen, J. Electrochem. Soc., 135(5) (1988) p.1085

Doyle, D. M., G. Palumbo, K. T. Aust, A. M. El-Sherik and U. Erb, Acta metal. mater. 43(8) (1995) p.3027

Eigen, M., Discuss. Faraday. Soc., 24 (1957) p.251

Elkedim, O., Cao, H. S. and Guay, D., Journal of Materials Processing Technology, 121 (2002) p.383

El-Moneim, A. A., Gebert, A., Uhlemann, M., Gutfleisch, O. and Schultz, L., Corrosion Science, 44 (2002) p.1857

El-Wakkad, S. E. S. and Hickling, H., Trans. Faraday Soc. 46 (1950) p.1820

Epelboin, I. and Keddam, M, J. Electrochem. Soc., 117 (1970) p.1052

Erb, U., Palumbo G., R. Zugic and K. T. Aust, "Processing and properties of nanocrystalline materials", TMS (1996) p.93

Erb, U, Canadian Metallurgical Quarterly, 34-3 (1995) p.275

Erb, U., Aust, K. T., Palumbo,.G, McCrea, J., and Gonzalez, F., Proceeding from Processing and Fabrication of Advanced materials IX,St.Louis, ASM, (2001) p. 253

Erlebacher, J., M. J. Aziz, A. Karma, N. Dimitrov and K. Sieradzki, Nature, 410 (2001) p.450

Fecht, H. J., Physical Review Letters, 65(5) (1990) p.610

Flis, J. and D. J. Duquette, Corrosion, 41(12) (1985) p.700

Foelske, A., and H. H. Strehblow, Surface and Interface Analysis, 29 (2000) p.548

Foelske, A., and H. H. Strehblow, Surface and Interface Analysis, 34 (2002) p.125

Foley, R. T. and Trzaskoma, "Passivity of Metals", (R.P. Franken and Krugen, eds) The electrochemical society, Pennington, (1978) p.337

Folleher, B. and Heusler, K. E., J. Electrochem. Chem., 180 (1984) p.77

Fontana, M. G., Corrosion Engineering, 3rd ed., McGraw-Hill, NY, (1986) p.46.

Gao, X. and M. Kowaka, Corrosion Engineering 40 (1991) p589, p701.

Gleiter, H., Proceeding of the Second Riso International Symposium on Metallurgy and Materials Science (edited by Hansen N. et al), Roskilde, (1981) p.15

Gleiter, H., Progress in Materials Science, 33 (1989) p.223

Gniewek, J., J. Pezy, B.G. Baker and O'M. J. Bockris, J. Electrochem. Soc., 125 (1978) p.17

Grake, H. J., Muller-Lorenz, E. M., Strauss, S., Pippel, E., and Woltersdorf, J., Oxid. Met., 50 (1998) p.314

Gudic, S., J. Radosevic and M. Kliskic, Electrochimica Acta, 47 (2004) p.3009

Hadjipanayis, G. C. and R W. Siegel, "Nanophase Materials", Kluwer Academic Publishers (1993)

Hansen, M., and Anderto, P., Binary Alloy System, McGraw-Hill, NY, (1958)

Hashmoto, U., Nippon Kinzoku Gakkai-Si, 2 (1938) p.67

Heusler K. E., Corro. Sci,. 39(7) (1997) p.1177

Heusler, K. E., Ber. Bunsengers. Phys. Chem., 7 (1967) p.620

Heusler, K. E., Z. Elektrochem. Ber. Bunsengens. Phys. Chem., 66, (1962) p.177

Heusler, K. E., Encyclopedia of Electrochemistry of the Elements, A. J. Bard, ed. Marcel Dekker, New York, (1982), Vol. 9A, p.230

Helfand, M. A., C. R. Clayton, R. B. Diegel, N. R. Sorenson J. Electrochem. Soc 139(8) (1992) p.2121

Hibbard, G., Aust, K. T., Palumbo, G., and Erb, U., Scripta mater. 44 (2001) p.513

Hillbert, F., Miyoshi, Y., Eicjkorn, G. and Lorenz, W. J., J. Electrochem. Soc., 117 (1971) p.1927

Holliday, J. E. and H. W. Pickering, J. Electrochem. Soc., 120 (1973) p.470

Horanyi, G. and M. Wasberg, J. Electroanalytical Chemistry, 404 (1996) p.261

Horanyi, G., J. Solid State Electrochem, 2 (1998) p.237

Horanyi, G., Corrosion Science, 46 (2004) p.1741

Hull, Phys. Rev., 14 (1919) p.540

Inturi, R. B., and Szklarska-Smialowka, Z., Corrosion, 48 (1992) p.398

Iofa, Z. A. and Wei Pao-ming, Russian J. Phys. Chem., 36 (1962) p.1395

Iofa, Z. A., V. V. Batrokov and Cho-Ngok Ba, Electrochimica Acta, 9 (1964) p.1645

Ishikawa, Y., Yishimura, T., and Ozaki, T., Corros. Eng. 40 (1991) p.643

Ismail, K. M. and Badawy, W. A., J. of Appl. Electrochem., 30 (2000) p.1303

Jaubert, G. F., Chem. Abst., 46 (1952) p.5516

Jean-Charles Dupin, Danielle Gonbeau, Philippe Vinatier and Alain Levasseur, Phys. Chem. Chem. Phys., 2 (2002) p.1319,

JCPDS, Joint Committee on Powder Diffraction Society, Powder Diffraction File (PDF) card No.5-725 (HCP Co); No.15-806 (FCC Co); No.6-595 (Co_2P) (1990)

Karimpoor, A. A, Erb, U., Aust, K. T., Wang, Z. and Palumbo, G., Materials Science Forum, 386-388 (2002) p.415

Kawashima, A., K. Asami, K. Hashmoto, Corros. Sci., 24(9) (1984) p.807

Keddam, M., Mattos, O. R., and Takenouti, H., Electrochim. Acta ,31 (1986) p.1147

Keddam, M., Mattos, O. R. and Takenouti, H., J. Electrochem. Soc., 128 (1981) p.257

Kim, S. H., Aust, K. T., Erb, U., Gonzalez, F. and Palumbo, G., Scripta Mater., 48 (2003) p.1379

Kim, S. H., Franken, T., Hibbard, G., Erb, U., Aust, K. T., and Palumbo, G., Journal of Metastable and Nanocrystalline Materials, 15-16 (2003) p.643

Kirchheim, R., Huang, X. Y., Cui, P., Birringer, R., and Gleiter, H., Nanostructured Materials, 1 (1992) p.167

Krautschick, H. J., Grabke and W. Diekmann, Corrosion Science, 28(3) (1988) p. 251

Krolikowski, A. and A. Wiecko, Electrochimica Acta, 47 (2002) p.2065

Krolikowski, A., Key Engineering Materials, 20-28(2) (1988) p.1169

Kravtsov, V. I, Acta. Chim. Acad. Sci. Hung., 18 (1959) p.321

Kupper, J., H. Erhart and H. J. Grabke, Corros. Sci., 21(3), (1981) p.227

Laurent, J. and D. Landolt, Electrochim. Acta, 36 (1991) p49

Lee, C. H. and K. O. Min, Surface and Coating Technology, 132 (2000) p.49

Longfei, Z., L. Shoufu and L. Pengxing, Surface and Coatings Technology, 36 (1988) p.455

Lopez-Hirata, V. M. and Elsa M. Arce-Estrada, Electrochimica Acta, 42 (1997) p.61

Li, R. and K. Sieradzki, Phys. Rev. Lett., 68(8) (1992) p.1168

Macdonald, D. D., Electrochim Acta, 35 (1990) p.1509

Macdonald, D. D., Corrosion, 46(13) (1990) p.229

Macdonald, J. R., Impedance Spectroscopy, Wiley, New York, (1987) p.1, p.8

Magnussen, O. M., Zitzler, L., Gleich, B., Vogt. M. R. And Behm, R. J., Electrochim Acta, 46 (2001) p.3725

Marcus, P., A. Teisser, and J. Oudar, Corros. Sci.24 (1984) p.259

McCrea, J. L., G. Palumbo, F. Gonzalez, A. Robertson and K. Panagiotopoulos, Proc. AESF SUR/FIN®'01, Session D (2001)

Michael Nastasi, Parkin, Don M. and Gleiter, H., "Mechanical properties and deformation behavior of materials having ultra-fine microstructures", Kluwer Academic Publishers (1992)

Mishra, R., and Balasubramaniam, R., Corrosion Science, 46 (2004) p.3019

Miyatani, K. K., Kohn, H. Kakimura and S. lida, J. Phs. Soc. Jap., 21 (1966) p.464

Morral, F. R., Metal Finish, June (1964) p.82; July (1964) p.59

Mottern, M. M. and Myers, J. R., Corrosion, 24(7) (1969) p.307

Mutschele, T. and Kirchheim, R., Scripta Met., 21 (1987) p.1101

Naka, M., Hashimoto, K. and Masumoto, T., Corrosion, 36 (1980) p.679

Newman, R. C. and Sieradzki, K., Corros. Sci., 263 (1994) p.1708

Nowotny, H., Z. Anorg. Chem., 254 (1947) p.31

Osmola, D. E., Renaud, E., Erb, U., Wong, L., Palumbo, G. and Aust, K. T., Mat. Res. Soc. Symp. Proc., 286 (1993) p.161

Oudar, J. and P. Marcus, Appl. Surf. Sci. 3 (1979) p.48

Palumbo, G., S. J. Thorpe, and K. T. Aust, Scripta Metal, 24 (1990) p.1347

Palumbo, G., Gonzalez, F., Brennenstuhl, A.M., Erb, U., Shmayda, F. W. and Lichtenberger, P.C., NanoStructured Materials, 9 (1997) p.737

Palumbo, G., Erb, U., McCrea, J. L., Hibbard, G. D., Brooks, I., Golzalez, F. and Panagiotopoulous, K., Proceedings-AESF SUR/FIN-American Electroplaters and Surface Finishers Society, (2002) p.676

Pangachiev, N., S. Rashkov and Z. Mutafchiev., C. R. Acad. Bulg. Sci. 13 (1960) p.705

Pickering, H. W. and Y. S. Kim, Corros. Sci. 22 (1982) p.621

Pickering, H. W., Corros. Sci. 23 (1983) p.1107

Pourbaix, M., Atlas of Electrochemical Equilbria, NY, Pergamon Press Inc., (1966) p.322, p.504

Rofagha, R., Langer R., El-Sherik A.M., Erb U., Palumbo G., and Aust K.T., Scripta Metall. Et Mater., 25 (1991) p.2867

Rofagha, R., Erb, U., Osrtander, D., Palumbo, G. and Aust, K. T., Nanostructures Materials, 2 (1993) p.1

Rofagha, R., Splinter, S. J., Erb, U. and McIntyre, N. S., Nanostructured Materials, 4(1) (1994) p.69

Roue, L., Blouin, M., Guay, R., and Schulz, R., J. Electrochem. Soc., 145(5) (1998) p.164

Safranek, W. H., The properties of the electrodeposited metals and alloys Handbook, American Elsvier, Chapter 5 (1974)

Sato Norio and Toshiaki Ohtsuka, J. Electrochem.Soc., 125-11 (1978) p.1735

Satoru Ando, Takeshi Suzuki, Kingo Itaya, J. Electroanal. Chem., 431 (1997) p.277

Schweickert, H., Doctoral Thesis, University of Karlsrulhe, (1978)

Schweickert, H., W. J. Lorenz and H. Friedburg, J. Electrochem. Soc., 127 (1980) p.1693; 128 (1981) p.1295

Smedley, S. and D. D. Macdonal, Proceedings Transient Techniques in Corrosion Science and Electrochemistry (Edited by W. H. Smyrl, D. D. Macdonald and W. J. Lorenz), , The Electrochemical Society, Pennington, NJ (1989) p.254

Sousa, C. A. C and Kiminami C. S., Journal of Non-Crystalline Solid, 219 (1997) p.155

Splinter, S. J., R. Rofagha, N. S. McIntyre, U. Erb, Surface and Interface Analysis, 24 (1986) p.181

Szklarska-Smialowska, Z., S. Shademan and R. Inturi. Mater. Sci. For., 185-188, (1995) p.1011.

Tadeusz Blaszczyk, Danuta Kazmierczak, Pawel Krzyczmonik, Henry Scholl and Krzysztof Polanski, J Solid State Electrochem., 4 (2000) p.95

Thorpe, S. J., Ramaswami, B. and Aust, K. T., J. Electrochem. Soc., 135 (1988) p.2162

Tikkanen, M. H. and T. Tuominen, Acta Polytechnica Scandinavica, Ch 70, (1968) p.1

Thomas, G. L., Siegel, R. W. and Eastman, J. A., Scripta Mat. et. mat., 24 (1989) p.201

Tomlinson, W. J. and Linzell, C. R., J. Mat. Sci., 23 (1988) p.914

Tromans, D. and Meech, J.A., Minerals Engineering, 14(11) (2001) p.1359

Tschope, A., Birringer, R., and Gleiter, H. J., J. Appl. Phys. 71 (1992) p.5391

US Patent #5,352,266, "Nanocrystalline metals and process of producing the same", November 30, 1992

US Patent #5,433,797, "Nanocrystalline metals", January 18, 1994

Wagner, C. D., Handbook of X-Ray Photoelectron Spectroscopy, Perkin-Elmer Corp., (1979) p.27

Wang, S., Ph.D. thesis, Queen's University, (1997)

Wang, S., Rofagha, P., Roberge, P. and Erb, U., Electrochem. Soc. Proc., 95-8 (1995) p.244

Wei Kun, Wu Xingfang and Fu Ying, Journal of Materials Science, 34 (1999) p.4633

Wu, Long, Chung-Chuang Wei, Tien-Shou Wu and Chain-Cheau Teng, J. Phys. C. Solid State Phys., 16 (1983) p.2803

Wurschum, R., Brossmann, U., and Schefer, H., Diffusion in nanocrystalline materials, in: C. C. Koch (Ed.) Nanostructured Materials: Processing, Properties, and Applications, Noyes Publ. Norwich, NY, (2002) p.267

Youssef, Kh. M. S., Koch, C. C., and Fedkiw, P. S., Corrosion Science, 46 (2004) p.51

Yukimi Jyoko, Izumi Ohno, and Shiro Haruyama, J. Japan. Ins. Matals, 51(1) (1987) p.51

Zeiger, W., M Schneider, D.Scharnweber and H.Worsch, Nanostructured Materials., 6 (1995) p.1013

Zidoune, M., Grosjean, M. H., Roue, L., Huot, J., and Schulz, Corrosion Science, 46 (2004) p.3041

9 Appendix

A-1. Phase Diagram (Co-P)

Phosphorous lowers the meting point of cobalt to a eutectic point (1023 °C) at which the liquid is in equilibrium with ε-cobalt and Co_2P, which melts at 1386 °C. The crystal structure of Co_2P is orthorhombic (a=6.63 Å, b=5.67 Å, C=3.52 Å) [Nowotny, H., 1947]. The phase CoP and CoP_3 also exist. The solid solubility of phosphorous in α- and ε-cobalt is insufficient to affect the lattice of the two forms of cobalt, but the temperature of α and ε transformation is reported to be affected by phosphorous, which may indicate a slight solubility not exceeding 0.63 at% phosphorous [Hansen, M., 1958].

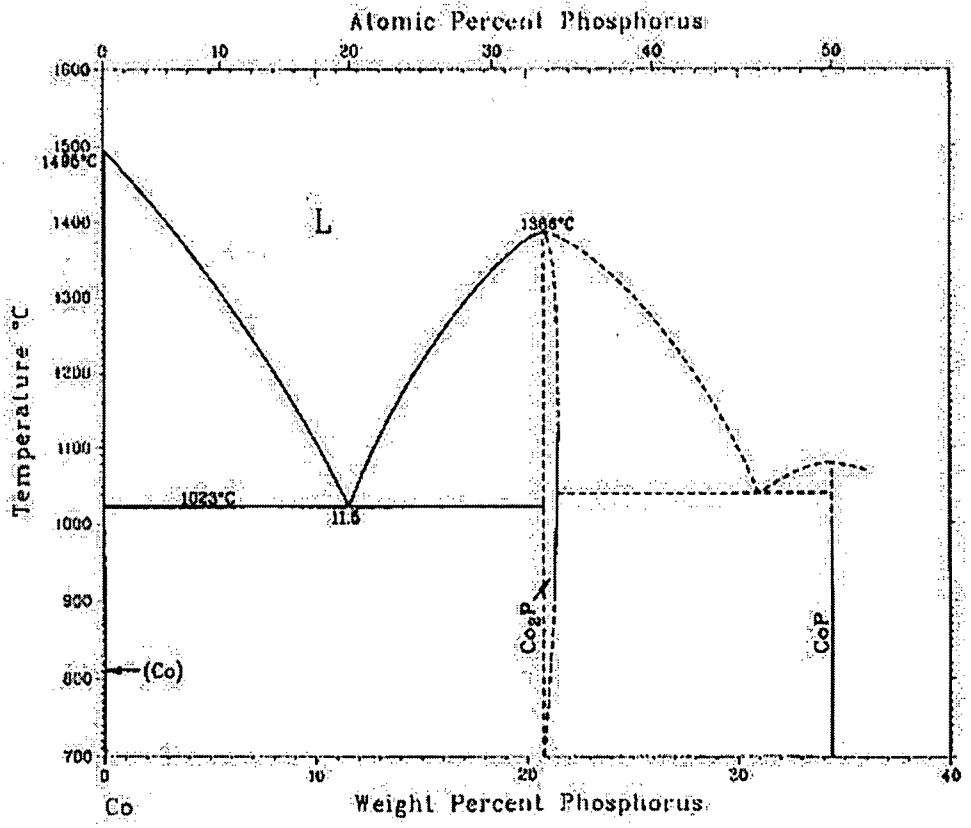

Figure A-1 Phase diagram for Co-P system [ASM Handbook, 1992]

A-2. Line Broadening Equations

The grain sizes of ultra fined crystalline materials (e.g. less than 100 nm) can be estimated by direct calculation using Scherrer's formula [Cullity, 1978] relating the broadening of X-ray diffraction peaks (B) to the grain size (d) of the material. This is given in equation:

$$d = 0.9\lambda / (B \cos \theta) \qquad \text{(A-1)}$$

where λ is the X-ray wavelength and θ is the Bragg angle of the peak.

To obtain the corrected peak width (full width half maximum) due to the grain size effect alone it is necessary to consider the broadening that occurs from other sources not related to the small grain diameter (e.g., goniometer misalignment or geometric factors). This is given by:

$$B^2 = B_t^2 - B_s^2 \qquad \text{(A-2)}$$

where B_t is the total broadening and B_s is the instrument broadening obtained using a standard with large grain size.

A-3 Phase Diagram (Co-S)

This system is of considerable complexity and includes the sulfides Co_4S_3, Co_9S_8, CoS, Co_3S_4, and CoS_2. The solid solubility of sulfur in cobalt is very small, and was given as 0.04 wt% sulfur by Hashimoto, U. [1938].

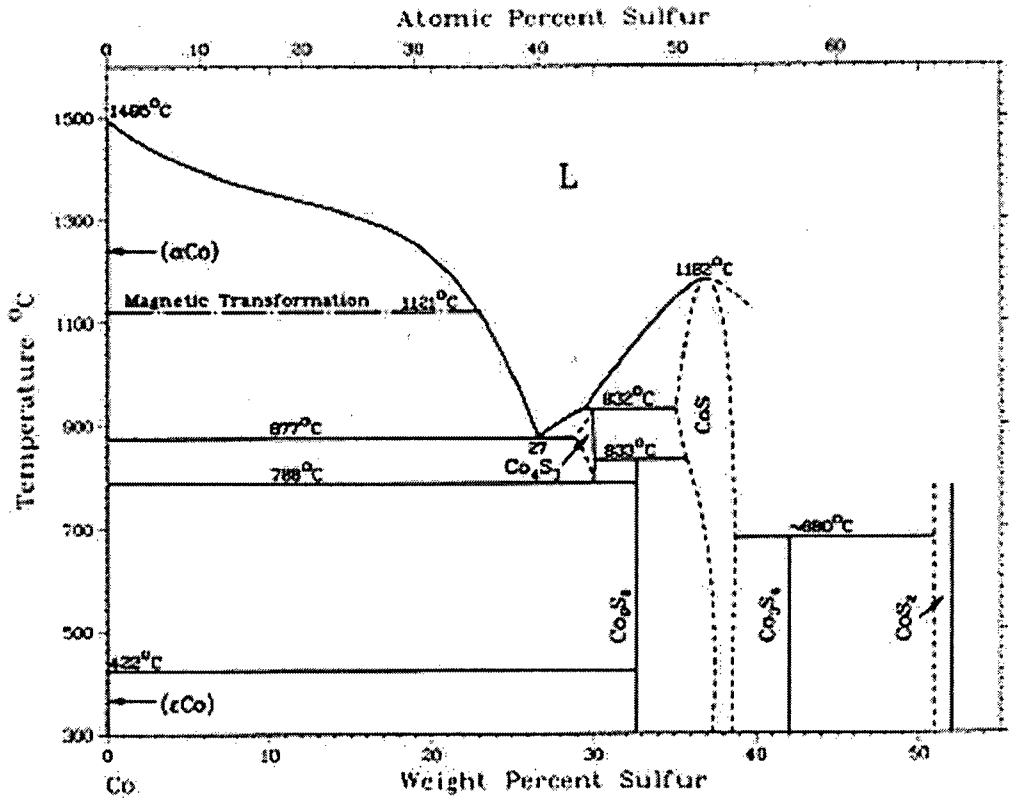

Figure A-2 Phase diagram for Co-S alloys [ASM Handbook, 1992].

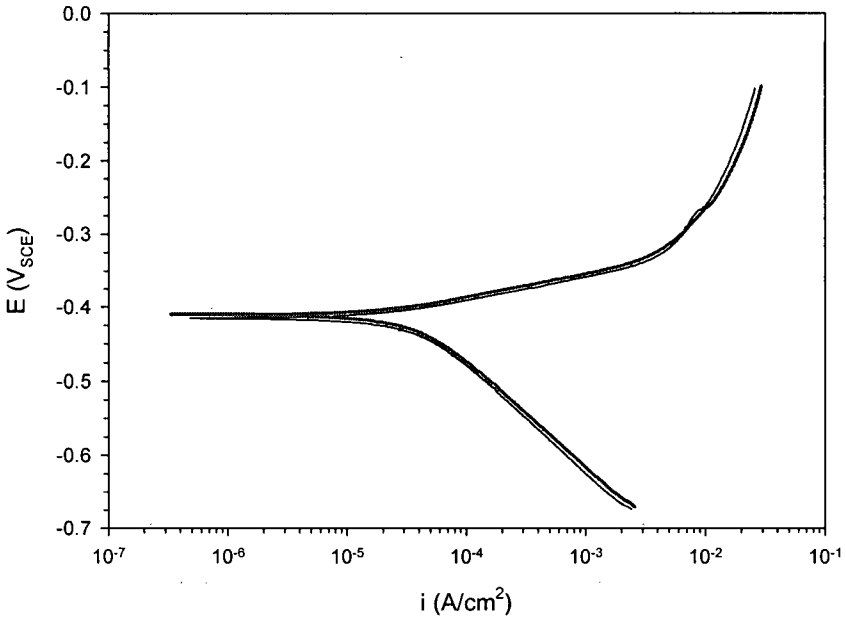

(a)

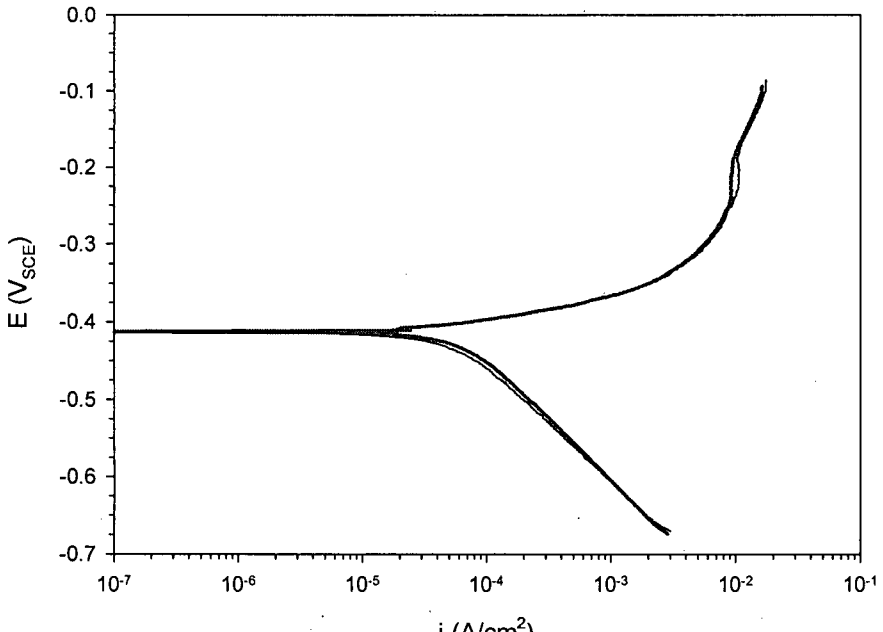

(b)

Figure A-3 Reproducibility of potentiodynamic polarization experiments for (a) annealed polycrystalline Co (27 μm, 370 ppm of S), (b) nanocrystalline Co (20 nm, 200 ppm of S), (c) nanocrystalline Co-1.1P (20 nm) and (d) nanocrystalline Co-2.1P (7 nm) in deaerated 0.1 M H_2SO_4 (pH=1) at scan rate of 0.5 mV/s.

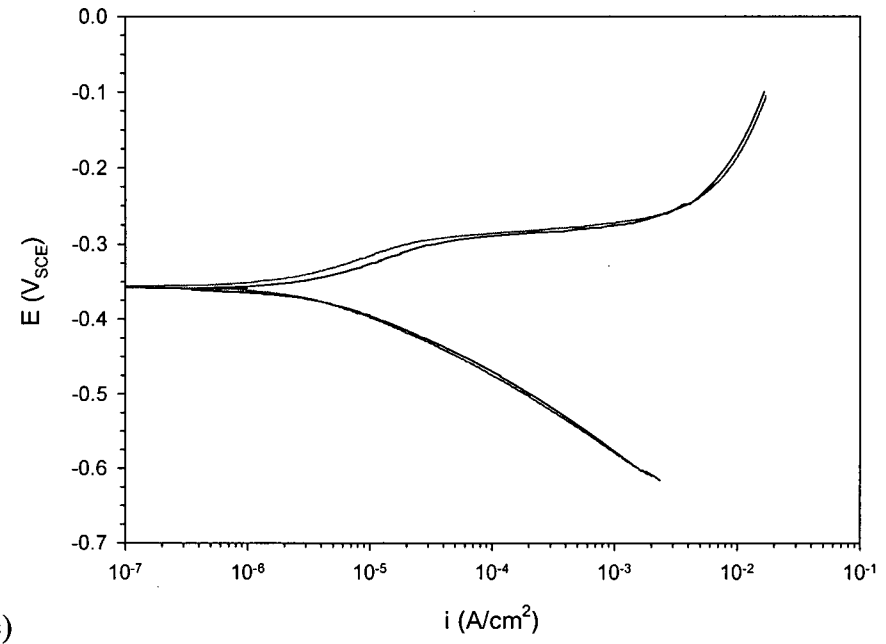

(c)

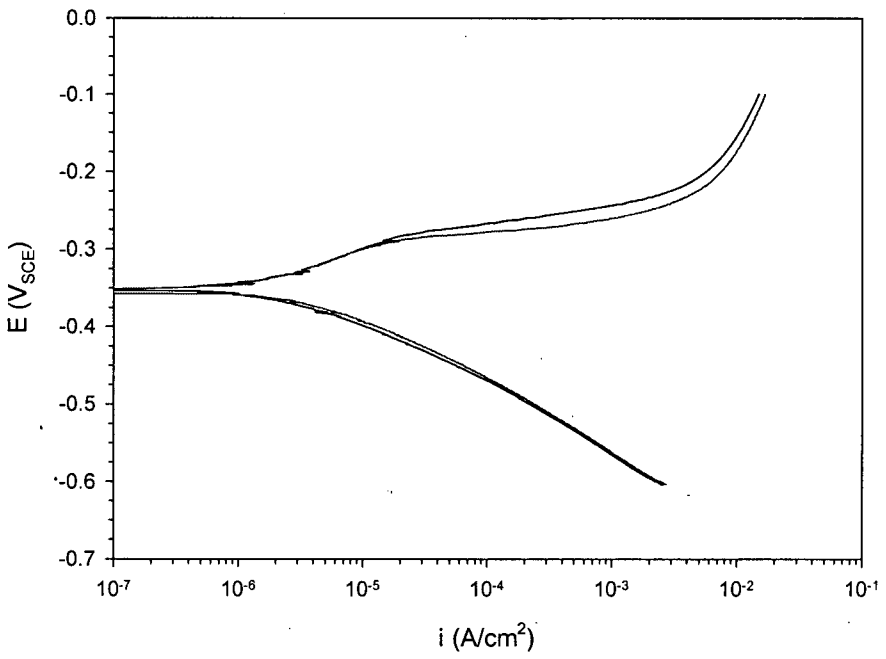

(d)

Figure A-3 (continued)

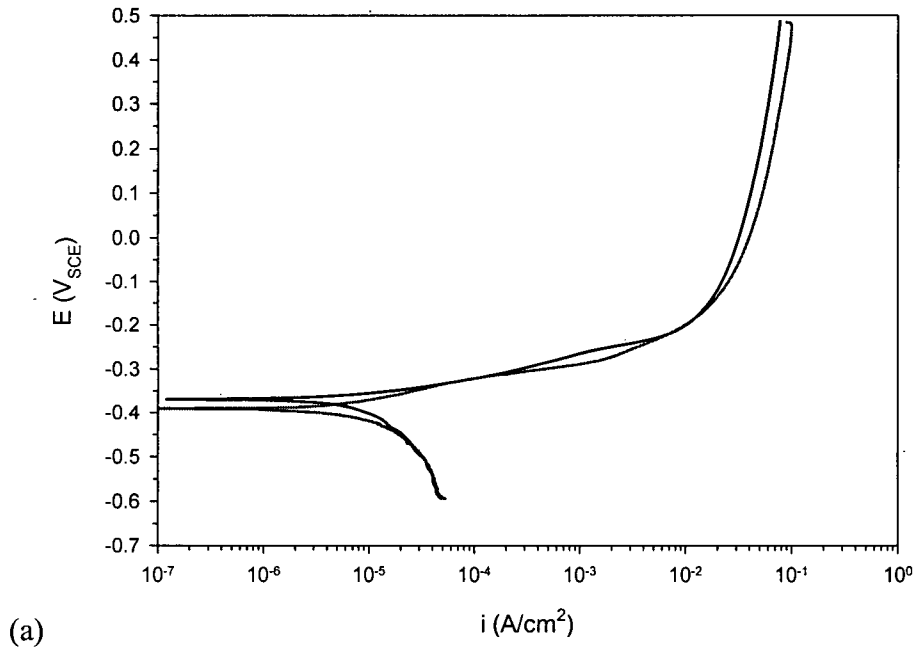

(a)

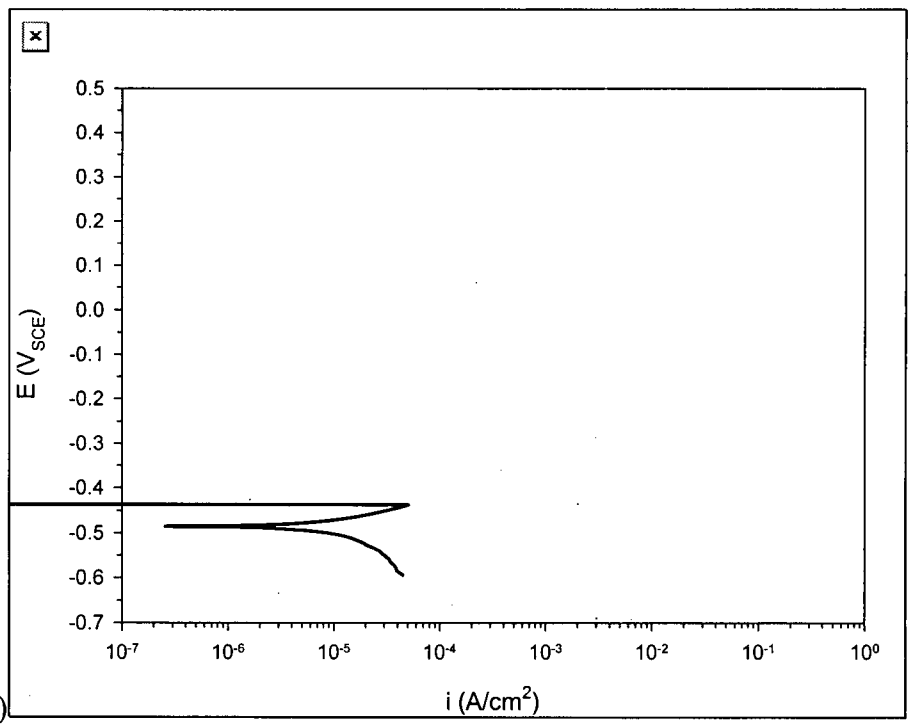

(b)

Figure A-4 Reproducibility of potentiodynamic polarization experiments for (a) nanocrystalline Co (20 nm, 200 ppm of S) and (b) nanocrystalline Co-1.1P (20 nm) in aerated 3.56 % (by weight) NaCl (pH=6.2) at a scan rate of 1 mV/s.

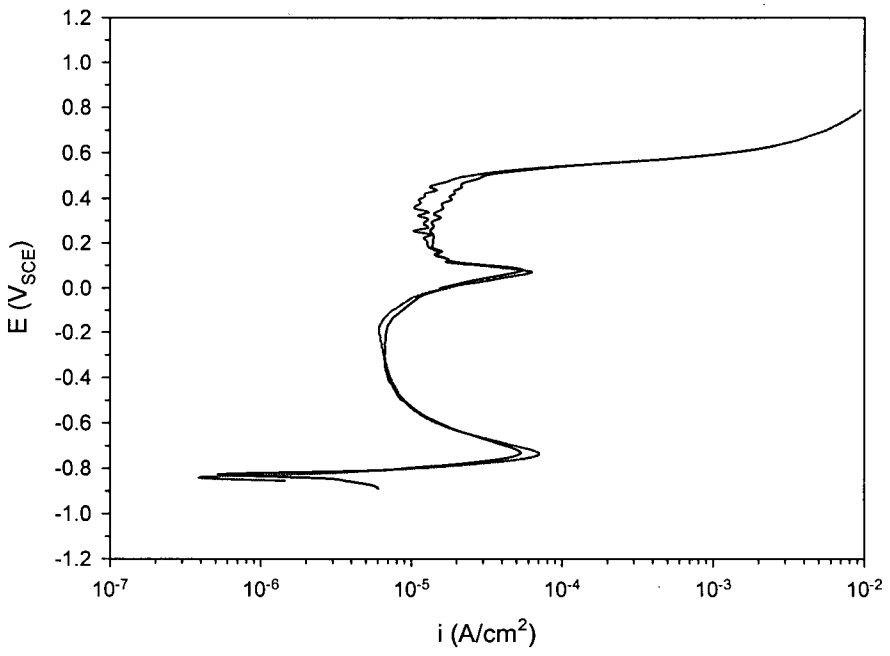

(a)

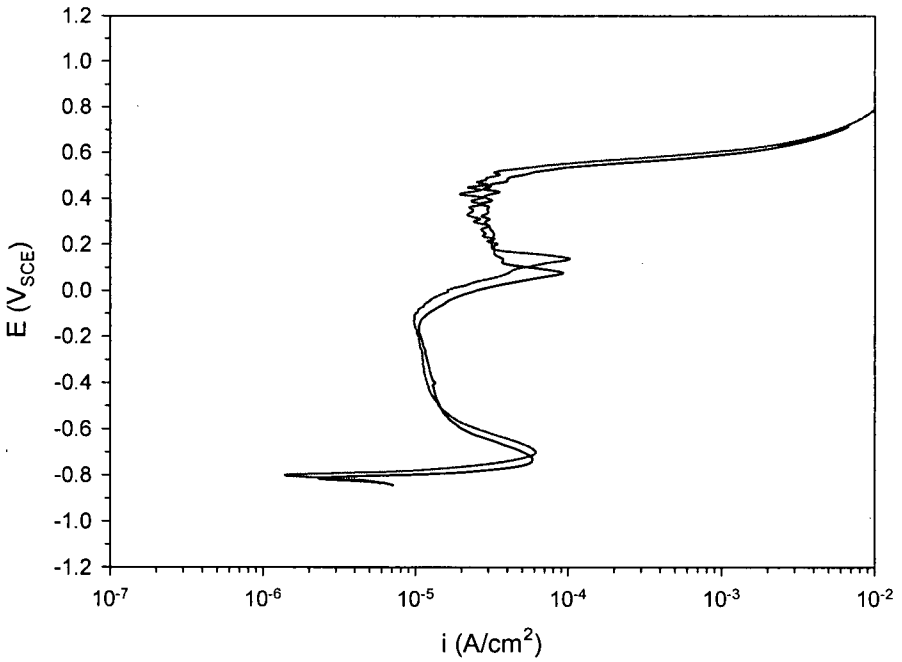

(b)

Figure A-5 Reproducibility of potentiodynamic polarization experiments for (a) annealed polycrystalline Co (27 μm, 370 ppm of S) and (b) nanocrystalline Co-2.1P (7 nm) in deaerated 0.1 M NaOH (pH=13) at a scan rate of 1 mV/s.

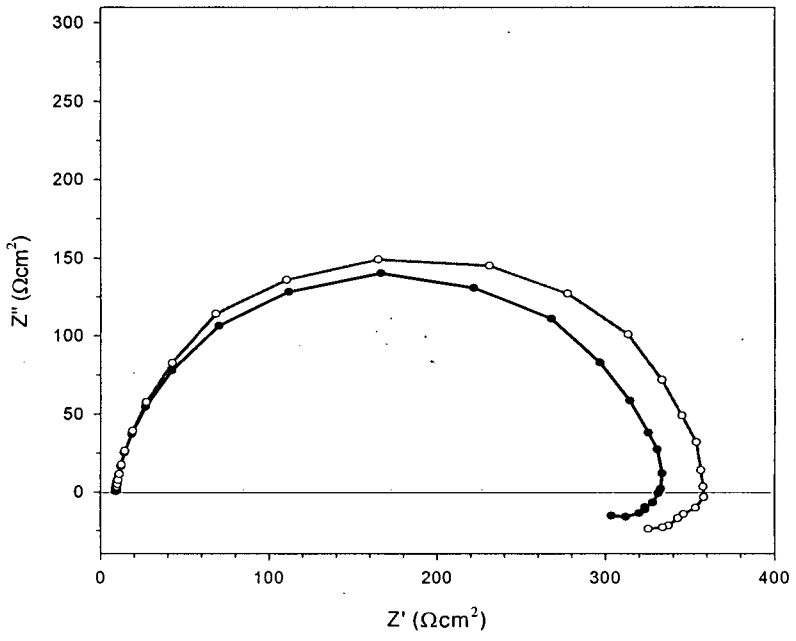

(a)

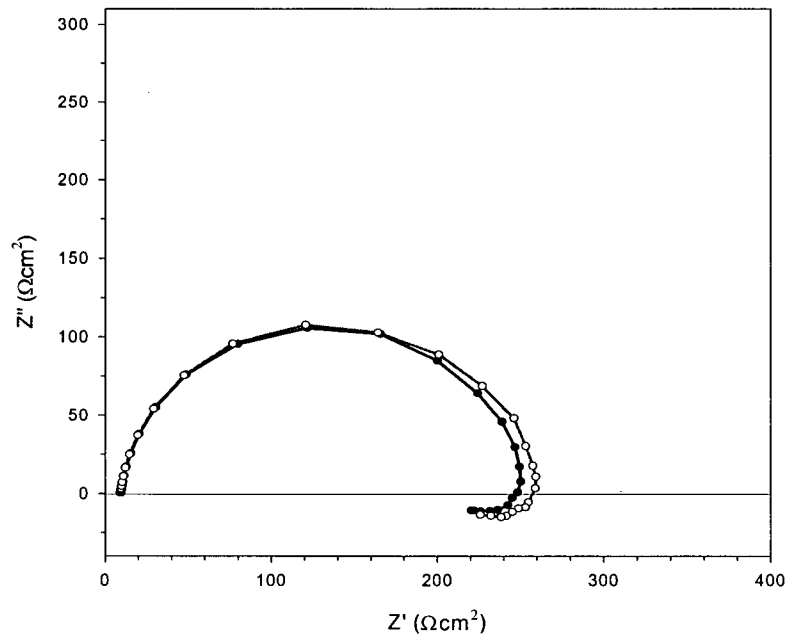

(b)

Figure A-6 Reproducibility of electrochemical impedance measurements for (a) annealed polycrystalline Co (27 μm, 370 ppm of S), (b) nanocrystalline Co (20 nm, 200 ppm of S), (c) nanocrystalline Co-1.1P (20 nm) and (d) nanocrystalline Co-2.1P (7 nm) obtained at E_{oc} in deaerated 0.1 M H_2SO_4 (pH=1)

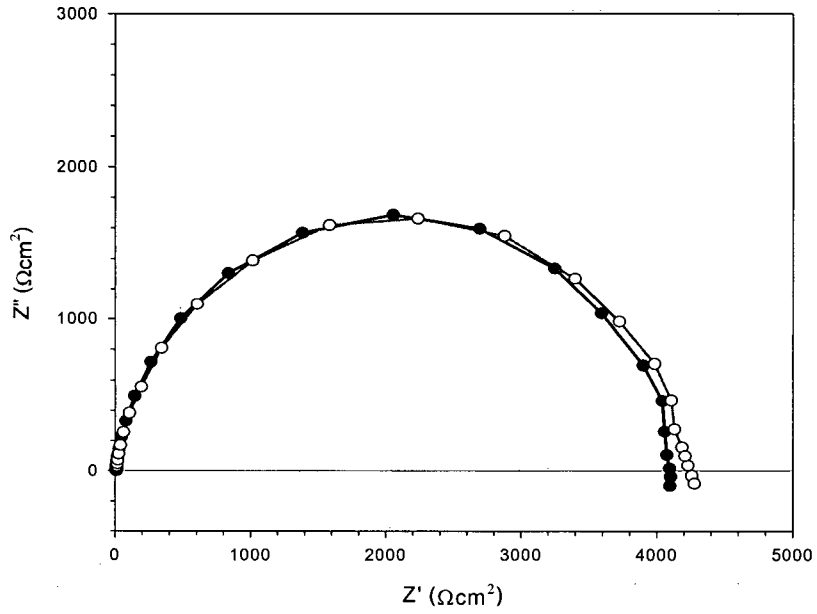

(c)

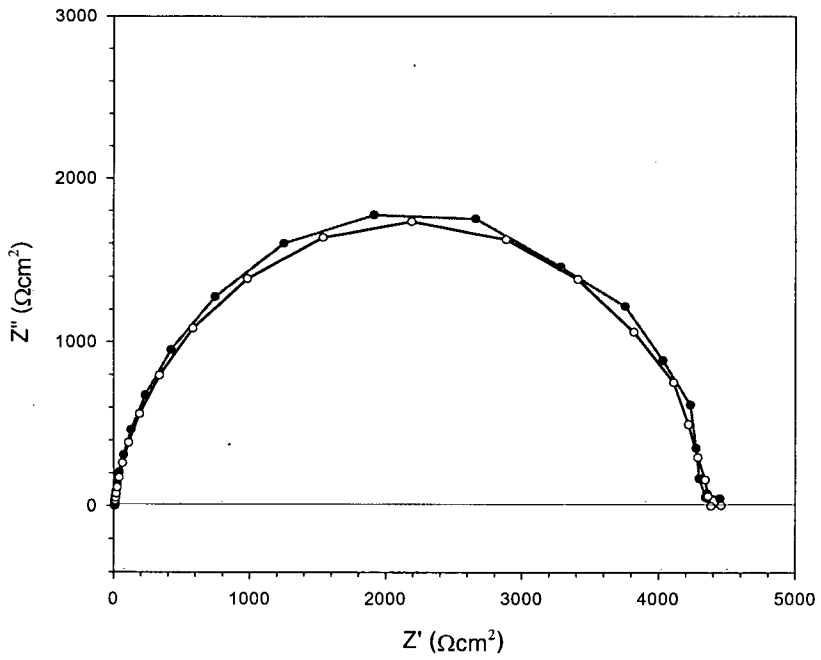

(d)

Figure A-6 (continued)

A-7 Thermal analysis

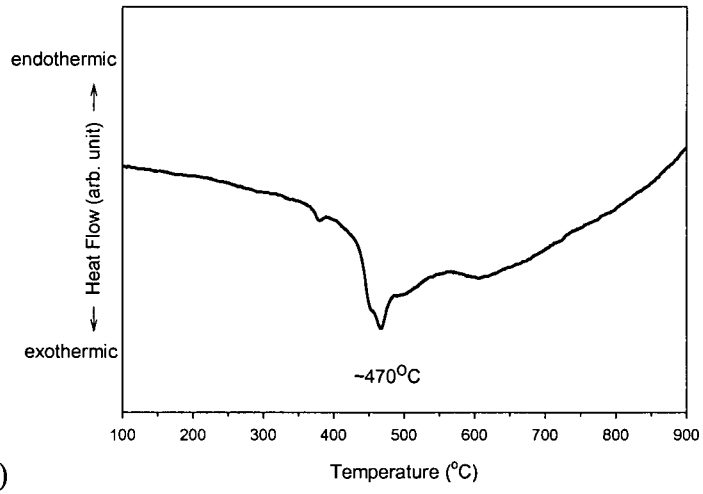

(a)

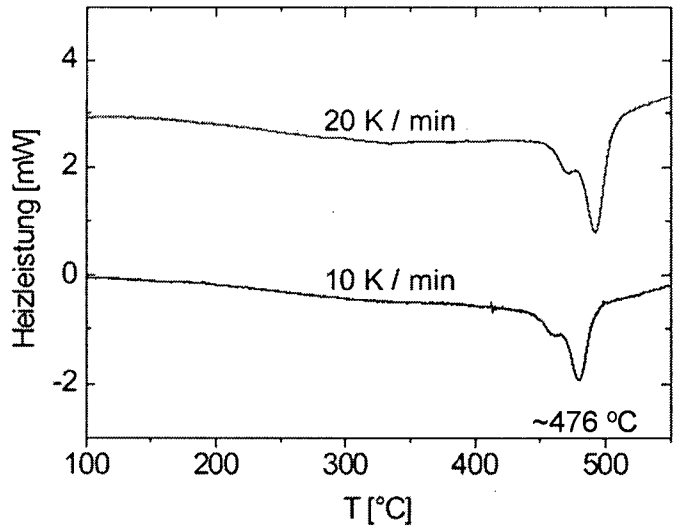

(b)

Figure A-7 Differential thermal analysis thermograms of (a) nanocrystalline Co-1.1P (10 K/min) using SETARAM TG-96 model purged with He gas in the current study and (b) nanocrystalline Co-0.6 wt% P electrodeposit in the reference [Choi, Pyuck-Pa, 2003].